New fabrication process for composite materials and numerical modelling for solar thermal applications

Shuyao Xiong

CENTRALE LILLE

THESE

Présentée en vue
d'obtenir le grade de

DOCTEUR

En

Spécialité : Molécules et Matière Condensée

Par

Shuyao XIONG

DOCTORAT DELIVRE PAR CENTRALE LILLE

Titre de la thèse :

Nouveau procédé de mise en forme de matériaux composites et modélisation numérique pour les applications par voie solaire thermique

New fabrication process for composite materials and numerical modelling for solar thermal applications

Soutenue le 07/12/2023 devant le jury d'examen :

Président	*David BALLOY, UMET, Université de Lille*
Rapporteur	*Hervé MUHR, LRGP, ENSIC-Université de Lorraine*
Rapporteur	*Lounès TADRIST, IUSTI, Aix-Marseille Université*
Membre	*Claudia COGNE, IUT, Université Claude Bernard Lyon 1*
Membre	*Gilles FLAMANT, PROMES-CNRS, Font Romeu-Odeillo*
Membre	*Guillaume TOQUER, ICSM, ENSC Montpellier*
Membre	*David BALLOY, UMET, Université de Lille*
Co-encadrant de thèse	*Fabien DHAINAUT, UCCS, Centrale Lille Institut*
Directrice de thèse	*Nouria FATAH, UCCS, Centrale Lille Institut*

Thèse préparée dans
Unité de Catalyse et Chimie du Solide (UCCS)
Ecole Doctorale SMRE 104

Centrale Lille
Cité Scientifique – CS20048 – 59651 Villeneuve d'Ascq Cedex – France
Tél. + 33 (0)3 20 33 53 53 – https://centralelille.fr

Acknowledgement

First and foremost, I sincerely thank all the jury members for devoting the time to read and examine this thesis.

I would like to express my heartfelt gratitude to my supervisor, Prof. Nouria Fatah, who has not only guided me in the research itself but also in understanding how to conduct research effectively. She is rigorous, meticulous, responsible and patient. She always gives me endless encouragement and assistance. Her optimism also influences my attitude towards life. I extend my gratitude to Mr. Fabien Dhainaut. He provides me with thorough guidance on the modeling work and is always responsive and prompt to my questions. It's a great pleasure to complete my doctoral project with their invaluable support.

I would like to thank Johann Jezequel for the help in density, BET and size distribution measurements, as well as other aide whenever I need; thank Edmond Boussekey, Allan Canipel for their various help in my daily experiments; thank Rose-Noëlle Vannier for offering me a detailed introduction and providing sintering device which is extremely important in my experiments; thank Maxence Vandewalle and Myriam Wastiaux for their help in sintering manipulation; thank Arnaud Beaurain for his enthusiastic help in LFA test; thank Nora Djelal, Alexandre Fadel and Maya Marinova for their help in SEM and TEM measurements; thank Xavier Cimetière, Mario Sanz-Lopez, Christophe Rymek and Fabien Verbrugghe for their help in electronics; thank Mohamed Safsafi for constructing the reflectors for me; thank Olivier Gardoll for the help in heat capacity test; thank Jean-Bernard Vogt and Rafeh Bechara for providing kind and detailed explanation for my doubts about the experimental results; thank Zohra Gueroui for the help in administrative affairs. Also, I want to express my thanks to the interns I've worked with: Hugo Czelaj, Simon Daumas, Adam Franchois, Hugo Capon and Amélie Kardache. It's obvious that without the assistance of these people, completing this comprehensive work would have been considerably

more challenging.

Specially, I would like to thank China Scholarship Council for providing me with the fellowship and studying opportunity.

Thanks to my friends in China and England. Despite the distance that makes it hard to meet, their care and concern always give me warmth. Thanks to all the friends and colleagues I've met in France. It's been a joy to meet them in a foreign land and create memories that will last a lifetime.

Finally, I would like to express my deepest love to my parents, and my boyfriend Zhuojun. My family will always have my back and provide unwavering support, something I never doubt. I believe this is one of the greatest joys in my life.

Content

Nomenclature

a_1	Linear Legendre coefficient
c	BET constant
c_p	Specific heat capacity of pellet
$c_{p,m}$	Specific heat capacity of the porous matrix
$c_{p,s}$	Specific heat capacity of solid phase
$c_{p,f}$	Specific heat capacity of fluid phase
C_1	First Planck´s radiation constant
C_2	Second Planck´s radiation constant
C_{2D}	Packing fraction
C_u	Uniformity coefficient
d	Diameter of pellet
d_i	Average dimension of particle in class i
$d_{i10\%}$	Particle size when the volume-cumulative percentage is equal to 10%
$d_{i60\%}$	Particle size when the volume-cumulative percentage is equal to 60%
d_p	Particle mean diameter determined by laser diffraction analysis
d_s	Particle mean diameter determined by image measurement
d_{pore}	Mean diameter of pores
$d_{3,2}$	Sauter mean diameter
D_{P1}	P1 diffusion coefficient
D	Strain rate tensor
e	Thickness of pellets
E_b	Blackbody emissive power
E_v	Illuminance
E_Ω	Internal energy
g	Gravitational acceleration
G	Irradiance
$G_{solar}(\lambda)$	Normal solar spectral irradiance
h	Convection heat transfer coefficient
HR	Hausner ratio
$I(\Omega_r)$	Radiative intensity at a given direction Ω_r
$I_b(T)$	Blackbody radiative intensity
J	Radiosity
k	Thermal conductivity
k_{eff}	Effective thermal conductivity
k_f	Thermal conductivity of fluid phase
k_s	Thermal conductivity of solid phase
k_r	Ratio of the radius of host particle to guest particle
k_R	Radiative conductivity
L	Characteristic length
m_{pellet}	Pellet mass

m_{sample}	Sample mass
$\mathbf{n}$	Normal vector
n	refractive index
N_A	Avogadro's constant
N_i	Number of particles in class i
p	Equilibrium pressure in BET measurement
p_A	Absolute pressure
p_0	Saturation pressure in BET measurement
$P_b(\lambda)$	Spectral radiance of blackbody
P_c	Surface perimeter
P_{str}	Stress power
P_1	Pressure in sample chamber before expansion
P_2	Pressure in sample chamber after expansion
q	Heat flux
$\mathbf{q}$	Conductive heat flux vector
q_{absorb}	Absorbed heat flux
$q_{conductive}$	Conductive heat flux
$q_{convective}$	Boundary convective heat flux
$q_{radiative}$	Radiative heat flux
$q_{reflective}$	Reflective heat flux
$q_{r,net}$	Net radiative heat flux
q_0	Inward heat flux
q"	Convective heat flux
Q	Additional heat source
Q_{exch}	heat exchange rate
Q_p	Pressure change work of fluid
Q_r	Radiative heat flux
Q_{ted}	Thermoelastic damping heat source
Ra_L	Rayleigh number
R_G	Radius of guest particle
R_H	Radius of host particle
s	Adsorption cross section of the adsorbing species
S	The second Piola-Kirchhoff stress tensor
S_{BET}	Specific surface area
S_c	Surface area
S_i	The ith discrete direction
S_t	Total surface area
$t_{0.5}$	Time at 50% of the temperature increase of the rear face
T_s	Absolute temperature
T_∞	Temperature at infinite distance
$\mathbf{u}$	Fluid velocity vector
V_g	Gas volume

v_m	Adsorbed N_2 quanyity corresponding to a monolayer
V_{cell}	Calibrated sample cell volume
$V_{expansion}$	Calibrated expansion volume
V_M	Volume occupied by 1 mol of adsorbate gas at STP
V_p	Total pore volume
$V_{particle}$	Volume of the particles in the pellet
V_{pellet}	Volume of the pellet
V_{sample}	Sample volume
V_{total}	Total volume
w	Mass fraction of guest particles
α	Absorptivity
α_{ab}	Absorptivity at ambient band
α_{sb}	Absorptivity at solar band
α_f	Thermal expansion coefficient of fluid phase
α_s	Thermal expansion coefficient of solid phase
α_t	Thermal diffusivity
ε	Emissivity
θ_s	Volume fraction of solid material in the porous matrix
κ	Absorption coefficient
λ	Wavelength
μ	Fluid's dynamic viscosity
ρ	Real density
ρ_b	Loose bulk density
ρ_f	Density of fluid phase
ρ_G	Density of guest particle
ρ_H	Density of host particle
ρ_m	Density of the porous matrix
ρ_{pellet}	Apparent density of the pellet
ρ_r	Reflectivity
$\rho_{r,d}$	Diffuse reflectivity
$\rho_{r,s}$	Specular reflectivity
ρ_s	Density of solid phase applied in modeling
ρ_t	Tapped density
σ	Stefan-Boltzman constant
σ_c	Cauchy stress tensor
σ_s	Scattering coefficient
τ	Optical thickness
φ	Porosity
φ_p	Porosity of the porous matrix
ω_j	Quadrature weights
Ω	Domain

Résumé

L'énergie solaire thermique est considérée comme une source d'énergie renouvelable, propre et durable pour la production de chaleur et d'électricité, et elle joue un rôle important dans la transition vers une économie plus verte et moins dépendante des combustibles fossiles. L'énergie solaire thermique peut être utilisée dans de nombreuses applications pour exploiter la chaleur du soleil à des fins pratiques, telles que le chauffage de parois de réacteurs pour différentes réactions, le traitement de matériaux à haute température, la production d'électricité, le chauffage domestique, le chauffage de piscines, le séchage solaire, la climatisation solaire et le dessalement solaire.

Le développement des propriétés des matériaux, notamment l'amélioration de l'absorption de l'énergie solaire et de la conductivité thermique, ainsi que la réduction des coûts, sont des facteurs clés contribuant à l'application des systèmes solaires thermiques. Dans cette étude, une nouvelle méthodologie a été proposée pour préparer de nouveaux matériaux composites de récepteur solaire appliqués dans les systèmes solaires thermiques, constitués d'une couche d'absorption solaire et d'un substrat conducteur thermique. Plusieurs poudres, dont l'AlN, l'α-SiC, le Cu, l'acier inoxydable, le graphite, le CaO (à l'échelle micronique, submicronique et nanométrique), le β-SiC, le γ-Al_2O_3 et le noir de carbone, ont été étudiées. Conformément aux progrès de l'énergie propre, des procédés innovants sans solvants ni traitement thermique ont été introduits pour le mélange et le revêtement des poudres. Les matériaux sous forme de pellets ont été fabriqués par SPS. Plus précisément, la céramique AlN à haute conductivité thermique a été préparée comme substrat avec des additifs CaO. Le

nouveau mélangeur à sec et à haute énergie de cisaillement (Picomix) a été utilisé pour le mélange des poudres. L'influence des propriétés de la poudre d'additif, de sa teneur et des conditions de mélange sur le comportement de mélange, ainsi que sur la porosité et la conductivité thermique des pastilles d'AlN, a été étudiée. Les pellets de Cu ont été obtenues par SPS de particules de Cu enrobées à sec de β-SiC dans le Picomix, dans le but de fournir une protection contre l'oxydation. Des pellets en acier inoxydable ont également été fabriquées à des fins de comparaison. Les matériaux composites des récepteurs solaires ont été enrobés avec du noir de carbone comme matériau d'absorption solaire. La céramique α-SiC a été mélangée avec des additifs Al_2O_3 et CaO dans un broyeur à boulets, puis élaborée avec le SPS, et elle a été directement utilisée comme matériau de récepteur solaire en raison de sa capacité d'absorption et de sa conductivité thermique élevées. Les propriétés physiques, chimiques, de coulabilité, texturales et structurelles des poudres et des pellets, ainsi que la porosité des matériaux, ont été mesurées et analysées. Un nouveau simulateur solaire expérimental a été conçu et construit, équipé d'une lampe de 1000 W simulant le spectre solaire et de deux réflecteurs de rayonnement (ellipsoïdal et pyramide hexagonale tronquée), et la température du matériau testé atteignant 580 °C. L'absorption de l'énergie solaire et l'efficacité du transfert de chaleur des matériaux composites du récepteur solaire ont été évaluées. De plus, la méthode des éléments finis a été utilisée pour simuler le processus de transfert de chaleur radiatif et conducteur dans les matériaux poreux. Divers modèles et géométries de matériaux poreux ont été définis et calculés afin de se rapprocher au plus près de la structure des matériaux réels (expériences) en vue d'une meilleure comparaison.

Les résultats expérimentaux ont montré que le Picomix est un excellent choix pour préparer des poudres mélangées par rapport au broyeur à boulets traditionnel, avec l'avantage d'être sans solvant et respectueux de l'environnement. La conductivité thermique de la pellet d'AlN pourrait atteindre 135,3 W/m·K avec l'ajout de 3 % en poids de nano CaO à une vitesse de rotation de mélange de 5 000 tr/min. Le revêtement à sec de β-SiC pourrait réduire le degré d'oxydation du Cu tout en assurant sa conductivité thermique élevée, faisant du revêtement à sec par Picomix une méthode de traitement anti-oxydation prometteuse. La conductivité thermique des pastilles d'α-SiC a été augmentée à 114 W/m·K avec l'ajout de 9 % en poids d'additifs Al_2O_3 et CaO. Sous le flux thermique radiatif élevé du simulateur solaire, les pellets à additif AlN avec des composites à couche de carbone, ainsi que les pellets à additif α-SiC, ont démontré des performances améliorées en termes d'absorption de l'énergie solaire et de transfert de chaleur. Les résultats de la modélisation ont montré que l'épaisseur, la porosité et la conductivité thermique avaient un effet combiné sur le transfert de chaleur des pellets poreuses. Lorsque l'épaisseur des pellets était inférieure à 50 mm, la porosité inférieure à 0,3 et la conductivité thermique supérieure à 100 W/m·K, l'efficacité de transfert de chaleur des différents pellets ne présentait pas de différences significatives. L'épaisseur de la couche d'absorption solaire a joué un rôle crucial dans le taux de transfert de chaleur de la pellet poreuse/composite. La conductivité thermique du matériau de l'absorbeur solaire avait peu d'impact sur l'absorption de l'énergie solaire et l'efficacité du transfert de chaleur de la pellet poreuse/composite lorsqu'elle dépassait 50 W/m·K. Les modèles configurés avec différentes géométries de la structure poreuse ont présenté des résultats de simulation comparables.

Abstract

Solar energy is regarded as a clean alternative to fossil fuel energy due to its non-polluting, sustainable, and easily accessible nature. The improvements in relevant materials' properties including enhanced solar energy absorption and thermal conductivity, and cost reductions, are key factors contributing to the widespread adoption of solar thermal systems. In this study, a new methodology was proposed to prepare novel composite solar receiver materials applied in solar thermal systems, which consist of the solar absorption layer and thermal conductive substrate. Several powders including AlN, α-SiC, Cu, stainless steel, graphite, CaO (micron-, submicron- and nano-scale), β-SiC, γ-Al_2O_3 and carbon black were studied. In alignment with the advancement of clean energy, innovative solvent-free and heat-treatment-free processes have been introduced for powder mixing and coating. Materials in the form of pellet were manufactured by spark plasma sintering. Specifically, AlN ceramic with high thermal conductivity was prepared as the substrate with CaO additives. The novel high-shear dry-mixer (Picomix) was applied for the powder mixing. The influence of additive powder properties, content and mixing conditions, on the mixing behavior and the porosity and thermal conductivity of AlN pellets, were investigated. Cu pellet was acquired through sintering Cu particles which were dry-coated with β-SiC in the Picomix, aiming to provide anti-oxidation protection. Stainless steel pellet was also fabricated for comparison. The composite solar receiver materials were prepared based on the above pellets with deposited carbon black as the solar absorber material. α-SiC ceramic was mixed with Al_2O_3 and CaO additives in a ball mill and sintered, which was directly used as the solar receiver material due to its high absorptivity and thermal conductivity. The physical, chemical, textural, and structural properties of the powders and pellets, as well as the materials' porosity, were measured and analyzed. An experimental solar simulator was designed and constructed, equipped with a 1000 W lamp that simulated the solar spectrum and two radiation reflectors (ellipsoidal and

secondary truncated hexagonal pyramid), with the temperature of the tested material reaching 580 ℃. The solar energy absorption and heat transfer efficiency of the composite solar receiver materials were assessed. Furthermore, the finite element method was employed to simulate the radiative and conductive heat transfer process in the composite porous pellet. Different geometric shapes were set to closely align the numerical model with the pellet structure for comparison.

The experimental results revealed that the Picomix is an excellent choice for preparing mixed powders compared to traditional ball milling, with the merits of being solvent-free and environmentally friendly. The thermal conductivity of the AlN pellet could reach 135.3 W/m·K with the addition of 3 wt% of nano CaO at a mixing rotational speed of 5000 rpm. Dry-coating of β-SiC could reduce the oxidation degree of Cu while ensuring its high thermal conductivity, making dry-coating by Picomix a promising anti-oxidation treatment method. The thermal conductivity of α-SiC pellet was increased to 114 W/m·K with the addition of 9 wt% of Al_2O_3 and CaO additives. Under the high radiative heat flux of the solar simulator, AlN-additive pellet with carbon layer composites, as well as α-SiC-additive pellet demonstrated improved performance in solar energy absorption and heat transfer.

The modeling results showed that the thickness, porosity, and thermal conductivity had a combined effect on the heat transfer of porous pellet. When the pellet's thickness was less than 50 mm, porosity was less than 0.3, and thermal conductivity was greater than 100 W/m·K, the heat transfer efficiency of different pellets did not show significant differences. The thickness of the solar absorption layer played a crucial role in the heat transfer rate of the composite porous pellet. The thermal conductivity of the solar absorber material had little impact on the solar energy absorption and heat transfer efficiency of the composite porous pellet when exceeding 50 W/m·K. Models configured with different geometries exhibited comparable simulation results.

General introduction

Solar energy is a valuable source of thermal energy for both domestic and industrial applications, owning to its cleanliness, renewability and extensive distribution. The solar receiver material, which consists of the absorption layer and thermal conductive substrate, holds a critical position in solar thermal applications. Currently, most studies apply metals such as stainless steel and Al, as the substrate. However, the expensive price, ease of corrosion and oxidation especially at high temperature, limit their application. Few studies have employed the ceramic which has high thermal conductivity, good chemical stability, wear resistance and high-temperature tolerance, making it a promising option.

For producing dense materials with high thermal conductivity for ceramics, spark plasma sintering is an essential technique. However, the strong covalent bonding, low diffusive nature of raw powders and impurities in ceramics lead to high porosity and low thermal conductivity of sintered ceramic. Hence, liquid phase sintering was introduced by adding proper solid sintering additives to facilitate the particle rearrangement and interparticle bonding, achieving dense ceramic. The additives could also react with the impurities, reducing its influence on internal thermal conduction. Ensuring the proper and uniform mixing of ceramic raw powders with additives is a significant challenge. Ball milling has been indeed a widely utilized mixing technique in the literature. However, it does have drawbacks, producing unevenly distributed powder mixtures, long duration, pollution from the milling balls and excessive energy consumption. It is thus of key importance to employ an alternative mixing technique. This also leads to a critical research point: the optimal mixing process, the impact of mixing condition and additive particle properties on the enhancement of thermal conductivity need to be investigated. In addition to fabricating high-performance ceramic-based substrates, the properties of composite solar receiver materials and their performance in solar thermal processes need to be explored. Consequently, the primary objective of this work is to establish a working methodology and process for developing materials with high solar energy absorption and high thermal conductivity for solar

thermal application. It's noteworthy that the development of this research area is relatively recent at both the laboratory and Hauts-de-France region.

In this study, a new methodology was employed to prepare the novel thermal conductive substrate applied in solar thermal systems, as well as the composite solar receiver materials. AlN and α-SiC were proposed for fabricating the ceramic substrate with high thermal conductivity. AlN and CaO additive powders were dry-mixed through a novel high-shear dry-mixer (Picomix), and then spark plasma sintered into pellet. The influence of CaO powder properties such as particle size (micron-, submicron- and nano-scale), dispersion, flowability on the mixed powders, and on the porosity and thermal conductivity of AlN pellets, were investigated. Additionally, the influence of mixing conditions, including additive content and rotational speed of Picomix, were studied. Different mixing techniques including high-shear mixing, ball milling and manual mixing were compared. α-SiC was mixed with CaO and Al_2O_3 additives in the ball mill and then sintered. Aside from ceramics, Cu pellet was sintered and applied as a representative of highly thermally conductive metal. Cu particles were dry-coated with β-SiC which has high intrinsic thermal conductivity through the Picomix, in order to provide anti-oxidation protection and enhance its stability. Stainless steel pellet was sintered for comparison as it has been commonly utilized in solar thermal researches. The composite solar receiver materials for solar thermal application were prepared based on the above pellets with carbon black as the solar absorption layer due to its high absorptivity. α-SiC-based pellet was directly used without absorbing layer, as SiC exhibited a relative high absorptivity. Various characterizations were conducted to assess the prepared powders and pellets, in terms of the physical property, morphology, chemical composition, structural property, thermal conductivity and absorptivity.

The performance of the prepared substrate was tested through the conductive heat transfer experiments using the hot plate. In order to test the solar energy absorption and heat transfer ability of the composite solar receiver materials, a solar simulator installation was constructed, and the relevant experiment was carried out. The temperature variation of the samples was measured and compared.

The pellets were exceptionally small in size (diameter of 10 mm, thickness ranging from 1.5 mm to 2.5 mm), and it was difficult to change the size due to the limitations of the sintering equipment. Despite notable variations in thermal conductivity and porosity among these pellets, the measured temperature and heat transfer efficiency showed minimal differences in the conducted experiments. Therefore, numerical modeling was employed to simulate the solar radiation absorption and heat transfer performance of porous materials. Finite element method was utilized for the study of thermal conduction through a porous medium, as well as the coupling of radiative and conductive heat transfer. For each model type, simulations were conducted with two different geometric shapes representing the pellet. One assumed the geometry as a solid matrix with uniformly distributed average porosity, while the other considered the pellet as a composition of orderly stacked spherical particles with a consistent porosity. A comprehensive study was undertaken to analyze the effects of various parameters, including porosity, thermal conductivity, thickness, and absorptivity.

Specifically, this thesis is organized as follows:

Chapter 1 gives a literature review of: solar thermal systems and applications, the composition and categories of solar receiver materials including absorber and thermal conductive substrate material, the design and manufacturing methods of the composite solar receiver materials including substrate sintering technique, powder mixing technique and absorption layer coating method, the numerical modeling of heat transfer in composite solar receiver material.

Chapter 2 presents the utilized powders, the methodologies of developing thermal conductive substrates and composite solar receiver materials, the employed characterization methods including the physical, chemical, structural aspects. Furthermore, it introduces the installation of solar simulator, and the experimental arrangements for investigating the thermal conduction and solar thermal application of the prepared materials.

Chapter 3 introduces the characterization analysis of the prepared “thermal conductive substrate” material utilized in solar thermal applications, including sintered AlN-based pellets, α-SiC-based pellets, Cu-based pellets and stainless steel pellet. The

effects of sintering additives and novel dry-mixing technique on the property of the mixed powder and sintered pellets are explored. The conductive heat transfer experimental results of these pellets are also introduced.

Chapter 4 contains the characterization analysis of the prepared composite solar receiver materials, with carbon black as the absorption layer material. The structure and effectiveness of the solar simulator are detailed. The practical solar thermal application performance of the composite materials by conducting the solar absorption and thermal conduction experiments are presented.

Chapter 5 introduces the numerical modeling of thermal conduction in the porous material (pellet) through two models. The first model (model I) assumes the geometry as a solid matrix with uniformly distributed average porosity. The second model (model II) considers the pellet as a composition of orderly stacked spherical particles with a consistent porosity. The investigation of various factors and the comparisons between the modeling and experimental results are given.

Chapter 6 presents the numerical modeling that couples the solar energy absorption with thermal conduction process of the composite porous material (pellet). Two models are presented, one (model III) assuming the geometry as a continuum and another (model IV) using a stacked spheres approach, as in Chapter 5.

At the end of the thesis, the general conclusions and perspectives are presented.

Chapter 1: Literature review

1.1 Background

Nowadays, the demand of energy around the world is increasing significantly due to the population growth and industrial evolution. Furthermore, serious environmental issues have prompted an urgent need to replace traditional fossil energy such as petroleum, coal, with clean energy. As a renewable energy source, solar energy is considered to be a clean alternative to fossil energy, since it does not produce greenhouse gases or radioactive waste. Fig. 1. 1 shows the amount of CO_2 emitted when different types of energy are used to generate electricity[1]. It is obvious that the amount of CO_2 emitted by solar energy production is much lower than that of fossil energy sources.

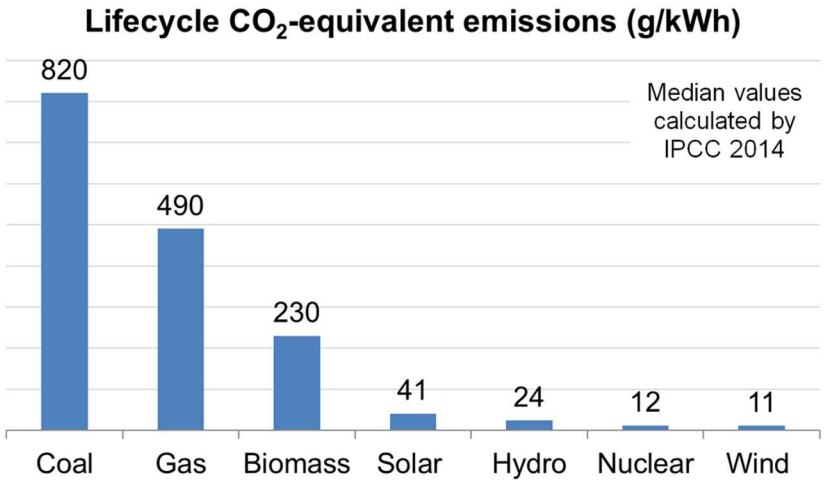

Fig. 1. 1 Lifecycle CO_2 equivalent emission from different energies[1]

In addition to the advantage of pollution free, solar energy attracts more attention and research interest due to its abundant reserves, and extensive distribution[2]. Fig. 1. 2 depicts the solar global horizontal irradiance. Globally, the annual solar irradiance ranges from 700 to 2700 kWh/m^2, which provides the possibility of its development and utilization around the world[3]. A solar energy system can be installed locally, which reduces transportation costs and energy dependencies. Many researches about

utilization of solar energy in a proper way are now under taken in order to avoid unwanted consequences arising from energy crisis and environment pollution.

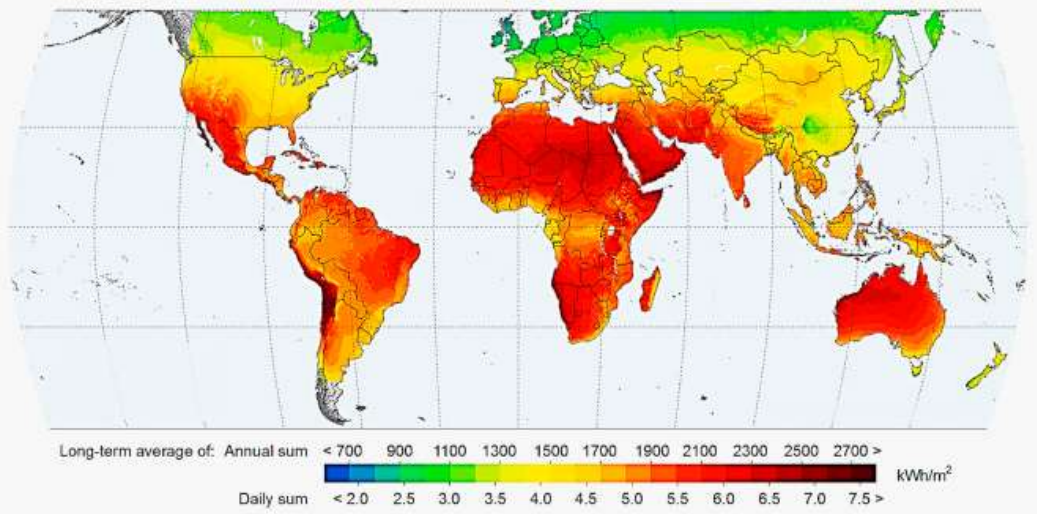

Fig. 1. 2 Maps of solar global horizontal irradiation[4]

The active technology of solar energy in industrial application has been widely explored and applied in many aspects, mainly including two categories: photovoltaic technology and solar thermal technology[5]. The photovoltaic technology is based on converting a portion of solar radiation using a photovoltaic cell. The incident light photon hits the cell and set electrons in motion, thereby generating an electric current. Whereas the solar thermal technology relies on the photothermal conversion effect to convert solar energy into thermal energy[6]. Solar-thermal power is capable of generating heat at a wide range of temperatures, from below 200 °C to over 1000 °C. Consequently, solar radiation can serve as a valuable source of thermal energy for both domestic and industrial applications, such as house heating, food processing and chemical manufacturing[7]. The solar thermal system is considered a highly attractive solution for fulfilling global thermal energy demands[8]. The research and development of solar thermal technology shows considerable strategic and practical significance.

1.2 Solar thermal systems and applications

1.2.1 Solar thermal systems

As described in the background, the development of solar thermal system is crucial. The solar thermal collector is the core component of this system (Fig. 1. 3). It absorbs incident solar radiation through the solar absorbers on the surface and converts it into thermal energy to heat the heat transfer fluid which could be water, steam or molten salts[9]. Then the heat transfer fluid can be transported to the target working area either for heating or storage.

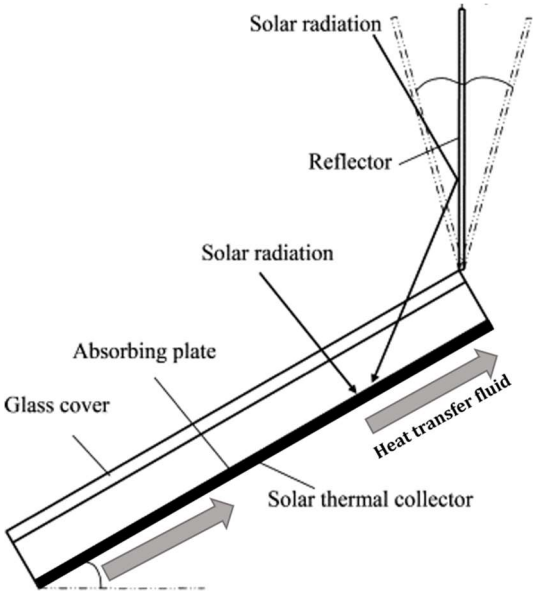

Fig. 1. 3 Schematic diagram of a solar thermal collector[10]

Depending on whether the solar rays are concentrated or not, solar thermal collectors are usually categorized into two types: non-concentrating collectors and concentrating collectors. Based on different constructions, forms or functioning principles, each type includes several sorts of collectors (Fig. 1. 4), which will be described in detail below.

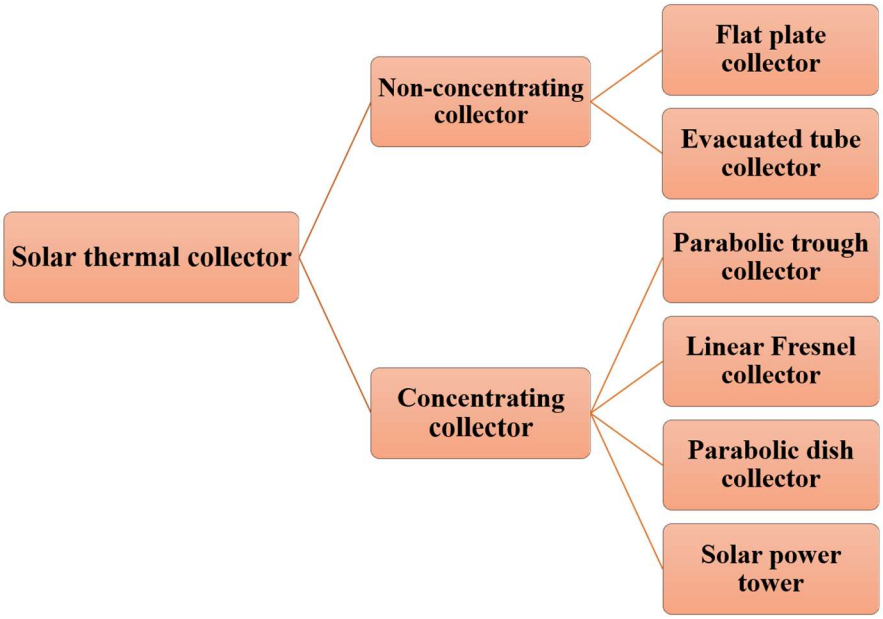

Fig. 1. 4 Classification of solar thermal collectors

1.2.1.1 Non-concentrating collectors

Non-concentrating collectors in solar thermal systems do not have reflectors, and the incident solar rays do not change the direction and are not concentrated on the absorption area. As a result, the surface of the collector receives less solar irradiation and the working temperature is low (about 30 ℃ to 200 ℃), which is more appropriate for small-scale systems with low temperature requirements[11]. The tilts and orientation angles of non-concentrating collectors vary according to different geographical latitudes and locales. Generally, they can be divided into two sorts: flat plate collector (FPC) and evacuated tube collector (ETC).

(1) Flat plate collector (FPC)

The schematic diagram of a typical flat plate collector is shown in Fig. 1. 5. It consists of a plate coated with material of high absorptivity, a transparent cover (usually glass plate), tubes or internal channels containing heat transfer fluid and a thermal insulating layer. Solar radiation transmits the glass plate and irradiates the absorption material, being converted into thermal energy and transferred to the fluid in the tube. The absorption material is typically black (such as carbon, black Ni) to absorb as much heat as possible. The glass plate not only reduces the heat loss caused by air convection

but also the radiation loss from the absorbing plate. FPC is the most extensively explored technique for producing domestic hot water and space heating[12]. FPC has relative high requirements for weather that are bright and hot, limiting its broad application.

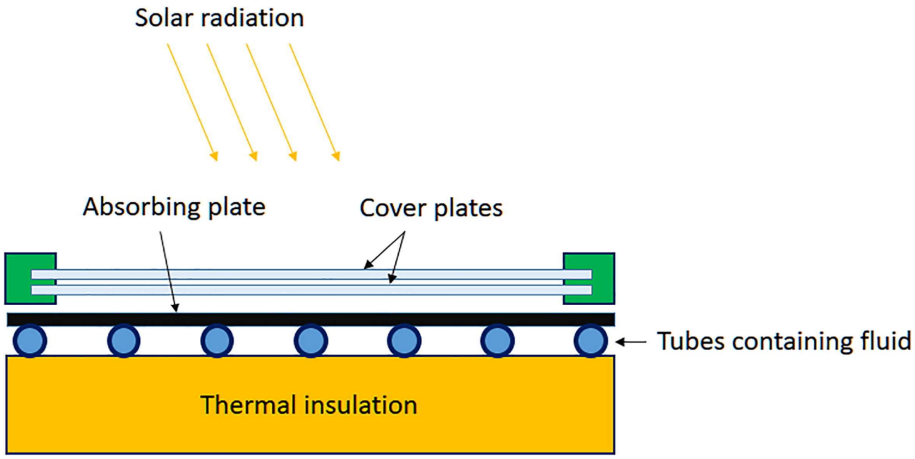

Fig. 1. 5 Schematic diagram of flat plate collector with fluid transport medium[13]

(2) Evacuated tube collector (ETC)

Evacuated tube collector is characterized by the composition of transparent vacuum glass tubes to minimize the convective heat loss. Specifically, ETC includes two kinds depending on the heat extraction ways: direct flow and heat pipe flow[14]. In the direct flow collector (Fig. 1. 6 (a)), there is a U-shaped absorbing tube with the absorption material coated on its surface in each glass tube. The cold heat transfer fluid enters from one end of the absorbing tube, gets heated as the tube absorbs solar radiation, and subsequently exits from the other end. In the heat pipe flow collector (Fig. 1. 6 (b)), there is a heat pipe on an absorber plate in each glass tube. Multiple tubes are arranged in parallel, with their upper ends connected to a manifold situated in the heating area. The heat pipe is filled with the liquid with a low boiling point which is usually alcohol or water. The absorber plate receives solar radiation, and transfers the absorbed heat to the liquid in the heat pipe, causing it to evaporate. The steam is transferred to the upper manifold to heat the heat transfer fluid in it[15]. Depending on the type of heat transfer fluid and flow rate, ETC can attain working temperatures ranging from 50 ℃ to 200 ℃, which are greater than those of FPC (30 ℃ to 80 ℃)[11].

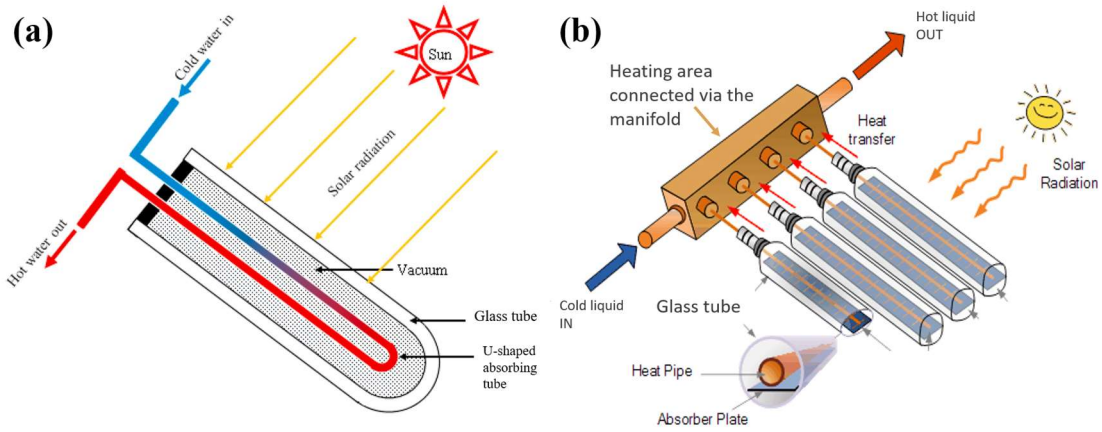

Fig. 1. 6 Schematic diagrams of evacuated tube collector, (a) direct flow[8]; (b) heat pipe flow[16]

1.2.1.2 Concentrating collectors

Generally, the concentrating collectors include the following main components: solar reflectors and solar receivers coated with absorption materials. The reflectors are employed to intercept and reflect solar rays and focus them onto a relatively small receiving area, resulting in increased heat flux and higher temperature (around 200 ℃ to 1000 ℃) compared with non-concentrating collectors[17]. So higher solar-thermal efficiency could be achieved due to less heat loss. The concentrated thermal energy could be utilized for a number of purposes including heating, electric energy generation and chemical processing. According to different shapes and working principles of reflectors, the systems are divided into four categories which are parabolic trough collector (PTC), linear Fresnel collector (LFC), parabolic dish collector (PDC) and solar power tower (SPT).

(1) Parabolic trough collector (PTC)

The parabolic trough collector is one of the most advanced and mature concentrating thermal technologies. It consists of a series of parallel parabolic trough reflectors and a linear receiver tube which located on its focal line. The solar radiation is reflected on the receiver tube by the reflector (Fig. 1. 7). The outside of the receiver is coated for high absorptivity and low thermal dissipation. The system's efficiency is calculated by dividing the generated thermal energy by the amount of collected solar

energy. The peak efficiency of PTC could rise up to 20%. The working temperature could reach 400 °C[18]. Besides, the collectors are scalable because their parabolic trough reflectors can be arranged along the common focal line, making PTC more flexible in practical application. At present, PTC is used in 80% of the world's operating plants, with the Andasol plant in Spain and the Solana plant in the United States as representative examples.

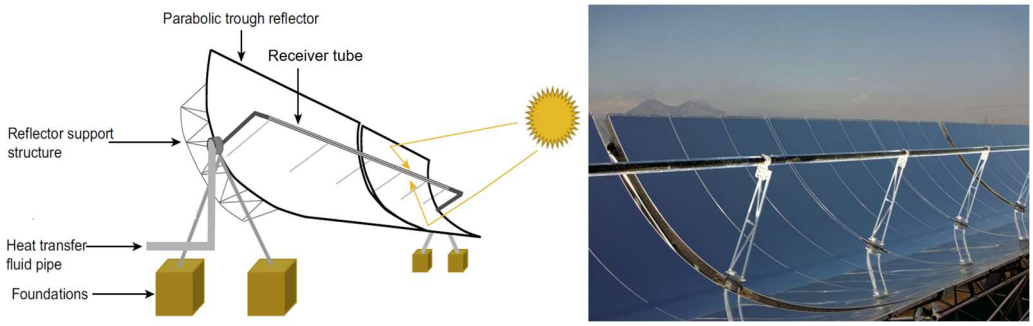

Fig. 1. 7 Schematic diagram and image of parabolic trough collector[19]

(2) Linear Fresnel collector (LFC)

In the linear Fresnel collector, the reflectors consist of an array of flat or slightly parabolic mirrors arranged at various angles relative to the ground, forming the shape of a parabolic trough. Likewise, the incident sunlight is reflected and concentrated onto the linear receiver tube (Fig. 1. 8). Compared with PTC, LFC is simpler in structure and arrangement, but its concentration ratio which is defined by the total area of the reflectors divided by the area of the receiver is lower and the maximum temperature it can reach is about 300 °C[11,20]. Puerto Errado 2 plant in Spain and Dhursar plant in India are the few commercial plants applying LFC.

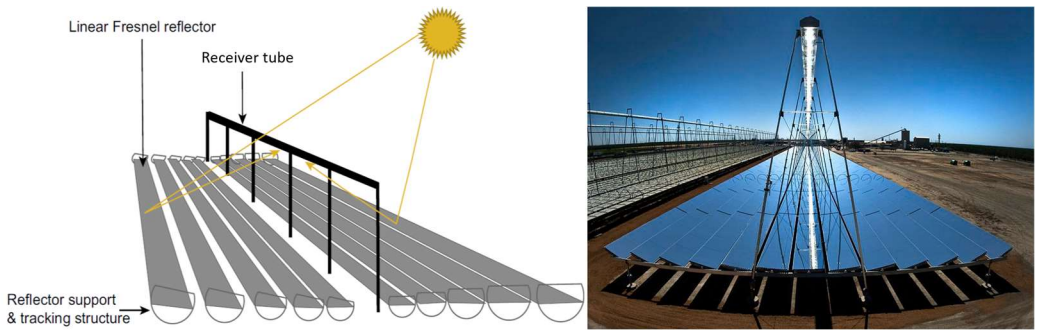

Fig. 1. 8 Schematic diagram and image of linear Fresnel collector[19]

(3) Parabolic dish collector (PDC)

The parabolic dish collector comprises a parabolic dish reflector, and a receiver positioned at the focus of the reflector (Fig. 1. 9). The Stirling engine is commonly installed at the receiver to directly generate electric energy. PDC is the most efficient in solar thermal system. It can efficiently reach the temperature ranging from 500 ℃ to 1200 ℃. Due to the difficulty of storing heat, PDC is the least commercialized technology despite owning the highest concentration efficiency of solar energy[18]. Currently it is only used for small-scale power generation.

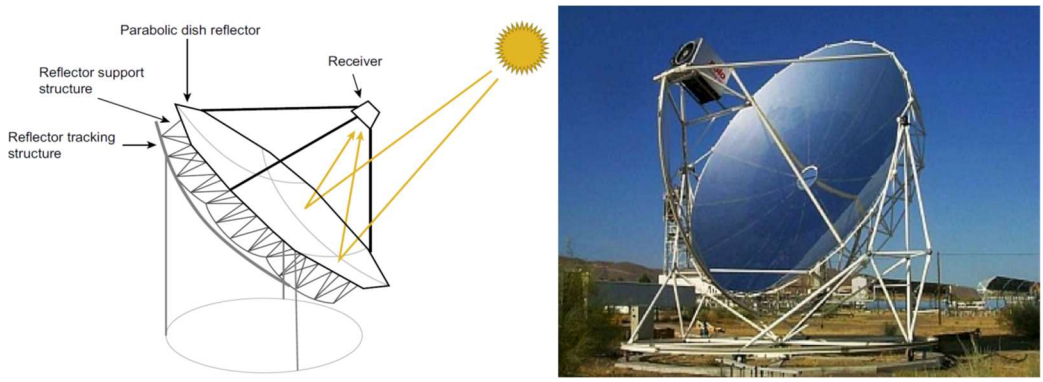

Fig. 1. 9 Schematic diagram and image of parabolic dish collector[19]

(4) Solar power tower (SPT)

The solar power tower is also known as the heliostat field collector. It consists of several mirrors that can track the location of the sun, and reflect the solar rays onto the central receiver[21]. The receiver is located on the top of the tower, of which the height is around 100 m to 150 m (Fig. 1. 10). Depending on their structure, the receivers are typically categorized into two types: external receiver and cavity receiver. The external receiver consists of absorber tubes arranged side by side in a circular configuration (Fig. 1. 10 (b-1)). The cavity receiver contains a small aperture, with the absorbing tubes arranged in parallel within the aperture (Fig. 1. 10 (b-2)). Due to their large scale and high radiation concentration efficiency, solar power tower can attain significantly high temperatures (up to 1000 ℃)[18]. However, conventional heat transfer fluid such as molten salts, has a limited working temperature range (e.g. typically 240–565 °C for binary sodium-potassium nitrate salt). Flamant et al.[22–24] proposed the innovative fluidized particle receiver that uses high-temperature-resistant particles as the heat

transfer fluid (Fig. 1. 10 (c)). This innovation enhances the working temperature effectively, presenting a promising avenue for advancing solar power tower technology.

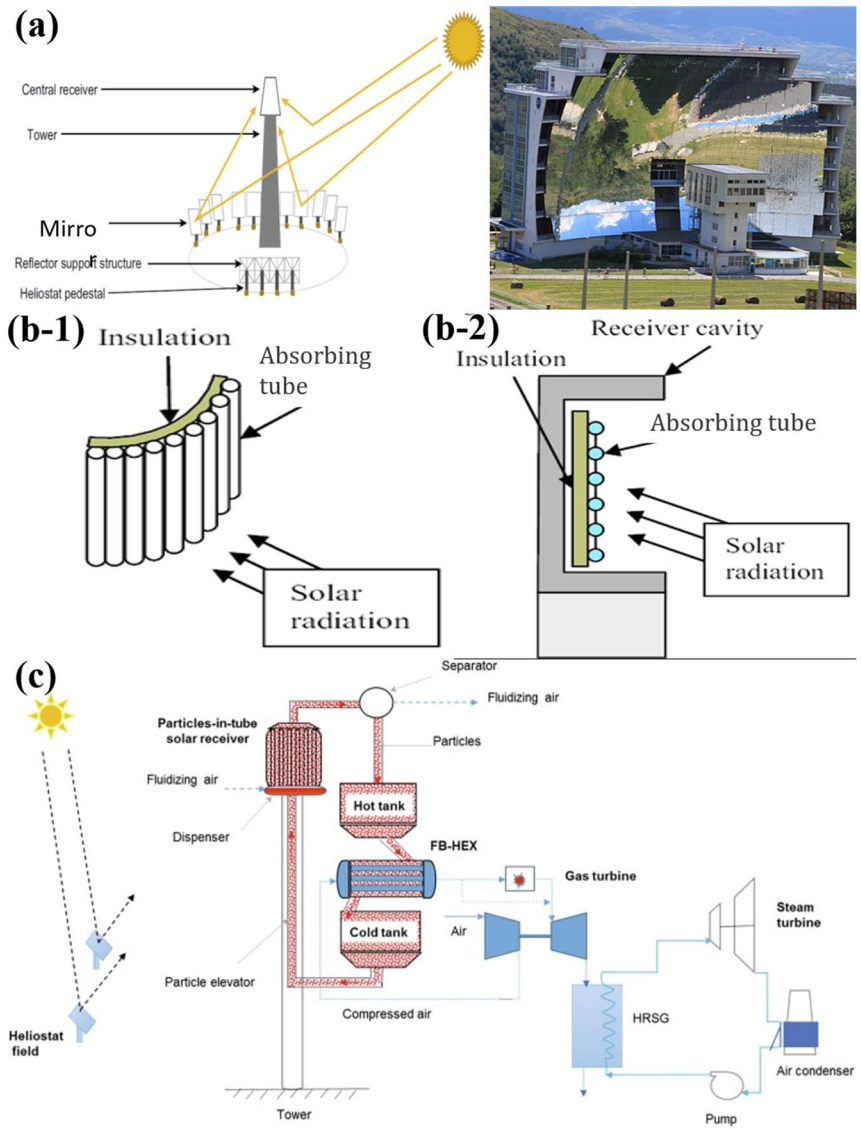

Fig. 1. 10 (a) Schematic diagram and image of solar power tower[19]; (b-1) External receiver, (b-2) Cavity receiver[25]; (c) Example of fluidized particle receiver[22]

1.2.2 Solar thermal applications

Many types of solar energy systems have been employed for diverse processes, and different applications require different kinds of solar collectors which will be introduced in this part.

1.2.2.1 Solar water/air heating

The bulk of solar thermal applications in the home and industrial parts are for solar water heating. The system usually consists of a solar collector and a storage tank as shown in Fig. 1. 11 which is a simplified version. The cold water flows through the collector to be heated and then was transferred to the storage tank by the pump or natural circulation for direct utilization or storage. The collector applied are basically non-concentrating collectors[6]. Ayompe et al.[26] compared the performance of domestic hot water systems with flat plate collector and heat pipe evacuated tube collector under the same weather conditions in Dublin. The heat generated per unit area of FPC and ETC in one year was 496 kWh/m^2 and 681 kWh/m^2, and the annual average system efficiencies of FPC and ETC calculated based on water temperature difference were 46.1% and 60.7%, respectively. It proved that the ETC system outperformed FPC in solar water heating.

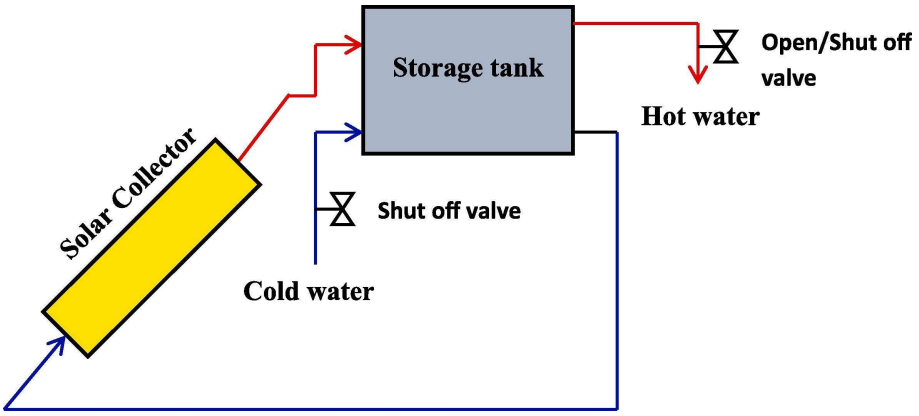

Fig. 1. 11 Schematic diagram of solar water heating system[27]

The principle of solar air heating is similar to that of water heating, and it also adopts non-concentrating collector. It is often used in houses, agricultural barns for hot air supply and industrial drying. Its schematic diagram is shown in Fig. 1. 12. Because air has a low density, volumetric heat capacity and thermal conductivity, the convective heat transfer coefficient of the surface in contact with air is low, resulting in a poor solar thermal usage efficiency. Many studies have been carried out to improve this problem. El-Sawi et al.[28] developed a novel collector with a chevron pattern folded sheet absorber through continuous folding technique, and compared its performance with a flat plate

collector under the same weather conditions. The results showed that due to the multiple reflection and absorption of radiation inside the chevron passage, this chevron collector had a reduced overall loss coefficient. Its thermal efficiency was 20% higher than that of FPC and the outlet air temperature was increased by 10 ℃.

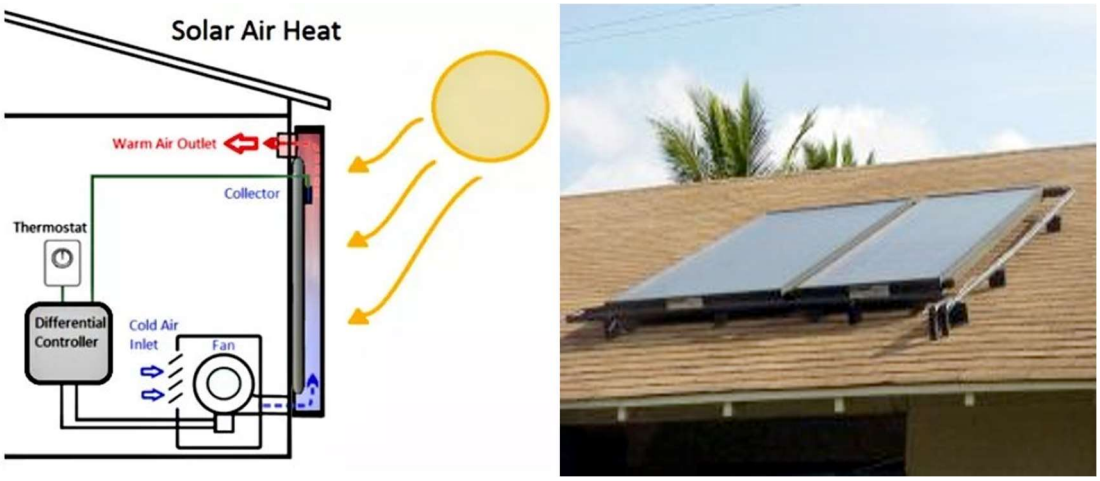

Fig. 1. 12 Schematic diagram and image of solar air heating system[29]

1.2.2.2 Solar desalination

The development of seawater desalination aims to alleviate the shortage of water resources and overcome the limitations of available water resources. This process requires a significant amount of energy, so the application of solar thermal technology is critical. Phase change and membrane technology are two commonly utilized technologies. The phase change technology involves using solar energy to generate heat and directly drive seawater through a phase change process of evaporation and condensation to separate water and salt. This system generally consists of the solar thermal collector and the desalination subsystem (Fig. 1. 13). The membrane technology converts solar radiation into heat through the solar thermal collector system, and the generated heat produces steam, driving turbines to generate electricity. A high-pressure water pump is powered by electricity and compresses seawater through a reverse osmosis membrane, separating water and salt ions[30]. Numerous studies on increasing desalination efficiency and reducing costs have been conducted. Selimefendigil et al.[31] applied nano CuO particles in the absorbing coating and thermal

storage system in the solar still. On the one hand, it could improve the absorbing layer's absorption of solar energy and solar thermal conversion efficiency, on the other hand the thermal conductivity of materials in the thermal storage system was improved and the heat energy loss was reduced. The results show that the efficiency of the solar desalination system after adding nano CuO is 19.3%, which is greater than the original system's efficiency of 15.96%. Arunkumar et al.[32] placed four carbon-impregnated foams with diameters of 0.17 m and thicknesses of 0.015 m in the water to be treated of a slope solar still, and analyzed the system efficiency through experiments and simulations. The productivity of the solar desalination system was found to be 3.1 L/m^2/day, a 24% improvement over that without foam, which might be attributed to the fact that the hydrophilic and interconnected carbon-impregnated foam acted as a heat absorbent and increased the water evaporation surface area in the basin.

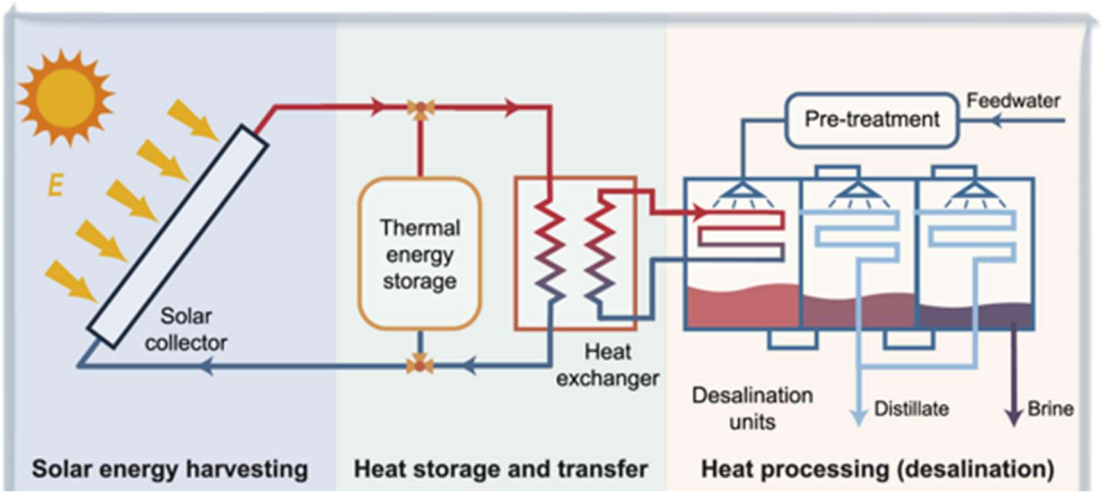

Fig. 1. 13 Schematic diagram of solar thermal desalination system[33]

1.2.2.3 Solar thermochemical reaction

Various chemical reactions including water pyrolysis, thermochemical cycling, heavy hydrocarbon molecule cracking, methane reforming, and carbonaceous solid gasification are indispensable and crucial parts in the current industrial development and application. These reactions are usually carried out in a reactor such as fluidized bed or packed bed under high temperature conditions. Concentrated solar thermal energy might be used as a high-temperature heat source to fuel all endothermic

processes. Therefore, solar reactor, which couples solar thermal conversion with chemical reactors, is a significant technological advancement for not only reducing the usage of fossil energy but also avoiding the pollution from combustion by-products to the gaseous reaction products[34].

Fig. 1. 14 (a) shows the schematic diagram of a solar reactor example. The incident solar energy is collected by the aforementioned collectors and then irradiated to the reactor chamber, providing medium-high temperature heat to fuel the thermochemical reactions. According to the different ways of heat integration, solar reactors can be divided into directly irradiated and indirectly irradiated reactors, as shown in Fig. 1. 14 (b). In directly irradiated reactors, the concentrated solar radiation is absorbed and transferred by the reactants directly, which can reduce the amount of radiation absorbed by the reactor wall and avoid heat loss through the intermediate layer. There is normally an aperture in the reactor to receive solar radiation and the system is classified as open or closed according to the absence or presence of glass windows in the aperture[35]. Because radiative heat transfer is the main way in this direct irradiation process, the capacity of reactants to absorb solar energy is critical. While in indirectly irradiated reactors, the conduction and convection are the main heat transfer modes. The reactants do not receive solar radiation directly, but are heated by the external absorber which absorbs and converts concentrated solar energy. Indirectly irradiated reactors also include two types. The first one has a separate reaction chamber that is directly irradiated. While the other contains two cavities, one of which receives solar radiation and the other functionalizes as the reaction chamber. This is for isolating the reaction area from the glass and avoiding the pollution of the glass window[36]. There are various studies on the structure and absorbing materials of reactors, aiming at improving the efficiency of solar thermochemical process. For example, Costandy et al.[37] verified that the temperature distribution of the spherical cavity is more uniform than that of the cylindrical cavity, which is conducive to the homogeneity of the reaction. Melchior et al.[38] discharged an array of tubular absorbers vertically in the cavity to absorb the incident solar radiation and a flow of water vapor reacted with carbonaceous particles in the tube. The reaction was carried out in partitions, so that the accumulation

of particles and uneven heating conditions could be avoided. In addition, various materials have been investigated as absorbers for reactors, such as graphite, Cu and SiC[39–41].

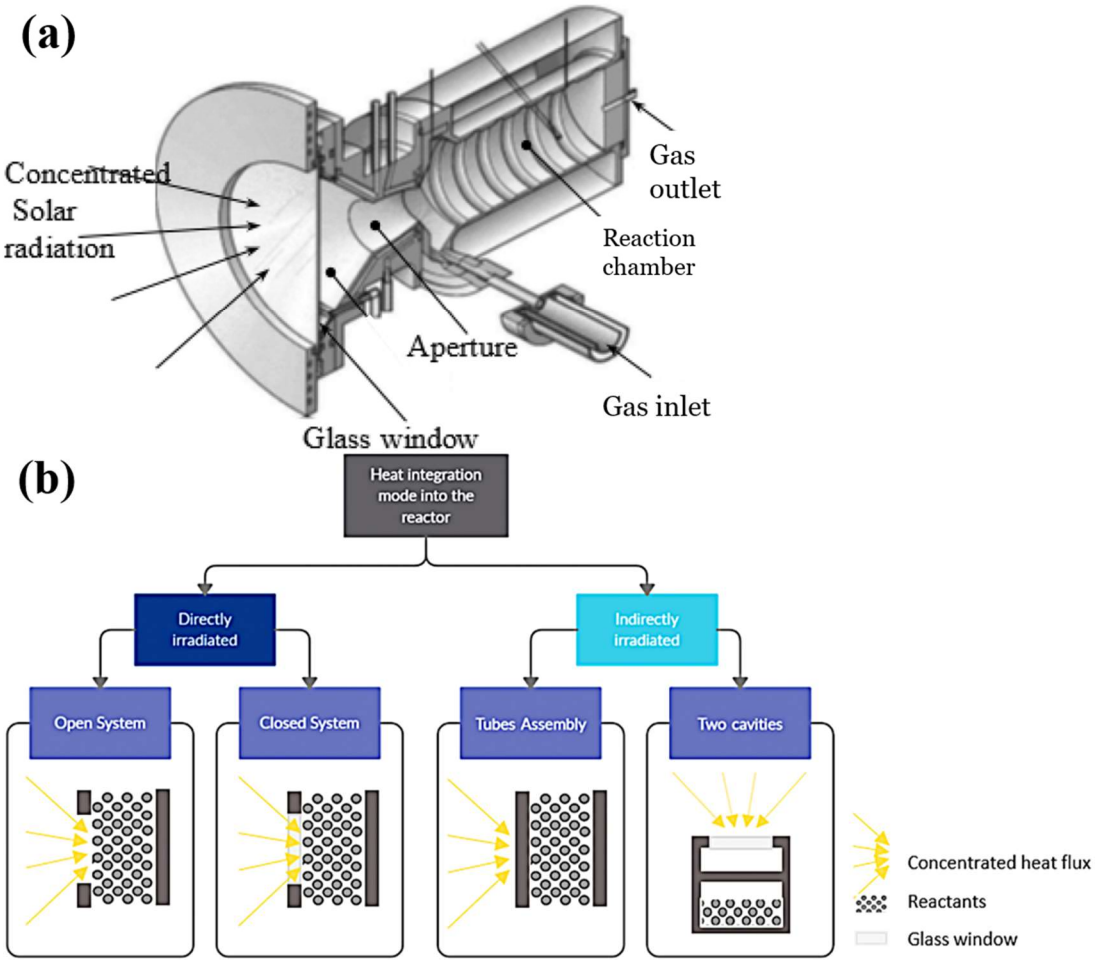

Fig. 1. 14 (a) Schematic diagram of a solar reactor example[42]; (b) Classification of solar reactors[35]

1.3 Composite solar receiver materials

The solar receiver materials, comprising the solar absorber material and a substrate, play a decisive role in the solar thermal collectors. Consequently, the principle of materials absorbing solar and converting it into heat energy, along with the classification and application of various materials are introduced in this section. As shown in Fig. 1. 15, solar energy input would be separated into several distinct energy outputs including reflected radiation, radiative heat loss from the composite solar

receiver material, conduction and convective heat loss to the heat transfer fluid in this system[43]. Therefore, excellent photothermal composites should have the following characteristics: a high solar absorptivity (α) and photothermal conversion ability of absorber, and a high thermal conductivity (k) of substrate (also named thermal conductive substrate in the following text). The mechanism of photothermal conversion as well as several absorber and substrate materials applied in the solar thermal processes are discussed.

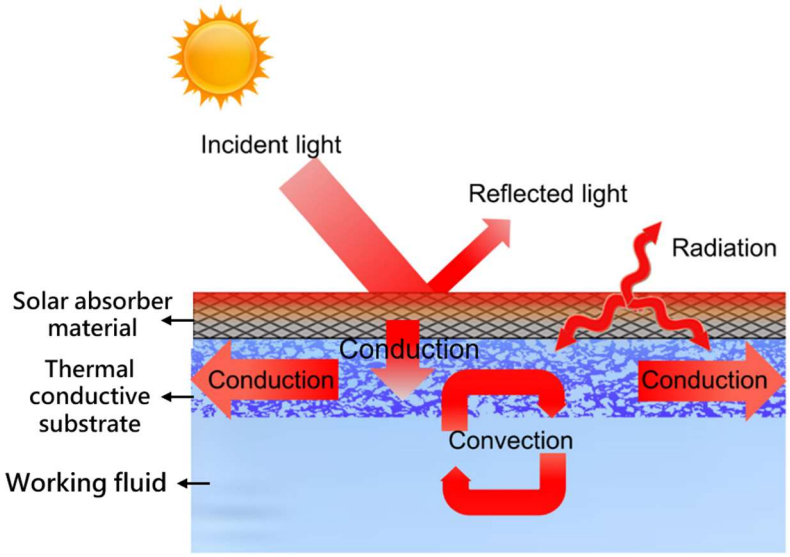

Fig. 1. 15 General schematic diagram of solar absorber photothermal conversion and substrate heat transfer working mechanism[43]

1.3.1 Photothermal conversion and solar absorber materials

1.3.1.1 Photothermal conversion mechanisms

Solar radiation exists in the form of electromagnetic waves comprising photons with varying vibration frequencies. When the materials are struck by these energy-carrying photons, the state of their internal electrons changes which results in energy conversion. According to the different interaction mechanisms between electromagnetic radiation and solar absorber materials, the photothermal conversion mechanism can be divided into three categories: plasmonic localized heating, non-radiative relaxation and thermal vibration in molecules[44] (Fig. 1. 16).

(1) Plasmonic localized heating in solar absorber materials

Plasmonic localized heating usually occurs in metals. The photothermal conversion is usually caused by the localized surface plasmon resonance (LSPR) effect as shown in Fig. 1. 16 (a). LSPR is a resonant photon-induced coherent oscillation of charges. When the frequency of incident photons coincides with the natural frequency of electrons on the metal surface, photons induce coherent oscillations of electrons and electrons are excited from occupied to unoccupied states. The vibrating electrons collide with other electrons, crystals lattice and surface ligands, so the kinetic energy of excited electrons are transformed into thermal energy through the joule mechanism, resulting in hot electrons[43]. The heat generated by hot electrons is rapidly transferred and distributed via phonon-phonon coupling, raising the metal temperature quickly[42]. The phonon is quantized lattice vibrational energy which can realize heat diffusion by vibration of the lattice within the material[45].

(2) Non-radiative relaxation in solar absorber materials

Non-radiative relaxation usually occurs in semiconductors. When a semiconductor is illuminated by sunlight with a wavelength longer than the excitation wavelength, electrons in the valence band would leap into the conduction band and opposite holes in the valence band are left, forming electron-hole pairs (Fig. 1. 16 (b)). Excited electrons eventually return to a lower-energy state (the ground state) and release energy either by radiative relaxation that emits photons or through non-radiative relaxation that forms phonons. The lattice is locally heated when energy releases in the form of phonons and the heat is transmitted based on the optical absorption to increase the temperature of the semiconductors[46].

(3) Thermal vibration in solar absorber materials

Photothermal conversion in carbon-based and organic materials are generally through thermal vibration mechanism in molecules. When the material is irradiated by the light with energy that matches the energy of an electron's transition within the molecule, the light-absorbing electron would jump from the highest occupied molecular orbital (HOMO) to the lowest occupied molecular orbital (LUMO). Excited electrons relax through electron-phonon coupling and the released energy is transferred to the

lattice in the form of heat through phonons. As this causes the vibration of the entire lattice, the temperature of the material would be increased[44].

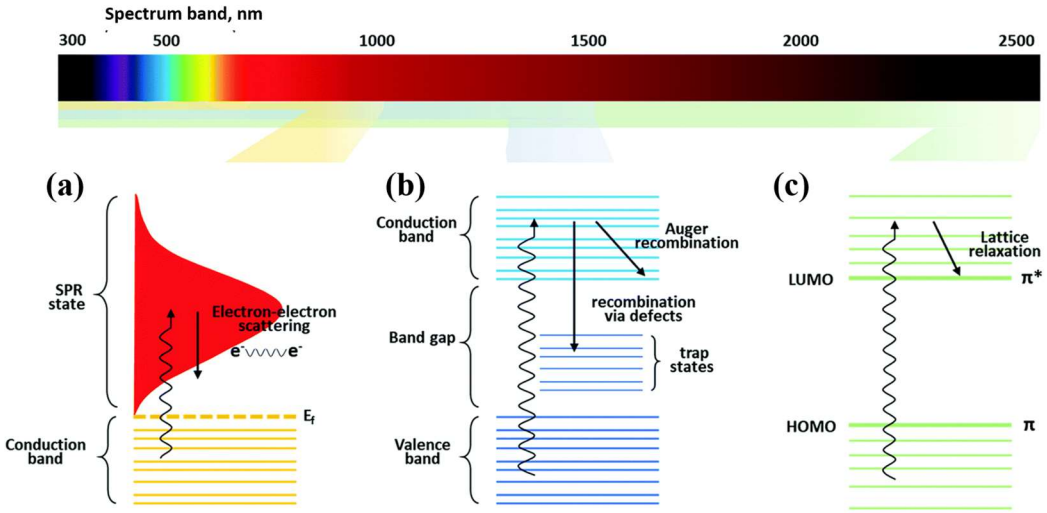

Fig. 1. 16 Photothermal conversion mechanisms with corresponding light absorption range: (a) Plasmonic localized heating; (b) Non-radiative relaxation and (c) Thermal vibration in molecules[44]

1.3.1.2 Material analysis for solar absorbers

1.3.1.2.1 Absorptivity and emissivity of the solar absorber materials

Before delving into the materials used as solar absorbers, it's essential to introduce two critical parameters: absorptivity (α) and emissivity (ε). These parameters are fundamental in assessing and quantifying the performance of materials concerning their interactions with solar radiation. α of the solar absorber materials is defined as the fraction of the radiation intensity absorbed by the material's surface to incident solar radiation. ε is the ratio of the radiation intensity emitted by the surface of the material to that emitted by a blackbody at the same temperature and over the same range of wavelengths.

The Sun is regarded as a 5800 K blackbody. Solar radiation is the radiative energy emitted by the Sun across the electromagnetic spectrum. When measuring outside of Earth's atmosphere, the average energy it emits is about 1353 W/m², which is often referred to as the "solar constant"[47]. The amount of solar energy received on Earth's

surface varies with the angle and intensity of the radiation due to the Earth's rotation and the tilt of its axis. The irradiance at which solar radiation reaches the Earth's surface is around 1000 W/m^2 on a clear day at solar noon near the equator [48]. Fig. 1. 17 shows the solar spectral irradiance distribution that reaches the Earth's surface defined by the American Society for Testing and Materials for an air mass 1.5 (AM1.5) on 37º sun facing tilted surface, commonly known as the ASTM G173-03 AM1.5 standard solar spectrum[49]. Solar radiation has a broad spectral range, with the majority of its energy concentrated in the short-wave area, including ultraviolet (UV, 0.25–0.4 μm), visible light (0.4–0.7 μm), and near-infrared (NIR, 0.7–2.5 μm) spectrum. Hence, investigations into the solar thermal application are predominantly focused within this wavelength range.

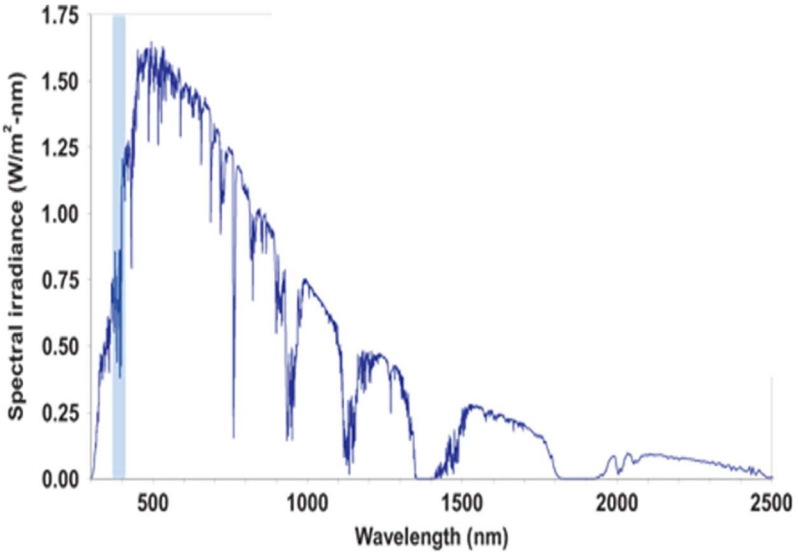

Fig. 1. 17 Solar spectral irradiance (ASTM G173-03 AM1.5 global tilted 37°)[50]

Based on the understanding of solar radiation, the absorptivity could be calculated according to Eq. 1. 1. The incident solar intensity in W/m² can be obtained by integrating the normal solar spectral irradiance $G_{solar}(\lambda)$ defined by ASTM G173-03 solar spectrum[51] over wavelength (λ) from 0.25 μm to 2.5 μm in W/m²/μm. By weighting $G_{solar}(\lambda)$ with the spectral absorptivity α(λ) of the material at each λ and integrating it over λ, the actual absorbed intensity of the material can be obtained[47].

$$\alpha = \frac{\int_{0.25\mu m}^{2.5\mu m} \alpha(\lambda) G_{solar}(\lambda) d\lambda}{\int_{0.25\mu m}^{2.5\mu} G_{solar}(\lambda) d\lambda} \quad \text{Eq. 1. 1}$$

The emissivity is determined by Eq. 1. 2. The former part is obtained by weighting the spectral radiance of the blackbody $P_b(\lambda)$ and the spectral emissivity $\varepsilon(\lambda)$ of the material and then integrating over λ from 2.5 μm to 30 μm. This wavelength range is where the emitted radiation from the surface is typically concentrated. $P_b(\lambda)$ is defined by Planck's law[47] as shown in Eq. 1. 3.

$$\varepsilon = \frac{\int_{2.5\mu m}^{30\mu m} \varepsilon(\lambda) P_b(\lambda) d\lambda}{\int_{2.5\mu}^{30\mu m} P_b(\lambda) d\lambda} \quad \text{Eq. 1. 2}$$

$$P_b(\lambda) = \frac{C_1}{\lambda^5 [exp(C_2/\lambda T) - 1]} \quad \text{Eq. 1. 3}$$

where the first and second Planck´s radiation constants are $C_1 = 3.742 \times 10^8$ W·μm^4/m^2 and $C_2 = 1.439 \times 10^4$ μm·K; T is the temperature of the blackbody. Therefore, α and ε are dimensionless values with magnitude between 0 and 1.

When solar radiation reaches a surface, some of the incident light is reflected to the ambient while the rest is absorbed by the material (transmission is not considered as most solar absorbers are opaque), as seen in Fig. 1. 15. Reflectivity (ρ_r) is defined as the ratio of the intensity of reflected light to incident light. The sum of ρ_r and α for each wavelength λ should equal 1. Furthermore, according to Kirchhoff's law[47], in thermal equilibrium any radiation that can be absorbed by a material at T at a certain λ may also be re-emitted at the same λ to maintain thermal equilibrium. Therefore, the following equation can be obtained:

$$\alpha(\lambda) = \varepsilon(\lambda) = 1 - \rho_r(\lambda) \quad \text{Eq. 1. 4}$$

The corresponding α and ε of the material are usually acquired by measuring ρ_r. In material selection applications, a good solar absorptivity is associated with a low reflectivity.

In this work, the absorptivity of the studied material powders was measured within the wavelength range of 0.2 to 2.5 μm at room temperature. This was achieved by measuring the reflectivity of the respective powder and subsequently calculating the

absorptivity by Eq. 1. 1 and Eq. 1. 4. The measurements were conducted utilizing the UV-Visible spectroscopy and Fourier-transform infrared spectroscopy.

1.3.1.2.2 Solar absorber materials

Generally, solar absorber materials can be divided into four categories: metal materials, semiconductor materials, carbon-based materials, and organic polymers. Among them, the metal materials and semiconductors are most commonly used absorbing coatings on substrates in solar thermal receivers. The details of these four categories will be introduced in this section. In particular, we will focus on introducing the absorptivity of each material. This parameter is crucial as it determines the material's capacity to absorb solar energy and its heat transfer efficiency.

(1) Metal materials

The absorptivity of metal materials is high because their absorption of solar radiation leads to the localized surface plasmon resonance effect, the principle of which was explained in Section 1.3.1.1, Chapter 1. Metals, mainly noble metals such as gold (Au), silver (Ag), copper (Cu) and palladium (Pd) with α near 1 have been widely studied and developed for photothermal applications (Tab. 1. 1). Various studies on modifying sizes and structures of metals were carried out to improve the thermal conversion efficiency. The total optical extinction, absorption, scattering cross section, and intensity of scattering quanta for spherical metallic nanostructures rise considerably with particle size[52]. Guo et al.[53] explored the diameter effect of Au nanoparticles on photothermal conversion. Au nanoparticles with different diameters were synthesized and applied for solar steam generation. The study found that the photothermal efficiency of Au nanoparticles with a diameter of 37.7 nm was 1.7 times higher than that of Au nanoparticles with a diameter of 3.7 nm, which might be attributed to that larger particle having higher absorption coefficients due to reduced scattering. Other than spheres, several structures such as rods, cages, and polyhedrons, have been produced one after another[54]. In addition, certain metals were compounded with other metals and applied in the form of composites to provide a combined effect. Amendola et al.[55] found that gold-iron alloy exhibited better solar absorption efficiency than pure gold. This was

because the alloying favored the fast generation of electron-hole pairs and photothermal conversion. Although noble metals exhibit considerable potential for absorption and photothermal conversion, their high cost remains a barrier for manufacturing and application. Various relatively inexpensive black metals such as black chromium, copper and black nickel have also been developed as solar absorber coatings[56,57].

(2) Semiconductor materials

Semiconductors commonly used in solar thermal applications include titanium oxides and nitrides (TiO_x, TiN_x), copper chalcogenides (Cu_xS/Se/Te), copper oxide (CuO), cobalt oxide (Co_3O_4), MoO_x, Si and Ge. Tab. 1. 1 lists the semiconductors used as solar absorber and their absorptivity. Due to the photothermal conversion mechanism of non-radiative relaxation, the absorption of semiconductors in the visible region is highly dependent on the band gap, which is generally 2.5–4 eV for organic semiconductors and 1–2 eV for inorganic semiconductors. Smaller bandgap semiconductors often have broader absorption spectra and high photon capture efficiency[43]. Ye et al.[58] synthesized narrow-bandgap TiO_x nanoparticles with different Ti-O ratios for solar water evaporation. The higher the Ti/O ratio, and the greater the photothermal conversion efficiency of TiO_x, which was about 50.3% with a solar irradiance of 1000 W/m^2. Dark oxide semiconductors such as CuO and Co_3O_4, known for their narrow band gaps, are also highly efficient photothermal conversion semiconductors. Moon et al.[59] synthesized a black coating based on Co_3O_4 nanoparticles for the concentrating collector. The Co_3O_4 coating exhibited strong absorption efficiency from visible light to NIR region with an absorptivity of 0.97, indicating its potential prospects.

(3) Carbon-based materials

The mechanism of carbon-based nanomaterial photothermal conversion is thermal vibration of its molecules. They are composed of carbon atoms-based frameworks, and different materials correspond to different combinations. Carbon black, carbon nanotube (CNT), graphene, graphene oxide, etc. have been extensively studied and developed[43], as seen in Tab. 1. 1. Zhang et al.[60] coated multi-walled CNTs and carbon black nanoparticles on the wood, and multi-walled CNTs were cross-linked with carbon

black particles to form a rough micro-nano structure. This black coating had superior light absorption and a wider absorption band range with an extremely high α of 97.5% and an extremely low light transmissivity of 2.5%. Lin et al.[61] coated 30 nm-thick graphene on a 3D trench-like metal substrate to form an structured graphene metamaterial for wavelength tunability and selectivity. The absorber layer achieved a photothermal conversion efficiency of up to 90.1%. Li et al.[62] used graphene oxide as the membrane to directly evaporate and desalinate seawater, which could absorb 94% of the incident light with a wavelength of 200 to 2500 nm, and the desalination rate could reach 99%.

(4) Organic polymers

Compared with other materials, organic polymer materials have advantages such as suitable flexibility, easy formability, high and broad solar absorption range and biocompatibility[43]. The photothermal conversion mechanism of polymers is similar to carbon materials in that they rely on the thermal vibration of molecules. Polyaniline (PAN), polypyrrole (PPy) and polydopamine (PDA) are commonly applied polymers (Tab. 1. 1). PAN is the most studied polymer because of its strong light absorption in the visible and NIR regions and its luminescence loss is low during conversion[63]. Wang et al.[64] coated PAN and carbon on foam to prepare porous composites for seawater desalination. The composite had a rich pore structure, good hydrophilicity, and most importantly, effective broad solar spectrum absorption (96.1%). Under 1 sun irradiation, the PAN composite exhibited a good photothermal conversion efficiency (87.3%) without an extra thermal insulator. Compared with PAN, PPy has better photostability[52]. Zhang et al.[65] deposited PPy onto a stainless steel mesh with hydrophobic modification to for self-floating on water. This PPy solar thermal evaporator showed an energy conversion efficiency of 58%, which was equivalent to systems employing noble metals or carbon-based materials. Wu et al.[66] evaluated the photothermal conversion performance of the PDA coating in water evaporation. Under the solar irradiation of 1000 W/m^2, the steam could be generated in only 5 s, and the solar-steam generation efficiency reached 87%.

Tab. 1. 1 Summarized solar absorber materials from literature[67–73]

Metal materials		Semiconductor materials		Carbon-based materials		Organic polymers	
Material	**α**	**Material**	**α**	**Material**	**α**	**Material**	**α**
Au	0.98	Ti_2O_3	0.93	Carbon black	0.89	Polyaniline	-
Ag	0.89	TiN	0.94	Carbon nanotube	0.91	Polypyrrole	-
Pt	0.92	Black TiO_2	0.89	Graphene		Polydopamine	-
Pb	0.9	CuS	0.84	Graphene oxide	0.91		
Cu	0.98	Cu_2S	0.89	Reduced graphene oxide	0.92		
Black Ni	0.94	CuO	0.93				
Black Cr	0.93	WO_3	0.93				
W	0.93	NiO	0.95				
Mo	0.95	Co_3O_4	0.9				
Co	0.95						

1.3.2 Thermal conductive materials applied in solar thermal systems

Thermal conductive substrate, in addition to solar absorber material, is a crucial component in solar receiver materials as shown in Fig. 1. 15 (also displayed below). As a substrate for the absorber coating, it transfers the heat and significantly affect the efficiency in solar thermal applications.

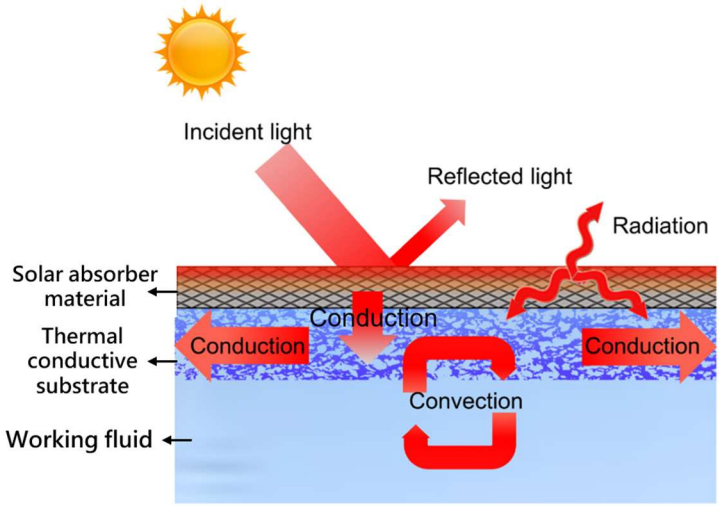

Fig. 1. 15 General schematic diagram of solar absorber photothermal conversion and substrate heat transfer working mechanism[43]

Thermal conduction occurs when a temperature gradient exists in a stationary medium (solid, gas or fluid) and heat flows through the medium from the side with higher temperature to the side with lower temperature. On a microscopic level, one atom's vibrational energy is transmitted to its neighboring atoms mainly by collision to achieve thermal equilibrium without moving[45]. When temperature increases, the atoms would vibrate more vigorously with greater thermal energy, facilitating a more efficient transfer of heat. In the situation of solid state, the conduction is synergized by two mechanisms: the migration of free electrons (dominant in metals) and phonon transport (dominant in Inorganic non-metallic materials and polymers). The schematic diagrams of the two mechanisms are shown in Fig. 1. 18. Electron migration is the action of energetic free outermost electrons on which the core has weak influence. They are easily detached and gather together inside the metal to form energy bands for heat transfer[74]. While phonon transport enables heat transfer through strongly vibrating lattices (or group) driving weaker lattice (or group) vibrations[47]. The transport of phonons in the material would be significantly disrupted if the internal crystal area is defective or even completely amorphous, the phonon scattering phenomenon would be severe, hindering the effective diffusion of heat.

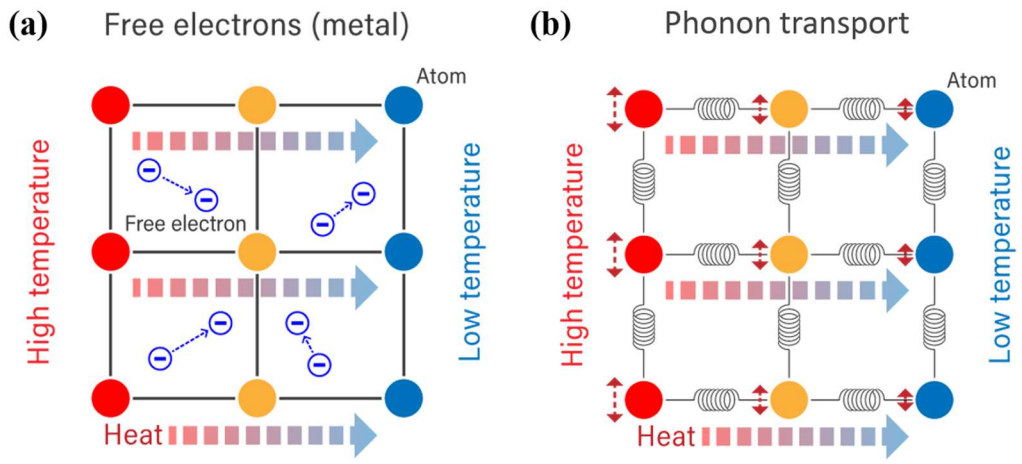

Fig. 1. 18 Schematic diagrams of thermal conduction in solid: (a) migration of free electrons and (b) phonon transport[75]

Thermal conductivity (k) is a property that reflects the inherent ability of a material to conduct heat. In specific, when the material is isotropic, k (W/m·K) could be defined based on Fourier's law[47]:

$$k = \frac{Q \cdot L}{A \cdot \Delta T} \quad \text{Eq. 1. 5}$$

where Q (W) is the amount of heat conducted through the material, L (m) is the length of the material over which the heat is conducted, A (m^2) is the cross-sectional area through which the heat is conducted, and ΔT (K) is the temperature difference across the length L through which the heat is conducted.

The materials with high thermal conductivity could be divided into three categories: metal materials, carbon-based materials and ceramic materials, as shown in Tab. 1. 2.

(1) Metal materials and their thermal conductivity

One of the notable properties of metals is high thermal conductivity due to its regular and perfect internal atomic structure. For example, the k of Ag is around 425 W/m·K and k of Au is around 315 W/m·K at 20 ℃[74]. Metal is the most prevalent type of material used as the substrate in solar receiver materials, such as stainless steel, Cu, Al, and Ni[70,72,73,76]. Arunkumar et al.[77] coated CuO on a stainless steel substrate and applied it for solar water evaporation. The evaporation efficiency reaches 53%. Aakib et al.[78] deposited Co_3O_4 films on the Cu substrate using reactive radio frequency sputtering at room temperature and in argon atmosphere. The results showed that the obtained Co_3O_4 coatings were stable and highly adherent with α as high as 0.97. Aside from functioning as a substrate, metals are used as fillers to promote heat transfer of materials in solar thermal processes. For example, Deng et al.[79] added Ag nanowires into polyethylene glycol (PEG), which greatly improved its thermal conductivity. The thermal conductivity of PEG added with 19.3 wt% Ag reached 11 times that of pure PEG.

Although metal has extraordinary thermal conduction ability, its expensive price and ease of corrosion and oxidation especially at high temperature, limit its extensive application. Moreover, the working temperature of certain metals is relatively low. For

example, the melting point of Cu is 1085 ℃, and the working temperature of stainless steel should not exceed 650 ℃[80].

(2) Carbon-based materials and their thermal conductivity

Carbon-based materials have long been recognized and widely applied for their superior heat transfer ability, stable chemical structure and low density. The thermal conduction of carbon materials is based on phonon transport, so its internal morphological structure (the π-bonding structure and the freedom from defects) has a significant impact on its conductivity[81]. Carbon fiber, carbon nanotube, graphite and graphene are the widely explored kinds with high thermal conductivities (Tab. 1. 2). In solar thermal systems, carbon-based materials are commonly applied as thermal fillers. Memon et al.[82] prepared a series of epoxy-based composites filled with different contents of graphite. The thermal conductivity of the composites with 20 wt% carbon fiber increased by 1.7 times compared to pure epoxy. Said et al.[83] suspended the carbon nanotubes in the heat transfer fluid to improve the thermal efficiency of a flat plate solar thermal collector. The thermal conductivity of the heat transfer fluid containing 0.3% volume fraction of carbon nanotubes was enhanced by 91% and the efficiency of the collector was tripled. Despite exhibiting ultra-high thermal conductivity, carbon-based materials also have disadvantages such as low strength and high cost.

(3) Ceramics and their thermal conductivity

Ceramics have somewhat poorer thermal conduction ability than metals or carbon-based materials (Tab. 1. 2), but have gained popularity due to their stable chemical characteristics, great tolerance to high temperatures, and inexpensive cost[84]. Ceramics with high thermal conductivity are generally characterized by a high degree of crystallinity and strong ionic or covalent bonding. Nitride ceramics such as aluminum nitride (AlN), carbide ceramics such as silicon carbide (SiC), and oxide ceramics such as beryllium oxide (BeO) are the most representative classes[85]. Some ceramics (mainly SiO_2 and Al_2O_3) have been fabricated as the substrate of the solar thermal collector, with vanadium-titanium as the absorber coating[86–88]. The maximum thermal efficiency of this ceramic collector achieved 0.88, according to the test completed by Ma et al.[86]. Besides, like carbon-based materials, ceramics are commonly applied as thermal fillers

in solar thermal systems. Liu et al.[89] developed porous AlN-based phase change material for solar thermal storage. The compounds incorporating AlN demonstrated a remarkable 30-fold increase in thermal conductivity (52.6 W/m·K). Chen et al.[90] added SiC nanoparticles into seawater to improve the thermal conduction within a solar desalination system. The experimental results revealed that the thermal conductivity of seawater containing SiC increased by approximately 5.2%.

In addition to having advantages such as good thermal conduction ability, good mechanical property, chemical stability, wear resistance, nontoxicity and low price, ceramic materials can tolerate working temperatures up to 1400 ℃, which is significantly higher than those of conventional metals and alloys[80].

Tab. 1. 2 Summarized high thermal conduction materials and their thermal conductivity at 20 ℃[84,91–94]

Metals		**Carbon-based materials**		**Ceramics**	
Material	**k (W/m·K)**	**Material**	**k (W/m·K)**	**Material**	**k (W/m·K)**
Ag	425	Pitch-carbon fiber	530–1100 (along axis)	AlN	200–320
Au	315	Carbon nanotube	1000–6000	BN	250–600
Cu	398	Diamond	2000	Si_3N_4	200–320
Al	237	Graphite powder	100–400 (on plane)	SiC	90–390
Ni	91	Expanded graphite	120–200	BeO	260
Zn	116	Exfoliated graphite sheet	300–400		
Mo	138	Graphene	500–6000		
Mg	153	Carbon black	6–174		

Few studies have used ceramics as thermal conductive substrates in solar receiver materials. AlN and SiC ceramics have attracted our research attention owing to their notable advantages, including high thermal conductivity, non-toxicity and chemical stability. Aside from its role as thermal fillers in solar thermal system which was introduced above, AlN is appealing for high temperature and refractory applications in other fields, such as for semiconductor devices, heat sinks, and electronic substrates[95,96].

SiC also possesses exceptional thermal properties and a wide range of applications. Particularly, SiC shows a high intrinsic absorptivity of approximately 0.83, making it a promising candidate for direct application as solar receiver materials[97]. For example, it has been used as the volumetric solar receiver material, with an interconnected porous skeleton structure[98]. The solar radiation permeates the porous structure and gets absorbed by SiC. The heat is then transferred to the heat transfer fluid for further utilization. As a result, AlN and SiC ceramics are expected to be a promising choice based on the above analysis and summary. To obtain dense bodies with high thermal conductivity, sintering is an emerging technique. However, the strong covalent bonds of AlN and SiC make achieving densification challenging during sintering, and the presence of oxygen impurities in the lattice hinder the efficient heat conduction. Hence, adding sintering additives is crucial to facilitate the sintering process and enhance their thermal conductivity, which will be introduced in the following section.

In addition to ceramics, this study delved into the potential applications of metals (Cu) and carbon-based materials (graphite) for comparison. According to the above review, Cu has been applied as the substrate material, whereas graphite has been employed as thermal fillers in solar thermal system. Sintering could also serve as a method for metal and carbon-based material to acquire dense substrate. For Cu, due to its high susceptibility to oxidation, the anti-oxidation treatment needs to be implemented. For example, Chen et al.[99] used chemical vapor deposition method to grow a graphene protective layer on the surface of Cu substrate. However, the use of chemical methods might cause a significant amount of waste solutions and environmental pollution. There is a need to develop environmentally friendly and more convenient methods for anti-oxidation treatment.

1.4 Design of composite solar receiver materials for solar thermal application

In this section, the fabrication techniques of thermal conductive substrate, and the manufacturing of composite solar receiver materials containing both substrate and absorber coating are introduced.

1.4.1 Material sintering process

1.4.1.1 Sintering mechanism and techniques

Whether for ceramics, metals or carbon-based materials, sintering is an essential technique for producing dense materials with high thermal conductivity. It is a densification process wherein powders are densely packed under high temperature (generally 0.5 to 0.7 times the melting point)[100]. In the early stage of sintering, the particles start to bond, and the contact points between the particles form sintering necks through processes such as nucleation and crystal growth. The shape of the particles and the internal grains do not change dramatically. As the gradual growth of the sintering neck, the internal atoms actively migrate to the bonding surface between the particles, reducing the distance between the particles continuously, and eventually forming a continuous pore network. The size of the grains increases and the density and strength of the particles are improved throughout this process. When the sintering behavior reaches the late stage, the pores between the particles spheroidize and shrink, and the majority of the pores are transferred to closed pores[100]. The substances on the grain boundaries continue to diffuse and fill the pores to promote the densification and grain growth[101]. Specifically, the mass transport in the sintering may be classified into six mechanisms: surface diffusion, lattice diffusion from surface or grain boundary, vapor transport, grain boundary diffusion and plastic flow, as depicted in a simplified three-particle sintering model (Fig. 1. 19)[102]. Grain boundary diffusion, lattice diffusion from grain boundary and plastic flow have great promotion effects on densification of materials.

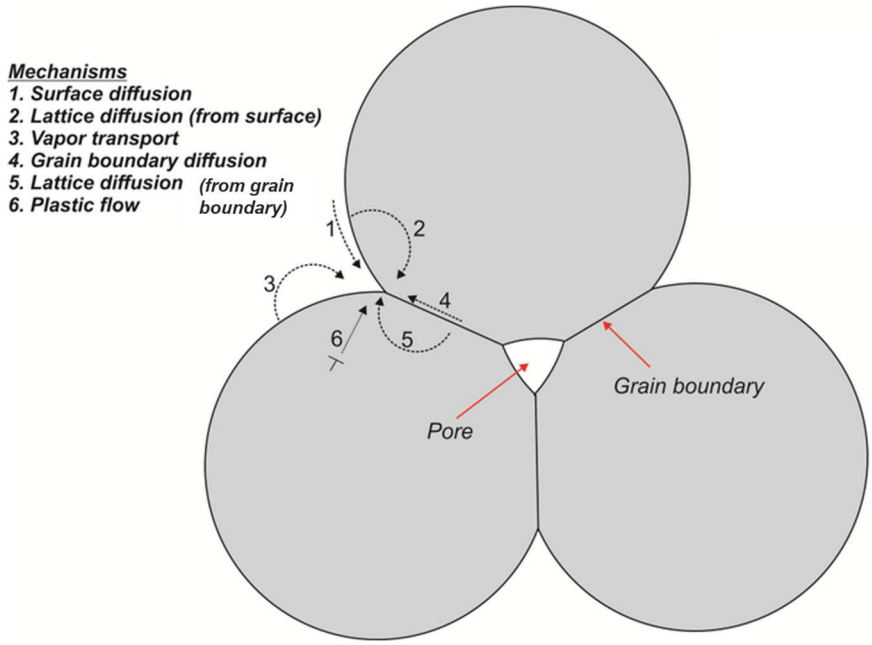

Fig. 1. 19 The mass transport mechanisms in sintering process[102]

Sintering process is typically carried out at high temperatures. In order to produce materials that are as dense as possible, various sintering techniques have been developed, such as pressureless sintering, microwave sintering, hot isostatic pressing sintering and spark plasma sintering[103]. Among them, spark plasma sintering (SPS) outstands due to its fast processing, low requirement of sintering temperature and versatility[104]. SPS is a process that energize the sample with low-voltage, high-current pulsed direct current, combined with uniaxial pressure at the same time. The powder is typically loaded into a graphite mold with good electroconductibility, and the two ends of the graphite mold are in contact with the electrodes (Fig. 1. 20). At the beginning of sintering, the current flows through the graphite mold, and the plasma generated during the discharge impacts the powders. The uniform heating is then obtained through Joule heating, and the sintering process is completed. SPS uses a rapid heating rate and short holding time to swiftly skip the surface diffusion stage and directly enter the grain boundary diffusion stage, which can reduce the growth of grains, fast densification rate and lower the necessary sintering temperature[100]. Since it was first developed in 1988, the SPS device has been widely employed in material research and fabrication[105].

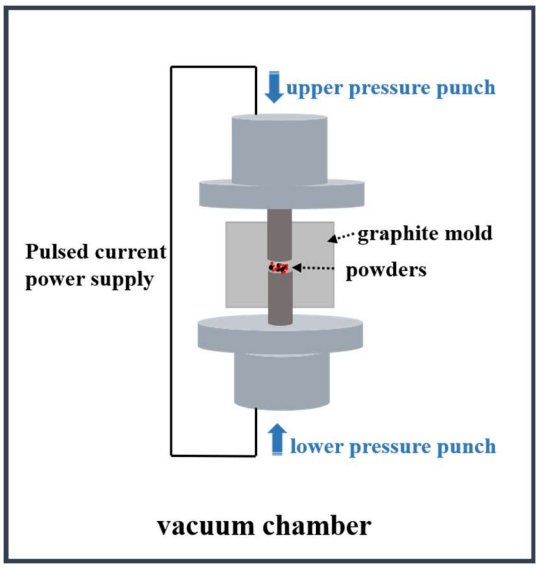

Fig. 1. 20 Schematic diagram of spark plasma sintering

1.4.1.2 Sintering additives

For ceramics, although the theoretical thermal conductivity is relatively high, the sintered body's thermal conductivity in practical applications is substantially lower than the theoretical value. This is attributed to the fact that the defects such as impurities, grain boundaries, and dislocations in ceramics would cause phonon scattering, increasing crystal thermal resistance since the thermal conduction principle of ceramics mainly relies on phonon transport[106]. In addition, direct sintering of powders is a kind of solid state sintering. The ceramic body acquired by solid state sintering has high porosity (φ) resulting from strong covalent bonding and low diffusive nature of raw powders during sintering. The large φ will drastically impede the thermal conduction due to the low k of air (0.03 W/m·K) trapped in the sample and the barrier of phonon transport[107]. Taking AlN as an example, Al_2O_3 impurities are inevitably generated during the production of AlN and are difficult to be completely eliminated. Certain oxygen impurities existed not only on the surface (Al_2O_3 form) but also in the lattice of AlN would substitute nitrogen. The aluminum vacancies appear subsequently since the tetrahedral covalent radius of oxygen is shorter than that of nitrogen. Vacancies scatter phonons thus decrease the k of AlN[108].

As a result, liquid phase sintering (LPS) was introduced as an effective way to achieve dense ceramic sintered body by adding proper solid additives. Fig. 1. 21 shows the mechanisms of LPS during different stages. When the mixed powder is heated to a relatively low temperature, the additives become liquid (generally 5 to 15% of volume fraction). Similar to the introduction for cold sintering, solid particles could be wetted in the liquid, providing capillary forces that draw the particles together and expedite the particle rearrangement, interparticle bonding and grain growth of the solid phase. The mass transfer in liquid is typically much faster than in solids, accelerating powder stacking and densification. The gas is progressively expelled as the viscous liquid diffuses and fills the voids between the particles, and the porosity diminishes. As the sintering advances, the dissolved small particles are transferred and diffused within the liquid phase and precipitate on the larger particles with limited solubility. The sample is densified further as the particles grow and change shape[109]. Besides, for ceramic like AlN, oxygen impurities in the lattice can be "captured" by the sintering additives, following which they react and precipitate at the grain boundaries, thereby reducing the influence of aluminum vacancies on the value of k[110,111]. Therefore, the type and content of additives, the degree of liquid phase dispersion and diffusion are all key parameters that affect the thermal conductivity of sintered body.

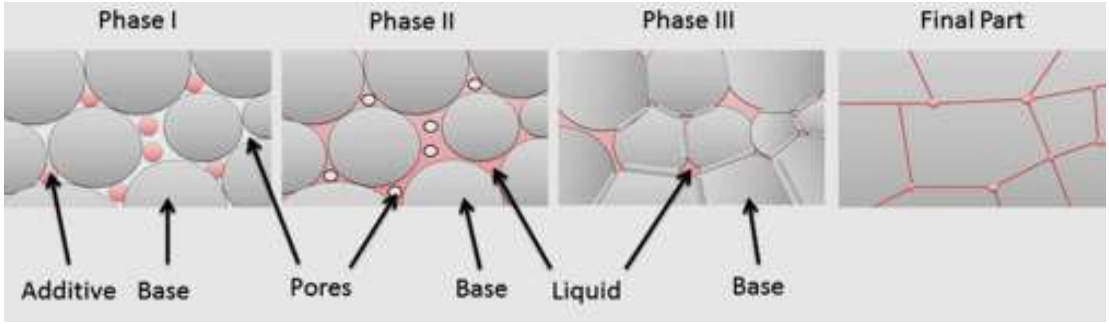

Fig. 1. 21 Liquid phase sintering mechanism[112]

Various sintering additives have been studied, such as calcium oxide (CaO) and yttrium oxide (Y_2O_3) for AlN[113–115], alumina (Al_2O_3) and Y_2O_3 for SiC[116]. The improvement in the value of k of the sintered ceramic substrate indeed depends strongly on the additive properties (additives content, particle size, etc.), and on its uniform

dispersion in the resulting mixed powder. Qiu et al.[117] ball-milled AlN with 2 to 5 wt% CaO and 3.5 wt% Y_2O_3 in ethanol for 3 h. Subsequently the mixed powders were pressed and fired at 1600 ℃ for 6 h under flowing high-purity nitrogen atmosphere. It was found that k of AlN pellet increased from 52 to 92 W/m·K, when the CaO additive concentration was increased from 2 wt% to 5 wt%. Lee et al.[118] added a type of glass frit (MCAS, comprising 5 wt% of MgO, 19 wt% of CaO, 26 wt% of Al_2O_3 and 50 wt% of SiO_2) to the AlN powders, and cold-isostatically compressed the mixture at 200 MPa after milling. Then the mixture was sintered at 1600 °C for 4 h. They found that the resulting MCAS particles decreased in size to nanometric dimensions, and that their thermal conductivity increased from 32 to 82.6 W/m·K. Seo et al.[119] ball milled SiC with 1.1 wt% Y_2O_3-Sc_2O_3 additive for 24 h in ethanol, and sintered the mixture at 2050 °C for 6 h under 60 MPa of pressure. The thermal conductivity of sintered SiC composite was 234 W/m·K, which was much higher than the pure sintered SiC ceramic.

Among these researches, ball milling is the most commonly used additive-matrix mixing technique. Few studies have systematically revealed the impact of mixing process or the additive particle size (ranging from micron- to nano-scale) on the enhancement of thermal conductivity in the sintered ceramic substrates, as well as explained the underlying mechanism. In addition, the proper and uniform mixing of ceramic raw powders with additives is a serious issue, raising the question of the optimal mixing process.

1.4.2 Mixing technique for powder sintering: Dry mixing process

As mentioned above, the uniform mixing of ceramic raw powders with sintering additives is a critical concern for achieving densification and high thermal conductivity. In the majority of sintering research, powders are typically mixed in an organic solvent for extended durations using ball milling. It is also challenging to rapidly produce uniform and well-distributed powder mixtures, especially in the case of nanometric and submicron particles. Hence, it is imperative to adopt novel techniques to accomplish highly efficient and environmentally friendly powder mixing. The dry mixing method

has emerged as a promising approach in this regard. Moreover, in the anti-oxidation treatment for Cu, dry coating might be a viable alternative to traditional chemical methods, which aligns with the green and solvent-free objective.

In summary, a comprehensive literature review on the fundamental principles, various types, and key influencing factors related to dry mixing and coating processes will be presented in this section.

1.4.2.1 Principles of dry mixing/coating

The process of combining dry powders under mechanical forces such as mechanical impact, collision, friction, compression and shear to produce a well-blended dry mixture without using any solvents and binders is known as dry mixing. This process has been applied in many research fields such as pharmaceutical material preparation, food processing and powder metallurgy[120]. It is a green and eco-friendly technique which generates no liquid waste and does not require drying or heating treatment. The significance of dry mixing is that the features of the final mixture will change due to the varied qualities of raw material powders, different functioning principles of instruments and equipment, and the effect of operating circumstances. Therefore, it can be regarded as a beneficial technique for blending raw powder and additives.

For non-cohesive, non-interacting systems, individual particles move randomly relative to one another during mixing, until equilibrium is reached in the mixture[120]. For cohesive and interacting systems, which is the case for most combinations of raw powder and sintering additives, the ordered mixing theory takes precedence. Since not all particles are precisely uniform in size, the ordered dry mixing takes into account the mixing and de-mixing mechanisms when the component powders vary in size, shape or density[121]. Fig. 1. 22 gives the schematic diagram of the mixing process. By the strong external mechanical force from the mixing device, the cohesive agglomerates are partially de-agglomerated and the fine aggregates adhere to the coarse particles nearby[122]. When these coarse particles collide with other coarse ones without fine aggregates on the surface, some of the fine particles are transferred to the latter. The fine agglomerates/particles are gradually dispersed onto the surface of the coarse

particles through the friction and collision between coarse particles[120]. The mixing process reaches completion when the system attains equilibrium.

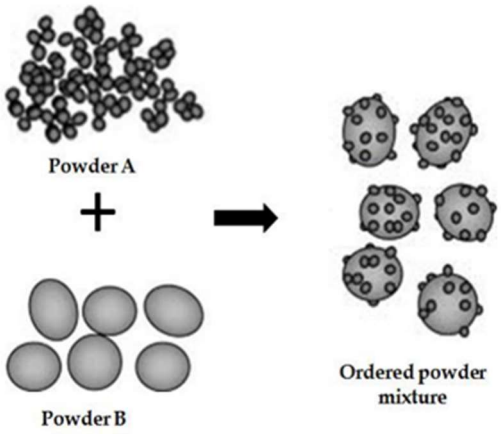

Fig. 1. 22 Schematic diagram of ordered mixing[123]

As the size ratio of the two component particles increases (coarse particle size/fine particle size), a single- or multi-layer discrete or continuous coating of fine particle (guest particle) will develop on the surface of the coarse particle (host particle). This evolves into the dry coating technique[124].

1.4.2.2 Dry mixing/coating techniques

Many factors can influence the effectiveness of powder dry mixing/coating, including particle shape, size, surface roughness, particle cohesiveness, proportion of components, mechanical force type and energy input[125]. In sintering process, the uniformity of mixture in turn impacts the thermal conductivity and densification of the resulting sintered body. Therefore, the careful selection and appropriate application of mixing techniques are crucial for preparing the thermal conductive substrate with high thermal conduction ability.

The ball mill is the most commonly employed device for dry mixing in sintering, or dry coating in other fields. The grinding bowl which contains the powders rotates around the axis in the ball mill. Several grinding balls made of stainless steel, agate or zirconia are also needed in the bowl during processing. Powders and grinding balls follow the bowl to rotate rapidly under the high speed. Extremely high centrifugal

forces result in high energies on the balls and particles, and deagglomerate powders through impact (collision and friction) and attrition[126]. The powders then collide, rub, grind and mix with each other[127]. The working principles of different ball mills are basically similar, yet there are design variances. For example, in a planetary ball mill which is the most applied in dry powder mixing, the grinding bowl rotates around the center of the turntable while also rotating around its own axis to perform planetary motion[128]. In vibratory mills, the grinding bowl is shaken back and forth at a high vibration frequency and low amplitude. The balls and powders are subject to the inertial forces, centrifugal force and alternating loads[129]. Due to high energy input and impact, ball milling may break fragile particles and generate high local temperature.

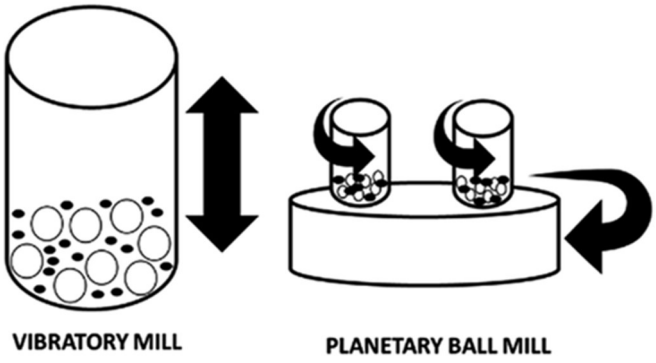

Fig. 1. 23 Working principle of vibratory mill and planetary ball mill[128]

Tab. 1. 3 summarizes the application of ball milling for preparing powder mixtures for sintering, including ceramic and metal materials. Indeed, it's evident that ball milling is extensively utilized in this research field. In addition, ball milling is used for dry coating research. Xi et al.[130] dry-coated silica and carbon black nanoparticles onto larger polyamide particles by the planetary ball mill and promoted the flowability of polyamide considerably, thereby facilitating its densification by sintering. Akpinar[131] dry-coated anhydrous borax particles with hydrophobic stearic acid by the planetary ball mill. This surface protection might prevent the hydration of anhydrous borax, which was beneficial for a diverse variety of water-based applications such as painting, medicine production and glazing.

Tab. 1. 3 Summary of mixing and sintering techniques for preparing some ceramics and metals with high thermal conductivity at room temperature

Main material	Sintering additives and mass fraction	Mixing mode	Sintering mode	Thermal conductivity (W/m·K)	Reference
AlN	2% CaO + 5.4% Y_2O_3 + 0.5% Li_2O	Ball-milled in ethanol	Calcined at 800 ℃ for 6 h in nitrogen with 5% H_2 and isostatically pressed at 20 MPa; then calcined at 1600 ℃	135	Watari et al.[113]
AlN	1% CaO + 3.1% Y_2O_3 + 0.1% B	Ball-milled in ethanol for 4 h	Sintered at 1550 ℃ in SPS; a constant uniaxial pressure was applied	70-80	Kobayashi et al.[132]
AlN	2% CaO + 3.5% Y_2O_3 + 1.9% nano-AlN	Ball-milled in ethanol for 3 h	Isostatically pressed under 150 MPa for 120 s and fired at 1600 ℃ for 6 h in N_2	133	Qiu et al.[117]
AlN	1% CaO + 3.1% Y_2O_3 + 0.1% B	Ball-milled in butanol for 4 h	Sintered at 1650 ℃ in SPS; a constant uniaxial pressure of 50 MPa was applied	80-90	Kobayashi et al.[133]
AlN	0.9% CaO + 1.2% Y_2O_3	Ball-milled in ethanol for 3 h	Uniaxially pressed under 430 MPa and sintered at 1700 ℃ in graphite furnace in N_2	136.7	Zhan et al.[134]
AlN	2% CaO + 2% Y_2O_3 + 2% Sm_2O_3	Ball-milled in ethanol for 3 h	Uniaxially pressed under 430 MPa and sintered at 1700 ℃ in graphite furnace in N_2	134.4	Zhan et al.[135]
AlN and BN	3% YF_3	Ball-milled for 6 h	Sintered at 1850 ℃ in N_2	112	Yang et al.[136]
SiC	2% graphene	Ball-milled in ethanol for 24 h	Isostatic pressed under 200 MPa and sintered at 2130 ℃ in flowing Ar	145.1	Li et al.[137]

SiC	1.6% TiN + 3% Y_2O_3	Ball-milled in ethanol for 24 h	Hot pressed at 2000 ℃ for 3 h under 40 MPa in N_2	210.8	Kim et al.[138]
SiC	5.5% Al_2O_3 + 3.1% Y_2O_3 + 0.4% CaO	Ball-milled in ethanol for 24 h	Isostatic pressed under 275 MPa and sintered at 1850 ℃ in Ar	80	Eom et al.[139]
SiC	0.9% Y_2O_3 + 0.3% Sc_2O_3	Ball-milled in ethanol for 24 h	Spark plasma sintered at 2050℃ under 60 MPa in N_2	262	Seo et al.[119]
Si_3N_4	3% YH_2 + 1.5% MgO	Ball-milled in ethyl alcohol for 4 h	gas pressure sintered at 1900 ℃ under a N_2 pressure of 1 MPa	123	Wang et al.[140]
Si_3N_4	2% GdH_2 + 1.5% MgO	Ball-milled in ethyl alcohol for 4 h	gas pressure sintered at 1900 ℃ under a N_2 pressure of 1 MPa	135	Wang et al.[141]
Si_3N_4	3% Y_2O_3 + 2% MgF_2	Ball-milled in isopropyl alcohol for 24 h	Spark plasma sintered at 1650 ℃ under 40 MPa in N_2	64	Yang et al.[142]
Cu	4% multi-walled carbon nanotube	Ball-milled for 10 h in Ar	Uniaxial hydraulic pressed under 450 MPa and microwave sintered in Ar	315.4	Darabi et al.[143]
Cu	5% ZrO_2 + 0.5% graphene	Planetary ball-milled for 20 h	Cold compacted at 700 MPa and sintered at 950 ℃ in H_2	345	Abd-Elwahed et al.[144]
Al	1% carbon nanofiber	Planetary ball-milled in stearic acid for 3 h	Spark plasma sintered at 560 ℃ under 50 MPa	237 in plane parallel to the press direction	Ogawa et al.[145]
W	30% Cu	Ball-milled for 50 h in Ar	Spark plasma sintered at 1200 ℃	140	Kim et al.[146]

Although ball milling is the most commonly used additive-matrix mixing technique reported in the literature[133,147–151], strong cohesion and agglomeration among particles mean that it is challenging to rapidly produce well-distributed powder mixtures, especially in the case of micron-, submicron- and nano-sized particles. This effect might lead to an inhomogeneous liquid phase, which in turn leads to a higher concentration of pores and oxygen impurities in the sintered substrate[152]. In addition, long-duration ball milling (2–24 h ball milling duration as shown in Tab. 1. 3) also leads to particle attrition and breakage, oxidation due to prolonged exposure to air, pollution from the milling balls, and excessive energy consumption[153]. It is thus of key importance to develop an alternative mixing technique, in order to mitigate these drawbacks and to ensure uniform dispersion of the additives, thereby further enhancing the thermal conductivity of sintered substrate.

Recent work from UCCS has shown that the novel, high-speed, dry shear batch "Picomix" mixer (Hosokawa Micron B.V., Japan) can enable fast, adequate mixing of fine cohesive powders without any solvent[154]. It is a small laboratory mixer with the same functionality as the industrial Cyclomix mixer (Fig. 1. 24 (a)), but is more suitable for small quantities of powders. Shear forces play a significant role in these mixers. As shown in Fig. 1. 24, Picomix mixer consists of a conical vessel with a volume of 100 mL, and a central rotor with 6 pairs of paddles of which the tip speed could reach 20 m/s. The high-speed paddle rotation provides strong centrifugal force, pushing the powder up along the vessel's wall. The particles are accelerated and intensively mixed due to the high shear and compressive force between the wall and the paddle. The impacting paddle at the top effectively disperses the cohesive powder[155]. In a very short time, it can provide sufficient mechanical energy to disperse fine particle agglomerations, while allowing multiple constituents to adhere and remain in contact (due mainly to van der Waals forces) through shearing forces[122]. Unlike conventional milling processes, the geometry of the working part of a shear-based device and its

clearance from the vessel wall is generally fixed, resulting in nearly little particle breakage.

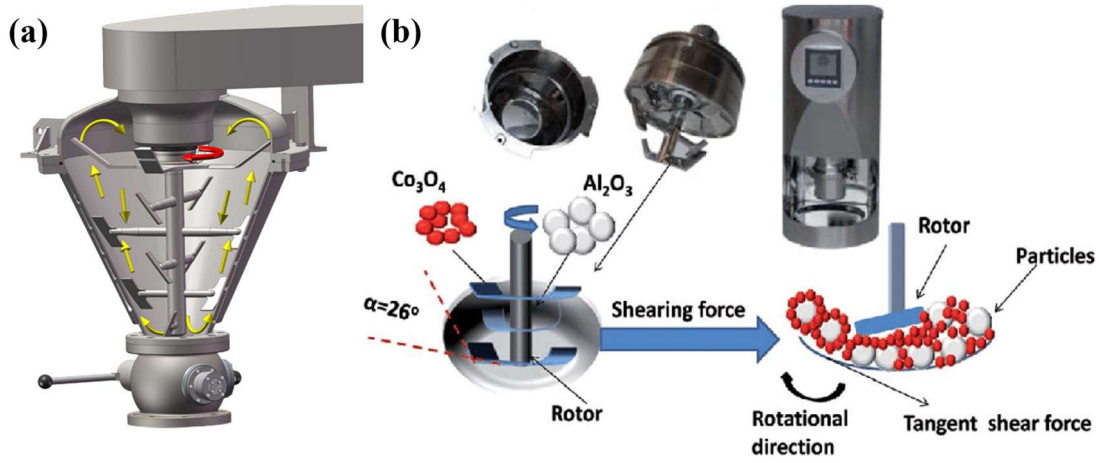

Fig. 1. 24 (a) Internal structure of Cyclomix[155]; (b) Picomix mixer and its working principle from the research of Lu et al.[154]

The Picomix dry shear mixer has been used to prepare supported catalysts by our research team (Lu et al.[154]), and dry powder inhaler drugs. Lu et al.[154] applied the Picomix to synthesize the alumina-supported cobalt catalyst for Fischer–Tropsch reaction. The process was solvent-free and produced no pollutants. Hertel et al.[156] used the Picomix to load fine active pharmaceutical ingredients onto coarse carrier particle successfully, and investigated the influence of rotational speeds and durations on the loading of fine particles. A high particle surface coating fraction was obtained, indicating the high adhesion between the fine and coarse particles in Picomix. These findings suggest that this high-shear mixer might effectively substitute ball milling for preparing mixtures of matrix powder with additives which are more uniformly dispersed, as well as dry coating on the Cu particle surface to resist oxidation.

1.4.3 Composite material manufacturing methods

The material selection and preparation method for thermal conductive substrates in solar thermal application have been introduced previously. For the subsequent preparation of composite materials comprising the solar absorber, some methods

utilized in the manufacturing of absorber coating onto the substrate are presented in this section.

(1) Chemical vapor deposition

Chemical vapor deposition (CVD) is applied to deposit most metals as well as compounds such as carbides, nitrides, oxides coatings[157]. CVD introduces different atoms or molecules in the form of vapor in a high-temperature vacuum or a protective atmosphere such as hydrogen, and then deposits them on the substrate surface after chemical reactions such as decomposition, cracking, and replacement[158]. CVD provides high deposition rates and controllable film composition and thickness, but its cost is relatively high.

(2) Physical vapor deposition

Physical vapor deposition is similar to the CVD process, while it transfers raw material atoms or molecules to the substrate surface to grow into a film through a physical process. It includes various methods such as vacuum evaporation deposition and sputter deposition[159]. In vacuum evaporation deposition, the raw ingredients are heated at high temperature under vacuum and evaporated or sublimed into gas-phase atoms, molecules or ion groups, and finally deposit on the substrate surface to restructure or bond and form a solid layer[72]. The sputter deposition uses high-energy ions to bombard the raw material target under vacuum, generating atoms, molecules or ion clusters from target sputtering, which are deposited on the substrate[159].

(3) Wet chemical coating

Wet chemical coating process applies liquid coating material. Specifically, there are several ways for applying the liquid coating on the substrate. For instance, dip coating involves dipping the substrate in the precursor solution, pulling it out at a steady speed after a period of reaction, and then evaporating the solvent to deposit a uniform film on the substrate. The evaporation process is often accompanied by heat treatment which is beneficial to accelerate evaporation, remove residues and induce crystallization[160]. The mechanism of spin coating is similar. The solution to be

deposited is typically placed in the center of the substrate, and spreads out as the substrate rotates under centrifugal force, resulting in a homogeneous thin coating. The film thickness is governed by the flow viscosity, evaporation of the solvent, rotating duration and rotational speed[161].

(4) Spray coating

Spray coating deposits the tiny droplets on the substrate surface forming a smooth film. The tiny droplets are formed through atomization, which can be achieved pneumatically or hydraulically by centrifugal force or electric power, either at high temperature or room temperature. The coating performance are affected by parameters like liquid flow, viscosity and droplet size[162].

1.5 Numerical modeling of heat transfer in composite solar receiver material

The numerical modeling and computation of the heat transfer process of the solar receiver material in solar thermal applications are critical. It involves the solar radiation absorption by the absorber material and heat transfer in the composite solid. Numerical modelling of heat transfer (radiative, conduction and convection) through composite materials is indispensable for the completion of experiments and a better understanding of the transfer phenomena applied to solar application.

1.5.1 Heat transfer process and analysis method

When sintering ceramic or metallic material as the substrate, the achieved sintered body is generally porous. Heat transfer of the composite porous media in solar thermal applications is a complex process involving three modes: conduction, radiation and convection. An introduction to phenomena of thermal conduction and radiation were introduced in Section 1.3.2 (Chapter 1), and the theoretical basis of convection will be introduced below to prepare for numerical modeling. Convection occurs between a surface and moving fluid with different temperatures which is due to a superposition of energy transmission through random motion of molecules and bulk motion of the entire fluid. Convection may be classified into two types. Forced convection occurs when the flow is induced by an external source such as a fan. Natural convection is caused by buoyancy forces due to density changes in the fluid caused by temperature variations without any external forces[47]. Regardless of the nature of convection, its equation can be expressed according to Newton's cooling law[163]:

$$q'' = h(T_s - T_\infty) \qquad \text{Eq. 1. 6}$$

where q" (W/m^2) is the convective heat flux, h ($W/m^2 \cdot K$) is the convection heat transfer coefficient, T_s (K) is the absolute temperature of the surface, T_∞ (K) is the temperature at infinite distance.

The following thermal processes exist in the heat absorption and heat transfer of porous medium: (1) solar radiation absorption; (2) thermal conduction of solid particles; (3) thermal conduction of fluid (often gas) in material pores and convection between fluid and solid; (4) radiation between solid particles. At high body temperatures (higher than 300 ℃), thermal radiation is the dominant heat transfer mode[164]. When the pore size is small enough (on the order of nanometers), gas convective heat transfer is negligible[165,166]. As a result, inside the composite porous medium, only conduction and radiation were taken into account for the modeling.

A vast number of research have been conducted at various levels for heat transfer models in porous structures. The first category is the analysis at the molecular level, which refines the internal motion into molecular motion. This method requires the establishment of a large number of mathematical equations, and there are significant inaccuracies. The second category is the pore-scale approach, in which the medium structure is explicitly modeled based on a thorough description of the pore shape. The pore structure is complicated, making it difficult to fully and accurately describe its complexity through a geometric model, which necessitates a significant amount of calculation as well[167]. Based on the limitations of these two approaches, a rougher method, the third category of macro-level analysis, also known as continuous-scale approach, is summarized. This approach considers the porous medium as a continuum, and takes the volume pixels that are bigger than the detail scale but smaller than the overall geometry as the control volume. The governing equations are applied to each volume pixel. This method focuses on the macroscopic state and ignores the internal structure; the set parameters are continuously changing, and can be described and solved by general mathematical equations which is simple and convenient, requiring much less computing workload[168].

1.5.2 Numerical model and governing equation

When solving the governing equations of solar radiation absorption and internal heat transfer in composite porous medium, the following assumptions are made typically: (1) the surface of the material is opaque; (2) the solid is a gray and optically thick medium with absorption, emission and isotropic scattering; (3) the porosity of the porous medium is constant; (4) the thermal physical properties of the solid phase remain constant whereas the thermal physical properties of the gas phase vary due to the wide temperature range; (5) the effects of buoyancy, thermal expansion, viscous dissipation and hydrodynamic dispersion on the medium are ignored; (6) the boundary effects are neglected since the pore size is substantially smaller than the medium.

1.5.2.1 Heat balance equation

The heat transfer equation in a continuum is derived from the first law of thermodynamics, also known as the law of conservation of energy. This equation (Eq. 1. 7) involves parameters in the microscopic continuous domain Ω, including heat exchange rate (Q_{exch}), internal energy (E_Ω) and stress power (P_{str}) that is converted into heat by dissipation, and focuses on the microscopic phenomenon of atomic vibrations[169].

$$\frac{dE_\Omega}{dt} = P_{str} + Q_{exch} \qquad \text{Eq. 1. 7}$$

where t is time. In order to obtain the localized form, the different terms are more detailed defined as following:

$$\frac{dE_\Omega}{dt} = \int_\Omega \rho \frac{dE}{dt} dv \qquad \text{Eq. 1. 8}$$

where ρ (kg/m^3) is the density, and dv denotes an elementary volume of Ω. The elementary volume changes as the domain expands or contracts. P_{str} is explained by the sum of pressure-volume work and viscous dissipation:

$$P_{str} = \int_\Omega (\sigma_c : D) dv \qquad \text{Eq. 1. 9}$$

where σ_c is the Cauchy stress tensor and D is the strain rate tensor. Q_{exch} includes thermal conduction, radiation and potentially additional heat sources, which can be summarized by:

$$Q_{exch} = -\int_{\partial\Omega}(q \cdot n)ds - \int_{\partial\Omega}(q_r \cdot n)ds + \int_{\Omega} Q dv \qquad \text{Eq. 1. 10}$$

where $\partial\Omega$ is the boundaries of the same domain in a spatial frame, ds is the elementary area, q (W/m^2) is the conduction heat flux, q_r (W/m^2) is the radiation heat flux, n is the external normal vector to the boundary, and Q (W/m^3) is the additional heat source. In the spatial frame, d/dt can be rewritten in the following form:

$$\frac{d}{dt} = \frac{\partial}{\partial t} + u_{(x,y,z)} \cdot \nabla_{(x,y,z)} \qquad \text{Eq. 1. 11}$$

where u is the fluid velocity vector. So Eq. 1. 7 becomes:

$$\int_{\Omega} \rho \frac{dE}{dt} dv + \int_{\partial\Omega}(q \cdot n)ds + \int_{\partial\Omega}(q_r \cdot n)ds = \int_{\Omega}(\sigma_c : D)dv + \int_{\Omega} Q dv \qquad \text{Eq. 1. 12}$$

which leads to the following localized form in the spatial frame:

$$\rho \frac{\partial E}{\partial t} + \rho u \cdot \nabla E + \nabla \cdot (q + q_r) = \sigma_c : D + Q \qquad \text{Eq. 1. 13}$$

1.5.2.2 Thermal model

When establishing the governing equation of internal energy in porous medium, there are two models that may describe the equilibrium state: local thermal equilibrium (LTE) and local thermal nonequilibrium (LTNE). The LTE assumption considers the point-wise equality of solid and fluid temperatures, whereas the LTNE assumption considers the presence of a solid-fluid temperature differential[170]. The LTE hypothesis is taken into account as the flow is not considered. For a time-dependent study in a composite porous medium, Eq. 1. 13 simplifies into[171]:

$$(\rho_m c_{p,m})_{eff} \frac{\partial T}{\partial t} + \rho_f c_{p,f} u \cdot \nabla T + \nabla \cdot q = Q + Q_p \qquad \text{Eq. 1. 14}$$

where ρ_m (kg/m^3) is the density of the porous matrix, $c_{p,m}$ ($J/(kg \cdot K)$) is specific heat capacity of the matrix, $(\rho_m c_{p,m})_{eff}$ (kg/m^3) is the effective volumetric heat capacity at constant pressure defined by[171]:

$$(\rho c_p)_{eff} = \theta_s \rho_s c_{p,s} + \varphi_p \rho_f c_{p,f} \qquad \text{Eq. 1. 15}$$

$$\varphi_p = 1 - \theta_s \quad \text{Eq. 1. 16}$$

where θ_s is the volume fraction of solid material in the porous matrix, ρ_s (kg/m^3) is the density of solid phase, $c_{p,s}$ (J/(kg·K)) is the heat capacity of solid phase at constant pressure, φ_p is the porosity of the porous matrix, ρ_f (kg/m^3) is the density of fluid phase, $c_{p,f}$ (J/(kg·K)) is the specific heat capacity of fluid phase at constant pressure. T (K) is the existing absolute temperature, q (W/m^2) is the conductive heat flux vector defined by:

$$q = -k_{eff} \nabla T \quad \text{Eq. 1. 17}$$

where k_{eff} (W/m·K) is the effective thermal conductivity of the matrix. Q_p (W/m^3) is the pressure change work of fluid which can be acquired through Eq. 1. 18:

$$Q_p = \alpha_f T \left(\frac{\partial p_A}{\partial t} + u \cdot \nabla p_A \right) \quad \text{Eq. 1. 18}$$

where α_f (1/K) is the thermal expansion coefficient of the fluid phase defined by Eq. 1. 19 and p_A (pa) is the absolute pressure:

$$\alpha_f = -\frac{1}{\rho_f} \frac{\partial \rho_f}{\partial T} \quad \text{Eq. 1. 19}$$

The effective thermal conductivity of the porous medium, k_{eff}, is related to the thermal conductivity of the solid (k_s) and the fluid (k_f), and is complexly dependent on the geometry of the medium. Various models have been proposed for computing k_{eff}. According to Nield et al., three models, volume average, reciprocal average and power law, are given for an isotropic medium[172]. Fig. 1. 25 gives simple patterns to symbolically simulate the internal structure of the material corresponding to different k_{eff} model[173].

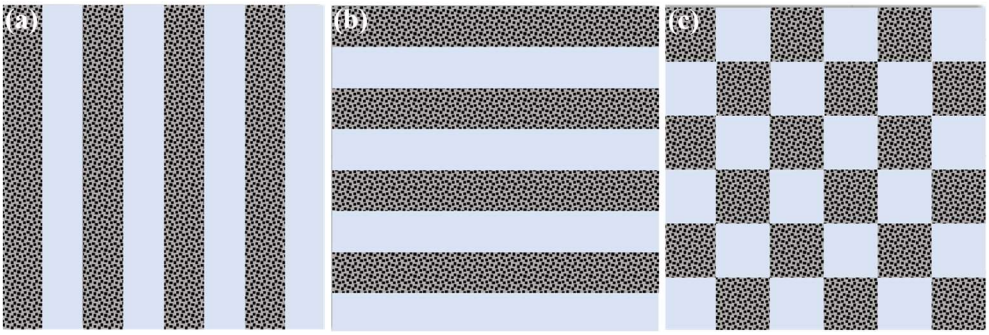

Fig. 1. 25 Different patterns (gray represents solid and blue represents fluid) simulating k_{eff} computing models: (a) volume average, (b) reciprocal average, (c) power law

Each model could be demonstrated according to the following equations:

(1) Volume average model computes the k_{eff} of the solid-fluid system as the weighted arithmetic mean of solid and fluid thermal conductivities, when the solid and fluid are parallel in the medium:

$$k_{eff} = k_s\theta_s + k_f\varphi_p \quad \text{Eq. 1. 20}$$

where k_s (W/m·K) is the thermal conductivity of solid material, k_f (W/m·K) is the thermal conductivity of fluid. This volume average model provides an overestimation for k_{eff}.

(2) Reciprocal average model computes the k_{eff} of the solid-fluid system as the weighted arithmetic mean of solid and fluid thermal conductivities when thermal conduction occurs in series, with all the heat flux passing through the medium:

$$\frac{1}{k_{eff}} = \frac{\theta_s}{k_s} + \frac{\varphi_p}{k_f} \quad \text{Eq. 1. 21}$$

This reciprocal average model provides an underestimation for k_{eff}.(3) Power law model computes the k_{eff} of the solid-fluid system as the weighted arithmetic mean of solid and fluid thermal conductivities:

$$k_{eff} = {k_s}^{\theta_s} \cdot {k_f}^{\varphi_p} \quad \text{Eq. 1. 22}$$

1.5.2.3 Radiative heat transfer model

In terms of radiative heat transfer, the model considers both cases without and with participating medium. For solar absorber materials, the absorption of solar radiation is involved. For a porous material, the radiation inside the matrix is considered. The distribution of radiative flux in relation to conduction and convection depends on the temperature of the material and its characteristics, which is generally described by Stefan-Boltzmann's law. As the temperature increases, the radiative heat transfer becomes increasingly significant or even dominant due to the dependence of T^4 in Stefan-Boltzmann's law.

1.5.2.3.1 Surface to surface radiation

Surface to surface radiation occurs when no medium is involved. For an opaque diffuse-gray surface, the total incoming radiative flux is called irradiance (G, W/m^2) and the radiation equation is as follows[174]:

$$J = \rho_{r,d} G + \varepsilon e_b(T) \qquad \text{Eq. 1. 23}$$

where J (W/m^2) is the radiosity representing the total diffuse outgoing radiative flux including reflected and emitted radiation, $\rho_{r,d}$ is the diffuse reflectivity, ε is the surface emissivity, $e_b(T)$ (W/m^2) is the blackbody total emissive power and defined by:

$$e_b(T) = n^2 \sigma T^4 \qquad \text{Eq. 1. 24}$$

where n is the refractive index meaning the ratio of the propagation speed of light in vacuum to the propagation speed in a medium, σ is the Stefan-Boltzman constant, T (K) is the surface temperature. As ε equals α, the net inward radiative heat flux of the diffuse surface, $q_{r,net}$, is then given by the difference between the irradiation and the radiosity:

$$q_{r,net} = (1 - \rho_{r,s})G - J = \alpha(G - e_b(T)) \qquad \text{Eq. 1. 25}$$

where $\rho_{r,s}$ is the specular reflectivity and equals $1 - \alpha - \rho_{r,d}$. As a result, the radiative heat source could be added to the heat equation (Eq. 1. 14, Chapter 1) as a separate physics feature through a source term along with the other boundary heat sources.

1.5.2.3.2 Radiation in the porous medium

The radiation can interact with a medium and transfer heat (also known as the participating medium). The radiative transfer equation (RTE) is commonly used to describe and explain the radiation process in participating medium, including absorption, emission and scattering (Fig. 1. 26).

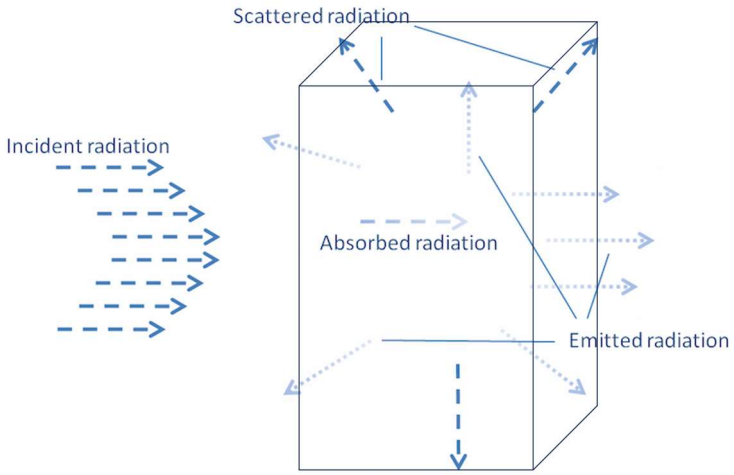

Fig. 1. 26 Examples of interactions between the medium and radiation[175]

According to RTE, the radiation intensity field is a function of ray position, orientation and spectral variables[176]. It can be defined as following[177]:

$$\Omega_r \cdot \nabla I(\Omega_r) = \kappa I_b(T) - (\kappa + \sigma_s) I(\Omega_r) + \frac{\sigma_s}{4\pi} \int_{4\pi} I(\Omega_r') \Phi(\Omega_r', \Omega_r) d\Omega_r' \quad \text{Eq. 1. 26}$$

where $I(\Omega_r)$ (W/(m^2·sr)) is the radiative intensity at a given direction Ω_r, κ (1/m) is the absorption coefficient and σ_s (1/m) is the scattering coefficient of the matrix material. The two optical properties are given by[168]:

$$\kappa = \frac{3\varepsilon\theta_s}{2d_{pore}} \quad \text{Eq. 1. 27}$$

$$\sigma_s = \frac{3(2-\varepsilon)\theta_s}{2d_{pore}} \quad \text{Eq. 1. 28}$$

where d_{pore} is the mean diameter of pores in the medium. $I_b(T)$ (W/(m^2·sr)) is the blackbody radiative intensity defined as:

$$I_b(T) = \frac{n^2 \sigma T^4}{\pi} \quad \text{Eq. 1. 29}$$

The intensity of directionally propagated light is attenuated by scattering and enhanced by radiation from different directions. As a result, the first term on the right side of RTE (Eq. 1. 26) accounts for the enhancement of emitted radiation, the second for the loss of absorption and scattering, and the last for the increase in scattering intensity of radiation coming from one direction Ω_r' scattered into direction Ω_r defined by the phase function $\Phi(\Omega_r', \Omega_r)$ (Fig. 1. 27). The phase function describes the probability distribution of the direction in which radiation is scattered.

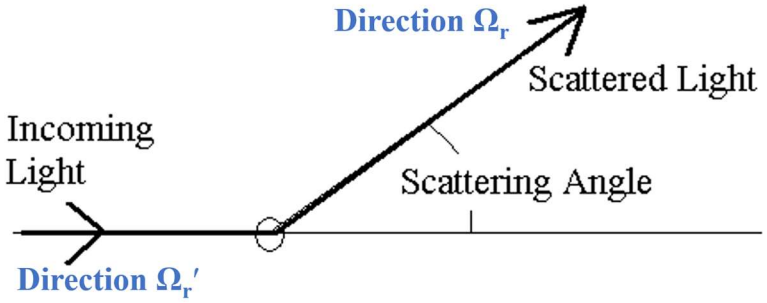

Fig. 1. 27 Schematic diagram of scattering related to phase function

The computing cost of solving this equation is substantial. In order to minimize the complexity, several models have been developed to simplify the RTE.

(1) Discrete ordinate method

The discrete ordinate method is the most common one for calculating the radiative transfer equation. The RTE is transformed into a set of partial differential equations, and the radiative component is calculated at each discrete solid angle, as shown in Fig. 1. 28[178]. Each dependent variable satisfies the following equation[177]:

$$S_i \cdot \nabla I_i = \kappa I_b(T) - (\kappa + \sigma_s) I_i + \frac{\sigma_s}{4\pi} \sum_{j=1}^{n} \omega_j I_j \Phi(S_j, S_i) \qquad \text{Eq. 1. 30}$$

where S_i is the i^{th} discrete direction and ω_j is the quadrature weights. In the application, i is usually selected as 4 to 12. The key benefit of this approach is that it has high orientation accuracy owning to the angular space discretization, but it is still computationally costly compared to other simplified methods[178].

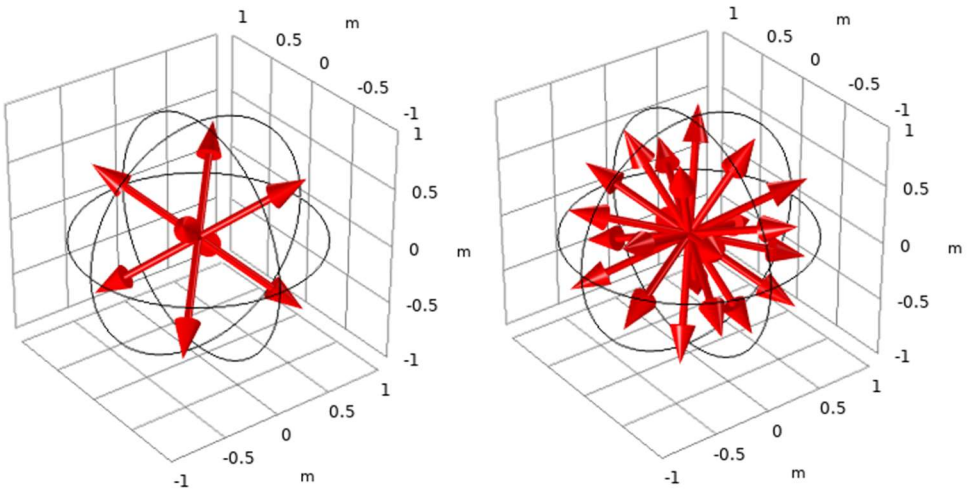

Fig. 1. 28 Example of different discrete solid angles[175]

(2) Rosseland approximation

The Rosseland approximation is appropriate for radiative heat transfer in optically thick media with optical thickness significantly greater than unity ($\tau \geq 1$)[178]. It analogizes the behavior of light propagation to thermal conduction, thus deriving a highly nonlinear "radiative conductivity (k_R)" based on the thermal conductivity theory [179]:

$$k_R = \frac{16\ {}^2\sigma T^3}{3(\kappa+\sigma_s)} \qquad \text{Eq. 1. 31}$$

Then the radiative heat flux (Q_r, W/m^2) value is obtained:

$$Q_r = -k_R \nabla T \qquad \text{Eq. 1. 32}$$

This method is simple and requires little calculation, but it does not consider the direction or distance from the radiation source, hence it has limitations and can only tackle specific application issues.

(3) P1 approximation

The P1 approximation simplifies the RTE by including the incident radiation G (W/m^2) and a radiative heat flux Q_r (W/m^2) to account for the contribution of radiative heat transfer[180]:

$$G = \int_{4\pi} I(\Omega_r) d\Omega_r \qquad \text{Eq. 1. 33}$$

$$Q_r = \kappa(G - 4\pi I_b(T)) \qquad \text{Eq. 1. 34}$$

so the G and Q_r can be related by the following equation:

$$\nabla \cdot (D_{p1} \nabla G) = Q_r \quad \text{Eq. 1. 35}$$

where D_{P1} is the P1 diffusion coefficient, defined as

$$D_{P1} = \frac{1}{3\kappa + \sigma_s(3 - a_1)} \quad \text{Eq. 1. 36}$$

where a_1 is the linear Legendre coefficient of the scattering phase function and equals 0 when scattering is modeled as isotropic.

1.5.3 Heat transfer models in applications

Based on the above summary, the thermal model and radiative heat transfer model along with their respective formulas, will be utilized for modeling the solar radiation absorption and heat transfer of the composite porous solar receiver materials in this study. As previously stated, the continuous scale research approach has been applied for simulating and solving heat transfer problems. The finite element method (FEM) in particular has sparked widespread interests. The core principle of the FEM is to discretize the field distribution issue in the continuous solution domain in time and space and subdivide the investigation object into small yet finite-sized elements. The physical property of an element is described by the degrees of freedom (DOF). Then the finite DOF is utilized to approximate the distribution characteristics of the infinite DOF in the solution domain[181]. Each element is assigned a set of characteristic equations describing the physical properties and boundary conditions. All the equations are then solved simultaneously in order to analyze physical processes or anticipate the behavior of objects. Since the elements have different shapes and can be combined in various ways, practically any geometry-shaped domain can be modelled and solved[182]. Generally, the heat transfer models can be run with a variety of commercial FEM software, such as Ansys, ABAQUS, COMSOL Multiphysics.

Pre-processing, processing and post-processing are the stages that must be performed for one model to be finalized. The pre-processing is also known as model preparation. It includes the following tasks: First, the solution domain and model

geometry are established, the relevant physical field for the model is selected and the physical quantities (such as material properties, loads, constraints) are defined, the general coefficients and constants, the initial and boundary conditions are input[183]; then the domain is discretized into finite elements and the finite element grid is created; finally, a file containing all the information and can be run at any time is generated to be imported into the solver for computation. In the processing stage, solution types are defined in the solver, such as steady-state or time-dependent, and a set of linear or nonlinear algebraic equations are concurrently solved to obtain results. In the post processing stage, the results are imported from the solver, and the environment and tools are provided to process model visualization and data analysis[184].

Some previous studies can serve as references to investigate the heat transfer in composite solar receiver materials. Reichl et al.[185] studied the working efficiency of a flat plate solar collector and the influence of different parameters through finite element numerical simulations. Different physical heat transfer mechanisms in the solar thermal process were described and distinguished. It was found that raising the heat transfer surface by five times and reducing the emissivity of the surface coating increased the heat transfer capacity of the system significantly. Wang et al.[186] applied the P1 approximation to simulate and evaluate the radiative heat transfer performance of a window-type volumetric solar receiver with SiC porous foam plates. Theoretical analysis demonstrated that a larger solid-phase thermal conductivity reduced the radiation heat loss of the windowed cavity, while a lower emissivity of the glass benefited the overall temperature rise.

1.6 Objectives of research

The objective of this work is to propose a new methodology to prepare novel composite solar receiver materials applied in solar thermal systems, which consist of the solar absorber material and thermal conductive substrate.

Many investigations on solar receiver materials have been conducted, but almost all the substrates were constructed of metals like stainless steel and Al. This leads to either low thermal conductivity, or metal scaling and embrittlement caused by the contact with the reaction raw components particularly at high temperatures. This study proposed the use of ceramics, AlN and SiC, for manufacturing the thermal conductive substrate by spark plasma sintering owning to the high thermal conductivity and high temperature resistance. CaO was chosen as the sintering additive for AlN, and the combination of Al_2O_3-CaO was chosen as the sintering additive for SiC, due to their cost-effectiveness and ready availability. In an effort to enhance the thermal conductivity and densification, a new dry-mixing approach (high-shear Picomix mixer) has been developed for the design of matrix-additive powder mixtures for sintering. Aside from applying the new mixing technique, the influence of the additive size, the process and mixing conditions (e.g. additive content, rotational speed) on the mixing behavior, and on the resulting porosity and thermal conductivity of sintered material need to be explored. In addition to ceramics, this study investigated the applications of metals (Cu) and carbon-based materials (graphite) as the thermal conductive substrate due to their high thermal conductivity for comparing. It is of great interest to employ the solvent-free dry coating on the Cu particle surface to achieve anti-oxidation treatment using Picomix. As a common material employed in solar receivers, the stainless steel was also sintered for comparison. To obtain composite solar receiver materials, carbon black was chosen as the solar absorber material and coated on the prepared substrate materials.

Numerical modeling of heat transfer in solar receiver materials provides computational insight into the material's performance in application. There have been few simulations conducted to investigate the performance of porous materials in solar thermal applications. In this study, the finite element method was chosen to simulate the solar absorption and heat transfer of the solar receiver materials. The numerical

investigation of various factors on the heat transfer performance might serve as the reference for material selection and design.

Chapter 2: Experiments and characterization

2.1 Introduction

In this chapter, the utilized powders, the methodologies of developing the thermal conductive substrates and composite solar receiver materials, the employed characterization methods including the physical, chemical and structural aspects are presented. Additionally, the experimental arrangements configured for investigating thermal conduction and solar thermal application of prepared materials are introduced.

To prepare the thermal conductive substrate in the composite solar receiver materials, AlN and α-SiC ceramic were chosen as the raw powder. This is attributed to the limited number of studies that have employed ceramics as substrates, and they have advantages such as high thermal conductivity, resistance to corrosion and high temperature. Cu and graphite powder were also fabricated as the thermal conductive substrate due to their high thermal conductivity for comparing. In order to compare with the most common material employed in solar receivers, the stainless steel was applied. The spark plasma sintering technique was used to form powder into pellet. In order to improve the thermal conductivity and densification of the pellet, it was necessary to add sintering additives to form a liquid phase and remove impurities of the raw powder. CaO was chosen as the additive for AlN, and for α-SiC, the composition of CaO and Al_2O_3 was added. AlN and CaO were dry-mixed through a novel high-shear mixer (Picomix), and then sintered into pellet. The effects of different additive sizes, contents, and rotational speeds of Picomix, on the porosity and thermal conductivity of AlN pellets were studied. Various mixing techniques including high-shear mixing, ball milling and manual mixing were compared. α-SiC-based sintered pellet was acquired through adding CaO and Al_2O_3 additives and mixing in the ball mill. Aside from ceramics, Cu pellet was sintered and applied due to its high thermal conduction ability. Given its high susceptibility to oxidation, Cu particles were dry-coated with β-SiC

which has high intrinsic thermal conductivity through the Picomix, in order to provide anti-oxidation protection for Cu. Stainless steel and graphite pellet were also sintered for comparison as they have been utilized in solar thermal researches. The composite solar receiver materials for solar thermal application were prepared based on the above pellets with carbon black as the solar absorbing coating due to its high absorptivity. α-SiC-based pellet was directly used without absorbing layer, as SiC exhibited a relative high absorptivity. Various methods were used to characterize the prepared powders and pellets, in terms of the physical property, morphology, chemical composition, structural property, thermal conductivity and absorptivity.

In order to test the thermal performance of the prepared pellets, the thermal conduction experiment through a hot plate was conducted on the thermal conductive pellets. A solar simulator system was set up, and the solar radiation absorption and heat transfer experiment was carried out on the composite solar receiver materials. The temperature variation of the samples was measured and compared.

2.2 Materials and methodology

The composite solar receiver material comprises two fundamental layers: the top layer, which is the solar-absorbing material for capturing solar radiation, and a thermal conduction substrate to efficiently conduct the heat (Fig. 2. 1).

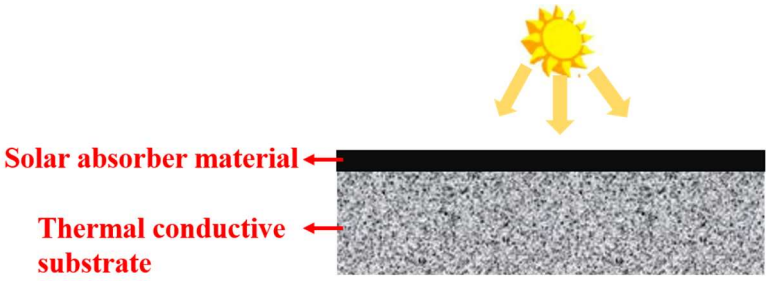

Fig. 2. 1 Schematic diagram of the composite solar receiver materials

2.2.1 Materials

All the used commercially available materials in this study are summarized and listed in Tab. 2. 1.

Tab. 2. 1 The list of commercially available materials used in current research

Material	Purity	Supplier	Application	Property
Aluminum nitride (AlN)	≥ 99%	Alfa Aesar	Thermal conductive material	Non-porous
Calcium oxide (CaO) (Mean diameter*: 30.6 μm)	99.5%	Sigma-Aldrich	Additive	Non-porous
Calcium oxide (CaO) (Mean diameter*: 4.1 μm)	99.5%	Sigma-Aldrich	Additive	Non-porous
Silicon carbide (α-SiC)	99.9%	VWR Chemicals	Thermal conductive material/Absorber	Non-porous
Silicon carbide (β-SiC)	99.8%	Fisher Scientific	Thermal conductive additive	Non-porous
Alumina (γ-Al_2O_3)	99.9%	Sasol	Additive	Porous
Copper (Cu)	99.9%	Fisher Scientific	Thermal conductive material	Non-porous
Stainless steel 316L	99%	Höganäs	Thermal conductive material	Non-porous
Graphite (C)	99%	Fisher Scientific	Thermal conductive material	Non-porous
Carbon black (C)	≥ 99%	Alfa Aesar	Absorber	Non-porous
Chlorobenzene (C_6H_5Cl)	≥ 99.5%	Sigma-Aldrich	Solvent	-
Ludox (Colloidal silica suspension)	-	Sigma-Aldrich	Binder	-

*: Mean diameter of particle obtained from laser diffraction particle size analyzer.

2.2.2 Preparation of pellet materials for thermal conduction study

The preparation of thermal conductive substrates will be introduced in this part. Several kinds of pellets with enhanced thermal conductivity were prepared by spark plasma sintering (SPS). The pellet has a diameter of 10 mm and a thickness ranging from 1.5 mm to 2.5 mm, which is due to the shape limitation of the mold in SPS. The AlN pellets were produced with and without CaO as the sintering additive to investigate the additive influence. A high-shear mixer was applied to mix AlN and CaO powders. The α-SiC powder and CaO-Al_2O_3 additive powder were dry-mixed by ball milling and

then sintered to obtain α-SiC pellet (with and without additives). The Cu particles were dry-coated with β-SiC for oxidation protection by the Picomix and sintered, acquiring Cu pellet with reduced oxidation. The stainless steel powder and graphite powder were also sintered into pellets for comparison. Tab. 2. 2 lists various properties of all the used powders in this work. The preparation methodologies are introduced in this part.

Tab. 2. 2 Properties of used powders

Powder	Intrinsic thermal conductivity of powder (W/m·K)	Melting point (°C)	Mohs hardness	Toxicity	Price (€/kg)
Aluminum nitride (AlN)	319	2200	7–8	No	280
Calcium oxide (CaO)	20	2570	3–4	No	50
Silicon carbide (α-SiC)	380	2730	9.5	No	150
Silicon carbide (β-SiC)	150	2730	9.5	No	180
Alumina (γ-Al_2O_3)	38	2054	9	No	130
Copper (Cu)	398	1085	3	No	386
Stainless steel 316L	13	1400	5.5	No	110
Graphite (C)	100–400	3652	1–2	No	820
Carbon black (C)	1–10	3550	1–2	No	175

2.2.2.1 Preparation of AlN-based pellet

2.2.2.1.1 Powder mixing procedure

The AlN powder and its mixture with sintering additives (CaO) are introduced firstly. CaO was applied as the sintering additive for AlN. AlN powders contain 0.7 wt% oxygen impurities. Three kinds of CaO powder with different particle sizes were tested to study the additive size influence on densification and thermal conductivity of pellet, using the following annotations: $CaO^{2.6}$ (micron-particles), $CaO^{0.8}$ (submicron-particles) and $CaO^{0.04}$ (nano-particles). The superscripts represent the measured mean diameters (d_s in microns), which are presented in greater detail in Section 3.2.1.2, Chapter 3. $CaO^{2.6}$ and $CaO^{0.04}$ powders were purchased, while $CaO^{0.8}$ powders with d_s of 0.8 μm (submicron) were obtained by ball-milling $CaO^{2.6}$ powders at room temperature and

atmospheric pressure. $CaO^{2.6}$ powder (20 g) were added into the agate cup of a planetary ball mill (PM100, RETSCH, Germany), with 100 agate balls (5 mm-diameter) also added. The rotational speed was 600 rpm and the duration was 20 h.

These three powders ($CaO^{2.6}$, $CaO^{0.8}$ and $CaO^{0.04}$) are cohesive and form agglomerates of varying shapes and sizes. Classical AlN + additive powder mixing techniques, such as ball milling, are ineffective and more importantly, inhomogeneous. In the present study, the new shearing and dispersion technique (Picomix process) made it possible to add additives efficiently. The shear mixing process was applied with a Picomix device (Hosokawa micron B.V., Japan), in order to prepare a powder mixture for sintering (Fig. 2. 2). The Picomix processor comprises a control unit, allowing the rotational speed (0 to 6000 rpm) and time to be set, a conical, stainless steel agitator vessel (100 ml), and a rotor with three pairs of vertically arranged, angled paddles (Fig. 2. 2). The lowest and middle paddles are set at an angle of 60° to the horizontal plane, whereas the highest paddles are set at an angle of 30°. The gap between the paddle extremities and the vessel wall is 1.3 ± 0.3 mm. After the vessel has been loaded with the desired powders, it is mounted onto the control unit. The paddle-equipped rotor rotates at the set speed, with the lowest paddles first mixing the powders, and centrifugal forces pushing them upwards along the conical vessel wall until they fall back down to the bottom of the device. During their ascent, the powders move rapidly and interact between the middle paddles and the wall, due to the high rotational velocity of the former and the resulting high shear and impact forces. The shearing force allows the two different powder types to be evenly dispersed without breakage. The high-energy impacts delivered by the upper set of paddles tend to disaggregate any remaining fine-particle agglomerates. This process is aimed at good mixing of two or more powders with the same or different sizes. Moreover, Picomix could be used for particle coating. In this case, when subjected to an external shearing force, fine (guest) particles are attracted and adhere to coarse (host) particles, due to the influence of strong van der

Waals forces, thus forming a uniform and continuous coating on the surface of the host particles.

The AlN and different CaO powders were mixed in the Picomix mixer at room temperature and atmospheric pressure. AlN powder and either $CaO^{2.6}$, $CaO^{0.8}$, or $CaO^{0.04}$ powders were loaded into the vessel at various mass ratios (mass of CaO/mass of AlN) equal to 0, 1%, 3% and 5%, which were based on previous researches[110,114] introduced in Section 1.4.1.2, Chapter 1. Pure AlN powder was also processed the mixing process in the mixer to facilitate a more precise comparison. According to recommendations from Hosokawa Micron B.V, the total powder volume was set at 40 ml, in order to ensure free flow of the particles with excellent particle mixing. Rotational speeds of 500 rpm, 3500 rpm and 5000 rpm were set with the control unit. All mixing time were set to 5 min, and the mixed powders were labeled as AlN+**X**%**Y**(**Z**rpm, 5min), where **X**% represents the mass ratio of CaO to AlN, **Y** indicates the different kinds of CaO, and **Z** indicates the rotational speed of the paddle spindle in the Picomix mixer. Detailed sample information and mixing conditions are listed in Tab. 2. 3.

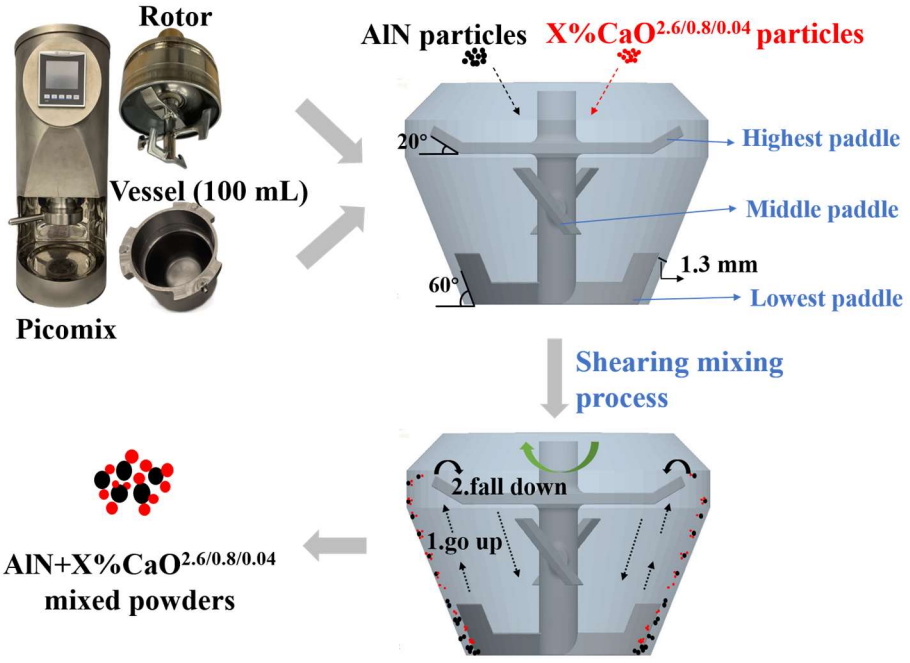

Fig. 2. 2 Picomix mixer and mixing process of AlN/CaO powders

To conduct a comprehensive comparison between the Picomix and methods introduced in the literature, other mixing techniques such as ball milling and manual operation were also studied here. For the mixture combining AlN with 3 wt% of $CaO^{0.04}$, ball milling and manual mixing were used. In the case of ball milling, 10.0 g of AlN powder and 0.3 g of $CaO^{0.04}$ powder were added into the agate cup (50 ml capacity) of the planetary ball mill (PM100), to which 100 agate balls (5 mm-diameter) were also added. A rotational speed of 250 rpm was then applied for 3 h. The mixed powder was labeled as AlN+3%$CaO^{0.04}$(BM). In the case of the manual mixing method, 10.0 g of AlN powder and 0.3 g of $CaO^{0.04}$ powder were placed in a beaker and stirred for 10 min with a spatula. The resulting mixed powder was labeled as AlN+3%$CaO^{0.04}$(M).

Tab. 2. 3 Mixing conditions and code names of AlN/CaO mixed powders

Main sintering material	Sintering additive	Mass ratio of CaO to AlN (%)	Mixing method	Rotational speed (rpm)	Mixing time (min)	Code name
AlN	-	0	Picomix	3500	5	AlN
AlN	$CaO^{2.6}$	1	Picomix	3500	5	AlN+1%$CaO^{2.6}$(3500rpm,5min)
AlN	$CaO^{2.6}$	3	Picomix	3500	5	AlN+3%$CaO^{2.6}$(3500rpm,5min)
AlN	$CaO^{2.6}$	5	Picomix	3500	5	AlN+5%$CaO^{2.6}$(3500rpm,5min)
AlN	$CaO^{2.6}$	3	Picomix	500	5	AlN+3%$CaO^{2.6}$(500rpm,5min)
AlN	$CaO^{2.6}$	3	Picomix	5000	5	AlN+3%$CaO^{2.6}$(5000rpm,5min)
AlN	$CaO^{0.8}$	3	Picomix	5000	5	AlN+3%$CaO^{0.8}$(5000rpm,5min)
AlN	$CaO^{0.04}$	3	Picomix	5000	5	AlN+3%$CaO^{0.04}$(5000rpm,5min)
AlN	$CaO^{0.04}$	3	Ball milling	250	180	AlN+3%$CaO^{0.04}$(BM)
AlN	$CaO^{0.04}$	3	Manual mixing	-	10	AlN+3%$CaO^{0.04}$(M)

2.2.2.1.2 Sintering powder into pellet procedure

All of the aforementioned powders (AlN with and without additives) were transformed into dense disk-shaped pellets by spark plasma sintering. As shown in Fig. 2. 3, each mixed powder sample was loaded into a 10 mm diameter graphite mold with constant tapping. The lower and upper surfaces of the powder were covered with a 0.5 mm thick graphite foil. After compacting the powder, the mold was placed in the vacuum chamber of the SPS device (630Sx, SUGA Ltd., Japan). The sintering process was performed under vacuum with a heating rate of 10 ℃/min and held at a final temperature of 1650 ℃ (the sintering temperature at which the AlN pellet has the highest thermal conductivity, according to Kobayashi et al.[133]) for 5 min under an external load of 5.1 kN (65 MPa) applied between the upper and lower punches. A pyrometer monitored the temperature in the chamber throughout the sintering process. The temperature and pressure changes during the sintering process are shown in Fig. 2. 3. The sintered pellets were labeled as AlN+**X**%**Y**(**Z**rpm,5min,pellet), AlN+3%$CaO^{0.04}$(BM,pellet) and AlN+3%$CaO^{0.04}$(M,pellet), respectively.

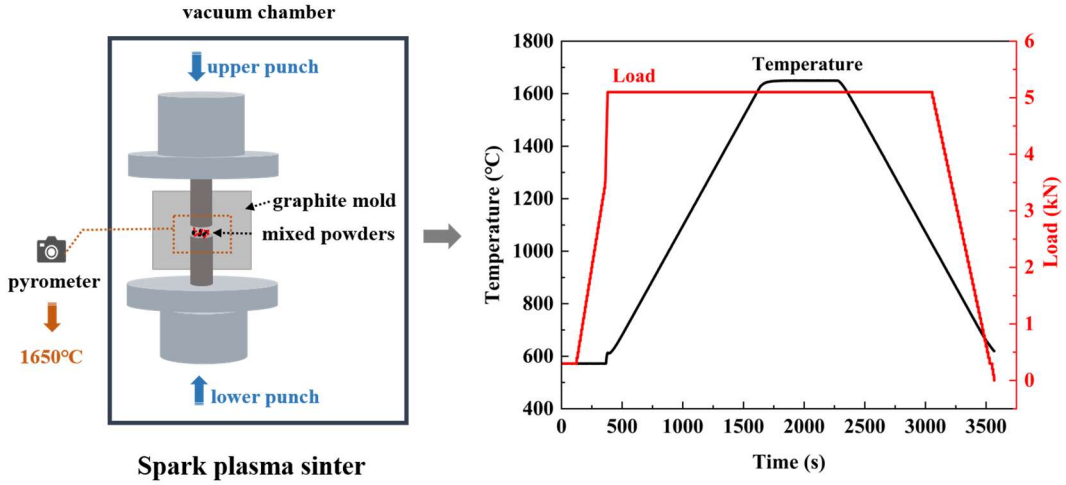

Fig. 2. 3 Schematic diagram of the SPS device and sintering process of AlN/CaO pellets

2.2.2.2 Preparation of α-SiC-based pellet

2.2.2.2.1 Powder mixing procedure

CaO and Al_2O_3 were mixed with α-SiC powder as sintering additives. The choice of α-SiC is because most of the large-sized SiC particles on the market are alpha phase. When the content of CaO and Al_2O_3 in their mixture each constitutes 50%, they might be eutectic at a relatively low temperature, approximately 1370 °C[187]. As a result, the addition of CaO-Al_2O_3 could reduce the vapor pressure of the liquid phase and promoting the formation of the liquid phase[188]. This makes CaO-Al_2O_3 a suitable additive for sintering of α-SiC. α-SiC has an extraordinarily high hardness (Mohs hardness 9.5), second only to the toughest diamond (Mohs hardness 10) in the world, and significantly higher than Picomix's material, stainless steel (Mohs hardness 5.5)[189]. Therefore, ball milling was applied to mix α-SiC and additive powders in order to avoid deformation or fracture of the Picomix parts, as suggested by Hosokawa B.V. Here, 20.0 g of α-SiC powder, 0.9 g of $CaO^{0.04}$ powder and 0.9 g of Al_2O_3 powder (mass ratio of CaO-Al_2O_3 to α-SiC was 9%) were added into the agate (Mohs hardness 6.5–7) cup of the planetary ball mill (PM100). This mass ratio was based on the previous studies which can effectively improve the thermal conductivity of the α-SiC pellet[139,188]. The content of CaO and Al_2O_3 in the CaO-Al_2O_3 mixture each constituted 50% because this composition corresponds to the lowest eutectic temperature. Aside from the powders, 100 agate balls (5 mm-diameter) were added. A rotational speed of 250 rpm was then applied for 3 h at room temperature and atmospheric pressure. The mixed powder was labeled as α-SiC+9%CaO-Al_2O_3(BM). The preparation condition and code name of α-SiC-based powder are summarized in Tab. 2. 4.

2.2.2.2.2 Sintering powder into pellet procedure

As detailed in Section 2.2.2.1.2 (Chapter 2), the mixed α-SiC+9%CaO-Al_2O_3(BM) powder was also prepared for sintering following the same method. The sintering process was performed under vacuum with a heating rate of 10 °C/min and held at a final temperature of 1850 °C (the sintering temperature at which the SiC pellet has the

highest thermal conductivity, according to Kim et al.[190]) for 5 min under an external load of 5.1 kN. The sintered pellet was labeled as α-SiC+9%CaO-Al_2O_3(BM,pellet). As a control, pure α-SiC was sintered in the same procedure, and the resulting pellet was denoted as α-SiC(pellet).

2.2.2.3 Preparation of Cu-based pellet

2.2.2.3.1 Powder coating procedure

Cu is an excellent choice for substrate in solar thermal application because of its extraordinarily high thermal conductivity, but its ease of oxidation makes it unsuitable for long-term use in reality. In this study, the surface of Cu particle was dry-coated with β-SiC which has high intrinsic thermal conductivity (150 W/m·K as reported by Nguyen et al.[191]) in the Picomix mixer, in order to provide anti-oxidation protection for Cu without impairing the overall thermal conductivity of the Cu substrate. The choice of β-SiC is because β-SiC powders are more refined and homogenized at the submicron and nanometer scale.

The "coating" was employed instead of "mixing" here primarily due to the considerable disparity in the size between Cu and β-SiC particles. The dry particle coating process involves the deposition of nano- or submicron-scale particles (guest particle ranging from 0.1 to 50 μm in size) onto larger micron-sized particles (host particle from 1 to 500 μm). The host and guest particles are blended under mechanical force (here is shear force), and the adhesion force (mainly van der Waals force) between the guest and the host particle exceeds the weight of the guest particle, facilitating a strong attachment of the guest onto the host particle[192]. The particle sizes of Cu and β-SiC are detailed in Section 3.4.1, Chapter 3. In the Picomix, Cu is the host particle, while β-SiC serves as the guest particle, thereby realizing the dry coating process.

The coating mass fraction (w) of β-SiC was calculated based on the model which supposes each host particle (Cu) is completely and orderly covered by one layer of guest particles (β-SiC). Besides, there are two assumptions. First, the guest particle and host particle are spherical and homogeneous in size. Second, the particles do not deform

throughout the coating process[193]. By dividing the area available for guest particle placement by the effective area occupied by the guest particle on the contact surface, the following equation is acquired[194]:

$$w = \frac{4C_{2D}(\frac{R_H}{R_G}+1)^2}{4C_{2D}(\frac{R_H}{R_G}+1)^2+\frac{\rho_H}{\rho_G}(\frac{R_H}{R_G})^3} \quad \text{Eq. 2. 1}$$

where C_{2D} is the packing fraction of guest particle on the surface of host particle. In this case, the ideal packing pattern for a 2D compact arrangement is hexagonal structure (Fig. 2. 4). So $C_{2D} = \frac{\pi}{2\sqrt{3}} = 0.906$. R_H and R_G are the mean radius of the host particle and guest particle. ρ_H and ρ_G are the density of host particles and guest particles, respectively.

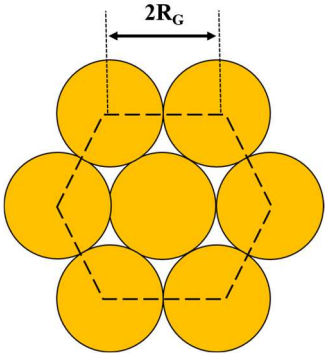

Fig. 2. 4 2D compact hexagonal arrangement of guest particles

The coating mass fraction of β-SiC particles was calculated to be 1.29% according to the size and density values measured and introduced in Section 3.4.1, Chapter 3. While in experiments, part of the powders might stick on the mixer's wall. As a result, the mass fraction of β-SiC was fixed at 2% to ensure better coverage of host particles. Here, 50.0 g Cu powder and 1.0g β-SiC powder were loaded into the vessel at room temperature and atmospheric pressure. A rotational speed of 5000 rpm and a duration of 5 min were set by the control unit. The acquired coated powder was labeled as Cu+2%β-SiC(5000rpm,5min). The preparation condition and code name of Cu-based powder are summarized in Tab. 2. 4.

2.2.2.3.2 Sintering powder into pellet procedure

As detailed in Section 2.2.2.3.1, Chapter 2, the coated Cu+2%β-SiC(5000rpm,5min) powder was also prepared for sintering following the same method. The sintering process was performed under vacuum with a heating rate of 10 ℃/min and held at a final temperature of 800 ℃ (the sintering temperature at which the Cu pellet has the highest densification[195]) for 5 min under an external load of 5.1 kN. The sintered pellet was labeled as Cu+2%β-SiC(5000rpm,5min,pellet). As a control, pure Cu was sintered in the same procedure, and the resulting pellet was denoted as Cu(pellet).

2.2.2.4 Preparation of the stainless steel and graphite pellet

In order to compare with the common materials employed in solar receivers, the stainless steel and graphite powder were used to prepare pellets, following the same sintering method. For stainless steel, the sintering process was performed under vacuum with a heating rate of 10 ℃/min and held at a final temperature of 1100 ℃ (the sintering temperature at which the stainless steel pellet has the highest densification[196]) for 5 min under an external load of 5.1 kN. The sintered pellet was labeled as SS(pellet). For graphite, the sintering process was performed under vacuum with a heating rate of 10 ℃/min and held at a final temperature of 1000 ℃ (according to the previous research[197]) for 5 min under an external load of 5.1 kN. The sintered pellet was labeled as graphite(pellet).

Tab. 2. 4 summarizes the α-SiC-based, Cu-based, stainless steel and graphite powder samples.

Tab. 2. 4 Preparation conditions and code names of α-SiC-based, Cu-based, stainless steel and graphite powders

Main sintering material	Second component	Mass ratio of second component to main sintering material (%)	Mixing method	Rotational speed (rpm)	Mixing time (min)	Code name
α-SiC	$CaO\text{-}Al_2O_3$	9	Ball milling	250	180	α-SiC+9%$CaO\text{-}Al_2O_3$(BM)
Cu	β-SiC	2	Picomix	5000	5	Cu+2%β-SiC(5000rpm,5min)
Stainless steel 316L	-	-	-	-	-	Stainless steel
Graphite	-	-	-	-	-	Graphite

2.2.3 Preparation of composite solar receiver materials

The material consists of 2 layers, as illustrated in Fig. 2. 1. In the preceding sections, the processing and preparation of materials specifically designed for thermal conduction were discussed. In this section, the deposition process of the solar absorption layer will be outlined. The thermal conductive material was fabricated in a pellet form. Due to the small size of the pellet (a thickness ranging from 1.5 mm to 2.5 mm, and a diameter of 10 mm), the composite solar receiver material was prepared by drop casting. AlN(pellet), AlN+3%$CaO^{0.04}$(5000rpm,5min,pellet) and SS(pellet) were applied as the substrate for coating (Fig. 2. 5). Carbon black was chosen as the absorber. 50 mg of carbon black powders were added into 10 ml chlorobenzene. 1 ml of Ludox binder was continuously added while stirring. The solution was ultrasonicated in a Sonic Dismembrator (Model 705, Fisher Scientific Company, USA) at 40 Hz for 30 min, resulting in a well-dispersed carbon suspension. Then the solution was deposited on the top of each pellet by a drop-casting method using a pipette. All the pellets were dried and hydraulically pressed under a pressure of 1 ton. Then the pellets were heated at 150 ℃ for 1 h under nitrogen atmosphere. The prepared composite

materials were labeled as AlN(pellet)-CB, AlN+3%$CaO^{0.04}$(5000rpm,5min,pellet)-CB, SS(pellet)-CB, respectively.

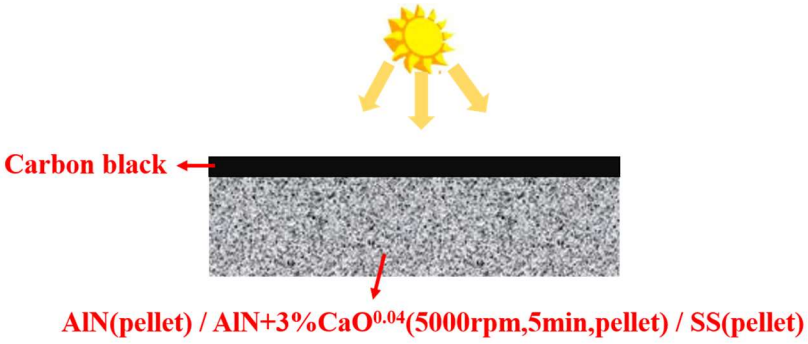

Fig. 2. 5 Prepared composite solar receiver materials in this work

2.3 Characterization methods

In this section, various methods used to characterize the prepared powders and pellets are introduced. The physical and bulk properties of powders were measured via density, size distribution, specific surface area, pore structure, flowability. The morphology and structural analyses of samples were conducted with scanning electron microscope and transmission electron microscope. The chemical properties of samples were determined by X-ray diffraction and X-ray fluorescence. The thermal conductivity of pellets was measured through laser flash apparatus and differential scanning calorimetry methods. The absorptivity of carbon powder was determined through UV-Vis spectroscopy and Fourier-transform infrared spectroscopy.

2.3.1 Physical and bulk properties measurements

2.3.1.1 Real density

The pycnometer method has been used to measure the real (true) density of solid samples. Its principle is to acquire the volume of the sample by measuring pressures and applying Boyle Mariotte's law[198].

In this work, the real density measurements were performed using the Helium Pycnometer (AccuPyc II 1340, Micromeritics Instrument Corporation, USA), as shown

in Fig. 2. 6. The sample was sealed in the sample chamber of known volume and appropriate helium (applied gas medium) was admitted and pressurized until the pressure was P_1. Then the expansion valve was open and the gas expanded into another precise expansion chamber. As a result, the pressure of sample chamber fell to P_2. The pressures before and after expansion were measured by the pressure transducer and used to compute the sample volume through the following equation:

$$V_{sample} = V_{chamber} - \frac{V_{expansion}}{\frac{P_1}{P_2} - 1} \quad \text{Eq. 2. 2}$$

where V_{sample} is the volume of sample, $V_{chamber}$ is the calibrated sample chamber volume, $V_{expansion}$ is the calibrated expansion volume, P_1 and P_2 are the pressures in sample chamber before and after expansion. Then the real density could be calculated through the following equation:

$$\rho = \frac{m_{sample}}{V_{sample}} \quad \text{Eq. 2. 3}$$

where ρ is the real density of the sample and m_{sample} is the sample mass. Before the measurement, the samples were dried to avoid the distorting effect of water vapor on the volume measurement. The instrument reported an average value from three runs of measurements.

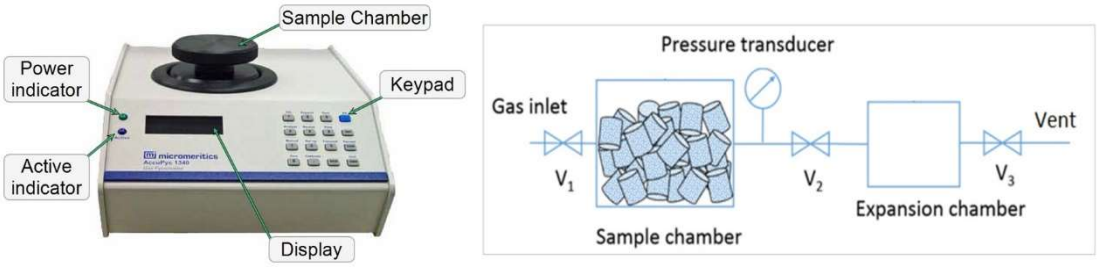

Fig. 2. 6 AccuPyc 1340 Pycnometer and its schematic diagram

2.3.1.2 Particle size distribution

Laser diffraction has been widely-used to measure the size distribution of powders ranging from nanometers to millimeters. The measurement is based on the angular variation in intensity of light scattered when a laser beam passes through dispersed

particulate samples in the sample cell. Light is scattered by large particles at small angles relative to the laser beam and small particles scatter light at large angles. The scattered angular intensity is then captured by a series of small, medium and wide angle detectors as shown in Fig. 2. 7. Signals are converted to data in relative software and then analyzed to calculate the size distribution of the particles that created the scattering pattern[199].

In this work, the particle size distributions were measured on the laser diffraction particle size analyzer (Mastersizer 3000, Malvern Panalytical Ltd., UK) which allows measurements from 10 nm to 3.5 mm using a single optical measurement path (Fig. 2. 7). This device is equipped with Hydro LV which is an automated wet dispersion unit with large volume (600 ml in maximum). It provides a rotational speed up to 3500 rpm and ultrasonic energy to ensure the good dispersion of particles. The powders were dispersed in deionized water and shaken repeatedly, following which sodium pyrophosphate decahydrate (concentration of 0.5 g/L) was added, in order to achieve improved powder dispersibility. The dispersed powder was sonicated using Sonic Dismembrator at 40 Hz for 10 s. Then the pre-dispersed samples were poured into Hydro LV and for each measurement, the rotation of 2500 rpm and the built-in ultrasonic energy with 30% of maximum intensity were applied. Then Mie theory was chosen as the calculation pattern which was applied for uniform isotropic particles of the simplest form[200]. Three times of measurements were conducted for each sample to ensure the data accuracy. The mean diameter (d_p) of particles were obtained based on the "Sauter mean diameter($d_{3,2}$)[201]" which is given by the following equation:

$$d_{3,2} = \frac{\sum_{i=1}^{k} N_i d_i^3}{\sum_{i=1}^{k} N_i d_i^2} \qquad \text{Eq. 2. 4}$$

where N_i is the number of particles in class i, and d_i is the average dimension of particle in this class which determined by the measurement. The uniformity coefficient (C_u) calculated by the volume-cumulative percentage was applied to quantify the particle size distribution range, specified by the following expression[122]:

$$C_u = \frac{d_{i60\%}}{d_{i1\ \%}} \qquad \text{Eq. 2. 5}$$

where $d_{i60\%}$ and $d_{i10\%}$ are the corresponding particle sizes when the volume-cumulative percentages are equal to 60% and 10%, respectively. $C_u > 2$ indicates a broad particle size distribution.

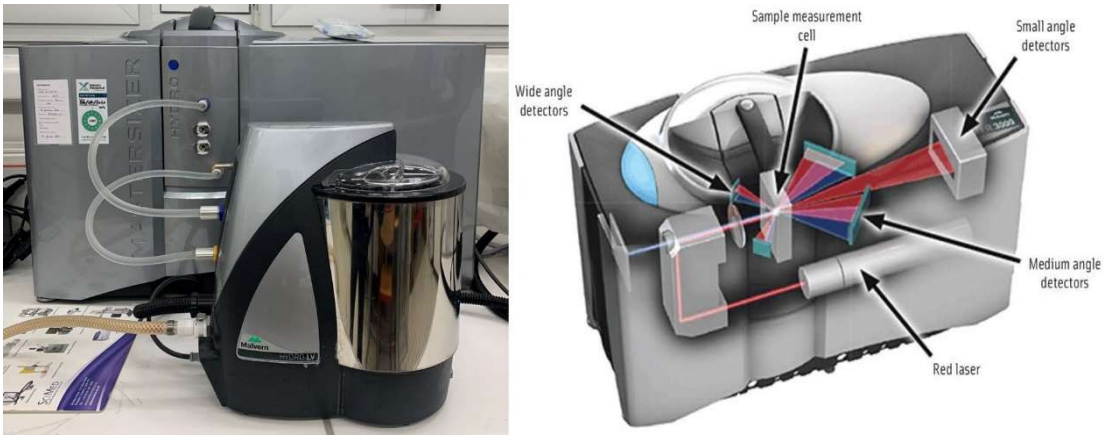

Fig. 2. 7 Mastersizer 3000 and its schematic diagram[202]

2.3.1.3 Specific surface area and porous structure

The specific surface area and porous structures of samples were measured by low temperature (77 K) N_2 adsorption-desorption method. An isotherm of relative pressure vs. volume adsorbed might be provided by measuring the quantity of N_2 gas that adsorbs onto the surface of samples and the following amount that desorbs at a constant temperature, which provides information on specific surface area and porous structures.

The surface area and porosity analyzer (TriStar II Plus, Micromeritics Instrument Corporation, USA) was applied in this work (Fig. 2. 8). Firstly, the sample was degassed under vacuum at 523 K for 3 h in a degasser (VacPrep 061, Micromeritics Instrument Corporation, USA) to remove atmospheric contaminants from sample surfaces and pores. Then the sample was transferred onto the analyzer and exposed to a stream of N_2 under different pressures. From the pressure variation, the N_2 adsorption-desorption isotherms were measured. The specific surface area of the sample was calculated according to the Brunauer-Emmett-Teller (BET)[203] theory at a relative pressure between 0.05 to 0.30. The evaluation of the BET theory is based upon the phenomenon of

physical adsorption of molecule of gases on the external and internal surfaces of the porous material which could be generalized by the BET equation[204] given below:

$$\frac{1}{v\left(\frac{p_0}{p}-1\right)} = \frac{c-1}{v_m c}\left(\frac{p}{p_0}\right) + \frac{1}{v_m c} \quad \text{Eq. 2. 6}$$

where v is the quantity of adsorbed N_2, p_0 and p are saturation and equilibrium pressures of N_2 respectively, v_m is the quantity of adsorbed N_2 corresponding to a monolayer and c is the BET constant which is determined experimentally and is specific to the gas being adsorbed and the temperature of the experiment. There is generally a linear relationship between $\frac{1}{v\left(\frac{p_0}{p}-1\right)}$ and $\frac{p}{p_0}$ which is also called isotherm in the range of monolayer adsorption ($0.05 \leqq \frac{p}{p_0} \leqq 0.30$). Then v_m could be solved by the slope ($\frac{c-1}{v_m c}$) and intercept ($\frac{1}{v_m c}$) of this linear relationship:

$$v_m = \frac{1}{\frac{c-1}{v_m c}+\frac{1}{v_m c}} \quad \text{Eq. 2. 7}$$

The total surface area (S_t) is then calculated from the value of v_m by the equation given below:

$$S_t = \frac{v_m * N_A * s}{V_M} \quad \text{Eq. 2. 8}$$

where N_A is Avogadro's constant (6.02×10^{23} mol^{-1}), s is the adsorption cross section of the adsorbing species and V_M is the molar volume of the adsorbate gas at standard temperature and pressure (STP) (22414 cm^3/mol). Then the specific surface area (S_{BET}) could be calculated by the equation given below:

$$S_{BET} = \frac{S_t}{m_{sample}} \quad \text{Eq. 2. 9}$$

Pore structures including pore volume and pore size distribution were calculated by the Barrett-Joyner-Halenda (BJH)[204] method. During the adsorption process, single-layer and multi-layer adsorption occur on the surface and the pore wall of the porous material to form liquid film as the gas pressure rises, then capillary condensation occurs in the pore to form a liquid-like meniscus. According to the adsorption data of the adsorption quantity and relative pressure, the volume change of the liquid film caused by the change of the film thickness and the change of the condensation volume in the

corresponding pore due to capillary condensation can be calculated between every two adjacent data, and then the pore volume (V_{pore}) and pore size (d_{pore}) can be obtained[205].

Fig. 2. 8 Surface area and porosity analyzer and degasser

2.3.1.4 Powder flowability

Hausner ratio (HR) was used to evaluate the flowability of powders. It is calculated through the following equation[206]:

$$HR = \frac{\rho_t}{\rho_b} \qquad \text{Eq. 2. 10}$$

where ρ_t is tapped bulk density and ρ_b is the aerated bulk density.

In this work, the test was carried out in a 50 ml cylinder filled with the powders, and a blade was used to scrape off the excess. The corresponding density was recorded as ρ_b. The cylinder was then placed on a horizontal surface and tapped vertically from above until no further decrease in volume was obtained. ρ_t was determined at this point. A HR $\leq$ 1.2 indicates good flowability of the material and a HR $\geq$1.4 suggests a poor flowability. While 1.2 < HR <1.4 indicates that the flowability of the particles is in the intermediate level[207].

2.3.1.5 Porosity of sintered pellets

The porosity of sintered pellets, which is the ratio of the internal pore volume to the pellet volume, was calculated using the following equation:

$$\varphi = \left(1 - \frac{V_{particle}}{V_{pellet}}\right) \times 100\% \qquad \text{Eq. 2. 11}$$

where V_{pellet} is the volume of the pellet, calculated using manual measurements, $V_{particle}$ is the volume of the particles in the pellet, derived from the mass of the mixed powder and its real density (for non-porous particle). The real volume of the solid part in the pellet was not determined using the real density of the pellet here. This was because closed pores might be formed inside the pellet after the sintering process, as explained in Section 3.2.2.3, Chapter 3.

2.3.2 Morphology and structural analyses

2.3.2.1 Scanning electron microscope (SEM) and Energy Dispersive X-ray Spectrometer (EDS)

The Scanning Electron Microscope (SEM) is commonly applied for observing the microscopic morphology of materials with a resolution between that of the optical microscope and that of the transmission electron microscope. This technique is based primarily on the detection of Secondary Electrons (SE) and Back Scatter Electrons (BSE) that scans the observed surface, and consequently the physical information is processed to obtain the morphology synchronized with the scanning, so that the observation can be performed intuitively. When the outer valence electrons of the atom obtain energy greater than the corresponding binding energy from the incident electrons, they could become free electrons. If this scattering process occurs relatively close to the surface of the sample (generally 5 to 10 nm depth), those free electrons are called SE. The SE images are very intuitive, which look the same as the visual image in real. The BSE are primarily beam electrons that have been scattered back out of the sample by elastic collisions with the nuclei of sample atoms, which have high energy (conventionally ranging from 50 eV up to the accelerating voltage of the beam). The

BSE originate in the depth range of several hundred nanometers from the sample surface and their yield increases with the increase of the atomic number of the sample, so it can not only be used for morphology analysis (the resolution is not as good as secondary electrons) but also be used to display the atomic number contrast and analyze composition qualitatively[208]. SEM also allows conducting semi-quantitative elemental analysis or chemical characterization of materials coupled with Energy Dispersive X-ray Spectroscopy (EDS) technique. This method collects the X-rays generated by the X-ray sources and the X-rays emitted when the sample interacts and analyzes. Since different elements have different emission spectra due to different atomic structures, they can be distinguished though various characteristic peaks. Also, element distribution can be presented in different colors in mapping.

In this study, the morphology and structure of the powders were observed by SEM (JSM-7800F, JEOL Ltd., Japan) (Fig. 2. 9). It is equipped with the super hybrid lens which consists of an electrostatic magnetic field overlapped with an electrostatic electric field and could provide extreme resolution of 0.8 nm at 15 kV and 1.2 nm at 1 kV. The accelerating voltage is as high as 30 kV. Several detectors that monitor a variety of signals resulting from the beam-sample interaction are installed including upper electron detector, upper secondary electron detector, backscattered electron detector, and a lower electron detector. An EDS coupled system from Oxford Instruments (80 mm^2 SDD spectrometer) is also equipped.

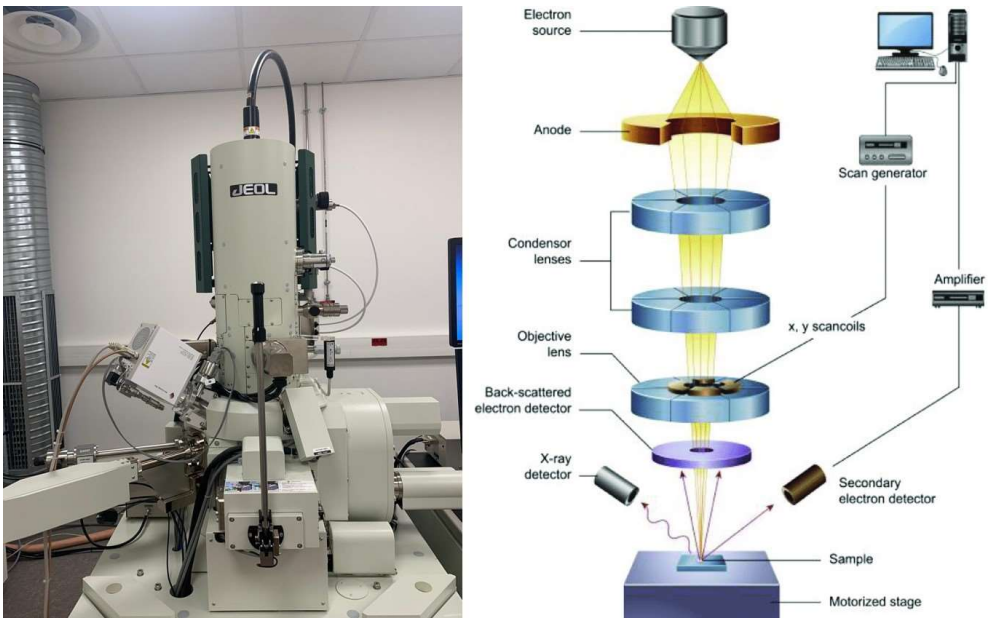

Fig. 2. 9 Scanning electron microscope and its schematic diagram[209]

2.3.2.2 Transmission electron microscope (TEM)

Transmission Electron Microscope (TEM) is used to give information about the internal structure of materials by dark and bright field imaging. In TEM, a high energy electron beam with low wavelength (less than 1 Å) as the source passes through a condenser to produce parallel rays and then is transmitted through a very thin specimen. The interaction between the primary electron beam and the sample leads to a number of detectable signals as schematized in Fig. 2. 10. The transmitted electrons are employed for generating high-resolution images. The electrons collide with atoms in the sample and change direction, resulting in solid angle scattering. The size of the scattering angle is related to the density and thickness of the sample, so it can form images with different brightness and darkness, presenting the structure of the sample[210]. Typical operating conditions of a TEM instrument are 100–200 keV, 10^{-6} mbar vacuum, 0.3 nm resolution and a magnification of 3.0×10^{5} to 3.0×10^{6}.

In this work, the sub-microscopic and ultra-microscopic structure of the samples were observed by TEM (TECNAI G2, FEI company, USA) (Fig. 2. 10) equipped with

LaB_6 filament and operating at 200 kV. Before the measurements, the sample powders were ultrasonically dispersed in ethanol and deposited on a copper grid.

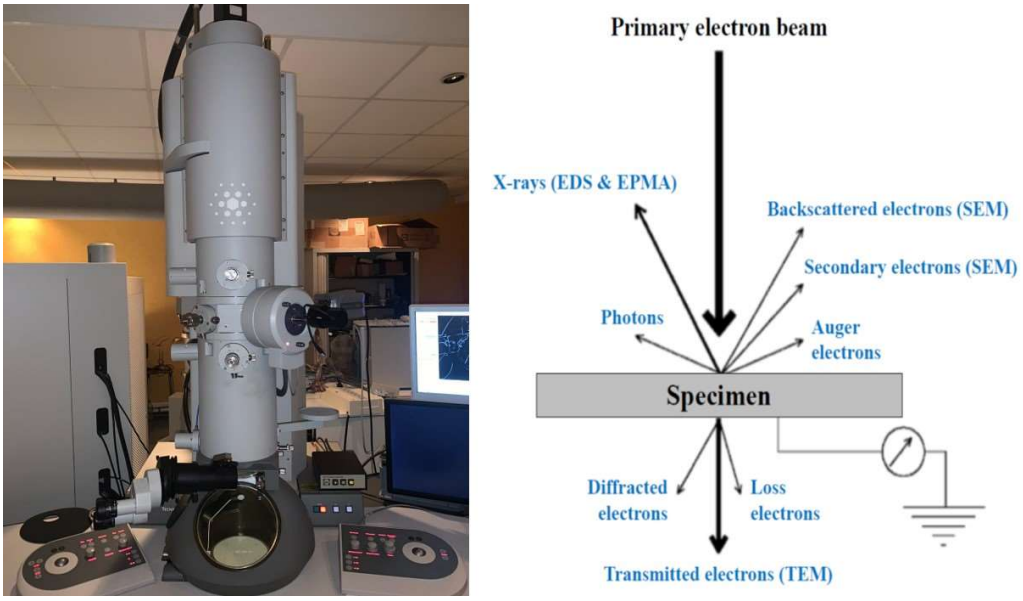

Fig. 2. 10 Transmission electron microscope and its schematic diagram[210]

2.3.3 Chemical properties analyses

2.3.3.1 X-Ray Diffraction (XRD)

X-ray diffraction (XRD) is an extensively employed technique for evaluating the crystallinity and structure of solid samples, founded on Bragg's law (Fig. 2. 11). Crystals usually exhibit periodic arrangements. Upon subjecting a crystal to X-ray bombardment using a fixed wavelength, highly reflected X-rays are generated through constructive interference of the scattered X-ray wavelengths. Diffraction intensities of X-rays will be strengthened when the difference in the pathlength is equal to an integer multiple of the wavelength and the angle of incidence equals the angle of scattering[211]. The general relationship between the wavelength of incident X-rays, the angle of incidence, and the spacing between atomic lattice planes is called Bragg's law, expressed by Eq. 2. 12.

$$n\lambda = 2dsin\theta \qquad \text{Eq. 2. 12}$$

where n is integer, λ is the wavelength of the incident X-rays, d is the interplanar spacing of the crystal and θ is the angle of incidence. In XRD measurement, the wavelength of

the incident X-ray is known. For this fixed wavelength of X-rays, each rational plane of atoms in the crystal will refract at a single, unique angle. According to the different diffraction peaks and their intensities presented in the material, the crystal structure can be qualitatively and quantitatively analyzed combined with the standard powder diffraction file (PDF published by the International Center for Diffraction Data) in the database.

In this study, the phase composition of the samples was characterized by X-ray Diffractometer (D8 Advance, Bruker, USA). The characterization was processed with Cu kα (λ = 0.154 nm) radiation at tube voltage of 40 kv, tube current of 30 mA, and 2θ angles ranged from 20° to 80° with a scanning rate of 0.02°/s. The average crystallite size of the particle was calculated based on the Scherrer equation as follows:

$$L = \frac{0.89\lambda}{\beta \cos\theta} \qquad \text{Eq. 2. 13}$$

where L is the volume-averaged crystallite size of particles (nm), θ is the Bragg angle (rad) and β is the full-width at half-maximum (FWHM) of the diffraction peak analyzed via the equipped EVA software (version 5.0) with “rad” in unit.

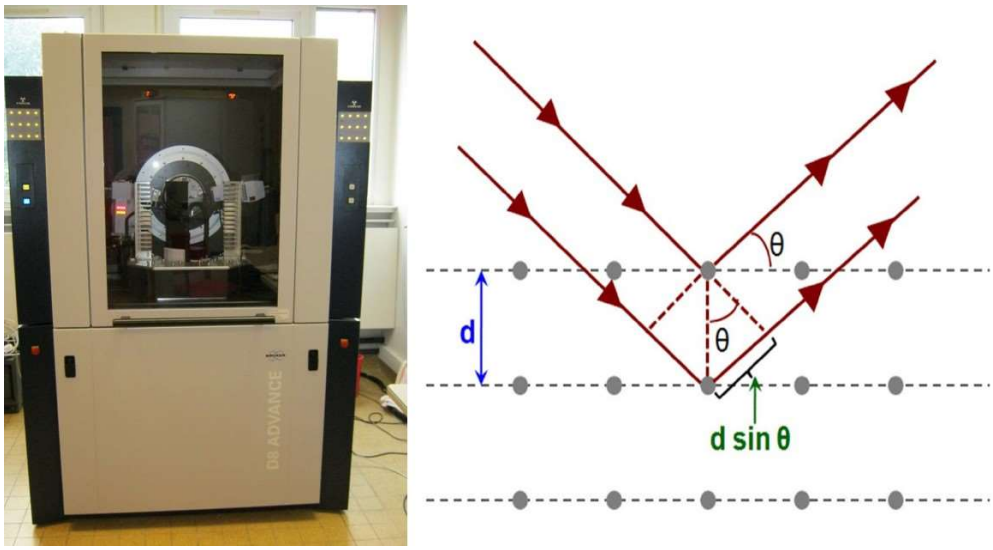

Fig. 2. 11 X-ray Diffractometer and Bragg’s law[212]

2.3.3.2 X-Ray Fluorescence (XRF)

One of the most frequent techniques for investigating the elemental composition of materials is X-ray fluorescence spectroscopy (XRF). X-rays are applied to ionize and excite atoms in the material. As shown in Fig. 2. 12, after absorbing primary X-ray energy, an electron from the K shell is emitted and the ensuing void is filled by an electron either from the L shell or the M shell. The wavelengths of the resultant K_α and K_β radiation are characteristic and correspond to different elements. Elemental quantification is accomplished by analyzing the emitted radiation intensity peaks and energy comparisons.

In the present work, a XRF spectrometer (M4 Tornado, Bruker, USA) was used to estimate the elemental composition of the Cu samples. In order to accurately quantify the elements in the samples, each sample was irradiated 30 times and the value of the content was averaged.

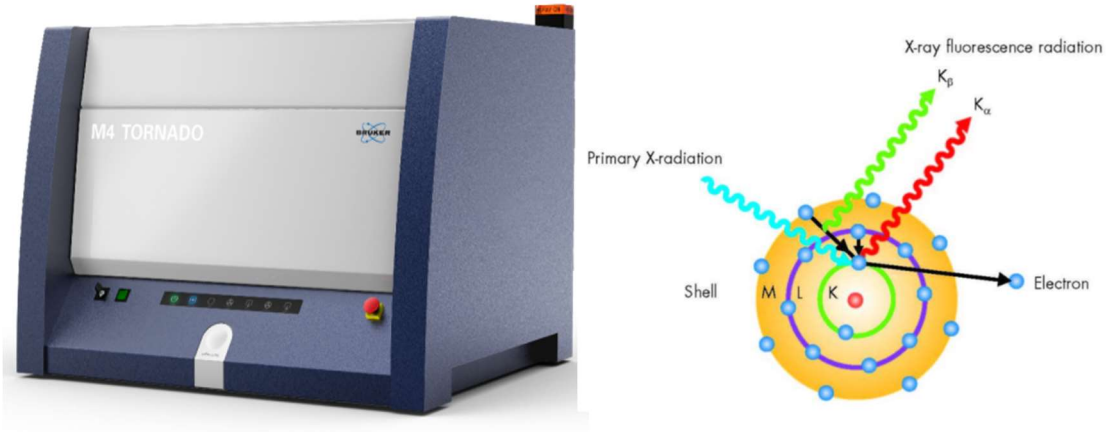

Fig. 2. 12 XRF spectrometer and its schematic diagram[213]

2.3.4 Thermal conductivity measurement

Several methods are applied to measure the thermal conductivity (k), including steady state method (hot disk method, heat flow meter method, etc.) and transient method (hot wire method, laser flash method, etc.)[214]. In this work, the thermal conductivity was obtained through the following equation[215]:

$$k = \alpha_t \cdot c_p \cdot \rho_{pellet} \qquad \text{Eq. 2. 14}$$

where α_t is the thermal diffusivity, c_p is the specific heat capacity and ρ_{pellet} is the apparent density of pellet, given by:

$$\rho_{pellet} = \frac{m_{pellet}}{V_{pellet}} \quad \text{Eq. 2. 15}$$

where m_{pellet} is the pellet's mass.

The thermal diffusivity (α_t) of the sample was measured on the Laser Flash Apparatus (LFA 457 MicroFlash, Netzsch, Germany) (Fig. 2. 13). The Laser Flash technique is a fast, non-destructive and non-contact method for determining thermal diffusivity. Its principle is shown in Fig. 2. 13. The front side of the pellet sample was heated by a short laser pulse. The absorbed heat propagated through the sample and induced a temperature increase on the rear surface. This temperature rise was measured versus time using an infrared detector[216]. So thermal diffusivity could be ascertained by the following equation:

$$\alpha_t = 0.1388 \frac{l^2}{t_{0.5}} \quad \text{Eq. 2. 16}$$

where l is the thickness of the pellet, $t_{0.5}$ is the time at 50% of the temperature increase of the rear face. During the test, the laser voltage was set at 1634 V and the beam diameter was 12.7 mm. All the samples were measured at room temperature.

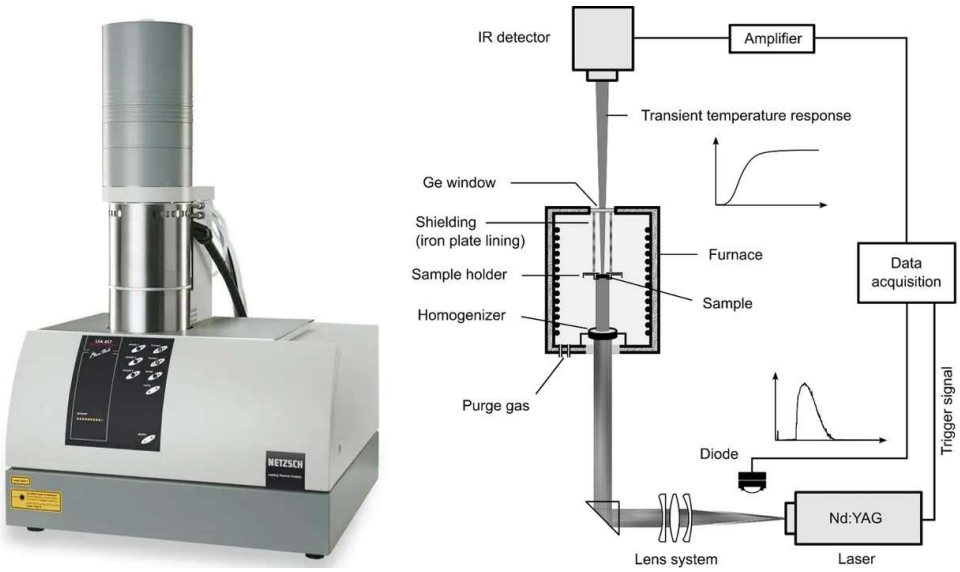

Fig. 2. 13 Laser flash apparatus and its schematic diagram[217]

Differential Scanning Calorimetry (DSC) analysis was then performed to acquire the c_p value. The principle of DSC is to measure the power difference (e.g., in the form of heat flow) input to a sample and a reference as a function of temperature at a programmed temperature. In this process, the exothermic and endothermic data of the sample could be measured which stands for the transition such as melting or crystallization. Various thermodynamic and kinetic parameters can also be determined, such as specific heat capacity, heat of reaction and heat of transformation[218]. In this work, a simultaneous thermal analyzer (Q600, TA instrument, USA) (Fig. 2. 14) was applied with samples sealed in the sample cup and heated from room temperature up to 1200 ℃ at a heating rate of 10 ℃/min under air atmosphere. According to the heat flow data given by DSC curves, the c_p could be calculated through the following equation[219]:

$$c_p = \frac{1}{m_{sample}} \frac{dH/dt}{dT/dt} \quad \text{Eq. 2. 17}$$

where dH/dt is the heat flow and dT/dt is the heating rate.

Fig. 2. 14 Simultaneous Thermal Analyzer

2.3.5 Absorptivity measurements of powders

The spectral absorptivity (α) was calculated through Eq. 1. 4 (Chapter 1). And the spectral reflectivity (ρ_r) was measured via the UV-Visible spectroscopy and Fourier-transform infrared spectroscopy from 0.2 μm to 2.5 μm. These two instruments provide light sources of different wavelength bands, and measure the ρ_r through the integrating sphere installed inside the instrument. There is white high-reflectivity diffuse reflection

coating on the inner wall of the integrating sphere. When the incident light irradiates the sample's surface, the diffused light of the sample could be collected efficiently by the integrating sphere, projected to the receiver and then converted into an electrical signal output[220]. The relationship between reflectivity and wavelength can be thus obtained. UV-Visible spectrophotometer (Lambda 650, Perkin Elmer, USA) and Fourier-transform infrared spectrometer (Nicolet iS50, Thermo Scientific, USA) were applied here (Fig. 2. 15). All the samples were measured in the form of powders under room temperature.

Fig. 2. 15 UV-Visible spectrophotometer (left) and Fourier-transform infrared spectrometer (right)

2.4 Installations and experiments for heat transfer studies

The prepared thermal conductive pellets were tested to assess their heat conduction capabilities (conductive heat transfer). The composite solar receiver materials were tested to evaluate their solar energy absorbing ability (radiative heat transfer), as well as the coupling of absorption and thermal conduction. In this work, we have set up two installations:

-a heating system, which provided the heat source and enabled the measurement of the pellet's surface temperature, assessing the material's thermal conduction ability.

-a solar simulator to simulate solar radiation, investigating the composite material's radiative effect.

2.4.1 Process for measuring conductive heat transfer through pellets

In the heating system, a resistive hot plate (C-MAG HS7, IKA company, Germany) with an output power of 1000 W was used (Fig. 2. 16 (a)). The tested pellet was placed on the hot plate, and its perimeter was insulated by the calcium-magnesium silicate fiber during the experiment (Fig. 2. 16 (c)). Three type K thermocouples with a diameter of 1 mm were placed on the top surface of the pellet to measure the temperature, denoted as T1, T2, T3 (Fig. 2. 16 (c)). The thermocouples were connected to a digital thermometer, which recorded the temperature changes over time (Fig. 2. 16 (b)). The heating temperature was set to 500 °C, T_{top} was computed as the average value of T1, T2 and T3. Three separate experiments were performed for each pellet to obtain reliable and consistent result. This system enabled the study concerning the influences of the pellet's thickness and thermal conductivity.

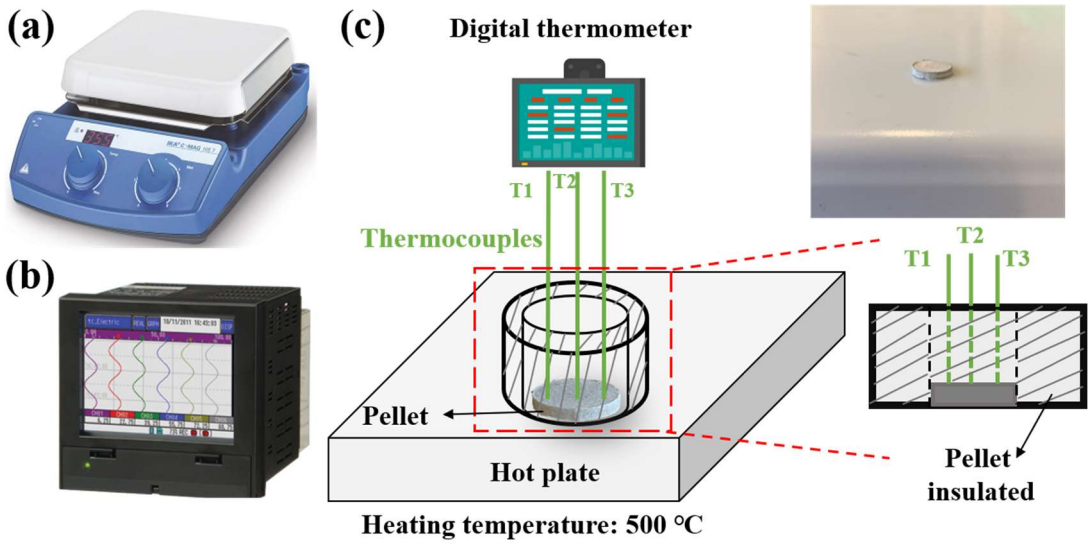

Fig. 2. 16 Heating system: (a) hot plate; (b) digital thermometer; (c) installation

In this work, all the pellets have a low thickness (1.5–2.5 mm). In order to study the effect of thickness and thermal conductivity on the conductive heat transfer, two materials with high and low thermal conductivity, Cu and stainless steel were applied as reference samples (reference thermal conductivity: 398 W/m·K for Cu and 13 W/m·K for stainless steel). The Cu and stainless steel cylinders (diameter: 10 mm) with three

thicknesses (1, 10 and 50 mm) were manufactured, as shown in Fig. 2. 17. For more accurate results, each cylinder contains a hole (diameter: 1.5 mm) at the bottom and at the center of the hole, the thermocouple was placed to measure the temperature, which was recorded as T_{bottom}. The T_{top} was measured in the same way presented above (Fig. 2. 15).

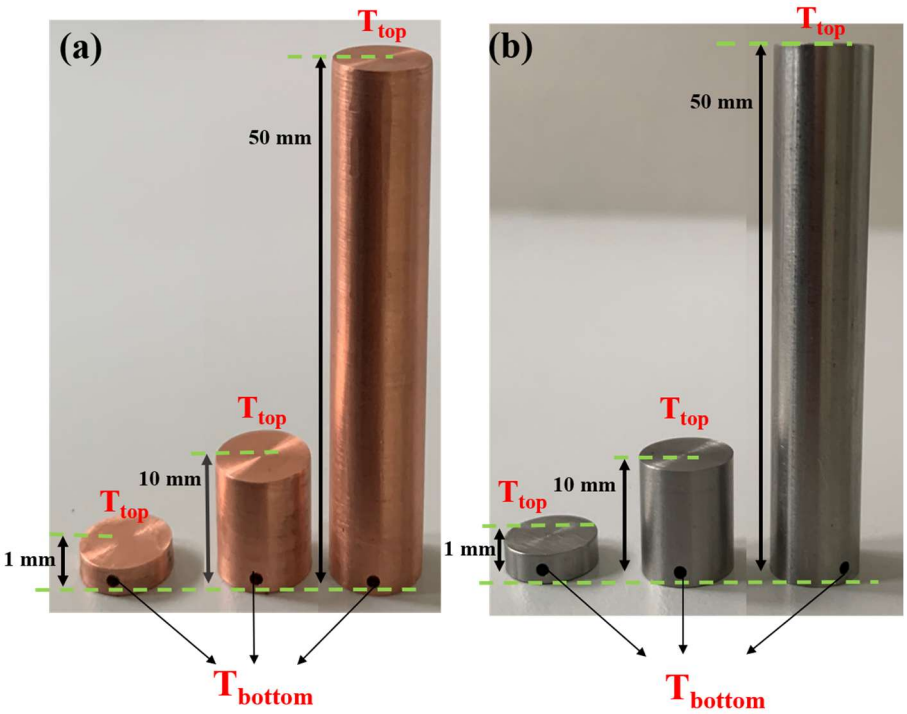

Fig. 2. 17 Cu and stainless steel cylinders with varying thicknesses

2.4.2 Solar simulator and solar absorption experiment

2.4.2.1 Solar simulator set-up

The investigation into solar absorption and heat transfer on the composite materials was conducted using a solar simulation facility. We have attempted to purchase a commercially available solar simulator; however, it proved challenging as there were no companies offering this equipment in France, and the price of that provided by other companies was exceedingly high. Thus it was determined that assembling the set-up by ourselves would be a more feasible approach. As a result, a low-cost and simple solar

simulator was designed, built, and characterized for experimental purposes. Specifically, it consists of the following parts:

1. Stainless steel framework

A stainless steel framework was manufactured by the CTA-France company (Fig. 2. 18 (a)). This framework was sealed to prevent any radiation leakage, achieved through the use of seals along the edges. Due to safety concerns, both doors of the framework were equipped with safety locks, ensuring the doors can be locked during the experiment. A stainless steel shelf was placed inside the framework, as the support for the lamp, radiation concentrating system and samples (Fig. 2. 18 (b)). Additionally, to enhance heat dissipation through convection and ensure proper cooling for the whole set-up during operation, two ventilators with a power of 5 W (UF60D, Fulltech, China) were installed side by side on the top of the framework (Fig. 2. 18 (c–d)). Its maximum rotational speed is 3000 rpm and it could provide an air flow of 0.29 m^3/min.

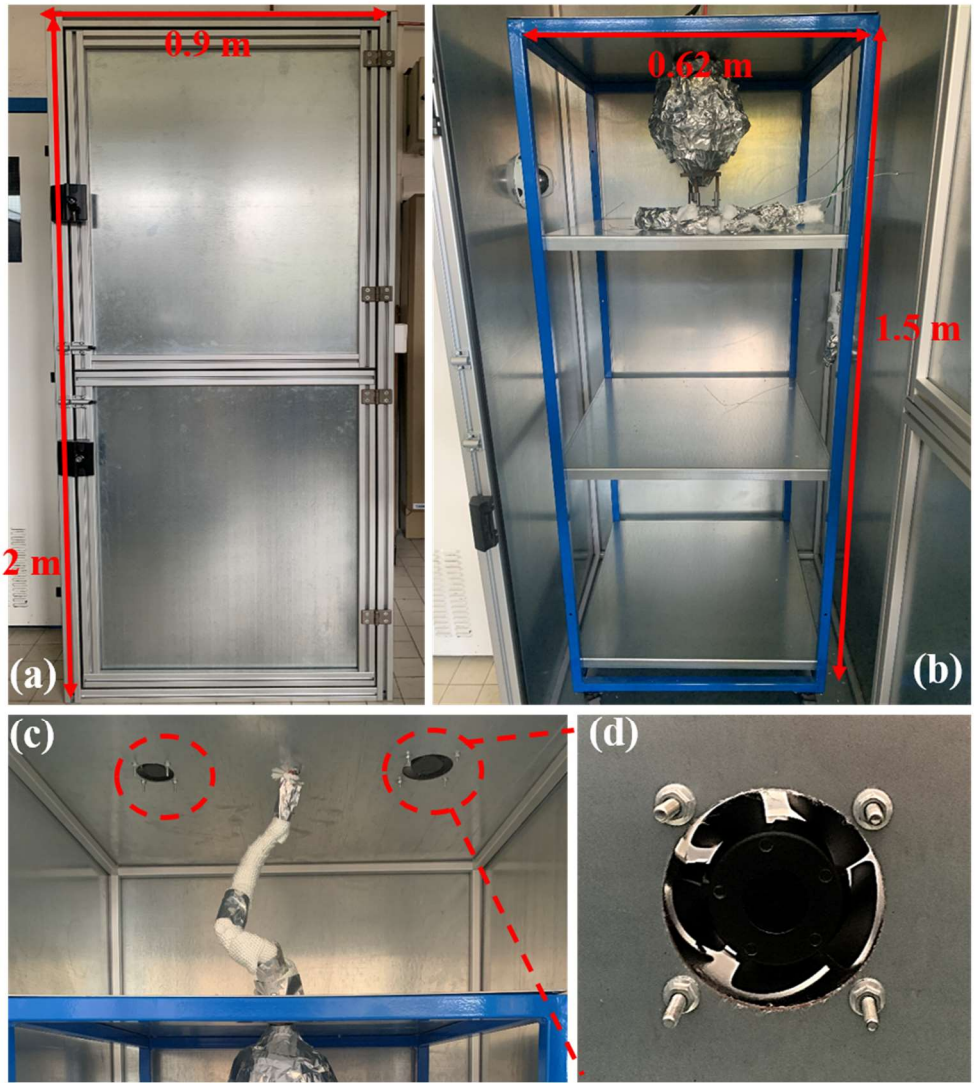

Fig. 2. 18 (a) Stainless steel framework; (b) Stainless steel shelf; (c–d) Ventilator

2. Light source

For the light source, a 1000 W quartz tungsten halogen lamp (QTH, 63362, Newport, USA) was utilized to simulate the spectrum of solar radiation (Fig. 2. 19 (a)). Fig. 2. 19 (b) gives its detailed size. The lamp has a coiled tungsten filament inside a quartz envelope, which is filled with rare gas and a small amount of halogen. It is rated at 120 Volts DC and the current flowing through the filament heats the tungsten to >3000 K. The lamp has an approximate flux of 27500 Lumens, a 3200 K color temperature, and a 300-hour average life. This lamp emits a high-intensity output from visible to infrared wavelengths with excellent stability, which closely resembles the spectral irradiance of the sun (Fig. 2. 19 (c)). In addition, the QTH lamp is readily available and relatively

inexpensive. These characteristics make it well-suited for simulating solar radiation in experimental settings.

The QTH lamp was connected to a high stability current and voltage lamp power supply (OPS-Q1000, Newport, USA), allowing precise control over the light switch and power output (Fig. 2. 19 (d)). This power supply serves as a highly stable current and voltage source for the operation of QTH lamps. The front panel features the LCD screen and buttons, providing convenient access to the power supply's functions such as the selection of power, current, and intensity control modes. It can also establish limits and monitor critical parameters in real-time for each operating mode. It can precisely adjust the lamp voltage within a range from 0 to 130 Volts DC, the current within a range from 0 to 10 A, and the power within a range from 0 to 1000 W.

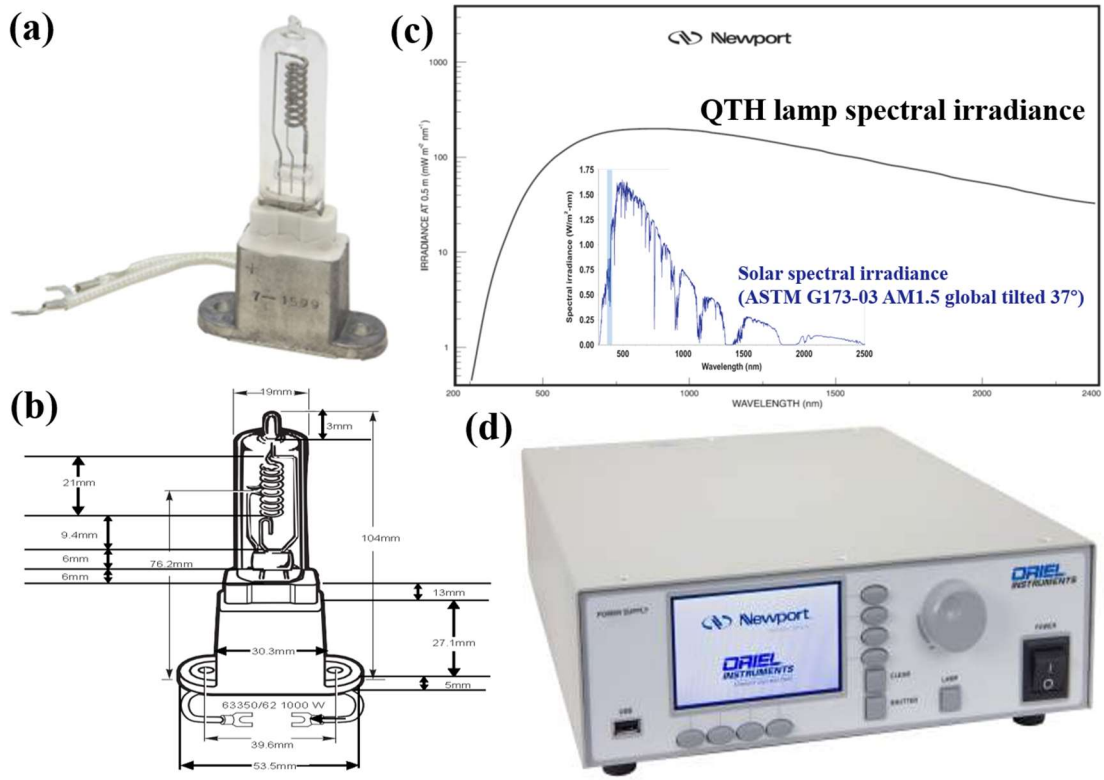

Fig. 2. 19 (a) The quartz tungsten halogen lamp applied in this work; (b) Lamp size; (c) Spectral irradiance curve of the lamp[221]; (d) Lamp power supply

(3) Radiation concentrating system

Given that the lamp emits light and radiation in various directions, the use of the concentrating system becomes imperative to efficiently focus and concentrate this radiation. The concentrator, also known as the reflector, helps in focusing and reflecting the emitted light and radiation onto a specific target area, effectively boosting the radiation intensity. Reflectors have different shapes depending on their specific working principles.

In this work, two types of reflectors were tried and applied: parabolic and ellipsoidal reflector. The parabolic reflector is a circular segment from one side of a full paraboloid, with the lamp placed at the focus during operation. The rays from the lamp are reflected as a parallel collimated beam as shown in Fig. 2. 20 (a). The employed parabolic reflector (Edmund Optics, UK) is made from 1 mm thick aluminum and features a center hole and (Fig. 2. 20 (b)). Its diameter is 457 mm, and its height is 119 mm. The effective focal length is 114 mm.

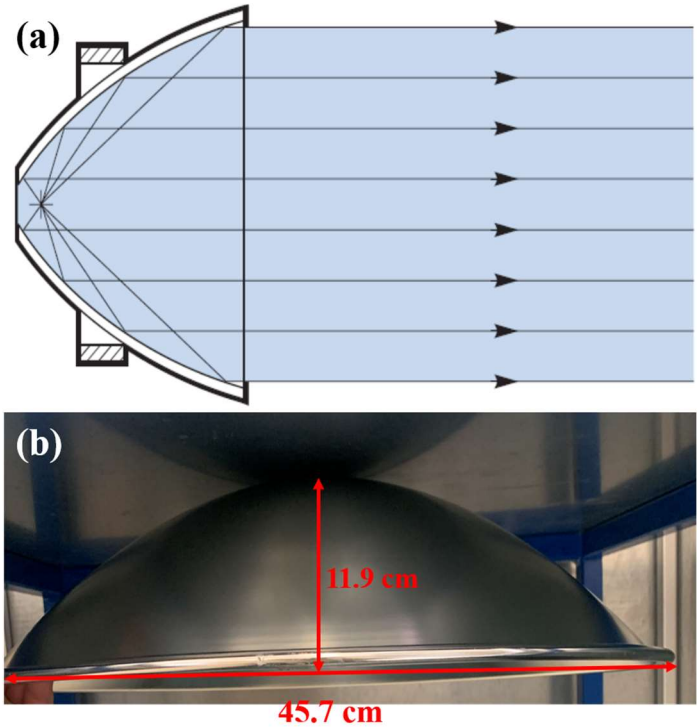

Fig. 2. 20 (a) Light reflection path and (b) Photo of the parabolic reflector

For the ellipsoidal reflector, its shape is derived from the surface of an ellipsoid. It has two conjugate foci (F1 and F2 in Fig. 2. 21 (a)). The optical characteristic of the ellipsoidal reflector is that any light projected onto the ellipsoid from one focus must pass through the other focus after reflection. By placing the lamp at F1, the light emitted from the source would be reflected and converge at F2 [222]. The size of the ellipsoidal reflector was determined through the following calculations. According to the dimension of the shelf, the distance between the lamp and the tested sample, which was also the distance between two foci, was set to 22 cm. So the value of c in Fig. 2. 21 (a) was 11 cm. The value of a was obtained by summing the length of the lamp (4 cm) and c value, which was 15 cm. As the three parameters of the ellipse formula, a, b and c are related by $a^2 = b^2 + c^2$. The value of b was acquired by solving this equation with a result of 10 cm. Here the outer radius of the reflector was assumed to be equated to b value. As a result, the detailed dimension of designed ellipsoidal reflector is displayed in Fig. 2. 21 (b). The top aperture diameter was set as 4 cm to place the lamp as well as fit its size. Due to the reduced height of the top aperture, the height of the reflector was 14.5 cm. The outer diameter was equal to 2b which was 20 cm.

Due to the long filament (3 cm) inside the QTH lamp, precise focusing by only one ellipsoidal reflector was challenging, and the focused spot size could be large. To avoid radiation leakage and enhance the ray concentration, a combination of the ellipsoidal reflector and a secondary reflector was applied following the design of Codd et al.[223]. Below the ellipsoidal reflector, a simplified secondary reflector was employed to enhance the available flux at the output aperture in accordance with the principle of the flow line concentrator as shown in Fig. 2. 21 (c). The incident flux which initially located between the two focus points of the hyperboloid (±c) will be converged on the ±a area after reflection, increasing the concentrated output flux[222]. To simplify the fabrication process, this secondary reflector was made from a truncated flow line concentrator to achieve the desired aperture size for light concentration, leading to a truncated hexagonal pyramid structure with favorable concentration properties. Its top

and bottom aperture size were determined based on the outer diameter of the ellipsoidal reflector (20 cm) and the diameter of the sample pellet (1 cm), respectively. The detailed dimensions are shown in Fig. 2. 21 (d).

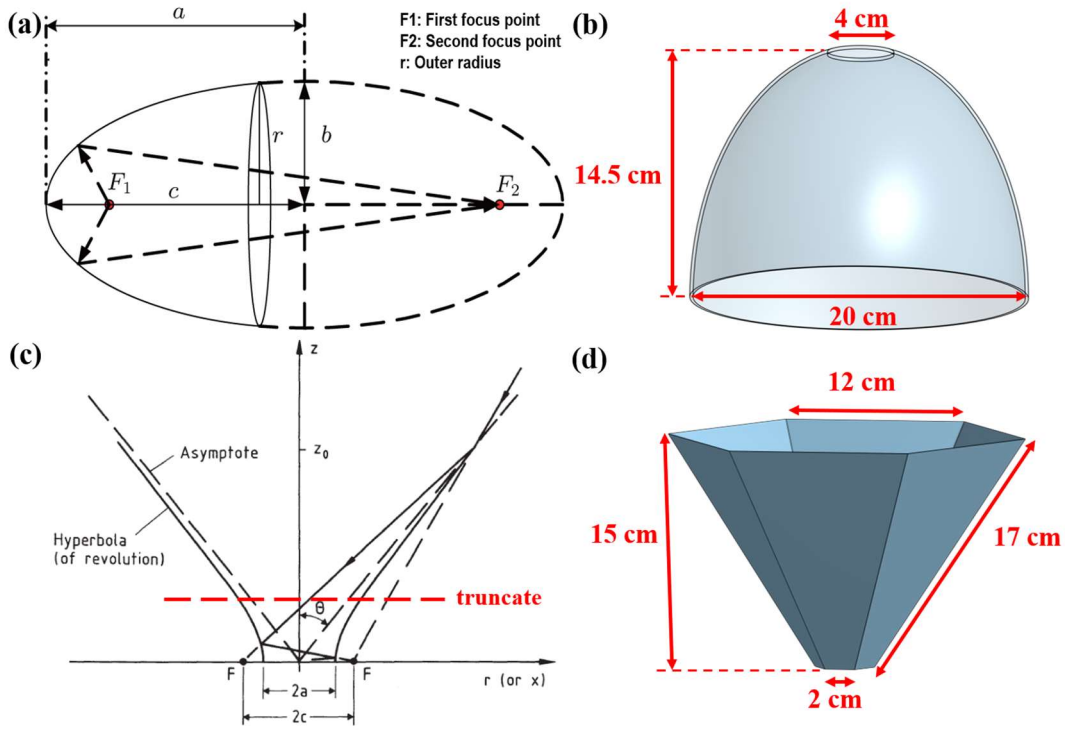

Fig. 2. 21 (a) Mechanism of the ellipsoidal reflector[224]; (b) Dimension of designed ellipsoidal reflector; (c) Mechanism of the flow line concentrator[222]; (d) Dimension of designed secondary reflector

Since no ellipsoidal reflectors or this kind of secondary reflectors on the market were found which matched the dimensions of the QTH lamp, we decided to make our own with the suitable size. Two mirror-polished stainless steel AISI 304 plates (mirrorINOX, Germany) with a thickness of 0.5 mm and 1.5 mm were ordered (Fig. 2. 22 (a)). The plates have very high reflectivity, good mechanical and optical flatness, good processability (laser, cutting, folding, forming processing) and low possible roughness to prevents adhesion. After calculating the dimensions, both the ellipsoidal and the secondary reflector were manufactured from the commercial mirror-polished plates by cutting and assembling in the mechanical atelier. The 0.5 mm thick

plate was cut by the waterjet cutter (Mach 200, Flow company, Germany) in the form of the annulus sector (Fig. 2. 22 (b)), and then the 4 annulus sectors were spot welded together (Titan XQ, EWM, Germany) to form the ellipsoidal reflector (Fig. 2. 22 (d)). Likewise, the 1.5 mm thick plate was cut into 6 parts of triangle, and spot welded to form the secondary reflector (Fig. 2. 22 (d-e)).

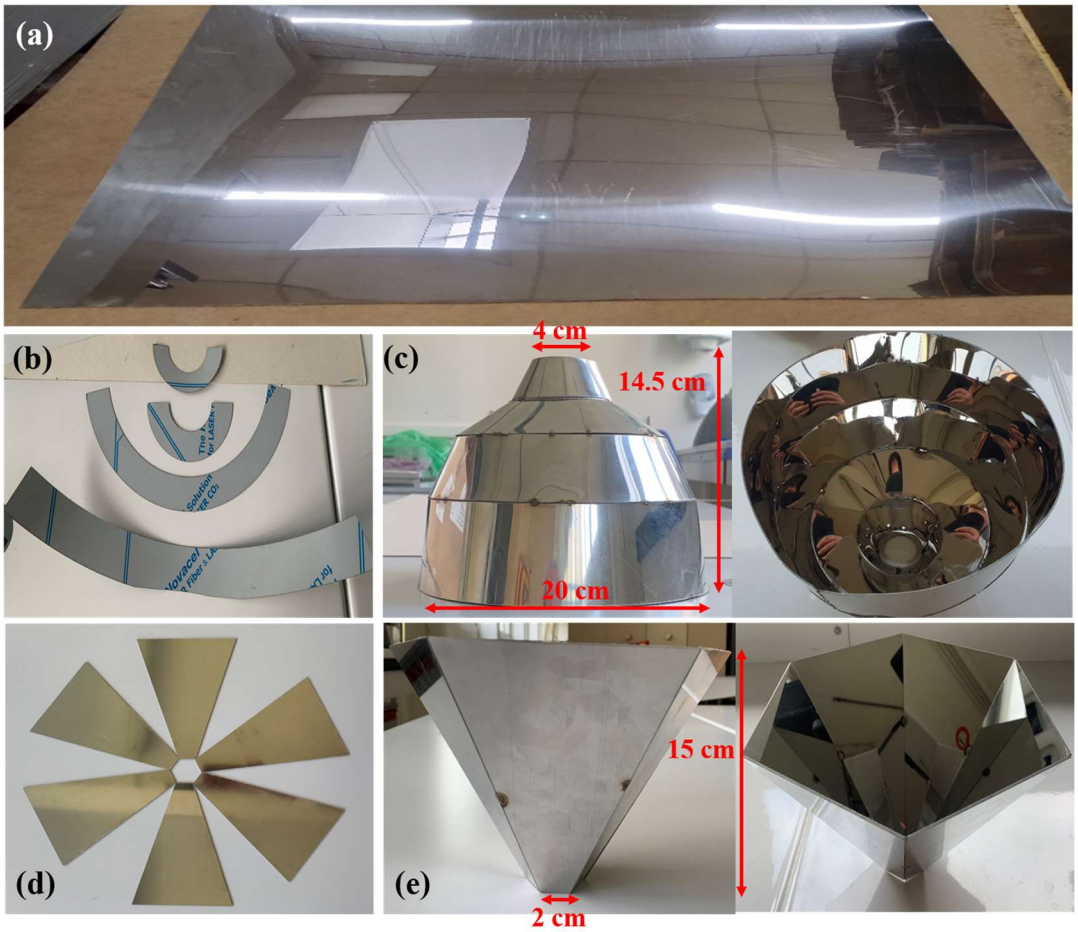

Fig. 2. 22 (a) Mirror-polished stainless steel plate; (b) Cut parts and (c) Assembled ellipsoidal reflector; (d) Cut parts and (e) Assembled secondary reflector

(4) Safety system

To ensure operational safety, a camera was installed within the framework to monitor its internal conditions in real-time during the experiment. Furthermore, protective equipment, including safety glasses, gloves, and helmet, was also provided (Fig. 2. 23).

Fig. 2. 23 Safety equipment

After the aforementioned components were processed, they were assembled onto the shelf and positioned within the framework to construct a fully functional solar simulator set-up (Fig. 2. 24). The upper part of the ellipsoidal reflector was fixed to the top of the shelf, while the lower part of the ellipsoidal reflector was supported by a small stand. The outer surface of the reflectors was covered with a layer of aluminum foil. Leveraging the light concentrating effect of the reflector, the emitted light from the lamp was focused to form high flux density radiation. This self-built solar simulator offers an efficient and cost-effective means of replicating solar radiation conditions for experimental study in the present work.

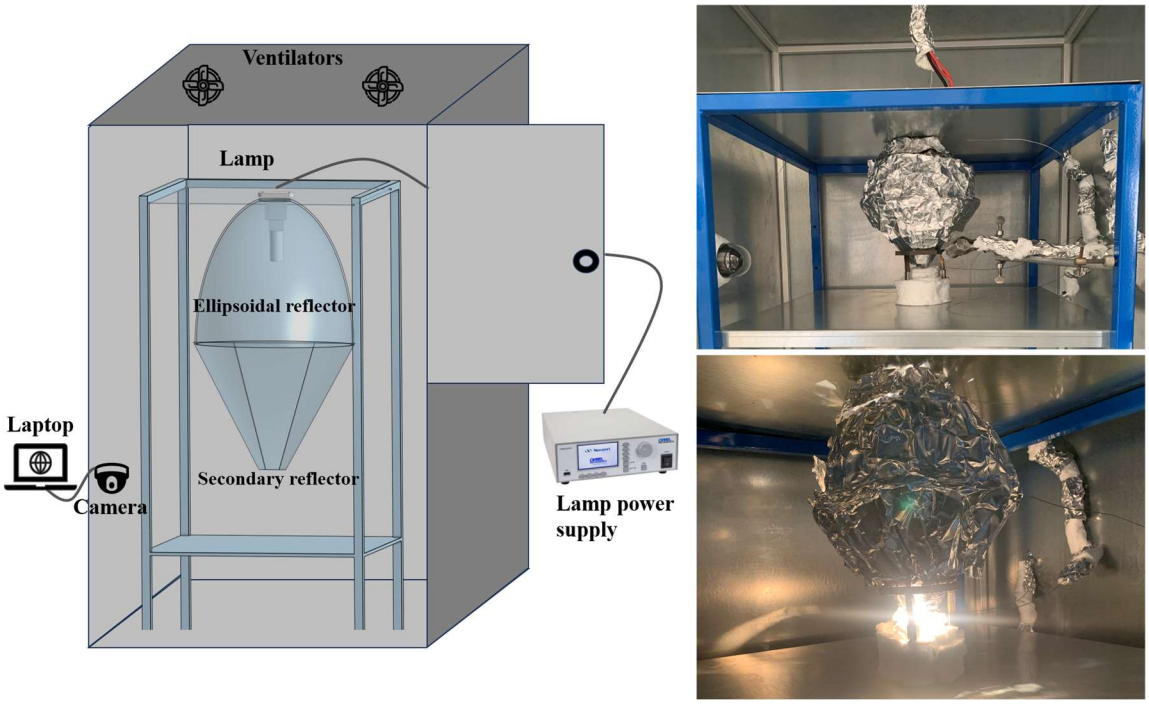

Fig. 2. 24 Schematic diagram and photograph of the solar simulator set-up

Tab. 2. 5 lists and summarizes the functional requirements of the solar simulator set-up and relative design parameters.

Tab. 2. 5 Functional requirements and design parameters of the solar simulator set-up

Functional requirement	Design parameter
Simulate solar radiation	1000 W quartz tungsten halogen lamp and lamp power supply
Small and precise output spot	Combination of ellipsoidal reflector and truncated hexagonal pyramid secondary reflector
Temperature control	Ventilators
Safety control	Stainless steel framework with lock, camera and personal protective equipment
Low cost	Commercially available and simple components

2.4.2.2 Irradiance measurement of the solar simulator

The common methods for measuring surface heat flux are generally indirect, involving techniques like measuring the spatial temperature gradients or changes in temperature over time[225]. A high heat flux sensor (HFS01, Hukseflux, the Netherlands) was initially ordered, but due to the extended delivery time, an existing light meter was utilized to measure illuminance, which was then converted into irradiance in the present work. The light meter (1308SI, Moineau Instruments, France) is capable of measuring up to 400 kLux. It was positioned at a vertical height of 8 cm from the bottom plate during the thermal performance test (Fig. 2. 25). This position also coincided with where the sample material was positioned during the experiment. Therefore, the measured illuminance corresponds to the one on the upper surface of the sample. When the ellipsoidal and secondary reflector were used, the corresponding illuminance (E_v, kLux) exceeds the range of the light meter when the lamp power is 1000 W. It was then measured at different lamp power settings of 100, 200, 300, 400, 500, 600, 700, 800 W, respectively. The illuminance could be converted to irradiance (G, W/m^2) approximately according to the following formula[226]:

$$G = 7.9 * E_v \quad \text{Eq. 2. 18}$$

In addition, the illuminance of the lamp at 1000 W was tested at the same location using the parabolic reflector, only an ellipsoidal reflector installed, and without any reflector for comparison.

2.4.2.3 Solar energy absorption and heat transfer test

The experimental set-up is depicted in Fig. 2. 25. Within the solar simulator, the tested pellet was positioned at a vertical height of 8 cm from the bottom plate, which was also 2.5 cm vertically downward from the output aperture of the secondary reflector. Six type K thermocouples (T1, T2, T3, T4, T5, T6) were placed at different locations to measure the temperature, and connected to a temperature recorder for data output. The temperature readings were taken every 0.1 s throughout the experiment. The lamp

power was set to 1000 W. The temperature was recorded simultaneously when the lamp was turned on.

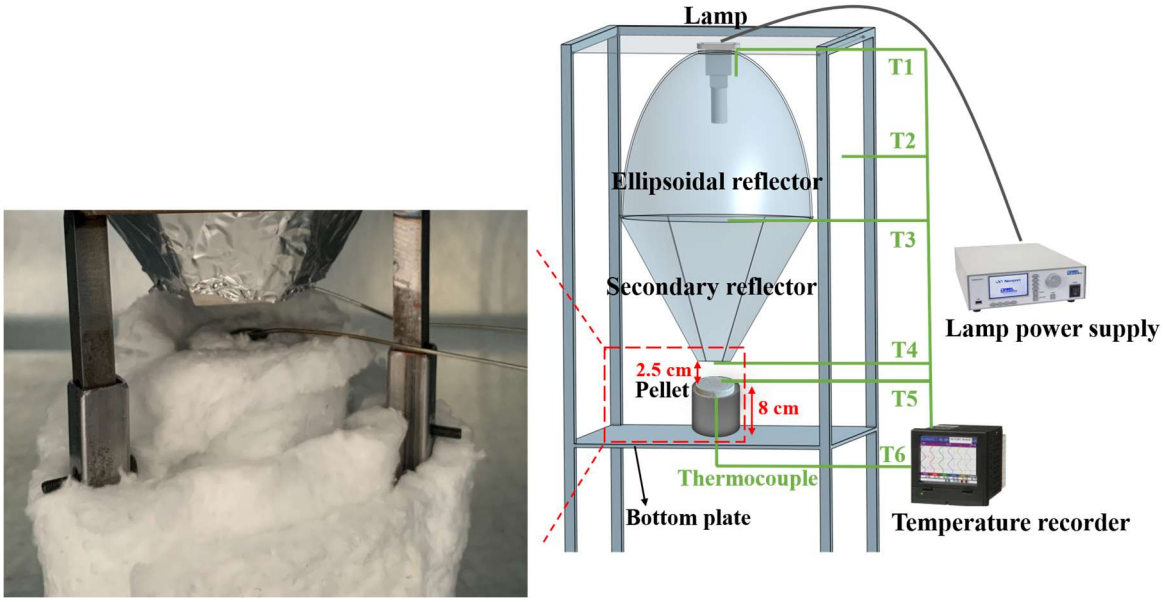

Fig. 2. 25 Schematic diagram and photograph of experimental set-up

Fig. 2. 26 gives the sectional diagram of the set-up including the lamp, reflectors, pellet, sample holder and thermocouples. Specifically, T1 to T4 measured the temperatures of air at different locations to monitor the temperature within the set-up: T1 was inside the ellipsoidal reflector, close to the lamp; T2 was at the outer half height of the ellipsoidal reflector in the framework; T3 was inside the junction of the ellipsoidal reflector and the secondary reflector; T4 was next to the output aperture. The tested pellet was put on a sample holder, and the calcium-magnesium silicate fiber was utilized for thermal insulation around and at the bottom of the pellet (Fig. 2. 26). The temperature of the center of the pellet's upper surface (T5) and lower surface (T6) was continuously measured over time during the experiment. The thermocouple for T6 was threaded through the bolts fixed on the shelf's plate and can be extended or adjusted as needed.

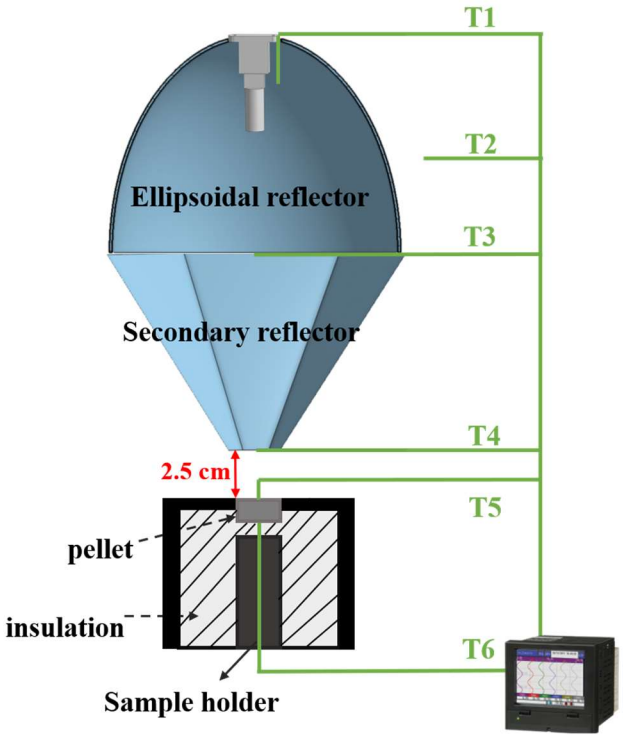

Fig. 2. 26 Sectional diagram of the experimental set-up

2.5 Conclusions

In this chapter, a novel technique was proposed for the preparation of thermal conductive substrate, and the composite solar receiver materials consisting of the absorption layer and thermal conductive substrate for solar thermal applications were manufactured. Various characterization methods were employed for analyzing the properties of prepared samples. Furthermore, the set-up of heating experiment and solar simulator, as well as the thermal performance experiments of the samples were introduced, which are crucial for assessing the efficiency and effectiveness of the composite solar receiver materials in capturing and utilizing solar energy.

Chapter 3 Experimental results and discussion of thermal conductive substrates

3.1 Introduction

In Chapter 3, experimental analysis of the prepared "thermal conductive substrate" material utilized in solar thermal applications is introduced. The primary objective of this study was outlined in Chapter 2: to develop a composite solar receiver material consisting of an absorber material layer with high emissivity which can efficiently absorb solar radiation (as detailed in Chapter 4), and a substrate material with high thermal conduction ability (Fig. 3. 1). The characterization and thermal performance experiment results of the prepared thermal conductive substrates will be presented and discussed in this chapter.

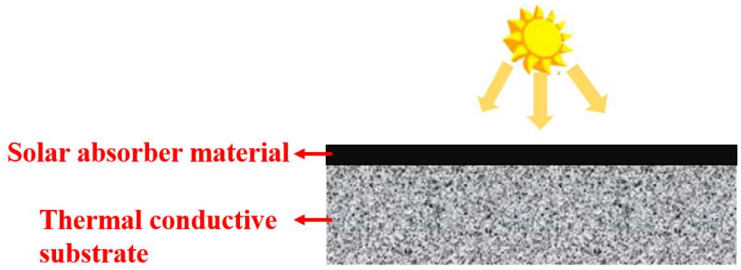

Fig. 3. 1 Schematic diagram of the composite solar receiver material

The AlN pellets with enhanced thermal conductivity and densification were produced by spark plasma sintering (SPS), using CaO as the sintering additive. A novel approach employing a high-shear mixer known as Picomix was applied for preparing AlN-CaO mixed powder. The influence of CaO powder properties such as particle size, dispersion, flowability on the mixed powders, and on the porosity and thermal conductivity of AlN pellets, were investigated. Additionally, the influence of mixing conditions, including additive content and rotational speed of Picomix, were studied. Various mixing techniques were compared. In addition to AlN substrates, the α-SiC

powder and CaO-Al_2O_3 additive powder were dry-mixed by ball milling and then sintered to obtain α-SiC pellet with high thermal conductivity. The Cu particles were dry-coated with β-SiC for oxidation protection by the Picomix and sintered, acquiring Cu pellet with reduced oxidation. For comparison, the stainless steel and graphite powder were sintered. Physical, chemical, thermal and other properties were characterized for both the powders and pellets. The heat transfer experiments were conducted on the prepared pellets to study their thermal performance.

3.2 Characterization of AlN-based samples

To begin, the analysis of AlN-based pellets will be elaborated. AlN powder was dry-mixed with CaO additive powder in the Picomix and subsequently sintered at 1650 ℃ and 5.1 kN (detailed in Section 2.2.2.1, Chapter 2). Different CaO addition, size and rotational speed of mixer were applied. In this section, the focus lies on the characterization of AlN-based powder and pellet samples. The characterization process includes the examination of raw powder (AlN and CaO) and the mixed powder, followed by the investigation of sintered pellets. Each analysis contributes crucial insights into the material's physical, chemical, morphological and thermal properties, in order to prepare for the use in solar thermal applications.

3.2.1 Powder properties

3.2.1.1 Physical and bulk property analysis

The real density (ρ) of the AlN, CaO and mixed powders are listed in Tab. 3. 1. It is evident that the density of the mixed powders is systematically greater than that of the AlN particles. This increase in density can be attributed to the presence of CaO particles in the mixture, which have a slightly higher density than AlN.

The size distributions of the raw and mixed AlN-based powders were measured with a laser diffraction particle size analyzer and are plotted in Fig. 3. 2. The corresponding mean diameter (d_p) and uniformity coefficient (C_u) are listed Tab. 3. 1.

The original AlN powder was observed to have an extremely broad size (diameter) distribution (C_u = 106.7), with two primary intervals located at 0.05 μm and 8.7 μm. All of the CaO powders are characterized by size distributions that are narrower than that of AlN (C_u of $CaO^{2.6}$ = 2.1, C_u of $CaO^{0.8}$ = 3.2 and C_u of $CaO^{0.04}$ = 4.5). However, the laser diffraction particle size measurements correspond primarily to the mean diameter of the agglomerates (d_p of $CaO^{2.6}$ = 30.6 μm, d_p of $CaO^{0.8}$ = 19.7 μm and d_p of $CaO^{0.04}$ = 4.1 μm). In the present study, it was imperative to measure the primary particle sizes in order to accurately analyze the dispersion of the additives within the AlN matrix. Although the mixed-powder size distributions are relatively similar to that of AlN, they are not characterized by a peak between 300 μm and 1000 μm, and their uniformity coefficient decreases compared to that of AlN. This suggests that the larger agglomerates were successfully broken up by the shearing forces (Picomix-mixing) and that no further aggregation of the mixed powders occurred during the dry mixing process. This promotes AlN particle rearrangements and complete contact with the liquid phase during the sintering process.

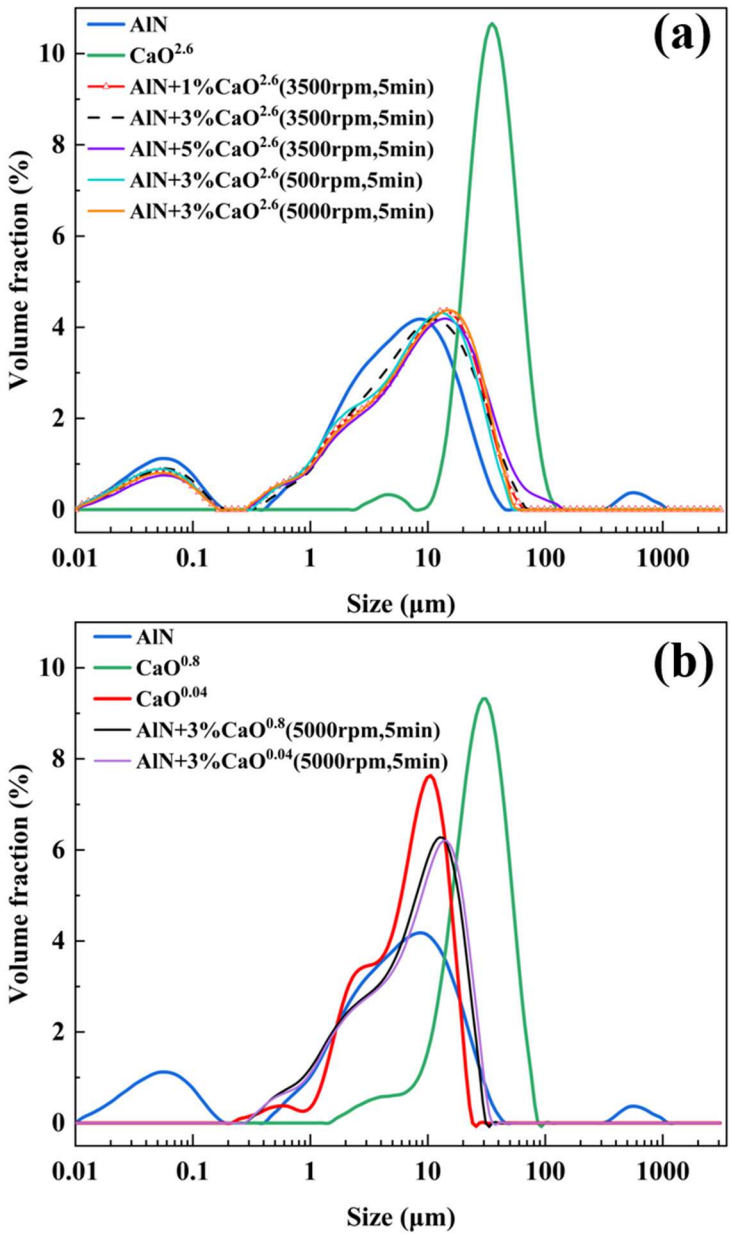

Fig. 3. 2 Size distributions of the AlN-based powders before and after mixing

All of the powders were characterized by low mean diameters, i.e. at micron-, submicron- and nano-scales. Due to the influence of van der Waals forces, the particles form agglomerates of completely random size and shape. The powders exhibit a cohesive and complex behavior that is more pronounced in the case of particles with smaller size. As a result, the flow of these powders was unstable and irregular. In order to assess the behavior of the powders and their flowability, the Hausner Ratio test (HR) was applied to the powder samples. The results are listed in Tab. 3. 1, which clearly

shows that AlN and CaO are both cohesive powders. When CaO and AlN powders are mixed together, the flowability of the resulting mixtures remains substantially similar to that of AlN alone, with a small improvement observed in the case of AlN+3%$CaO^{0.04}$(5000rpm,5min). Considering the typical behavior of nano-scale powders, this result represents a major improvement, with the enhanced flowability being advantageous in terms of a reduction in powder packing porosity, which also contributes to the densification of the pellets during sintering as reported by Saifullah et al.[227].

Tab. 3. 1 Physical properties of AlN, $CaO^{2.6}$, $CaO^{0.8}$, $CaO^{0.04}$ and mixed powders

Samples	**$\rho^{(a)}$ (g/cm^3)**	**$d_p^{(b)}$ (μm)**	**$C_u^{(c)}$**	**HR$^{(d)}$**
AlN	3.23	2.7	106.7	1.54 ± 0.03
$CaO^{2.6}$	3.50	30.6	2.1	2.50 ± 0.01
$CaO^{0.8}$	3.50	19.7	3.2	2.67 ± 0.01
$CaO^{0.04}$	3.44	4.1	4.5	2.86 ± 0.02
AlN+1%$CaO^{2.6}$(3500rpm,5min)	3.33	0.34	95.3	1.54 ± 0.01
AlN+3%$CaO^{2.6}$(3500rpm,5min)	3.35	0.35	88.7	1.58 ± 0.03
AlN+5%$CaO^{2.6}$(3500rpm,5min)	3.46	0.41	26.4	1.58 ± 0.03
AlN+3%$CaO^{2.6}$(500rpm,5min)	3.35	0.32	107.4	1.58 ± 0.01
AlN+3%$CaO^{2.6}$(5000rpm,5min)	3.45	0.35	87.6	1.54 ± 0.01
AlN+3%$CaO^{0.8}$(5000rpm,5min)	3.40	0.44	6.9	1.56 ± 0.01
AlN+3%$CaO^{0.04}$(5000rpm,5min)	3.38	0.42	7.1	1.47 ± 0.01

(a): ρ, particle real density (The standard deviation from the three measurements was less than 0.01).
(b): d_p, particle mean diameter calculated according to $d_{3,2}$ (Eq. 2. 4, Chapter 2) obtained from laser diffraction particle size analyzer.
(c): C_u, uniformity coefficient (Eq. 2. 5, Chapter 2). $C_u > 2$ indicates a broad particle size distribution.
(d): HR, Hausner Ratio (Eq. 2. 10, Chapter 2). HR < 1.2 corresponds to free flow (non-cohesive powders), HR > 1.4 corresponds to non-free flow (cohesive powders), and 1.2 < HR < 1.4 indicates that the powder's flowability lies at an intermediate level.

3.2.1.2 Morphology analysis

As stated in Section 2.2.2.1.1 (Chapter 2), the superscripts added to the powder annotations ($CaO^{2.6}$, $CaO^{0.8}$, $CaO^{0.04}$) correspond to their respective mean diameters (d_s), which were determined as described in the following paragraph. The SEM images of AlN, $CaO^{2.6}$ (micron-particles), $CaO^{0.8}$ (submicron-particles) and the TEM image of $CaO^{0.04}$ (nano-particles) are shown in Fig. 3. 3. The mean diameters of these three types of CaO are substantially smaller than those detected with a laser diffraction particle size analyzer (d_p), because it was impossible to completely break up the agglomerates during the laser diffraction measurement. As a result, the images of AlN and CaO powders were processed using the "Nano Measurer 1.2" image analysis software. The sizes of 300 representative particles for each sample were acquired by manually determining each particle's maximum linear dimension (i.e. red line in Fig. 3. 3 (a)) using the aforementioned software. These dimensions and the corresponding particle counts were then processed to create dimension classes, allowing the corresponding particle size (μm or nm) histograms to be plotted (Fig. 3. 3). The Sauter diameter (referred to as d_s) of the particles was computed from these distributions, according to Eq. 2. 4 (Chapter 2). The d_s of AlN, $CaO^{2.6}$, $CaO^{0.8}$, $CaO^{0.04}$ were calculated as 1.32, 2.6, 0.8, 0.04 μm respectively.

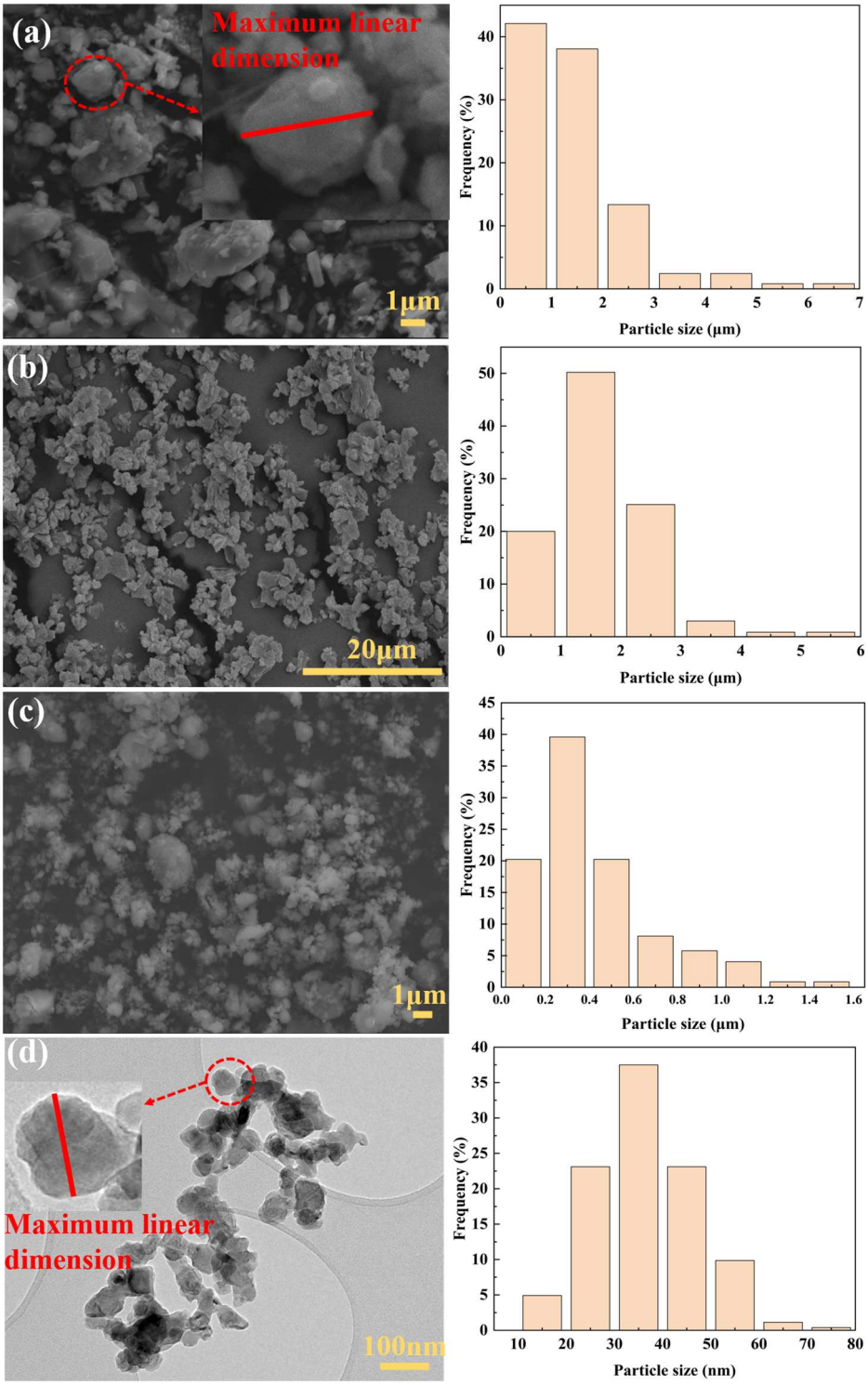

Fig. 3. 3 SEM images and size distribution histograms of (a) AlN, (b) $CaO^{2.6}$, (c) $CaO^{0.8}$; (d) TEM image and size distribution histogram of $CaO^{0.04}$

Before shaping the powders into pellets by spark plasma sintering, the AlN-CaO additive ($CaO^{2.6}$, $CaO^{0.8}$, $CaO^{0.04}$) mixtures were analyzed. It was important to ensure

that the CaO additives were well dispersed in the AlN matrix, in order to facilitate uniform distribution of the liquid phase among the particles, resulting in a decrease in porosity and an increase in thermal conductivity. Fig. 3. 4 shows the SEM images of the mixed powders AlN+3%$CaO^{2.6}$(500rpm,5min), AlN+3%$CaO^{2.6}$(3500rpm,5min), AlN+3%$CaO^{2.6}$(5000rpm,5min) and EDS mappings of elemental Ca, corresponding to each sample. At 500 rpm, large agglomerates of $CaO^{2.6}$ (micron-scale) could be observed, indicating that this rotational speed is too low to achieve suitable dispersion of the particles. When the rotational speed is increased from 500 rpm to 5000 rpm, large agglomerates are no longer observed and de-agglomeration of the $CaO^{2.6}$ particles is increasingly uniform, which is beneficial to the distribution of the liquid phase and the movement and reorganization of particles in this phase during sintering.

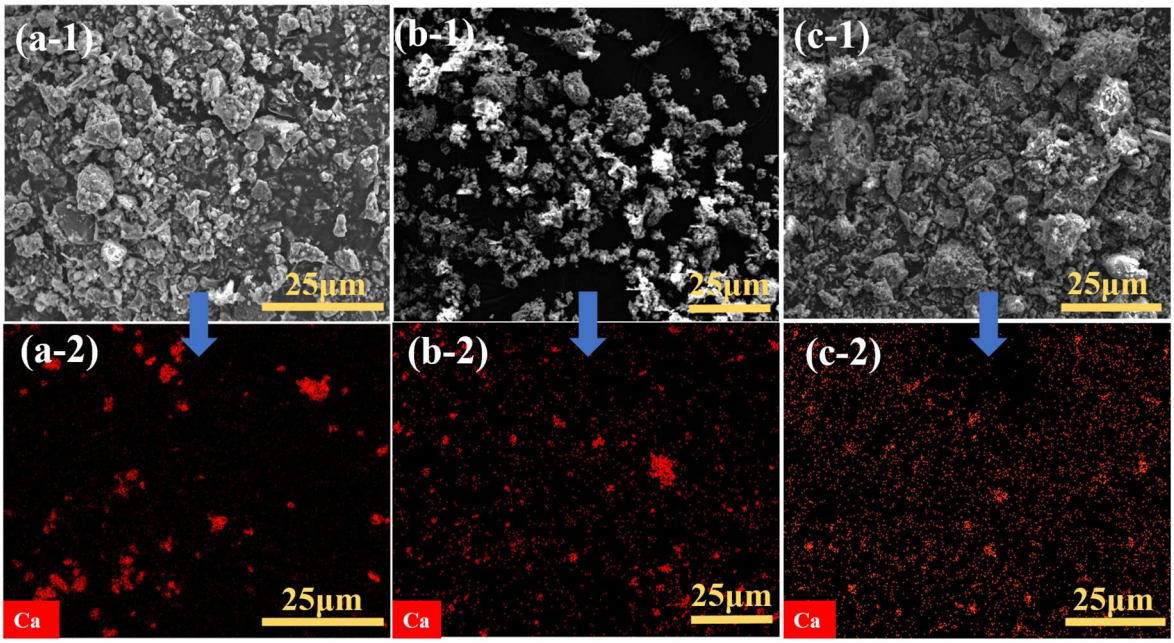

Fig. 3. 4 (a-1) SEM image of AlN+3%$CaO^{2.6}$(500rpm,5min) and (a-2) corresponding EDS mapping of Ca; (b-1) SEM image of AlN+3%$CaO^{2.6}$(3500rpm,5min) and (b-2) corresponding EDS mapping of Ca; (c-1) SEM image of AlN+3%$CaO^{2.6}$(5000rpm,5min) and (c-2) corresponding EDS mapping of Ca

The SEM images of AlN+3%$CaO^{0.8}$(5000rpm,5min) and AlN+3%$CaO^{0.04}$(5000-rpm,5min), and the corresponding EDS mappings of elemental Al and Ca are shown in

Fig. 3. 5. The submicron $CaO^{0.8}$ and nano $CaO^{0.04}$ powders are found to adhere to the surface of AlN bulk, forming discontinuous coatings. When AlN and CaO with smaller sizes were mixed at high rotational speeds in the Picomix, the powder's behavior changed from mixing to coating. This is due to the adhesion force (usually referred to as van der Waals force) being stronger than the weight of the guest particles, when submicron- or nano-scale guest (CaO) particles are mechanically coated onto larger, micron-sized host (AlN) particles (see Fig. 2. 2, Chapter 2). Lu et al.[154] also reported a similar phenomenon, with small Co_3O_4 guest particles covering the surface of large Al_2O_3 host particles in the Picomix, thereby forming a continuous coating. This behavior could explain the increased flowability of AlN+3%$CaO^{0.04}$(5000rpm,5min), since the irregular particle surfaces obtained by the coating process reduces the contact surface area and the cohesion between particles[227]. As a consequence, this property could be used to wrap the AlN in a continuous liquid phase during sintering.

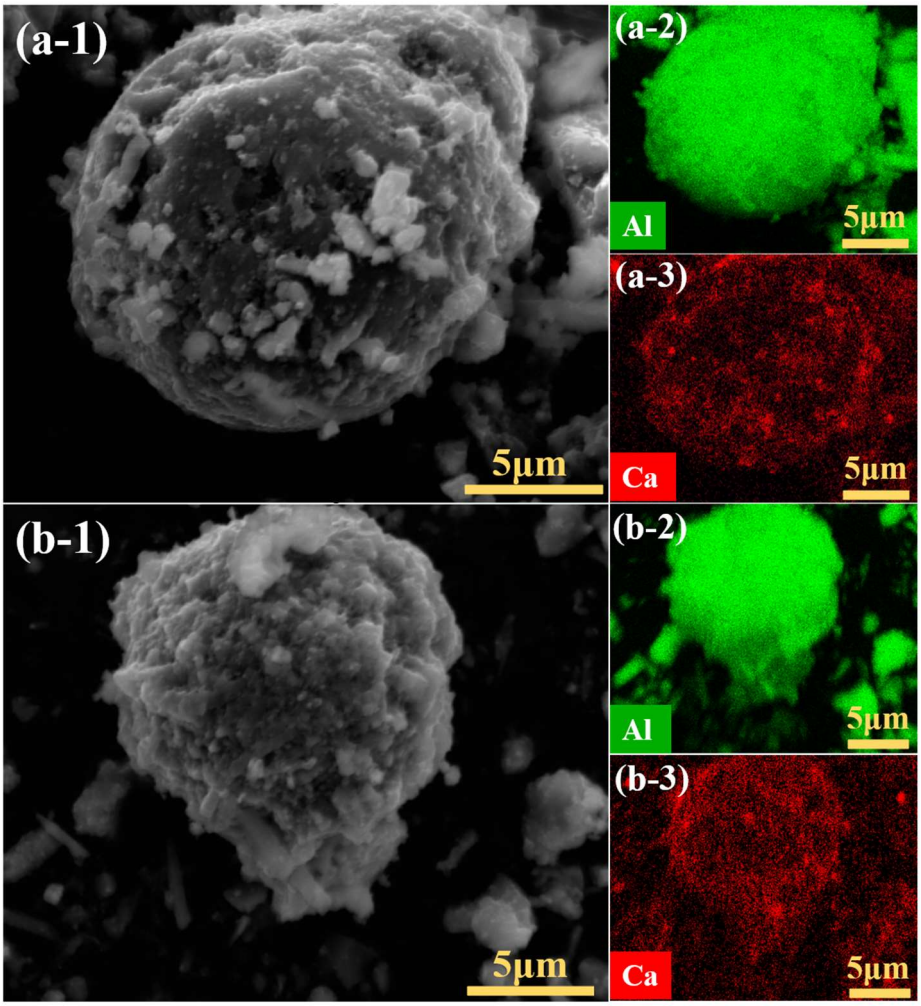

Fig. 3. 5 (a-1) SEM image of AlN+3%$CaO^{0.8}$(5000rpm,5min) and corresponding EDS mappings of (a-2) Al, (a-3) Ca; (b-1) SEM image of AlN+3%$CaO^{0.04}$(5000rpm,5min) and corresponding EDS mappings of (b-2) Al, (b-3) Ca

3.2.1.3 Chemical structure analysis

The phase and size of crystallites in the original (AlN, $CaO^{2.6}$, $CaO^{0.8}$ and $CaO^{0.04}$) and mixed powders were verified using XRD. As shown in Fig. 3. 6 (a), the AlN diffraction peaks correspond to the aluminum nitride phase (JCPDS PDF No. 76-0702). The diffraction peaks of 3 different kinds of original CaO can be attributed to the calcium oxide phase (JCPDS PDF No. 78-0649) and calcium hydroxide phase (JCPDS PDF No. 72-0156), since CaO readily absorbs moisture from the air and reacts with it to form $Ca(OH)_2$. The initially sharp diffraction peaks are significantly broadened and

their intensities are decreased in the $CaO^{0.8}$ XRD pattern, due to refinement of the crystallite size and the ball milling-induced increase in atomic level strain. Diffraction in the (200) lattice plane (i.e. 2θ at 37.4°) is barely present, which could be due to some of the CaO reacting with moisture in the air and forming $Ca(OH)_2$ during the long ball milling procedure. All the diffraction peaks of mixed powders are indexed to the aluminum nitride and calcium oxide phases, implying that no phase transitions of AlN and CaO occurred during high-shear treatment in the Picomix device (Fig. 3. 6 (b)). The diffraction peak corresponding to the (200) lattice plane is also absent from the spectra of AlN+1%$CaO^{2.6}$(3500rpm,5min) and AlN+3%$CaO^{0.8}$(5000rpm,5min). The absence of the former can be attributed to the very small quantity of $CaO^{2.6}$ present in the mixture, whereas the absence of the latter is due to the decreased peak intensity of $CaO^{0.8}$ produced by ball milling.

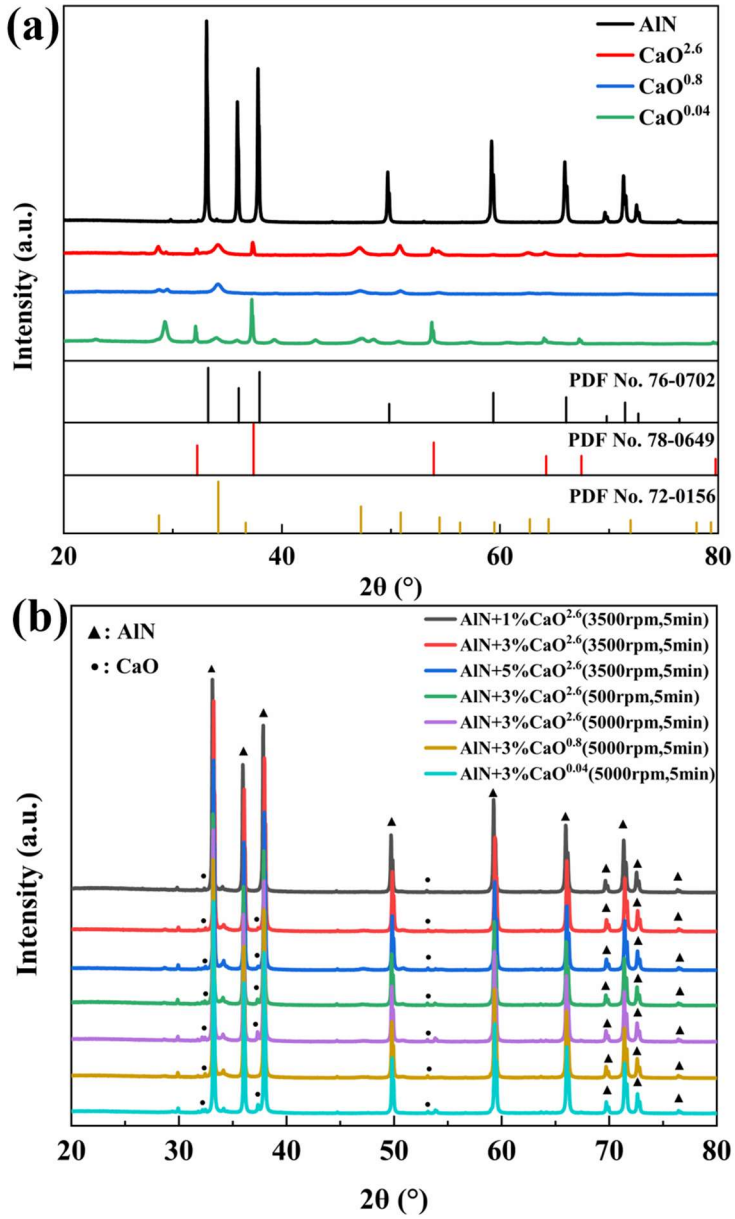

Fig. 3. 6 (a) XRD patterns of AlN, $CaO^{2.6}$, $CaO^{0.8}$, $CaO^{0.04}$ powders and relevant JCPDS PDFs; (b) XRD patterns of AlN-based mixed powders

The crystallite size of the AlN phase was determined from the "Scherrer Equation" (Eq. 2. 13, Chapter 2) on the basis of diffraction in its (002) lattice plane (i.e., 2θ at 35.9°). CaO crystallite size was calculated on the basis of diffraction in its (220) lattice plane (i.e., 2θ at 53.9°). The resulting data is listed in Tab. 3. 2. As can be seen, the crystallite size of $CaO^{0.8}$ decreased significantly after 20 hours of ball milling. Following treatment in the Picomix device, the crystallite sizes of AlN and CaO phases

were both slightly reduced, in particular in the case of the highest rotational speed (5000 rpm).

Tab. 3. 2 Crystallite size of the AlN and CaO phases in raw and mixed powders

Sample	Crystallite size of AlN (nm)	Crystallite size of CaO (nm)
AlN	58.0	-
$CaO^{2.6}$	-	49.5
$CaO^{0.8}$	-	16.9
$CaO^{0.04}$	-	13.7
AlN+1%$CaO^{2.6}$(3500rpm,5min)	56.9	47.4
AlN+3%$CaO^{2.6}$(3500rpm,5min)	55.9	47.4
AlN+5%$CaO^{2.6}$(3500rpm,5min)	55.5	47.1
AlN+3%$CaO^{2.6}$(500rpm,5min)	57.4	48.6
AlN+3%$CaO^{2.6}$(5000rpm,5min)	55.6	45.2
AlN+3%$CaO^{0.8}$(5000rpm,5min)	55.1	13.3
AlN+3%$CaO^{0.04}$(5000rpm,5min)	54.0	13.4

3.2.2 Characterization of pellet properties

Following the application of spark plasma sintering to the AlN-based powder mixture, the resulting pellets have a thickness ranging from 1.5 mm to 2.5 mm, and a diameter of 10 mm (Fig. 3. 7).

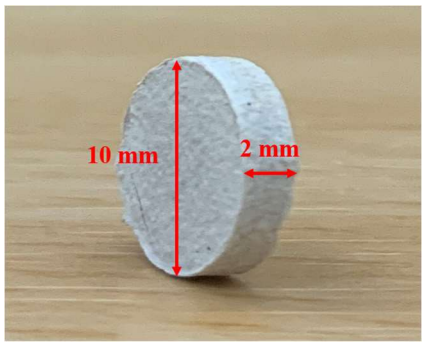

Fig. 3. 7 Photograph example of sintered AlN(pellet)

3.2.2.1 Chemical structure analysis

Fig. 3. 8 illustrates the XRD patterns of the sintered AlN-based pellets. AlN clearly remains the dominant phase in the pellets after sintering. When compared to the mixed powder samples, none of the corresponding pellet spectra indicate the presence of a CaO phase. With the exception of AlN+1%$CaO^{2.6}$(3500rpm,5min,pellet), new phases were detected in the spectra of pellets containing the CaO additive. The diffraction peaks at 2θ are located at 25.5°, 29.4° and 32.3°, corresponding to the (331), (430) and (521) lattice planes of tri-calcium aluminate ($Ca_3Al_2O_6$, $3CaO{\cdot}Al_2O_3$) (JCPDS PDF No.38-1429). In addition, calcium meta-aluminate ($CaAl_2O_4$, $CaO{\cdot}Al_2O_3$) (JCPDS PDF No.23-1036) was also identified from the diffraction peaks observed at 2θ = 30.1° and 35.5°, corresponding to its (123) and (006) lattice planes. In studies reported by Molisani et al.[110] and Kang et al.[228], related secondary phases were also detected in sintered AlN-CaO pellets. The eutectic temperatures of $Ca_3Al_2O_6$ and $CaAl_2O_4$, also known as secondary phases, were reported to be approximately 1400 °C, which is lower than the sintering temperature[115]. This demonstrates that during the sintering process, CaO reacted with the oxide layer (Al_2O_3) on the AlN surface to form a liquid phase, and then precipitated in the form of secondary phases, which significantly contributed to the densification (low porosity) of the pellets, to a reduction in the oxygen content, and to an overall improvement in the thermal conductivity of the sintered AlN. The reason for which the secondary phase was not detected in the AlN+1%$CaO^{2.6}$(3500rpm,5min,pellet) could be the addition of only a very small quantity (1 wt%) of CaO, as shown by the XRD pattern of AlN+1%$CaO^{2.6}$(3500-rpm,5min).

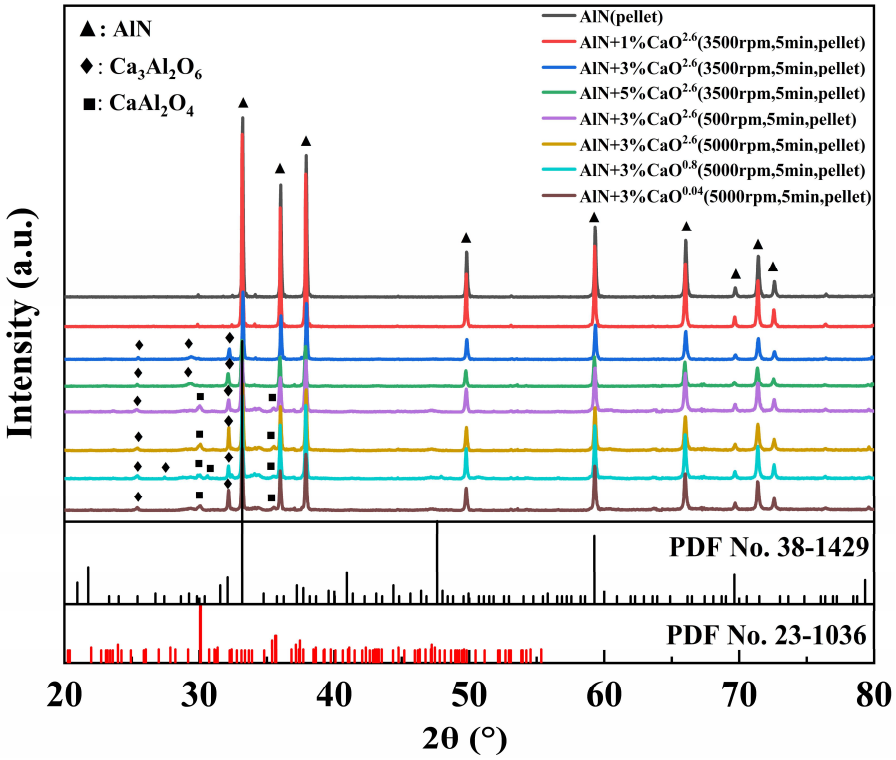

Fig. 3. 8 XRD patterns of the sintered AlN-based pellets and relevant JCPDS PDFs

3.2.2.2 Porosity and thermal conductivity of AlN-based pellets

The porosity (φ) and thermal conductivity (k) of AlN-based sintered pellets are known to be correlated with their physical properties (density, mean diameter, shape, size distribution), as well as the flowability, morphology and chemical composition of their constituent particles, i.e. the particles that the pellets are made from. The influence of these properties and mixing conditions were assessed in the analysis of the pellets' porosity and thermal conductivity. Fig. 3. 9–Fig. 3. 11 plot the variation of porosity and computed thermal conductivity as a function of three variables: CaO/AlN mass ratio, rotational speed and size (d_s) of the CaO additive particles. Error bars were incorporated based on the standard deviation derived from three measurements.

The φ and k of sintered AlN with different values of $CaO^{2.6}$ sintering additive content are shown in Fig. 3. 9 for a rotational speed of 3500 rpm. The value of φ for the sintered pellets decreases with increasing $CaO^{2.6}$ content, which is due to the addition of CaO which leads to the formation of a liquid phase during sintering. The

densification of the pellets is improved when their liquid phase content is increased. Accordingly, as the CaO content progressively increases, the pellet's thermal conductivity first increases due to the reduction in pellet porosity and Al_2O_3 impurities, reaching a peak value of 112.9 W/m·K for 3 wt% of $CaO^{2.6}$ additive before decreasing to 73.1 W/m·K. Molisani et al.[110] obtained comparable results with the optimal addition of 2 wt% CaO. The increased content of $CaO^{2.6}$ and the secondary phases can be expected to reduce the heat transfer efficiency. Qin et al.[229] compared the thermal conductivity of AlN sintered bodies with different secondary phase amounts and determined that excessive secondary phases were not conducive to thermal diffusion.

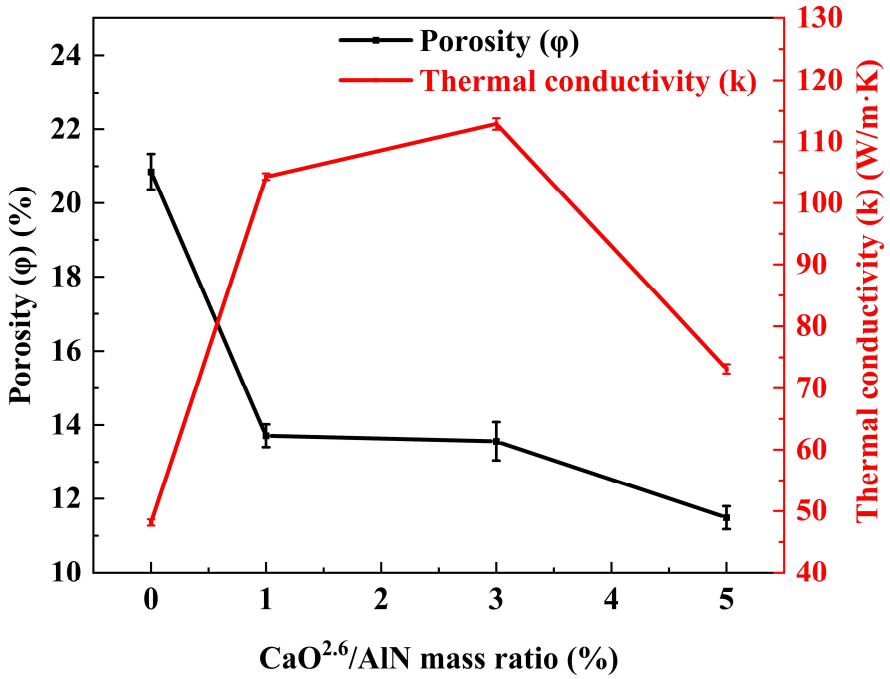

Fig. 3. 9 Porosity and thermal conductivity of sintered AlN-based pellets with different $CaO^{2.6}$/AlN mass ratios when mixed at 3500 rpm

Fig. 3. 10 shows the porosity and thermal conductivity of sintered AlN with 3 wt% $CaO^{2.6}$ as the sintering additive for different rotational speeds of the mixer. The highest value of φ for the sintered pellet occurs at 500 rpm. It also shows that k increases with increasing rotational speed. The increase of φ at 5000 rpm might be attributed to disaggregation of the agglomerates and a more uniform particle size, leading to fewer instances of voids between large particles being filled by smaller particles. Higher

rotational speeds are also beneficial since they ensure a more uniform additive distribution and better particle mixing, as revealed by the EDS mappings in Fig. 3. 4 and the values of C_u in Tab. 3. 1. The homogeneous liquid phase distribution is formed during sintering and as shown by Luo et al.[230], it could create a favorable environment for mass transfer and crystal growth, thereby increasing the thermal conductivity of AlN.

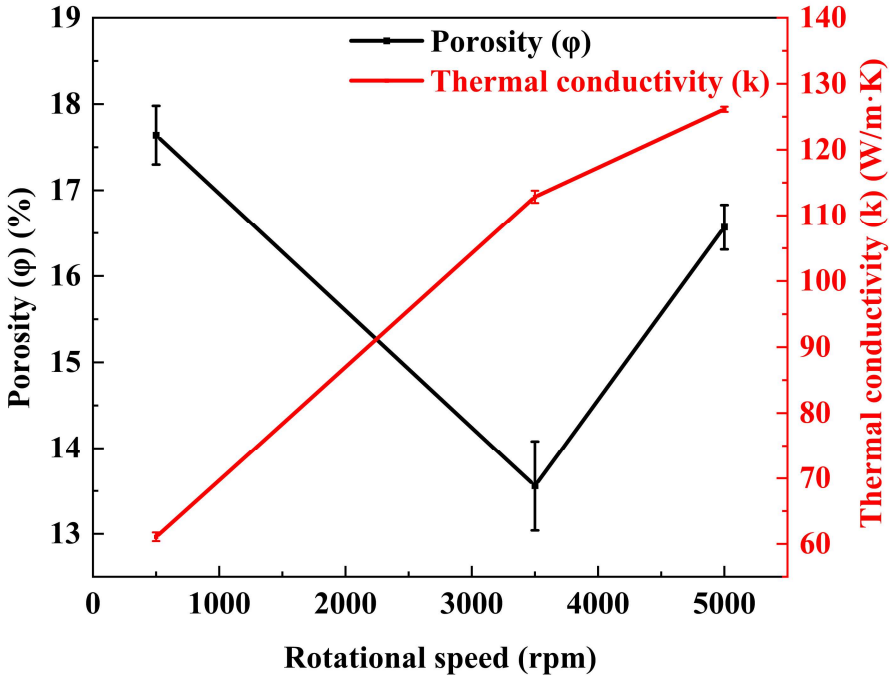

Fig. 3. 10 Porosity and thermal conductivity of sintered AlN-based pellets with the 3% $CaO^{2.6}$ additive at different rotational speeds

Fig. 3. 11 plots the porosity and thermal conductivity of sintered AlN with 3 wt% CaO of different particle sizes as sintering additive, at a rotational speed of 5000 rpm. When the size of the CaO particles decreases from the micron- to the nano-scale, the slight increase in φ might be due to the fact that some of the $CaO^{0.8}$ and $CaO^{0.04}$ particles still form agglomerates, and that a narrow particle size distribution is not conducive to a reduction in pellet porosity as discussed above. However, applying nano-scale powder as additive with mixing in the Picomix remains a promising option given its considerable degree of particle cohesion. On the other hand, when the size of the particles is nanometric ($CaO^{0.04}$), the value of k reaches a maximum (135.3 W/m·K).

One explanation for this behavior could be that after high-speed mixing in the Picomix, the nanometric CaO particles were uniformly coated onto the surface of the AlN particles (Fig. 3. 5). This allows the AlN to be constantly surrounded by the liquid phase during sintering, thereby facilitating the removal of oxygen impurities and enhancing its thermal conductivity[148]. Nie et al.[231] implemented a chemical precipitation process to coat AlN powder with Y_2O_3 additive and observed a 9.43% improvement, relative to the ball milling process, in the thermal performance of the resulting sintered AlN ceramic.

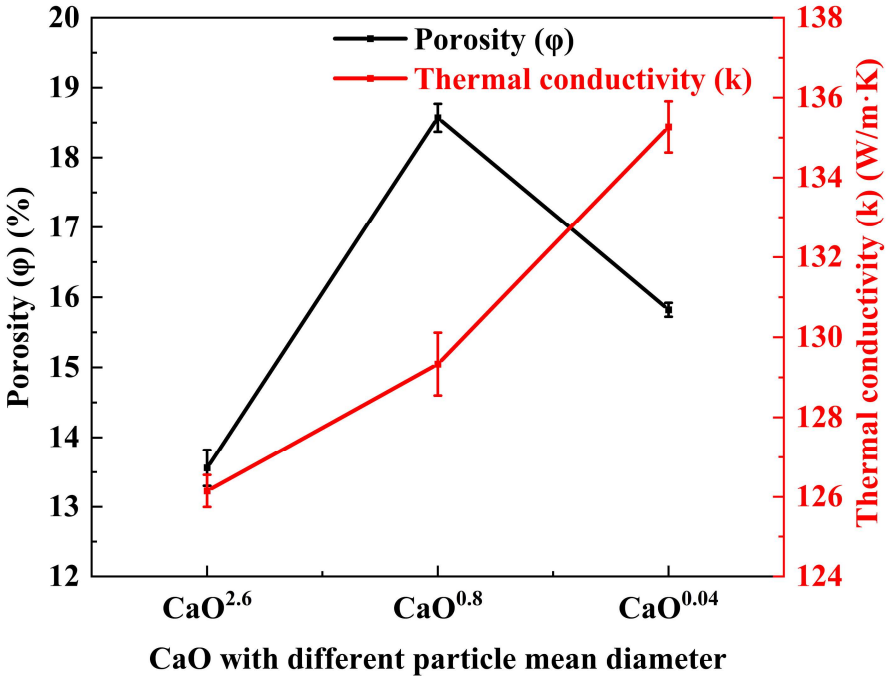

Fig. 3. 11 Porosity and thermal conductivity of sintered AlN-based pellets with different sizes of CaO additive at 5000 rpm

3.2.2.3 Textural property analysis

Fig. 3. 12 shows the N_2 adsorption-desorption isotherms and Barrett–Joyner–Halenda (BJH) pore width distribution of the AlN-based sintered pellets. Their Brunauer-Emmet-Teller specific surface area (S_{BET}), BJH desorption average pore width (d_{pore}) and pore volume (V_{pore}) are listed in Tab. 3. 3. AlN(pellet) exhibits typical type-I isotherm of microporous solids with relatively small external surface areas[232].

The S_{BET} and V_{pore} of AlN(pellet) are very small when compared to other pellets, while its porosity is 20.8% which is the highest displayed in Section 3.2.2.2, Chapter 3. It suggests that the majority of the pores are closed ones located inside AlN(pellet). The other pellets with CaO as a sintering additive exhibit isotherms that are similar to type-IV with a type-H3 hysteresis loop at relative pressure (P/P^0) ranging from 0.4 to 1.0. This indicates the presence of a mesoporous structure and a single type of possible nonuniform slit-shaped pores in these pellets[232]. Their monomodal pore width distributions in Fig. 3. 12 (b) and d_{pore} values further support this observation, as all the d_{pore} values are ranged between 4.5 and 6 nm.

Among the AlN-CaO pellets, it can be observed that the adsorbed quantity at the same relative pressure, as well as the values of S_{BET} and V_{pore} of AlN+5%$CaO^{0.26}$(3500rpm,5min,pellet), are apparently lower than other pellets. This is consistent with it having the lowest porosity as shown in Fig. 3. 10. When comparing the pellets with varying rotational speeds, it is evident that AlN+3%$CaO^{2.6}$(500-rpm,5min,pellet) exhibits the largest S_{BET} and V_{pore}. This finding aligns with the fact that it has a lower porosity compared to AlN+3%$CaO^{2.6}$(3500rpm,5min,pellet) and AlN+3%$CaO^{2.6}$(5000rpm,5min,pellet). When the particle size of CaO is reduced, S_{BET} and V_{pore} of the sintered pellets increase which is inconsistent with the trend of their porosity, indicating that the addition of larger-sized CaO might be more likely to form closed pores.

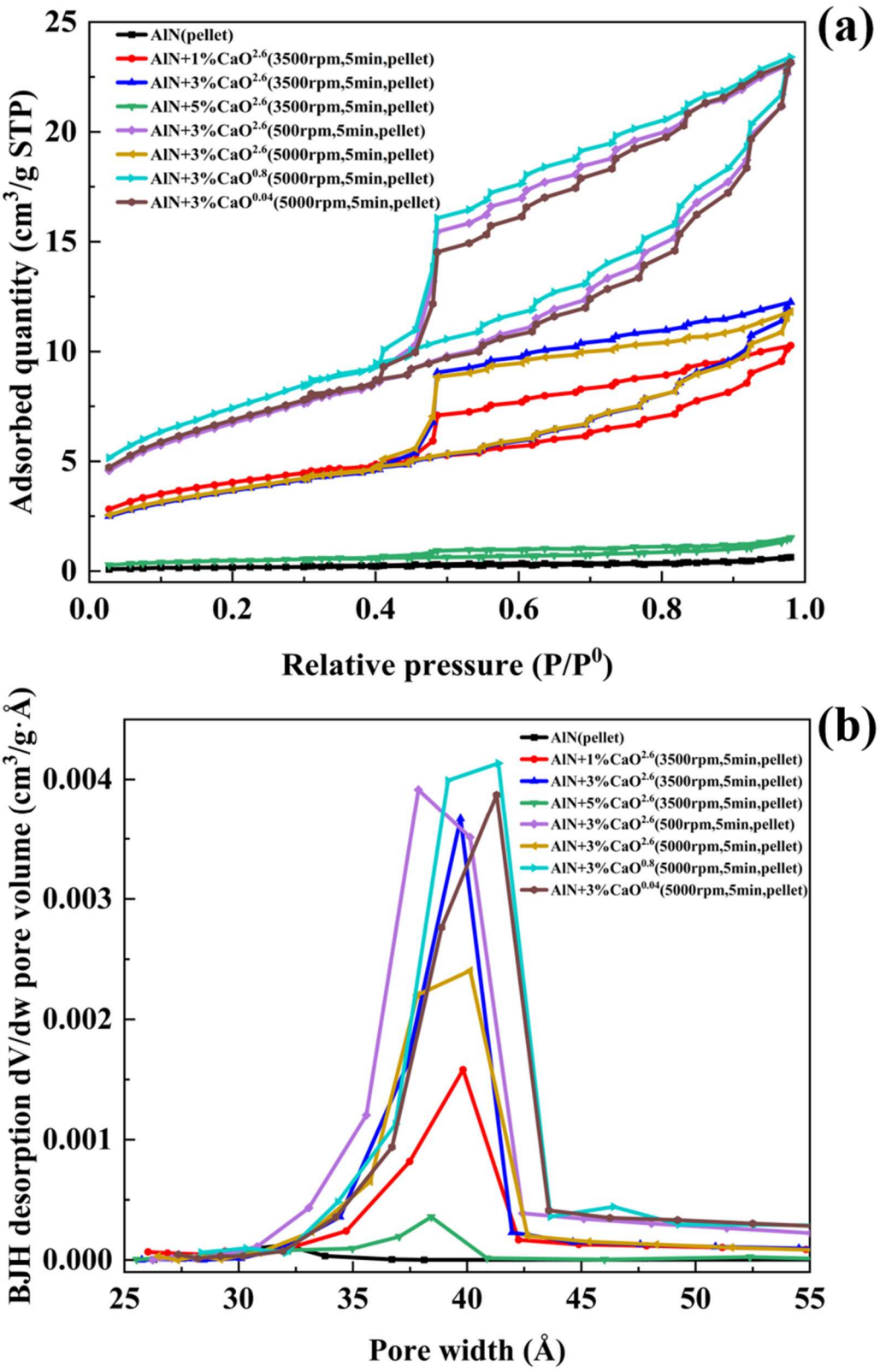

Fig. 3. 12 (a) N_2 adsorption-desorption of AlN-based sintered pellets; (b) BJH pore width distribution of AlN-based sintered pellets

Tab. 3. 3 Textural properties of AlN-based sintered pellets

Sample	S_{BET}[(a)] (m^2/g)	d_{pore}[(b)] (nm)	V_{pore}[(c)] (mm^3/g)
AlN(pellet)	0.6	7.4	0.8
AlN+1%$CaO^{2.6}$(3500rpm,5min,pellet)	14.0	5.1	14.8
AlN+3%$CaO^{2.6}$(3500rpm,5min,pellet)	13.0	4.7	17.7
AlN+5%$CaO^{2.6}$(3500rpm,5min,pellet)	1.7	5.5	1.9
AlN+3%$CaO^{2.6}$(500rpm,5min,pellet)	23.9	5.0	32.9
AlN+3%$CaO^{2.6}$(5000rpm,5min,pellet)	13.2	4.7	16.9
AlN+3%$CaO^{0.8}$(5000rpm,5min,pellet)	26.4	5.0	33.8
AlN+3%$CaO^{0.04}$(5000rpm,5min,pellet)	24.4	5.3	33.0

(a): S_{BET}, Brunauer-Emmet-Teller specific surface area

(b): d_{pore}, Barrett–Joyner–Halenda desorption average pore width

(c): V_{pore}, Barrett–Joyner–Halenda desorption average pore volume

3.2.2.4 Morphology analysis

SEM images of the sintered pellets are shown in Fig. 3. 13 and Fig. 3. 14. A porous microstructure accompanied by the formation of "necks" (bonding) between the AlN particles can be observed in the AlN(pellet), indicating the solid-state sintering (SSS) process (Fig. 3. 13 (a)). The high porosity (20.8%) of the AlN(pellet) is typical for pellets produced by the SSS process. A similar phenomenon was observed in the AlN+1%$CaO^{2.6}$(3500rpm,5min,pellet) (Fig. 3. 13 (b)), which could be attributed to the small addition of $CaO^{2.6}$, also shown in the XRD results (Fig. 3. 8). As the $CaO^{2.6}$ addition further increases to 3 wt% and 5 wt%, the area within the red dotted box in the image was analyzed by relevant EDS results as the secondary phase (Fig. 3. 13 (c-d)). The presence of more secondary phase was observed as the amount of $CaO^{2.6}$ increases, which may lead to a decrease in thermal conductivity as shown in Fig. 3. 9.

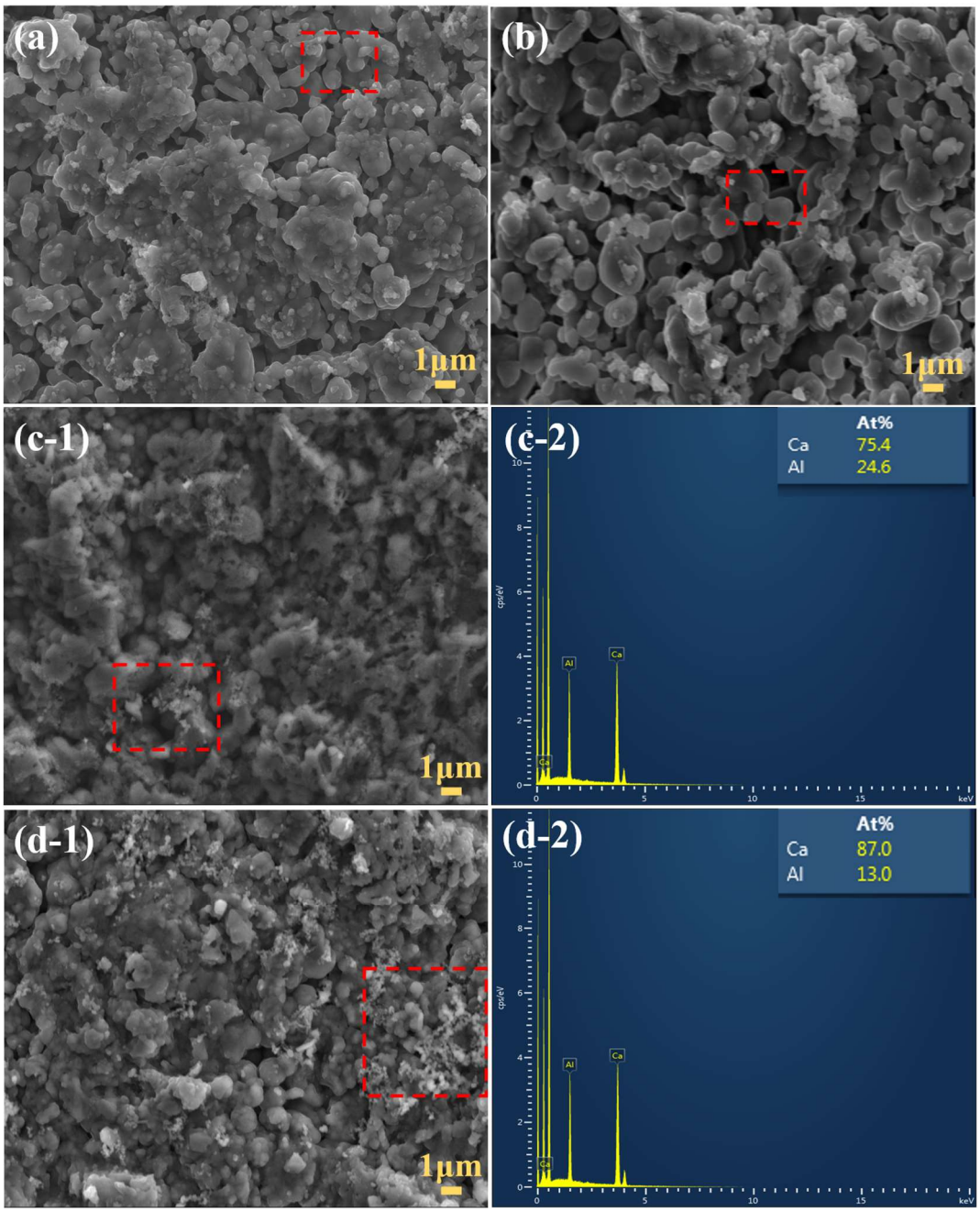

Fig. 3. 13 SEM images of (a) AlN(pellet), (b) AlN+1%$CaO^{2.6}$(3500rpm,5min,pellet); (c-1) SEM image and (c-2) EDS analysis within the red dotted box in (c-1) of AlN+3%$CaO^{2.6}$(3500rpm,5min,pellet); (d-1) SEM image and (d-2) EDS analysis within the red dotted box in (d-1) of AlN+5%$CaO^{2.6}$(3500rpm,5min,pellet)

When the SEM images of pellets made from powders obtained at different rotational speeds are compared, it can be seen that a considerable number of agglomerates still remain at 500 rpm as shown by the area within the red dotted box

(Fig. 3. 14 (a-1)), which are identified as secondary phase through EDS analysis (Fig. 3. 14 (a-2)). This observation also suggests that the distribution of additives and the liquid phase becomes more uniform at high rotational speeds. When the CaO particle size is sufficiently small, the polyhedral structures are transformed into spherical particles in the AlN+3%$CaO^{0.8}$(5000rpm,5min,pellet) and AlN+3%$CaO^{0.04}$(5000rpm,5min,pellet) (Fig. 3. 14 (c-d)), which is not the case in the mixed powders prior to sintering. Similar phenomena have also been observed by Qiao et al.[150] and Zhan et al.[134]. As $CaO^{0.8}$ and $CaO^{0.04}$ form a coating on the surface of AlN in the mixed powders (Fig. 3. 5), this indicates that throughout the sintering process, the AlN particles were completely encapsulated by the liquid phase, and that certain sharp corners were wetted and dissolved in the liquid, thereby facilitating the removal of Al_2O_3 and increasing the pellets' thermal conductivity.

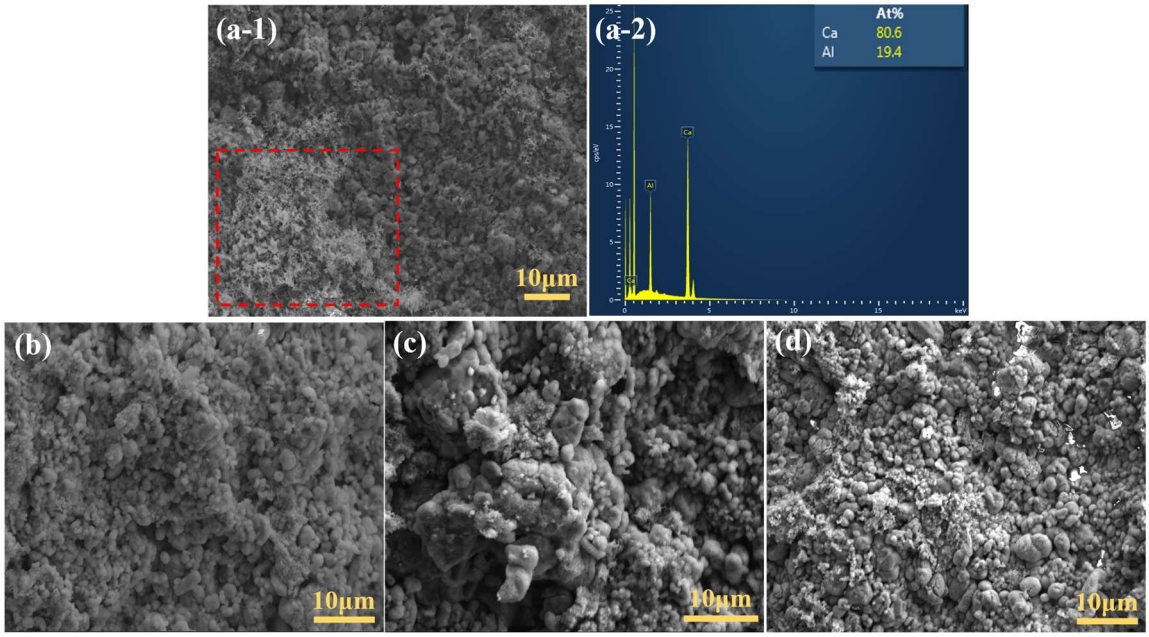

Fig. 3. 14 (a-1) SEM image of AlN+3%$CaO^{2.6}$(500rpm,5min,pellet); (a-2) EDS analysis within the dotted box in (a-1); SEM images of (b) AlN+3%$CaO^{2.6}$(5000rpm,5min,pellet), (c) AlN+3%$CaO^{0.8}$(5000rpm,5min,pellet), (d) AlN+3%$CaO^{0.04}$(5000rpm,5min,pellet)

Further observation of the secondary phase distribution in pellets with different additive particle sizes are provided by the TEM images and corresponding EDS mapping of Ca element (Fig. 3. 15). When CaO is at the micron-scale, large-scale agglomerations of secondary phases exist at AlN grain boundaries. However, when CaO is at the nano-scale, the secondary phases are considerably smaller in size and uniformly distributed as thin layers, resulting in the close contact and connection of the grains.

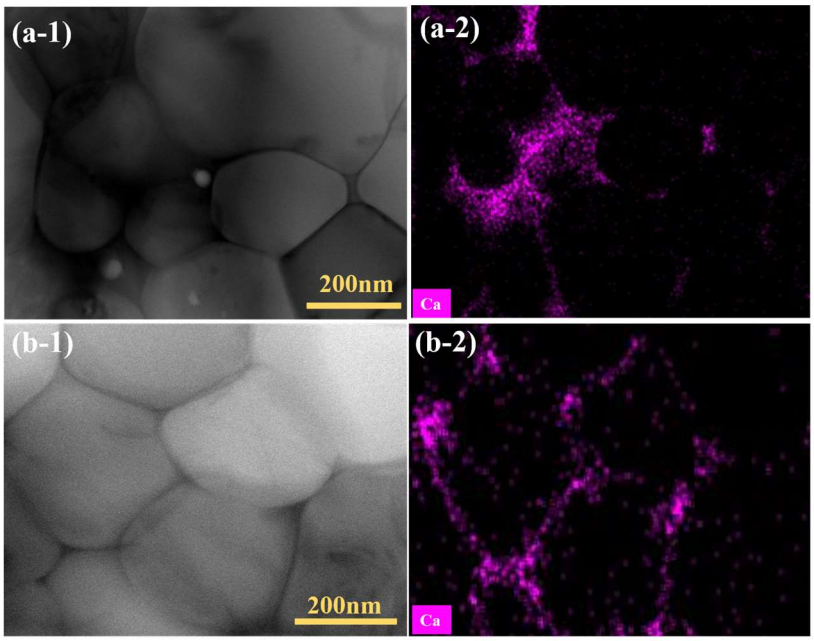

Fig. 3. 15 (a-1) TEM image of AlN+3%$CaO^{2.6}$(3500rpm,5min,pellet) and (a-2) corresponding EDS mapping of Ca; (b-1) TEM image of AlN+3%$CaO^{0.04}$(5000rpm,5min,pellet) and (b-2) corresponding EDS mapping of Ca

3.2.3 Influence of powder mixing techniques on the properties of sintered pellets

The utilization of Picomix as a mixing technology was previously discussed. A comprehensive comparison between the Picomix and other common mixing techniques such as ball milling and manual operation was conducted and introduced here.

Fig. 3. 16 shows the SEM images and corresponding elemental Ca EDS mapping of mixed powders, obtained by mixing AlN and 3 wt% $CaO^{0.04}$ using three different methods, namely: high-shear mixing, ball milling and manual mixing, respectively (see Section 2.2.2.1.1, Chapter 2). After mixing in the Picomix or with a ball mill, the $CaO^{0.04}$ in the former mixed powder exhibits a slightly better dispersion, as could be expected. The dispersion of $CaO^{0.04}$ in both AlN+3%$CaO^{0.04}$(5000rpm,5min) and AlN+3%$CaO^{0.04}$(BM) powder is considerably higher than that obtained with manual mixing (AlN+3%$CaO^{0.04}$(M)), in which the CaO is present in the form of large agglomerates. A small number of large agglomerates remain in the ball milling mixture, which may be due to the fact that collisions and frictional forces are still insufficient to dis-agglomerate the nanoparticles. These results demonstrate the influence of mixing on the dispersion and homogeneity of the cohesive powders, as well as the superior results obtained in just a few minutes with the Picomix high-shear mixer.

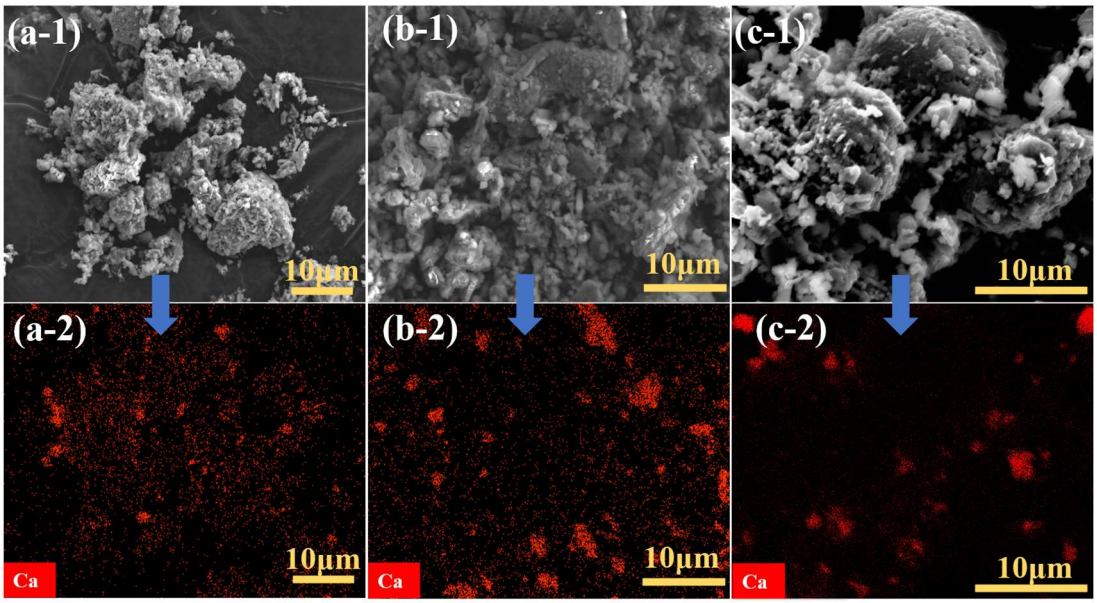

Fig. 3. 16 (a-1) SEM image of AlN+3%$CaO^{0.04}$(5000rpm,5min) and (a-2) corresponding EDS mapping of Ca; (b-1) SEM image of AlN+3%$CaO^{0.04}$(BM) and (b-2) corresponding EDS mapping of Ca; (c-1) SEM image of AlN+3%$CaO^{0.04}$(M) and (c-2) corresponding EDS mapping of Ca

Fig. 3. 17 shows the XRD pattern of sintered AlN+3%$CaO^{0.04}$(5000-rpm,5min,pellet), AlN+3%$CaO^{0.04}$(BM,pellet) and AlN+3%$CaO^{0.04}$(M,pellet). The AlN+3%-$CaO^{0.04}$(M,pellet) exhibits a similar chemical composition and crystalline structure to the AlN+3%$CaO^{0.04}$(5000rpm,5min,pellet). In addition to the presence of small quantities of a $Ca_3Al_2O_6$ secondary phase observed in the AlN+3%$CaO^{0.04}$(5000rpm,5min,pellet), a different $CaAl_4O_7$ secondary phase ($CaO{\cdot}2Al_2O_3$) (JCPDS PDF No.23-1037) was detected in the AlN+3%$CaO^{0.04}$(BM,pellet). When the same amount of $CaO^{0.04}$ is added to the AlN, after ball milling the ratio of Al_2O_3 and $CaO^{0.04}$ forming a secondary phase in the sintered pellet is increased by 2:1, when compared to the sample mixed in the Picomix. This is most likely due to the oxidation of AlN exposed to air during the ball milling process, which thus produces greater quantities of Al_2O_3.

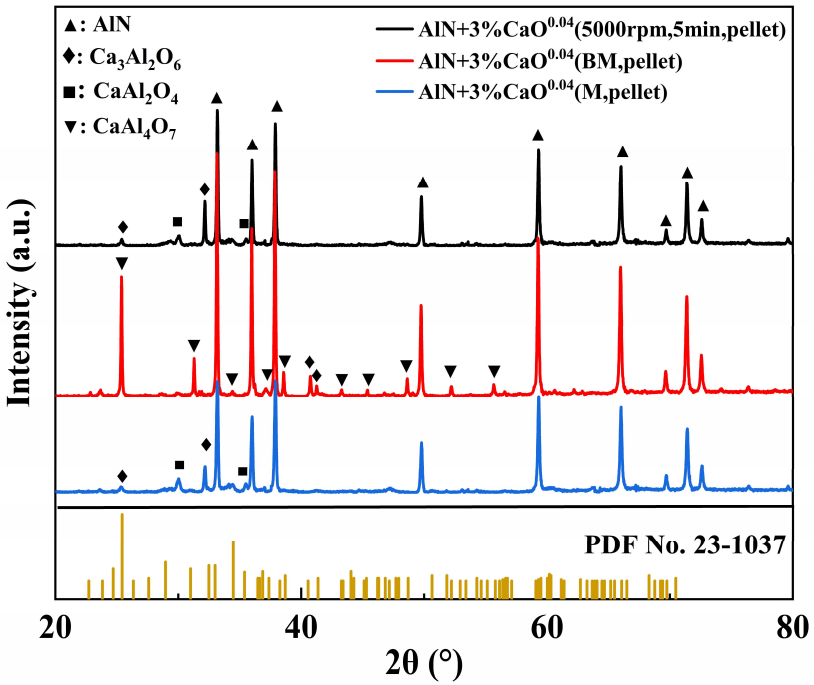

Fig. 3. 17 XRD pattern of sintered AlN+3%$CaO^{0.04}$(5000rpm,5min,pellet), AlN+3%$CaO^{0.04}$(BM,pellet) and AlN+3%$CaO^{0.04}$(M,pellet) and relevant JCPDS PDFs

The porosity (φ) and thermal conductivity (k) results of AlN+3%$CaO^{0.04}$(5000rpm,5min,pellet), AlN+3%$CaO^{0.04}$(BM,pellet) and AlN+3%-

$CaO^{0.04}$(M,pellet) are shown in Fig. 3. 18. Although the φ value of AlN+3%$CaO^{0.04}$(BM,pellet) is similar to that of AlN+3%$CaO^{0.04}$(5000-rpm,5min,pellet), the value of k is slightly lower (128.4 W/m·K). This could be due to the presence of a significant quantity of the secondary phase (Fig. 3. 18). Among these three samples, the AlN+3%$CaO^{0.04}$(M,pellet) has the highest value of φ and the lowest value of k.

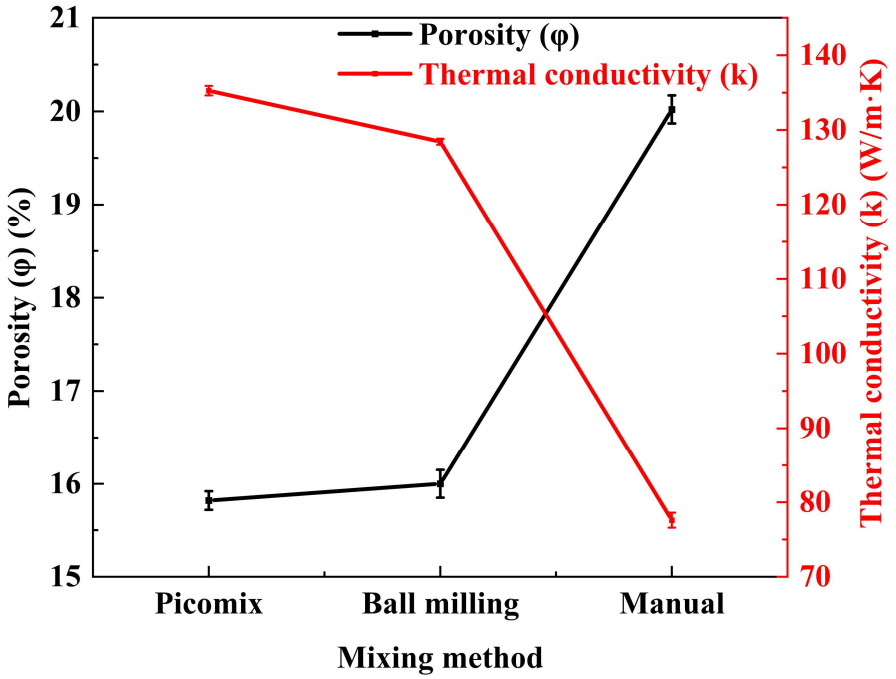

Fig. 3. 18 Porosity and thermal conductivity of sintered AlN+3%$CaO^{0.04}$(5000rpm,5min,pellet), AlN+3%$CaO^{0.04}$(BM,pellet) and AlN+3%$CaO^{0.04}$(M,pellet)

Tab. 3. 4 compares the present work's result by high-shear mixing with previous publications, which have analyzed the thermal conductivity of AlN samples when CaO is added as a sintering additive and mixing is achieved by ball milling. It can be seen that in these previous studies, ball milling usually lasts for several hours, and the highest value of k in the resulting pellets is similar to that obtained in the present study with the Picomix mixer, after only 5 minutes of mixing.

Tab. 3. 4 Summary of literature on the sintered pellets with CaO added as a sintering additive and mixed by ball milling, and comparison with the present work's result (High-Shear mixed)

Main material	Sintering additives and mass fraction	Mixing mode	Sintering mode	Thermal conductivity (W/m·K)	Reference
AlN	2% CaO + 5.4% Y_2O_3 + 0.5% Li_2O	Ball-milled in ethanol	Calcined at 800 °C for 6 h in nitrogen with 5% H_2 and cold isostatically pressed at 20 MPa; then calcined at 1600 °C	135	[113]
	1% CaO + 3.1% Y_2O_3 + 0.08% B	Ball-milled in ethanol for 4 h	Sintered at 1550 °C in SPS; a constant uniaxial pressure was applied	70-80	[132]
	2% CaO + 3.53% Y_2O_3 + 1.89% nano-AlN	Ball-milled in ethanol for 3 h	Cold isostatically pressed under 150 MPa for 120 s and fired at 1600 °C for 6 h under nitrogen atmosphere	133	[117]
	1% CaO + 3.1% Y_2O_3 + 0.08% B	Ball-milled in butanol for 4 h	Sintered at 1650 °C in SPS; a constant uniaxial pressure of 50 MPa was applied	80-90	[133]
	0.9% CaO + 1.2% Y_2O_3	Ball-milled in ethanol for 3 h	Uniaxially pressed under 430 MPa and sintered at 1700 °C in graphite furnace under N_2 atmosphere	136.7	[134]
	2% CaO + 2% Y_2O_3 + 2% Sm_2O_3	Ball-milled in ethanol for 3 h	Uniaxially pressed under 430 MPa and sintered at 1700 °C in graphite furnace under N_2 atmosphere	134.4	[135]
	3% CaO	High-shear mixed in Picomix at 5000 rpm for 5 min	Sintered at 1650 °C and under a constant uniaxial load of 5.1 kN (65 MPa) in SPS	135.3	The present work

When combined with the above results, the feasibility and superiority of the high-shear mixer is evident. This machine provides a considerable improvement in terms of the contact established between particles and dispersion of the sintering additive, both of which are achieved through the shearing process. The resulting end products (sintered pellets) have an improved thermal conductivity, without requiring the use of a solvent. Tab. 3. 5 details the advantages and disadvantages of high-shear mixing and ball milling. The high-shear mixer (Picomix) is found to be substantially superior, as it is a solvent-free process, requires a considerably shorter mixing time, consumes less energy, generates less powder-oxidation, and leads to a higher value of thermal conductivity.

Tab. 3. 5 Comparison of different mixing techniques

Technique	Advantages	Disadvantages
High-shear mixing (Device: Picomix)	1. Intensive but homogeneous and fast blending of the powder 2. High rotational speed provided 3. Short processing time 4. No breakage of particles 5. Simple operation process 6. Process chamber is easy to clean 7. Solvent-free 8. No grinding media needed 9. Low energy consumption	1. Difficult to extend the device's capacity to very large quantities 2. Not suitable for extremely hard particles
Ball milling (Device: Ball mill)	1. Available in a variety of configurations and types 2. Available in various volumes	1. Long processing time 2. May abrade, attrite, fracture or break particles 3. Organic solvents are used to avoid particle oxidation in long-duration milling 4. Low work efficiency 5. High energy consumption

3.3 Characterization of α-SiC-based samples

α-SiC-based pellet was obtained from spark plasma sintering the α-SiC and CaO-Al_2O_3 additive powders (detailed in Section 2.2.2.2, Chapter 2). Since the hardness of

α-SiC is greater than that of stainless steel, the material of the high-shear mixer (Picomix), Picomix is not suitable for processing α-SiC. The traditional ball milling method was used to prepare α-SiC-additive mixed powder. α-SiC powder was dry-mixed with 9 wt% of CaO-Al_2O_3 additive in the planetary ball mill at 250 rpm for 3 h, and then sintered at 1850 ℃ and 5.1 kN. In this section, the characterization results of these α-SiC based powder and pellet samples are exhibited. The characterization process involves both the raw powder (comprising α-SiC, CaO, γ-Al_2O_3) and the mixed powder, concluding with a thorough study of the sintered pellets. Through these analyses, valuable insights are gained into the material's physical, chemical, morphological, and thermal properties, which are essential for its successful implementation in solar thermal applications.

3.3.1 Physical and bulk properties of powders

The real density (ρ) of the α-SiC, CaO, Al_2O_3 and mixed powder are listed in Tab. 3. 6. It is obvious that the ρ of the mixed powder is higher than that of the α-SiC raw powder, which might be due to the addition of CaO and Al_2O_3 particles in the mixture, as they are slightly denser than α-SiC.

The size distributions of the α-SiC, CaO, Al_2O_3 and mixed powder were measured with a laser diffraction particle size analyzer and are plotted in Fig. 3. 19. The α-SiC particles present a narrow size distribution with one main interval located between 120 μm to 520 μm. Al_2O_3 also has a narrow size distribution with one main interval located between 20 μm to 100 μm. CaO exhibits wide size distribution with more than one interval, which implied the agglomeration phenomena of CaO additive. The α-SiC+9%CaO-Al_2O_3(BM) (BM refers to “ball milling”, see Section 2.2.2.2.1, Chapter 2) mixed powder displays quite similar size distribution as α-SiC. However, there is an additional peak in the smaller particle size range, indicating that agglomerates still exist in the mixed powder after ball milling. The corresponding mean diameter (d_p) and uniformity coefficient (C_u) are listed in Tab. 3. 6. The values of d_p and C_u of the α-

SiC+9%CaO-Al_2O_3(BM) mixed powder (d_p of 276 μm, and C_u of 1.6) are nearly equal to that of the original α-SiC particles (d_p of 280 μm, and C_u of 1.6). It demonstrates that the particle size distribution of the mixed powder was not significantly influenced by the operating conditions.

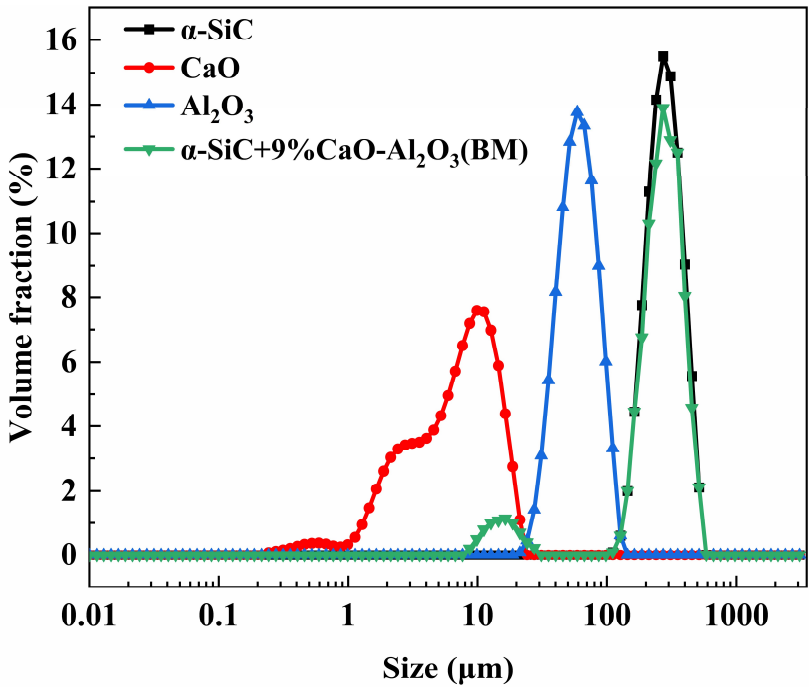

Fig. 3. 19 Size distributions of the α-SiC-based powders before and after mixing

The flowability test was applied to the powder samples and the resulting Hausner Ratio (HR) are listed in Tab. 3. 6. The HR of CaO is greater than 1.4, indicating its cohesive characteristics, which corresponds to its wide particle size distribution. On the other hand, the remaining powders all exhibit non-cohesive properties. The addition of CaO slightly decreases the flowability of the α-SiC+9%CaO-Al_2O_3(BM) mixed powder compared to α-SiC, but it still falls within the good flowability range.

Tab. 3. 6 Physical properties of α-SiC-based powders before and after mixing

Sample	$\rho^{(a)}$ (g/cm^3)	$d_p^{(b)}$ (μm)	$C_u^{(c)}$	$HR^{(d)}$
α-SiC	3.16	280	1.6	1.09 ± 0.02
CaO	3.44	4.1	4.5	2.86 ± 0.02
Al_2O_3	3.86	59.1	1.7	1.05 ± 0.01
α-SiC+9%CaO-Al_2O_3(BM)	3.19	276	1.6	1.14 ± 0.04

(a): ρ, particle real density (The standard deviation from the three measurements was less than 0.01).
(b): d_p, particle mean diameter calculated according to $d_{3,2}$ (Eq. 2. 4, Chapter 2) obtained from laser diffraction particle size analyzer.
(c): C_u, uniformity coefficient (Eq. 2. 5, Chapter 2). $C_u > 2$ indicates a broad particle size distribution.
(d): HR, Hausner Ratio (Eq. 2. 10, Chapter 2). HR < 1.2 corresponds to free flow (non-cohesive powders), HR > 1.4 corresponds to non-free flow (cohesive powders), and 1.2 < HR < 1.4 indicates that the powder's flowability lies at an intermediate level.

3.3.2 Morphology analysis

Fig. 3. 20 shows the SEM image of α-SiC and α-SiC+9%CaO-Al_2O_3(BM) powder, as well as corresponding EDS mappings of elemental Si, Ca, Al in α-SiC+9% CaO-Al_2O_3(BM) powder. No significant fragmentation of SiC particles is observed after the mixing process, which aligns with the size distribution of α-SiC and α-SiC+9%CaO-Al_2O_3(BM). This might be attributed to the hardness of SiC (Mohs hardness 9.5) being greater than that of the stainless steel milling balls (Mohs hardness 5.5)[189]. It is also observed that after the mixing process, a significant portion of the fine CaO particle adheres to the surface of larger irregular SiC particles in α-SiC+9%CaO-Al_2O_3(BM) powder, forming a discontinuous coating. This could be attributed to the large difference in particle mean diameter between α-SiC (d_p of 280 μm) and CaO (d_s of 0.8 μm). This difference leads to the presence of a strong van der Waals force between them, causing the smaller CaO particles to adhere onto the larger SiC particles when external mechanical energy is applied during the mixing process[122]. Additionally, numerous dispersed CaO aggregates and Al_2O_3 are present around the SiC particles. The larger particle size ratio of Al_2O_3 (d_p of 59.1 μm) and α-SiC (d_p of 280 μm) makes

Al_2O_3 mostly scattered in the mixture uniformly. This observation highlights the interaction between additives and SiC, which contributes to the formation of the composite material.

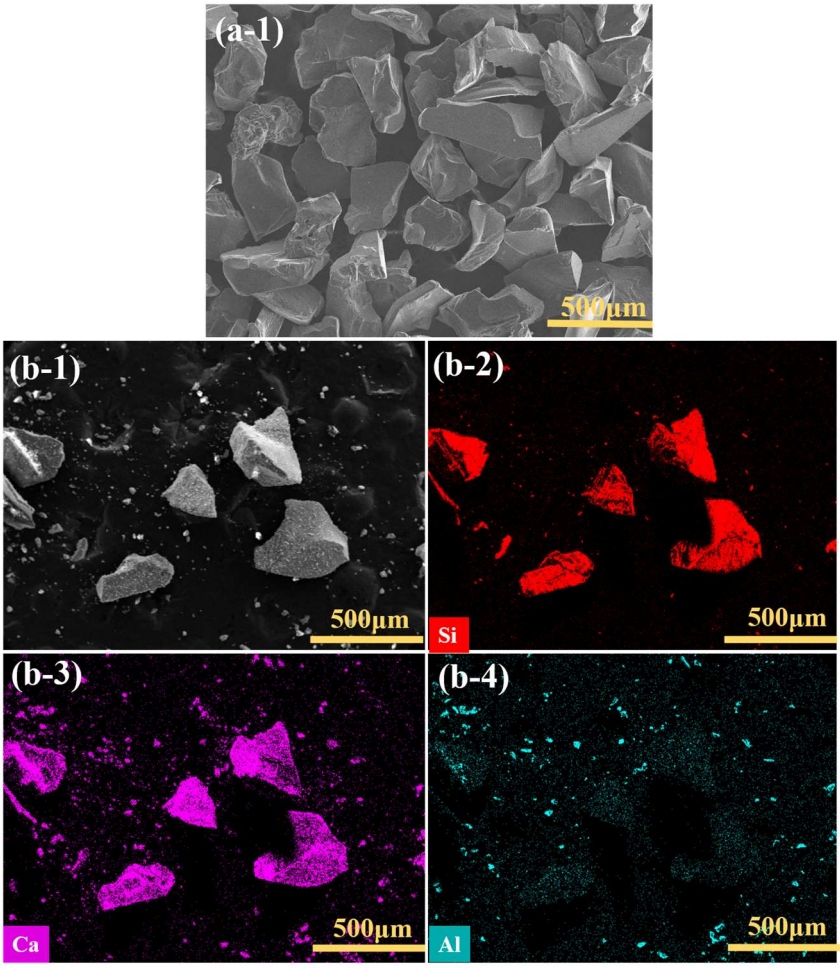

Fig. 3. 20 (a-1) SEM image of α-SiC powder; (b-1) SEM image of α-SiC+9%CaO-Al_2O_3(BM) powder; EDS mapping of (b-2) Si element, (b-3) Ca element and (b-4) Al element of α-SiC+9%CaO-Al_2O_3(BM) powder

The SEM image of the α-SiC(pellet) and α-SiC+9%CaO-Al_2O_3(BM,pellet) (the pellet sintered from α-SiC+9%CaO-Al_2O_3(BM) powder) are shown in Fig. 3. 21. In the case of pure sintered α-SiC(pellet), there are several larger pores (as seen in the red circle) scattered throughout the pellet. In contrast, the α-SiC+9%CaO-Al_2O_3(BM,pellet) obtained after sintering with the addition of Al_2O_3 and CaO additives exhibits a relatively reduced number of pores. The additives may facilitate better particle packing

and decrease the formation of larger pores, resulting in a more uniform and denser microstructure during sintering. The reduction in larger pores and the achievement of a more uniform microstructure in the pellet with additives sintering may contribute to improved thermal conductivity.

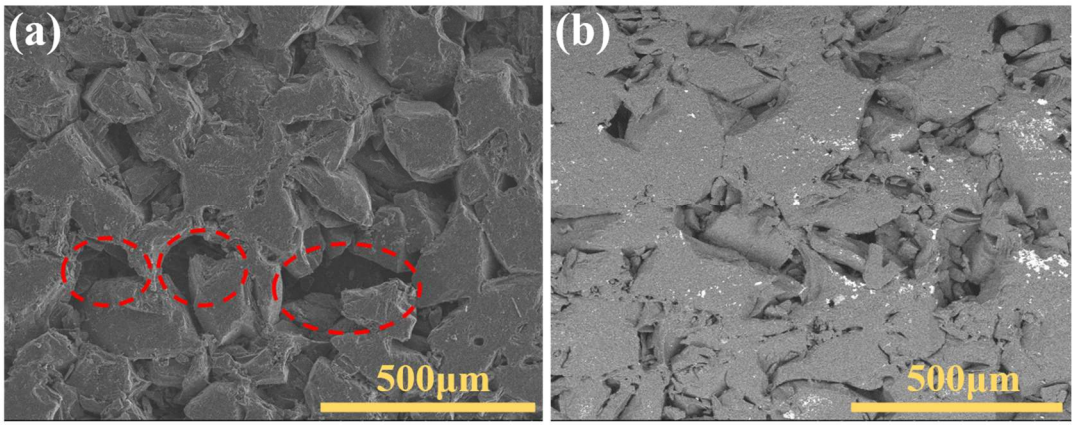

Fig. 3. 21 (a) SEM image of α-SiC(pellet); (b) Backscattered electron image of α-SiC+9%CaO-Al_2O_3(BM,pellet)

3.3.3 Chemical structure analysis

The phase of the original (α-SiC, CaO, Al_2O_3) and mixed powder, as well as the sintered α-SiC(pellet) and α-SiC+9%CaO-Al_2O_3(BM,pellet) were verified using XRD. As shown in Fig. 3. 22, the α-SiC diffraction peaks correspond to the alpha silicon carbide phase (JCPDS PDF No. 72-0018). The diffraction peaks of the α-SiC+9%CaO-Al_2O_3(BM) mixed powder can be mainly attributed to the silicon carbide phase, and several peaks correspond to the alumina (JCPDS PDF No. 74-1081) and calcium oxide (JCPDS PDF No. 78-0649) phase, as marked in the figure. The sintered α-SiC(pellet) retains the same diffraction peaks as α-SiC powder. α-SiC+9%CaO-Al_2O_3(BM,pellet) also contains Al_2O_3 and CaO phases in addition to α-SiC phase, but the presence of the secondary phase was not detected. This could be due to the uneven distribution of the secondary phase, making it difficult to detect in a small sample.

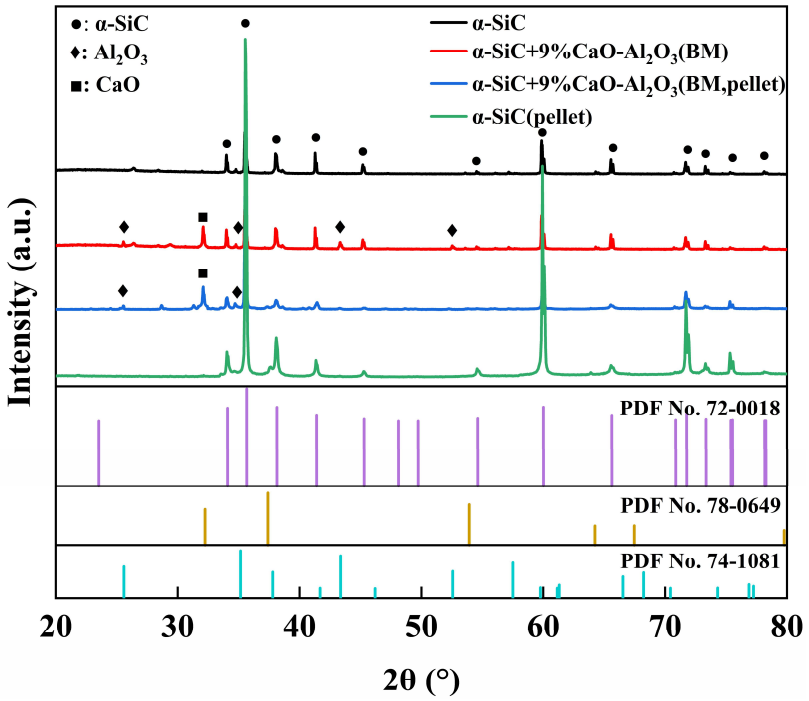

Fig. 3. 22 XRD patterns of α-SiC, α-SiC+9%CaO-Al_2O_3(BM) powder, α-SiC(pellet) and α-SiC+9%CaO-Al_2O_3(BM,pellet) and relevant JCPDS PDFs

3.3.4 Porosity and thermal conductivity of α-SiC-based pellets

The porosity and thermal properties of α-SiC-based pellets were investigated. The porosity (φ) and thermal conductivity (k) of α-SiC(pellet) and α-SiC+9%CaO-Al_2O_3(BM,pellet) are shown in Fig. 3. 23. Error bars were incorporated based on the standard deviation derived from three measurements. After sintering with additives, the φ value of the α-SiC pellet decreases from 30% to 22%. The observed reduction in porosity aligns with the comparison of the number and size of pores as depicted in Fig. 3. 21. The k of the α-SiC pellet increases from 57 W/m·K to 114 W/m·K when 9 wt% of CaO- Al_2O_3 additive was added to α-SiC matrix. This value of k is higher than the results reported in the literature. For example, Malik et al.[233] pressureless sintered SiC with Al_2O_3-Y_2O_3-CaO additive at 1850 °C for 2 h. When the total additive content was 3 vol%, the sintered SiC ceramic had the highest thermal conductivity of 71.7 W/m·K. Eom et al.[139] sintered SiC with a mass fraction of 9 wt% of Al_2O_3-Y_2O_3-CaO additive under a pressure of 50 MPa and at 1850 °C for 2 h. The thermal

conductivity of the SiC ceramic was 80.1 W/m·K. The reduction in porosity is highly advantageous as it helps to minimize the scattering of phonons within the material's microstructure. Phonons, which are quantized lattice vibrations, play a crucial role in the heat transfer in solids. When the material contains fewer pores and exhibits a more continuous and interconnected structure, the movement of phonons encounters fewer barriers, leading to increased thermal conductivity.

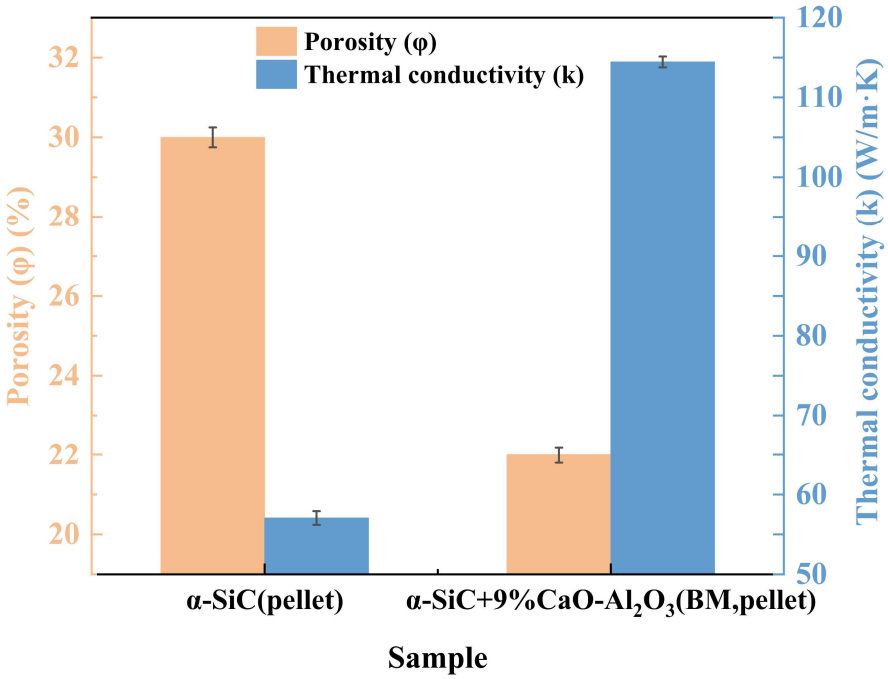

Fig. 3. 23 Porosity and thermal conductivity of α-SiC(pellet) and α-SiC+9%CaO-Al_2O_3(BM,pellet)

3.4 Characterization of Cu-based samples

The Cu particle was dry-coated with 2 wt% β-SiC in Picomix and sintered at 800 ℃ and 5.1 kN (detailed in Section 2.2.2.3, Chapter 2), in order to provide anti-oxidation protection for Cu in the application of solar thermal process. The characterization results involving physical, chemical, morphological, and thermal properties of the raw powder (Cu, β-SiC), mixed powder (Cu+2%β-SiC(5000rpm,5min)) and the sintered pellets are shown in this section.

3.4.1 Physical and bulk properties of powders

The real density (ρ) of Cu, β-SiC powder and Cu+2%β-SiC(5000rpm,5min) mixed powder are listed in Tab. 3. 7. It is evident that the ρ of the mixed powder is lower than that of the Cu powder, which can be attributed to the addition of β-SiC particles in the mixture, as its density is slightly lower than Cu particle.

As introduced in Section 2.2.2.3.1 (Chapter 2), the mass fraction of β-SiC was calculated based on the values of real density and mean diameter of both Cu and β-SiC powder. Fig. 3. 24 (a) displays the size distributions of Cu and β-SiC powder measured with the laser diffraction particle size analyzer. Cu has a narrow size distribution with one main interval, with a mean diameter (d_p) of 61 μm and a uniformity coefficient (C_u) of 1.9 (Tab. 3. 7). β-SiC exhibits a wide size distribution with two consecutive intervals, as well as a large C_u value (5.1). This indicates the presence of a large number of agglomerates in the β-SiC powder, and the laser diffraction particle size measurement gives the d_p of these agglomerates (1.9 μm). Therefore, in order to obtain the accurate particle size for the calculation of mass fraction, the image analysis was performed on the SEM image of β-SiC using the "Nano Measurer 1.2.5" software. The sizes of 300 representative particles were acquired by manually determining each particle's maximum linear dimension (i.e. red line in Fig. 3. 24 (b)) in "Nano Measurer". These dimensions and the corresponding particle counts were organized and the dimension classes were created, allowing the corresponding particle size (μm) histograms to be plotted (Fig. 3. 24 (c)). The Sauter diameter (referred to as d_s) of the β-SiC particle was computed from the distribution as 0.6 μm, based on Eq. 2. 4 (Chapter 2).

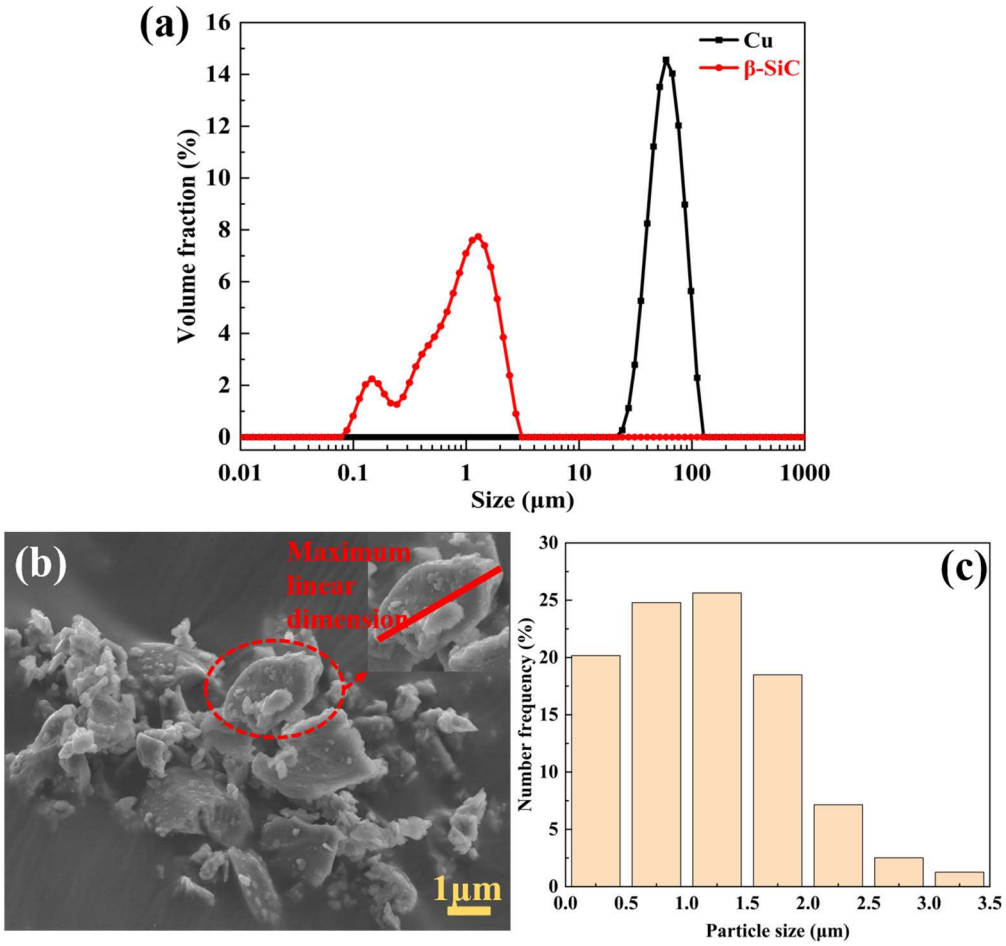

Fig. 3. 24 (a) Size distribution from laser diffraction particle size analyzer of Cu and β-SiC; (b) SEM image and (c) Size distribution histogram from SEM image analysis of β-SiC

Fig. 3. 25 displays the comparison of size distribution between Cu and Cu+2%β-SiC(5000rpm,5min) powder. The coated Cu exhibits a similar size distribution to that of Cu, and its d_p and C_u are nearly identical to that of the Cu particles as shown in Tab. 3. 7. This suggests that the particle size distribution after dry-coating will not change significantly.

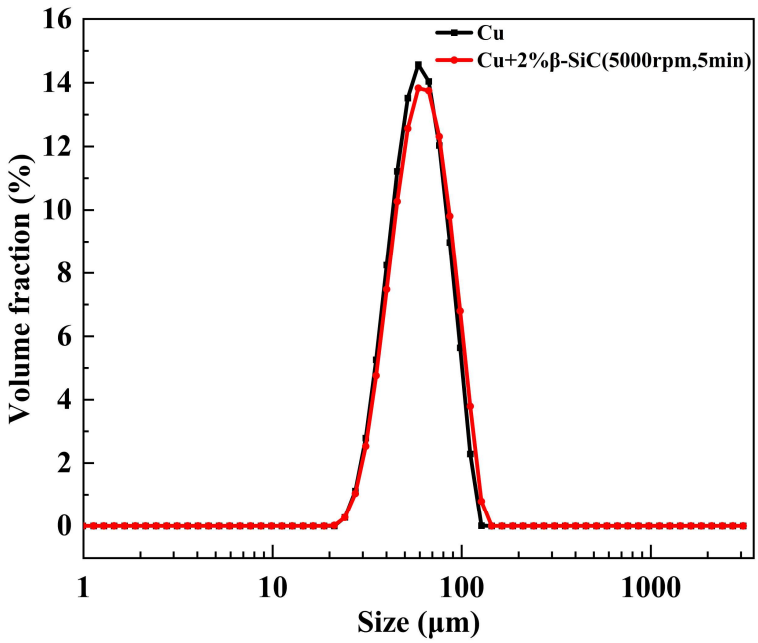

Fig. 3. 25 Size distribution of Cu and Cu+2%β-SiC(5000rpm,5min) powder

The flowability test was applied to the powder samples and the resulting Hausner Ratio (HR) are listed in Tab. 3. 7. The HR of Cu is smaller than 1.2, indicating that it is a non-cohesive powder. On the other hand, the HR of β-SiC is greater than 1.4, indicating its cohesive behavior, which aligns its broad particle size distribution. The HR of Cu+2%β-SiC(5000rpm,5min) is slightly smaller than that of Cu, suggesting that the coating of β-SiC might increase the flowability of the raw powder.

Tab. 3. 7 Physical properties of Cu-based powders before and after coating

Sample	$\rho^{(a)}$ (g/cm^3)	$d_p^{(b)}$ (μm)	$d_s^{(c)}$ (μm)	$C_u^{(d)}$	$HR^{(e)}$
Cu	8.74	61	-	1.9	1.15 ± 0.01
β-SiC	3.15	1.9	0.6	5.1	2.46 ± 0.03
Cu+2%β-SiC(5000rpm,5min)	8.67	59	-	1.9	1.08 ± 0.01

(a): ρ, particle real density (The standard deviation from the three measurements was less than 0.01).
(b): d_p, particle mean diameter calculated according to $d_{3,2}$ (Eq. 2. 4, Chapter 2) obtained from laser diffraction particle size analyzer.
(c): d_s, particle mean diameter calculated according to $d_{3,2}$ (Eq. 2. 4, Chapter 2) obtained from analysis of SEM images by "Nano measurer 1.2" software.

(d): C_u, uniformity coefficient (Eq. 2. 5, Chapter 2). $C_u > 2$ indicates a broad particle size distribution.

(e): HR, Hausner Ratio (Eq. 2. 10, Chapter 2). HR < 1.2 corresponds to free flow (non-cohesive powders), HR > 1.4 corresponds to non-free flow (cohesive powders), and 1.2 < HR < 1.4 indicates that the powder's flowability lies at an intermediate level.

3.4.2 Morphology analysis

Fig. 3. 26 shows the SEM images of Cu+2%β-SiC(5000rpm,5min) powder and sintered Cu+2%β-SiC(5000rpm,5min,pellet), as well as Cu, Si element EDS mappings. After the dry coating process at a rotational speed of 5000 rpm for 5 min in the high-shear mixer (Picomix), it is observed that the fine β-SiC particles predominantly adhere to the surface of the spherical Cu particle which retains the shape, creating a discontinuous coating. The incomplete coating on the surface of Cu particles could be attributed to their smooth surface and relatively small roughness. According to Li et al.[234], the intrinsic adhesiveness between particles caused by van der Waals force is strongly influenced by the particle roughness. When the roughness of the surface is too small, it becomes less conducive to the adhesion of small particles onto the surface of larger particles. After the sintering, it is evident that no pores are observed in the fine surface morphology of Cu+2%β-SiC(5000rpm,5min,pellet), indicating its dense and compact structure. The β-SiC phase distributes relatively uniformly among the Cu particles, exhibiting a good bonding with Cu matrix and creating a well-integrated composite pellet. This is similar to the phenomenon reported by Shabani et al.[235]. The absence of structural defects and pores, along with the dense structure, significantly contributes to the high thermal conductivity of the Cu-based pellet.

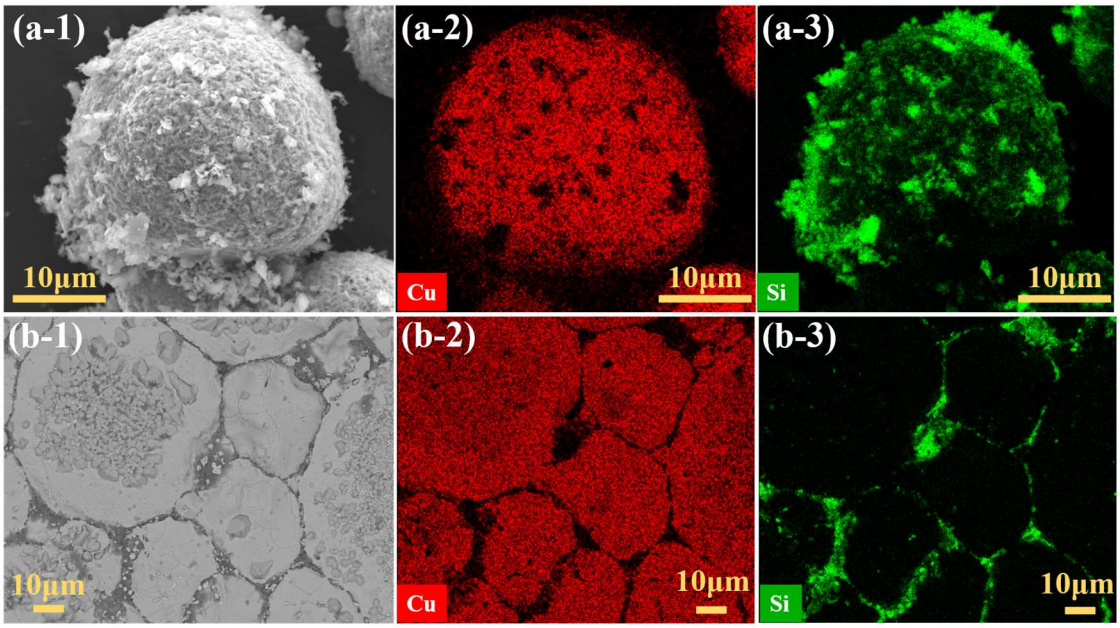

Fig. 3. 26 Cu+2%β-SiC(5000rpm,5min) powder: (a-1) SEM image, (a-2) EDS mapping of Cu element and (a-3) EDS mapping of Si element; Cu+2%β-SiC(5000rpm,5min,pellet): (b-1) SEM image, (b-2) EDS mapping of Cu element and (b-3) EDS mapping of Si element

3.4.3 Chemical structure analysis

The phase of the Cu and Cu+2%β-SiC(5000rpm,5min) powder, as well as the sintered Cu(pellet) and Cu+2%β-SiC(5000rpm,5min,pellet) were verified using XRD (Fig. 3. 27). The diffraction peaks of Cu powder correspond to the copper phase (JCPDS PDF No. 85-1326). In order to ensure the accuracy of the data, the samples were sintered simultaneously and stored under identical conditions, and the chemical analysis test was conducted after the same duration. In the diffraction peaks of the Cu+2%β-SiC(5000rpm,5min) powder, in addition to the copper phase, there is the presence of beta silicon carbide phase (JCPDS PDF No. 29-1129), which also exists in the sintered Cu+2%β-SiC(5000rpm,5min,pellet). The Cu_2O phase (JCPDS PDF No. 75-1531) was detected in both powders and sintered pellets, with the characteristic peaks becoming more intense after sintering. The oxidation occurred might be due to the reaction between Cu and the entrapped residual oxygen in the mold. Notably, the

XRD curve of Cu(pellet) shows a significantly higher intensity of the diffraction peak corresponding to Cu_2O phase compared to Cu+2%β-SiC(5000rpm,5min,pellet). This difference suggests that the β-SiC coating on the surface of the Cu particle might play a protective role by preventing direct contact between the Cu particles and oxygen during the sintering process. As a result, the occurrence of oxidation is reduced, leading to a lower presence of the Cu_2O phase in Cu+2%β-SiC(5000rpm,5min,pellet). XRF results of both pellets in Tab. 3. 8 also proves the decreased oxidation. It shows that the content ratio of O element to Cu element in Cu(pellet) (0.014) is higher than that in Cu+2%β-SiC(5000rpm,5min,pellet) (0.009).

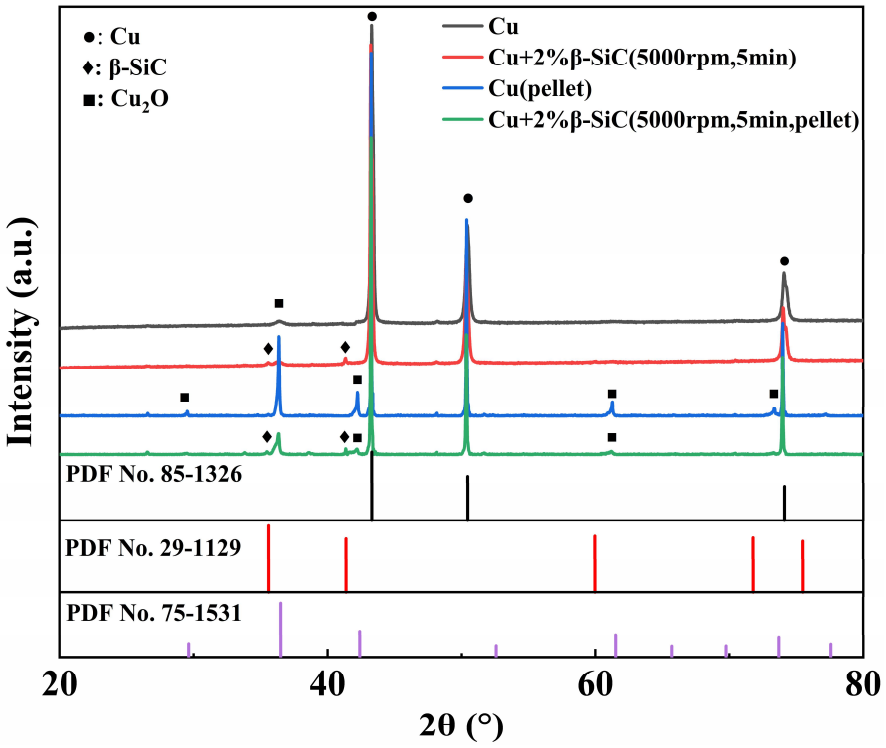

Fig. 3. 27 XRD patterns of Cu, Cu+2%β-SiC(5000rpm,5min), Cu(pellet), Cu+2%β-SiC(5000rpm,5min,pellet) and relevant JCPDS PDFs

Tab. 3. 8 XRF results of Cu and O element in Cu-based pellets

Sample	Cu (wt%)	O (wt%)
Cu(pellet)	98.5	1.35
Cu+2%β-SiC(5000rpm,5min,pellet)	96.91	0.84

3.4.4 Porosity and thermal conductivity of Cu-based pellets

The porosity and thermal properties of Cu-based pellets were investigated. The porosity (φ) and thermal conductivity (k) of Cu(pellet) and Cu+2%β-SiC(5000rpm,5min,pellet) are shown in Fig. 3. 28. Error bars were incorporated based on the standard deviation derived from three measurements. When compared with the pellet obtained by sintering pure Cu powder, both the φ and k value of Cu+2%β-SiC(5000rpm,5min,pellet) decrease. The decrease in porosity suggests that the β-SiC coating on the surface of the Cu particles may promote the densification of the samples, which aligns with the results observed by previous studies conducted by Shabani et al.[235] and Bazarnik et al.[236]. This may be due to the presence of β-SiC between Cu particles, which hinders the grain overgrowth and recrystallization process, resulting in a more uniform grain size distribution and reducing the formation of pores and defects[236]. The decrease in thermal conductivity is primarily attributed to the distribution of the β-SiC within the pellet. While β-SiC possesses high thermal conductivity, its presence between the Cu boundary still impedes effective heat transfer because the movement of heat-carrying free electrons is hindered.

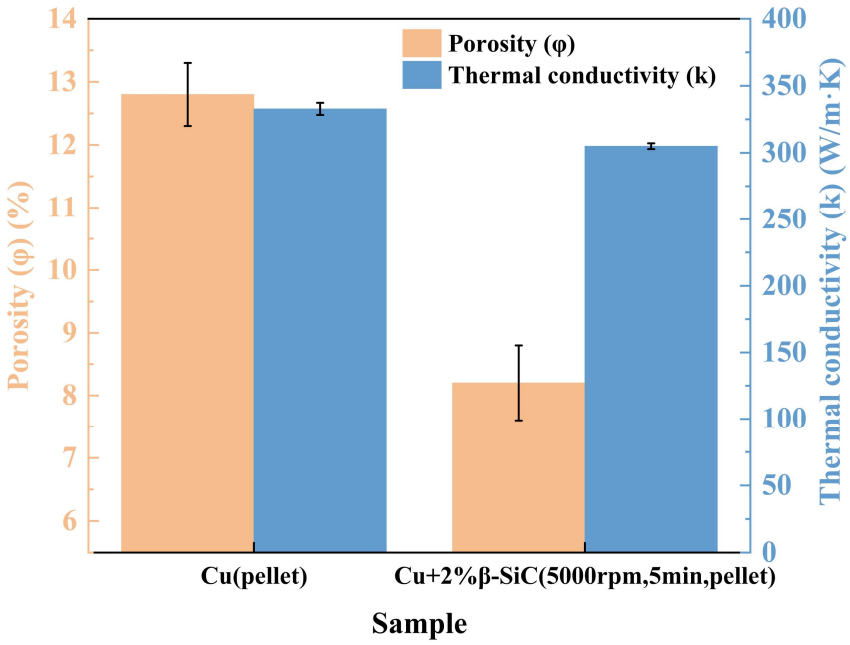

Fig. 3. 28 Porosity and thermal conductivity of Cu(pellet) and Cu+2%β-SiC(5000rpm,5min,pellet)

3.5 Characterization of stainless steel and graphite samples

The stainless steel and graphite powder were sintered for comparison with the above samples. Given the widespread utilization of stainless steel as solar receiver substrates and in solar reactor manufacturing, a stainless steel pellet was prepared through spark plasma sintering (labeled as SS(pellet)). The intention was to establish a direct comparison between the material predominantly employed at present and those put forth in this study. The density of stainless steel powder was 7.86 g/cm^3. Its size distribution is given in Fig. 3. 29, with a mean diameter of 111 μm. In order to enhance the clarity of this comparison, both thermal conductivity and porosity measurements were performed on SS(pellet), of which the thermal conductivity was 14.4 W/m·K and the porosity was 9.8%.

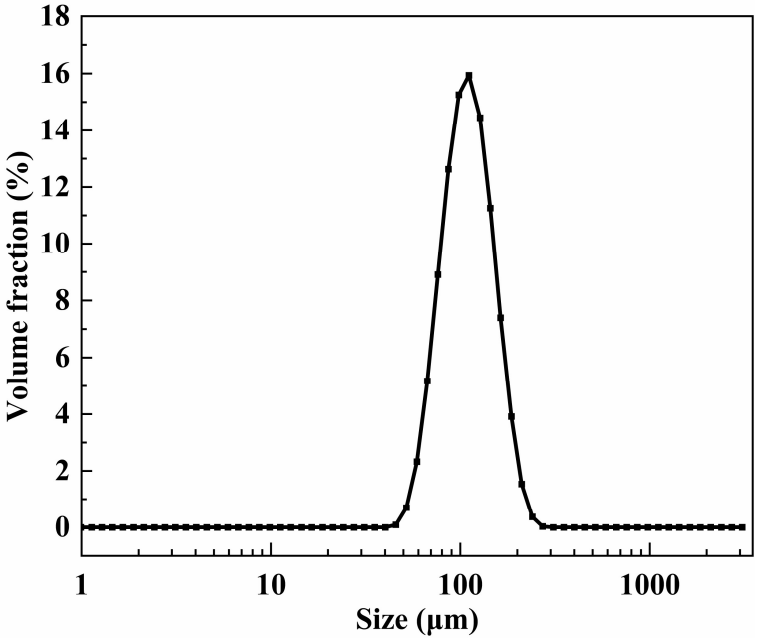

Fig. 3. 29 Size distribution of stainless steel powder

Despite the attempts to sinter graphite powder, no complete pellets were obtained. This may be due to the fact that the layered structure of graphite is held together by relatively weak van der Waals forces and slips rather than fusing during sintering. Moreover, it transforms from a solid directly to a gas at high temperatures easily.

Tab. 3. 9 summarizes the porosity and thermal conductivity of all prepared pellets.

Tab. 3. 9 Porosity and thermal conductivity of all prepared pellets

Sample	Porosity (%)	Thermal conductivity (W/m·K)
AlN(pellet)	20.8 ± 0.4	48.1 ± 0.5
AlN+1%$CaO^{2.6}$(3500rpm,5min,pellet)	13.7 ± 0.3	104.3 ± 0.5
AlN+3%$CaO^{2.6}$(3500rpm,5min,pellet)	13.6 ± 0.5	112.9 ± 0.9
AlN+5%$CaO^{2.6}$(3500rpm,5min,pellet)	11.5 ± 0.3	73.1 ± 0.7
AlN+3%$CaO^{2.6}$(500rpm,5min,pellet)	17.6 ± 0.3	61.1 ± 0.7
AlN+3%$CaO^{2.6}$(5000rpm,5min,pellet)	16.6 ± 0.2	126.2 ± 0.4
AlN+3%$CaO^{0.8}$(5000rpm,5min,pellet)	18.6 ± 0.2	129.3 ± 0.8
AlN+3%$CaO^{0.04}$(5000rpm,5min,pellet)	15.8 ± 0.1	135.3 ± 0.6
AlN+3%$CaO^{0.04}$(BM,pellet)	16.0 ± 0.2	128.4 ± 0.4
AlN+3%$CaO^{0.04}$(M,pellet)	20.0 ± 0.2	77.6 ± 1.0
α-SiC(pellet)	30.0 ± 0.3	57.0 ± 0.9
α-SiC+9%CaO-Al_2O_3(BM,pellet)	22.0 ± 0.2	114.0 ± 0.7
Cu(pellet)	12.8 ± 0.5	332.8 ± 4.5
Cu+2%β-SiC(5000rpm,5min,pellet)	8.2 ± 0.6	305.0 ± 2.1
SS(pellet)	9.8 ± 0.3	14.4 ± 0.3

3.6 Heat transfer test of prepared thermal conductive substrates

To assess the thermal conduction ability of the prepared thermal conductive substrates (sintered pellets), heat transfer tests were conducted and compared. As shown in Fig. 3. 30, the tested pellet was placed on a hot plate, and its perimeter and top surface were insulated by the calcium-magnesium silicate fiber during the experiment. The heating temperature was set to 500 ℃, and three type K thermocouples were placed on the top surface of the pellet to measure the temperature, denoted as T1, T2, T3. The thermocouples were connected to a digital thermometer, which recorded the temperature changes over time. T_{top} was computed as the average value of T1, T2 and T3. Three separate experiments were performed for each pellet to obtain reliable and consistent result. AlN(pellet), AlN+3%$CaO^{0.04}$(5000rpm,5min,pellet), α-SiC(pellet), α-

SiC+9%CaO-Al_2O_3(BM,pellet), Cu(pellet), Cu+2%β-SiC(5000rpm,5min,pellet) and SS(pellet) were investigated and their property values are shown in Tab. 3. 9.

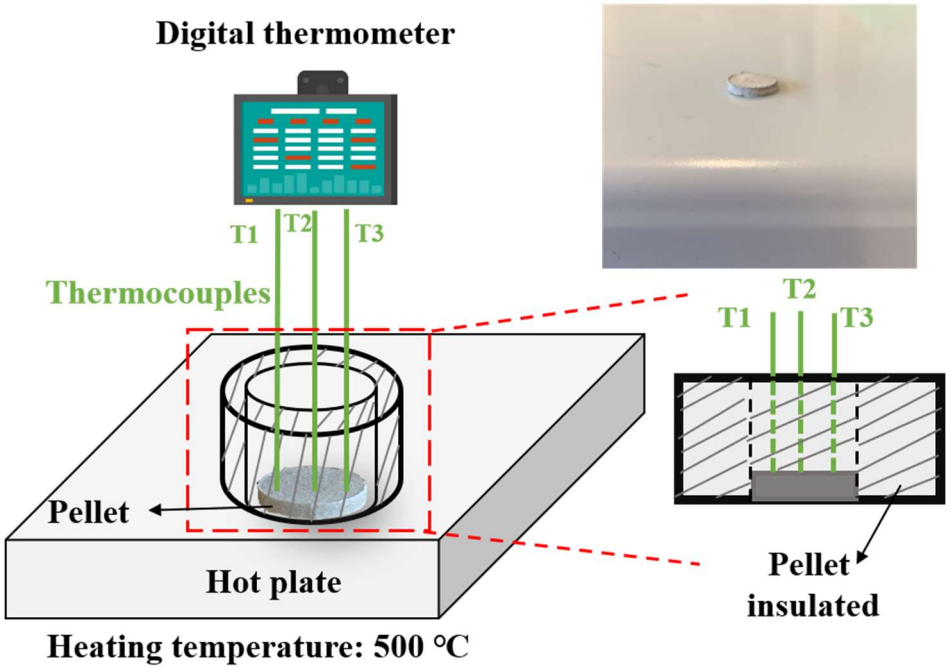

Fig. 3. 30 Heat transfer experiment set-up

The variations of T_{top} with heating time are shown in Fig. 3. 31. Despite the significant difference in thermal conductivity and porosity among these pellets, the heating curves for their top surface are very close. The T_{top} values at steady state are almost identical, showing that the difference of heat transfer efficiency among the pellets is very small. This could be attributed to the relatively small thickness of the pellets (less than 3 mm), as well as the minimal variation in thickness among pellets. Therefore, to validate the results, additional experiments were conducted on two types of materials, one with high thermal conductivity (Cu) and the other with low thermal conductivity (stainless steel) to investigate the effect of thermal conductivity. While their thicknesses were varied to investigate its impact.

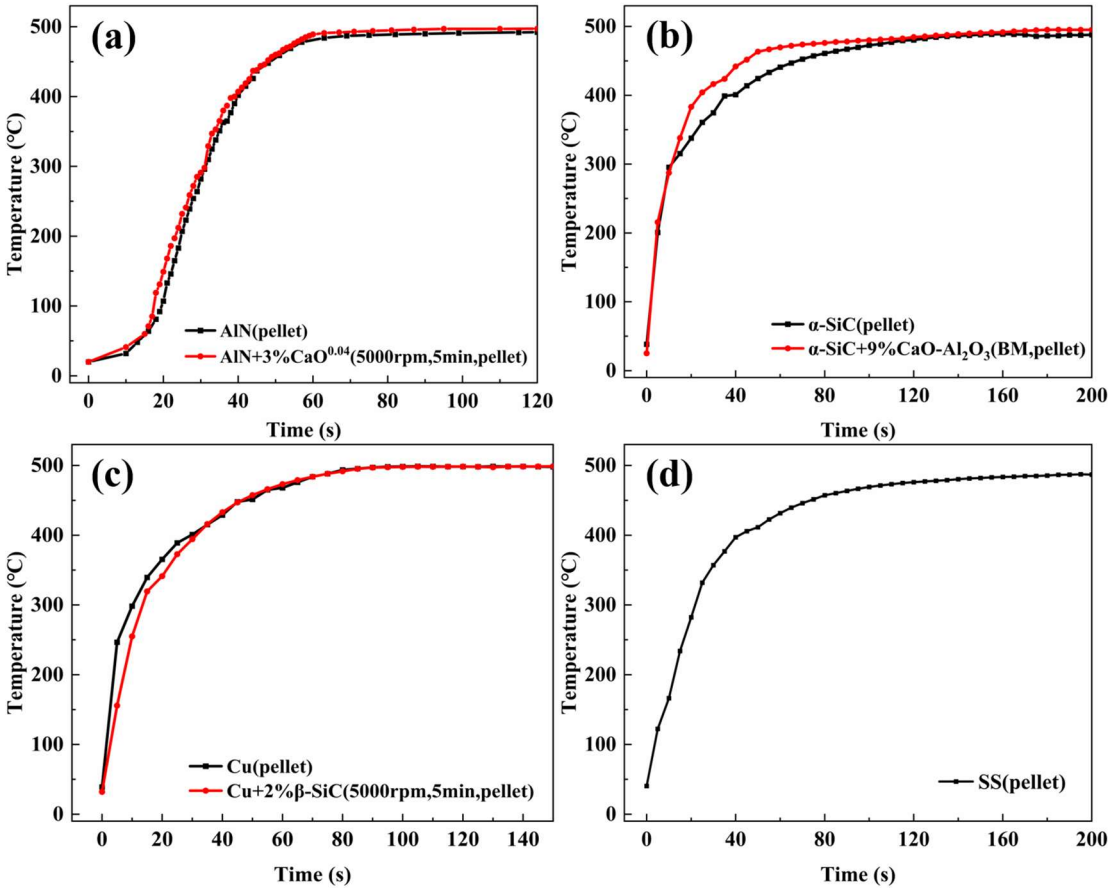

Fig. 3. 31 Variation of T_{top} with time of tested pellets

Copper and stainless steel cylinders with varying thicknesses (1 mm, 10 mm, and 50 mm) were manufactured as samples for the heat transfer experiments described above (reference thermal conductivity: 398 W/m·K for Cu and 13 W/m·K for stainless steel). For more accurate results, each cylinder contains a hole at the bottom, and the thermocouple was placed at the center of the hole to measure the temperature, which was recorded as T_{bottom} (Fig. 2. 17, also displayed below for reference). T_{top} was measured in the same way presented above (Fig. 3. 26). Other experimental set-up and procedures remained consistent as described above. ΔT was calculated according to the following formula:

$$\Delta T = T_{bottom} - T_{top} \qquad \text{Eq. 3. 1}$$

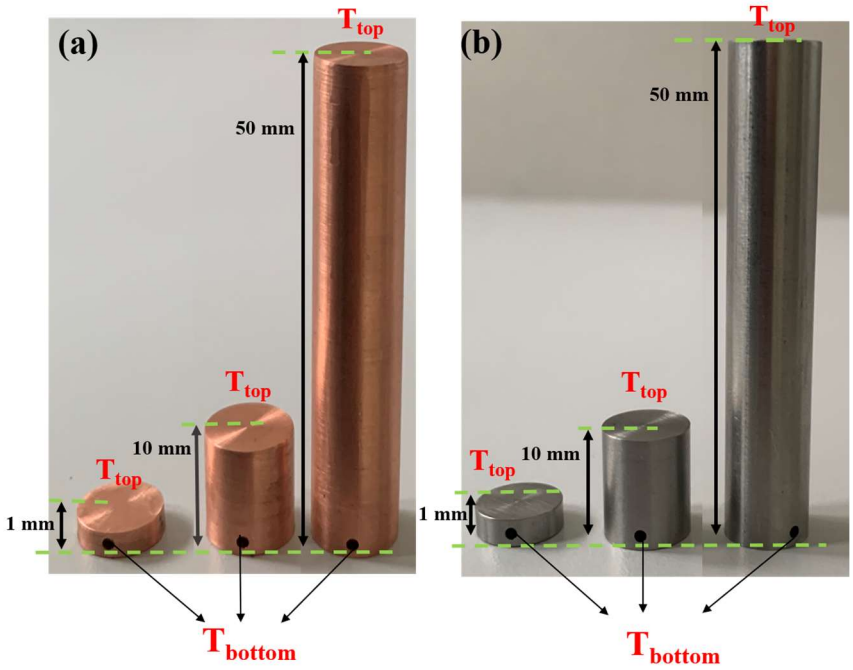

Fig. 2. 17 Cu and stainless steel cylinders with varying thicknesses

The variation of ΔT with time is shown in Fig. 3. 32. In the case of stainless steel samples, the ΔT at steady state increases significantly with increasing thickness. For instance, when its thickness is 50 mm, the ΔT value is 51 ℃, whereas it is much lower for thicknesses of 10 mm (19 ℃) or 1 mm (5 ℃). On the other hand, Cu samples exhibit relatively small differences in ΔT at steady state when varying its thickness. This shows that for materials with high thermal conductivity, thickness has less impact on heat transfer efficiency. In addition, the difference of ΔT at steady state between Cu and stainless steel cylinder is very small when their thickness is 1 mm, which is similar to the experimental results of the aforementioned pellets. As a result, when the sample thickness is small, the thermal conductivity has little impact on its heat transfer efficiency. Additional numerical modeling results are presented in Chapter 5 and compared with the experimental findings.

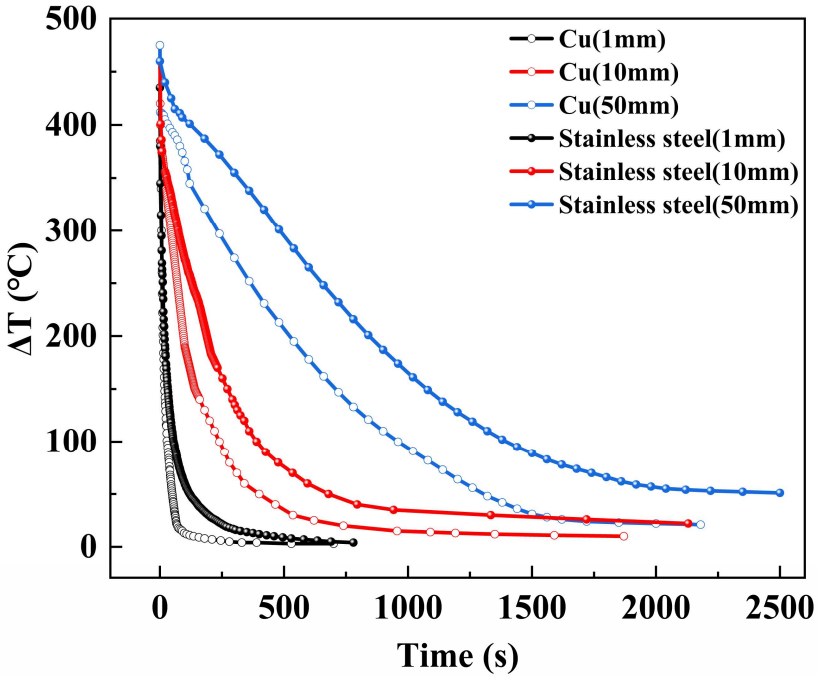

Fig. 3. 32 Variation of ΔT with time of Cu and stainless steel cylinders

3.7 Conclusions

The work conducted in this chapter holds significant importance for the advancement of materials utilized in solar thermal applications. The primary objective is to establish an advanced experimental method for material preparation. Consistently aligning with the aim of environmental sustainability, this work introduced a green, solvent-free material fabrication process.

In this chapter, highly thermal conductive AlN-based, α-SiC-based ceramic samples, Cu-based samples and stainless steel sample were prepared for the application in solar thermal process. Various properties were characterized and analyzed. Relative thermal tests were conducted to study the substrate's heat transfer performance. The following conclusions can be summarized:

(1) AlN powders were dry-mixed with CaO sintering additive by a high-shear mixer (Picomix) and then spark plasma sintered. The optimal CaO content was found to be 3 wt% and the optimal rotational speed of the Picomix was 5000 rpm. Under these conditions, the CaO additive could be distributed throughout the AlN powder matrix,

forming a homogenous liquid phase and improving the pellet's thermal conductivity. Reduced dimensions of the CaO (especially in the case of submicron- and nano-scale particles) led to coating of the AlN after mixing in the Picomix, which improved the flowability of the mixed powder. This in turn promoted the formation of a continuous liquid phase which encapsulated the AlN particles during sintering, leading to a higher thermal conductivity of the resultant AlN pellets (135.3 W/m·K). Additionally, it confirmed the feasibility of applying nano-scale additives to AlN. When compared with traditional ball milling and manual mixing, the high-shear mixer (Picomix) was found to be substantially superior, as it is a solvent-free process, requires a considerably shorter mixing time, consumes less energy, generates less powder-oxidation. This process is ideally suited for the environmental protection strategies and the application of clean energy (solar energy).

(2) The α-SiC powder and 9 wt% CaO-Al_2O_3 additive powder were dry-mixed by ball milling and then sintered. The fine CaO particle (submicron-scale) adhered onto the surface of larger α-SiC particles after dry-mixing process, forming a discontinuous coating. While Al_2O_3 particles were relatively evenly distributed with the mixed powder. When compared with pure α-SiC pellet, the porosity of the pellet with additives decreased from 30% to 22% and the thermal conductivity increased from 57 W/m·K to 114 W/m·K. The reduced number of pores in pellet was also observed through SEM images, indicating that the additives may facilitate better particle packing and result in a denser microstructure during sintering.

(3) The Cu particles were dry-coated with 2 wt% β-SiC in the Picomix and sintered. The fine β-SiC particles predominantly adhered to the surface of the spherical Cu particle, creating a discontinuous coating. After sintering, the β-SiC phase exhibited a uniform distribution and a good bonding with Cu matrix, resulting in a dense structure and decreased porosity of the pellet. Although the thermal conductivity of the β-SiC coated Cu pellet has decreased, its degree of oxidation has also been relatively reduced.

The dry coating process using Picomix may also be an effective method for treating particle surfaces to impart antioxidant properties.

(4) Heat transfer experiments showed that when the thickness of the thermal conductive substrate was small, the thermal conductivity might have little effect on its heat transfer efficiency.

Chapter 4 Experimental results and discussion of composite solar receiver materials

4.1 Introduction

As outlined in Chapter 3, various types of pellets applied as thermal conductive substrates were fabricated for solar thermal process. The AlN was mixed with CaO sintering additive powder by Picomix and then spark plasma sintered to obtain pellets with enhanced thermal conductivity and densification. The α-SiC and CaO-Al_2O_3 additive powder were dry-mixed by ball milling and then sintered to obtain α-SiC pellet with high thermal conductivity. For comparison, the most common material employed in solar receivers, stainless steel, was also fabricated into pellet. In this chapter, the composite solar receiver materials were prepared and presented (Fig. 4. 1).

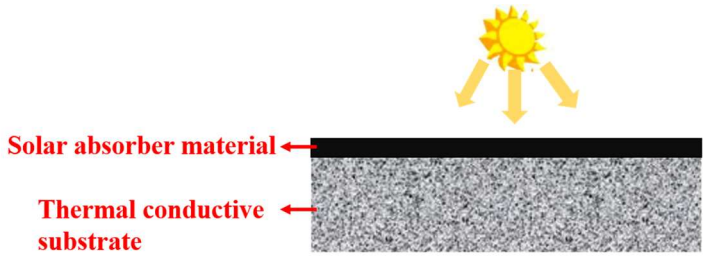

Fig. 4. 1 Schematic diagram of the composite solar receiver materials

AlN(pellet), AlN+3%$CaO^{0.04}$(5000rpm,5min,pellet) and SS(pellet) were used as substrates and coated with carbon black absorption layer (detailed in Section 2.2.3, Chapter 2). α-SiC+9%CaO-Al_2O_3(BM,pellet) and α-SiC(pellet) were applied directly due to its high absorptivity. The characterization results of the absorptivity of each sample and the morphology of the composite material are presented. Solar absorption and heat transfer experiments were performed on the composite pellets, with continuous recording of the material's temperature within the solar simulator installation. The incident irradiance and the heat flux absorbed by the sample surface were estimated.

The comparison primarily involved analyzing the temperature of each sample, as well as the temperature difference between the top and bottom surface of the pellet. Through the analysis of these findings, a comprehensive evaluation of the practical solar thermal application performance of various composite materials was undertaken. The effects of different factors including the absorptivity of the absorber, the thermal conductivity and the porosity of the substrate pellet, on the thermal properties of the prepared composite materials were explored.

4.2 Characterization of the absorption layer of the composite material

This section provides an overview of the characterization conducted on the solar absorption layer of composite solar receiver materials, encompassing analyses of their optical and morphological properties. Carbon black was added as the absorption layer for AlN(pellet), AlN+3%$CaO^{0.04}$(5000rpm,5min,pellet) and SS(pellet), with the composites labeled as AlN(pellet)-CB, AlN+3%$CaO^{0.04}$(5000rpm,5min,pellet)-CB and SS(pellet)-CB respectively (see Section 2.2.3, Chapter 2). Given the relatively high absorptivity of SiC according to the researches[237,238], the pellet fabricated using SiC as the matrix will be directly employed for solar thermal applications. This is intended to establish a direct comparison between the material put forth in this study (AlN and SiC ceramics) and those predominantly employed at present (stainless steel).

The solar absorption spectra in the UV−Visible and near IR range of carbon black, α-SiC, AlN and stainless steel powder at room temperature are shown in Fig. 4. 2. The spectra were acquired from measuring the spectral reflectivity using an UV-Visible spectroscopy and a Fourier-transform infrared spectroscopy from 0.2 μm to 2.5 μm (see Section 2.3.5, Chapter 2). So it is important to highlight that, due to the switching and coupling of the two instruments during the experiment, there may be some alterations of the spectra at around 0.8 μm. It is observed that carbon black and α-SiC both exhibit a high absorption rate with a relatively low dependence on wavelength. This

observation shows that the carbon black and α-SiC have effective absorbing properties across a wide range of the solar radiation spectrum, indicating the potential of the two materials as a robust absorber for solar thermal applications. While AlN and stainless steel exhibit relatively low absorptivity. Combining the spectral absorptivity data with the solar spectrum at the Earth's surface based on Eq. 1. 1 (Chapter 1), the total absorptivity (α) for each sample could be computed, shown in Tab. 4. 1.

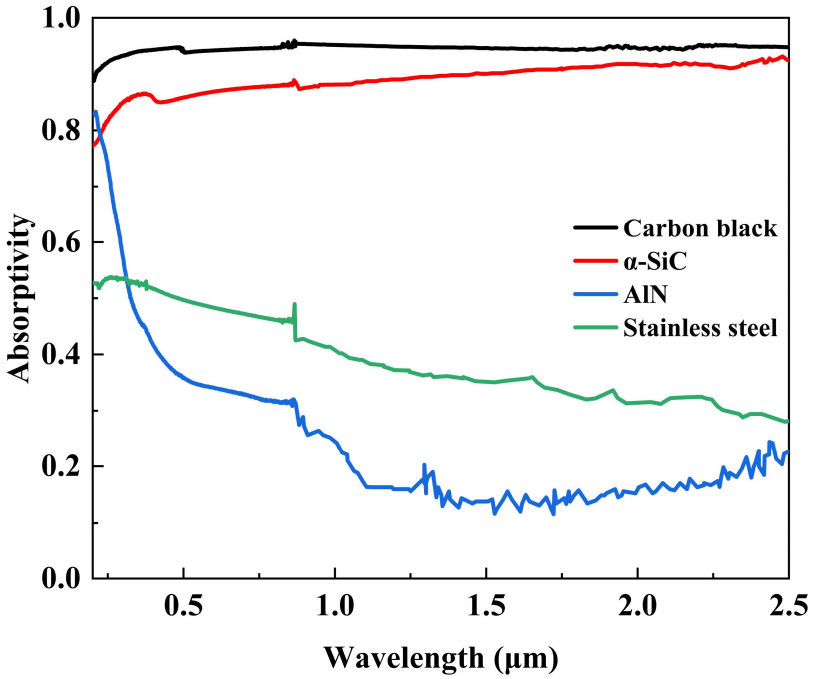

Fig. 4. 2 Absorption spectra of carbon black, α-SiC, AlN and stainless steel powder at room temperature

Tab. 4. 1 Total absorptivity of tested powders (room temperature)

Powder	α
Carbon black	0.94
α-SiC	0.89
AlN	0.34
Stainless steel	0.46

The SEM images of carbon black powder and layer on AlN+3%$CaO^{0.04}$(5000rpm,5min,pellet), as well as the backscattered electron image of the cross section of carbon black layer on the pellet are shown in Fig. 4. 3. The image

and size distribution (Fig. 4. 3 (b)) reveal that the carbon black powder is characterized by a nano-scale size (mean diameter d_p = 0.8 μm) and exists in the form of aggregates. Upon deposition, a relatively uniform and sufficient carbon layer was formed on the pellet's surface, with a thickness of approximately 95.7 μm. When observing the cross-section of both the layer and the pellet, distinct differentiation between the two compositions is evident. The interfaces between the distinct layers exhibit clear contrast, which is due to different electron interactions and scattering caused by different components. Within the carbon layer, subtle traces of AlN particles become discernible upon examination. This phenomenon suggests that during the deposition process, a portion of the surface AlN particles might undergo migration into the absorber layer. This migration could be attributed to the dynamic interactions occurring at the interface between the carbon layer and the AlN substrate. As a consequence of this migration, these particles become embedded within the carbon layer, resulting in the observed subtle presence. The carbon black layer deposited on the stainless steel pellet also exhibits similar morphological properties. Since SiC pellet would be directly applied for solar absorption, its morphology analysis was introduced in Section 3.3.2, Chapter 3.

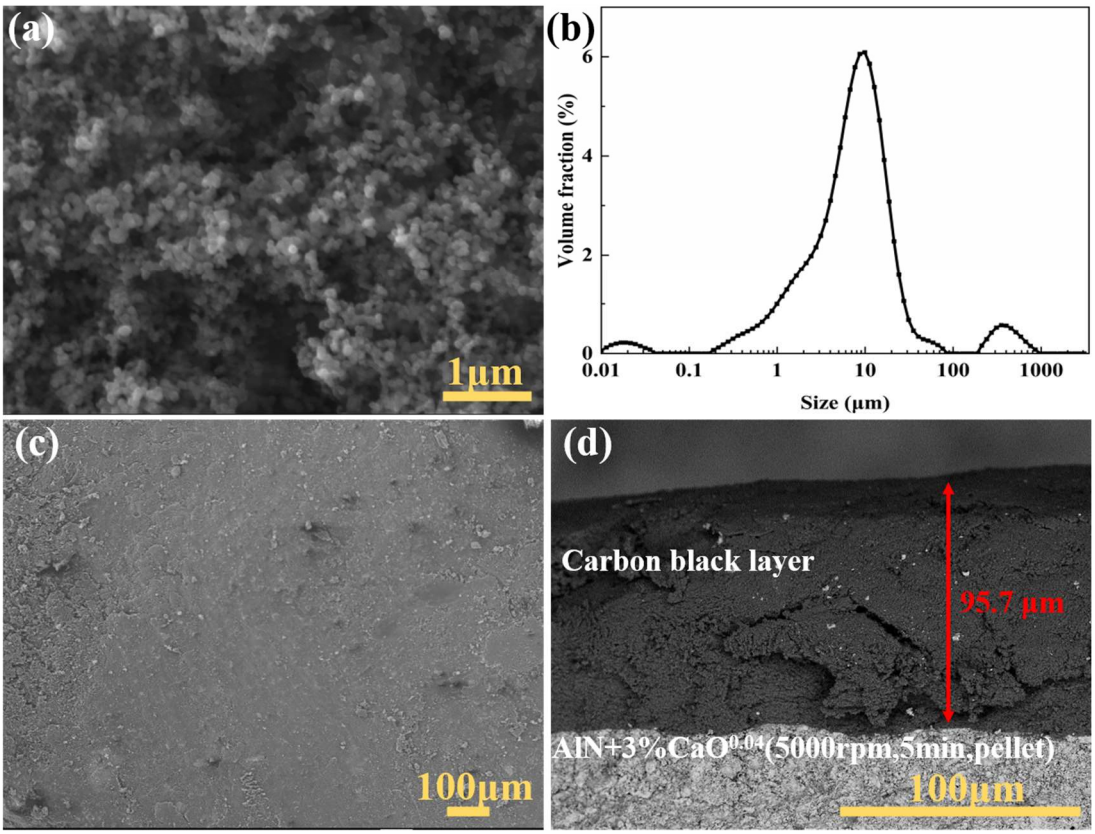

Fig. 4. 3 (a) SEM image and (b) size distribution of carbon black powder; (c) SEM image of carbon black layer; (c) Backscattered electron image of the cross section of AlN+3%$CaO^{0.04}$(5000rpm,5min,pellet)-CB

4.3 Solar simulator feasibility verification

When constructing the solar simulator, it involved multiple stages and the utilization of different reflectors. Consequently, it's crucial to compare the various reflectors to validate the efficiency of the configuration. This section provides an introduction to this content.

(1) Parabolic reflector installed

At the initial stage of constructing the solar simulator, a parabolic reflector was purchased and installed. To assess the efficacy of the solar simulator, an initial test was conducted to acquire the irradiance (G) resulting from the reflected radiation. The irradiance represents the amount of radiant energy incident on a surface per unit area. Given that the lamp power remained at 1000 W throughout the experiment, acquiring

irradiance value at this point was necessary. As described in Section 2.4.2.2 (Chapter 2), the illuminance was measured at a specific position, which was 8 cm vertically from the bottom plate (Fig. 4. 4 (a)). With the parabolic reflector installed, the result of irradiance was 235 W/m². Following this, a stainless steel block was utilized as the subject to assess the temperature achievable under this irradiance. The block was positioned at a height of 8 cm from the bottom plate (Fig. 4. 4 (a)). The temperature at the center of its top surface was measured using a type K thermocouple and labeled as T_{top}. Fig. 4. 4 (b) shows the variation of T_{top} over time, the tested stainless steel block can reach a peak temperature of 192 °C . The rays from the lamp are reflected as a parallel collimated beam by the parabolic reflector, resulting in a relatively low irradiance at the target. It is essential to apply a reflector that can concentrate the radiation more effectively, providing a higher irradiance.

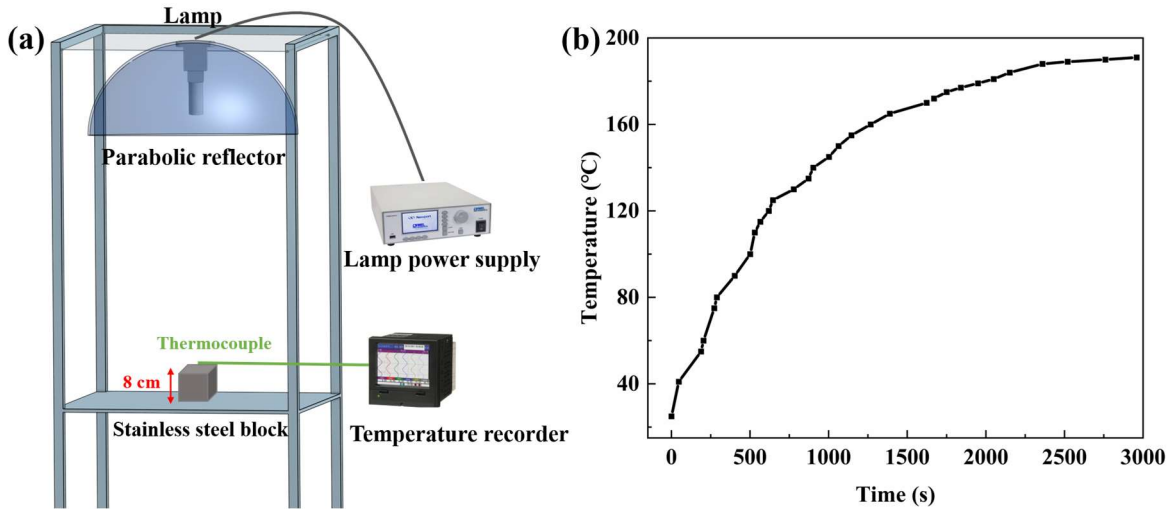

Fig. 4. 4 (a) Solar simulator with the parabolic reflector installed; (b) Variation of the T_{top} of the stainless steel block with time

(2) Ellipsoidal reflector installed

As described in Section 2.4.2.1 (Chapter 2), an ellipsoidal reflector was designed, assembled and installed then (Fig. 4. 5 (a)). The irradiance from the lamp using the ellipsoidal reflector configuration measured a 2654 W/m², which was much higher than that reflected by the parabolic reflector. Similarly, the thermal performance test was

conducted, with the α-SiC(pellet) as the tested sample here. Under identical experimental conditions, the temperature of the top surface of the pellet (T_{top}) was recorded (Fig. 4. 5 (b)). At this increased irradiance, the pellet's surface temperature reached approximately 330 °C. It's important to highlight that the mirror-polished plate of the reflectors was not subjected to anti-oxidation treatment, resulting in oxidation under high temperature. Consequently, the mirror surface underwent a transformation. This oxidation process led to a reduction in the internal reflectivity of the reflector, subsequently diminishing the achievable concentration of radiation. As such, the data displayed here was obtained subsequent to the oxidation of the mirror surface. The pellet's temperature was expected to be higher, without the issue of mirror oxidation and reduced reflectivity of the reflector. Further details on this matter are provided in Section 4.4.2, Chapter 4. In summary, the experimental results validate the improvement of the ellipsoidal reflector in concentrating radiation compared to the parabolic reflector applied in the solar simulator in this study.

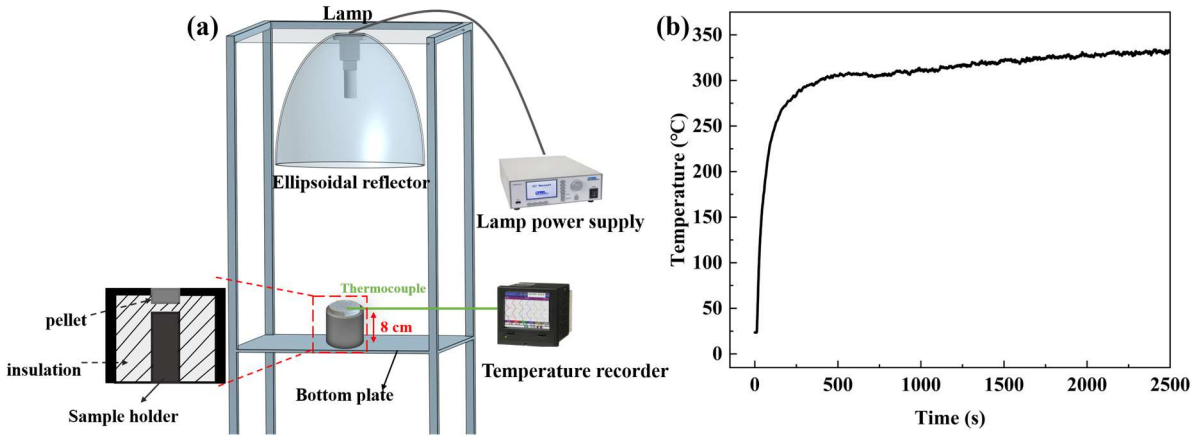

Fig. 4. 5 (a) Solar simulator with the ellipsoidal reflector installed; (b) Variation of the T_{top} of α-SiC(pellet) with time*

* This data was experimentally obtained after oxidation of the mirror-polished plate, which is detailed in Section 4.4, Chapter 4.

(3) Ellipsoidal and secondary reflector installed

In the previous experiment, it was observed that the radiation was not fully concentrated. Therefore, a secondary reflector with a truncated hexagonal pyramid structure was connected under the ellipsoidal reflector to focus the light from the lamp (Fig. 4. 6).

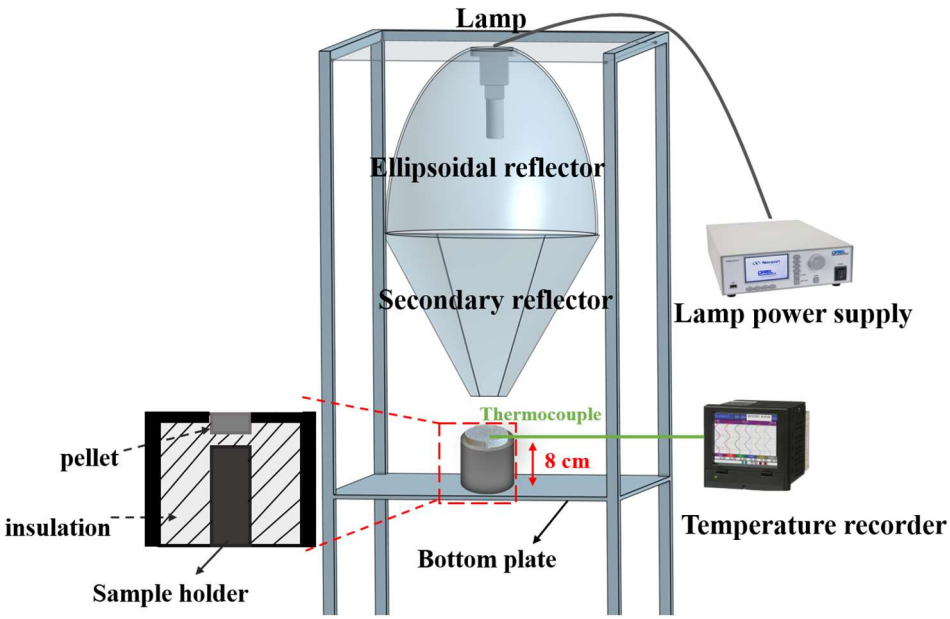

Fig. 4. 6 Solar simulator with the ellipsoidal and secondary reflector installed

The irradiance of the lamp, set at a power of 1000 W, was measured under this configuration. Due to the limit of the light meter's range (maximum 400 kLux), several illuminance values were systematically measured by varying the lamp power below 1000 W. The obtained data points were collected and plotted, as shown in Fig. 4. 7 (a). At the same time, the data were fitted, and an exponential fitting curve as shown in the figure was acquired. A similar fit was also found in the study by Sarasook et al.[239]. This aims to establish a correlation between lamp power and illuminance, and then estimate the corresponding irradiance when the lamp power is 1000 W.

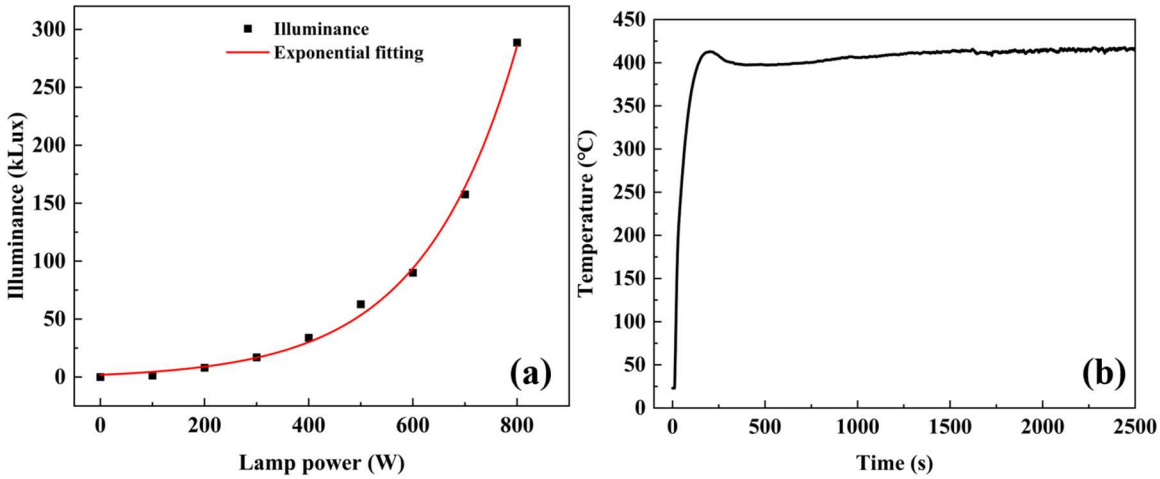

Fig. 4. 7 (a) Correlation between illuminance and lamp power; (b) Variation of the T_{top} of α-SiC(pellet) with time*

It can be determined that the relationship between illuminance and lamp power follows an exponential function. The fitting function is as follows:

$$y = A * exp(B * x) - C \qquad \text{Eq. 4. 1}$$

where A = 3.502 ± 0.809, B = 5.510E-3 ± 2.859E-4 , C = 1.612 ± 3.749. The quality of the curve fitting can be assessed by the coefficient of determination, often denoted as R^2. The closer the value of R^2 is to 1, the more accurate and better the fit. The R^2 of this fitting is 0.997, indicating the reliability of calculating illuminance with this function. As a result, when the lamp power is 1000 W, the relative illuminance is calculated to be 854.8 kLux. Then the illuminance can be converted to irradiance, of which the result is 6753 W/m^2. Likewise, the α-SiC(pellet) was used as the sample to conduct the thermal performance test. Under identical experimental conditions, the temperature of the top surface of the pellet (T_{top}) was recorded (Fig. 4. 7 (b)). Under this irradiance, the pellet's surface temperature reached approximately 420 °C, which was the highest among these three sets of configurations with different reflector combinations. It should be emphasized that the results presented here, including irradiance and temperature, were from tests conducted after the mirror-polished plate experienced oxidation. In

* This data was experimentally obtained after oxidation of the mirror-polished plate, which is detailed in Section 4.4, Chapter 4.

summary, the combination of the ellipsoidal and secondary reflector showed efficient radiation concentration capabilities, affirming the effectiveness in simulating solar radiation of this set-up. The solar simulator installation will be utilized in subsequent experiments focused on exploring the thermal performance of prepared composite solar receiver materials.

4.4 Solar energy absorption and heat transfer test of composite solar receiver material

In this section, an introduction along with a comparative analysis of the test results, related to solar energy absorption and thermal performance of several prepared composite solar receiver materials, are provided. The temperature difference among the materials was utilized as a reference point for assessment. The influences of several factors, such as the absorption layer's absorptivity, the substrate pellet's thermal conductivity and porosity, on the thermal performance of the composite material are clearly and intuitively discussed. The constructed solar simulator set-up served as a device for simulating solar radiation and conducting solar absorption and heat transfer experiments. A series of tests were carried out, of which the detailed experimental procedures and testing methodologies are elaborated in Section 2.4.2.3, Chapter 2.

4.4.1 Experimental status and limitations

When testing solar energy absorption and heat transfer capabilities of the prepared composite materials under simulated solar irradiation, the small, conductive material's surface is assumed to be at a uniform temperature. This gives an indication of a simple heat flux balance of the tested pellet[223], as shown in Fig. 4. 8. Given that all pellets are opaque, the incident irradiance is partly absorbed by the top surface (q_{absorb}) and partly reflected into the air ($q_{reflective}$) (Eq. 4. 2, Chapter 4). Among the absorbed heat flux (Eq. 4. 3, Chapter 4), the heat loss includes the convection ($q_{convective}$) on the surface and the radiation to a lower temperature surrounding that determined by its emissivity

($q_{radiative}$). The residual heat flux denoted as "$q_{conductive}$", is conducted through the pellet to its bottom surface. Negligible consideration is given to the insulated thin edge regions of the pellets as they are characterized by a thickness ranging from 1.5 mm to 2.5 mm.

$$G = q_{reflective} + q_{absorb} \quad \text{Eq. 4. 2}$$

$$q_{absorb} = q_{radiative} + q_{convective} + q_{conductive} \quad \text{Eq. 4. 3}$$

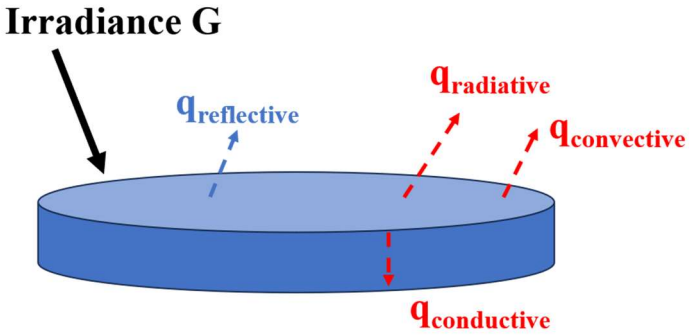

Fig. 4. 8 Simplified heat flux balance for the top surface of the material

According to the simplified heat flux balance, a straightforward calculation of the absorbed energy by each pellet by taking into account the absorptivity can be performed. It is noted that this only allows a basic comparative estimation. The actual absorption energy can depend on various properties and characteristics including surface condition, incident radiation angle and the specific spectrum. Consequently, under the assumption of an idealized situation, where the absorptivity (α) of the pellet's top surface remains consistent with the raw powder and does not vary with temperature, the approximate heat flux absorbed by each pellet was estimated and presented in Tab. 4. 2, according to the following equation[223,240]:

$$q_{absorb} = \alpha \cdot G \quad \text{Eq. 4. 4}$$

Tab. 4. 2 Estimated absorbed heat flux of the tested samples

Sample pellet	α	q_{absorb} (W/m^2)
AlN+3%$CaO^{0.04}$(5000rpm,5min,pellet)	0.34	2296
AlN+3%$CaO^{0.04}$(5000rpm,5min,pellet)-CB	0.94	6348
AlN(pellet)	0.34	2296
AlN(pellet)-CB	0.94	6348
α-SiC+9%CaO-Al_2O_3(BM,pellet)	0.89	6010
α-SiC(pellet)	0.89	6010
SS(pellet)	0.46	3106
SS(pellet)-CB	0.94	6348

Despite the simplification of the heat balance equation, determining the corresponding $q_{convective}$, $q_{conductive}$ and $q_{radiative}$ remains challenging due to the constraints of the existing data and measurable values. Owing to the initial preparation by spark plasma sintering and the necessity to measure the sample's thermal conductivity, the size of the sample is confined to a diameter of 10 mm and a thickness of a few millimeters. Consequently, computing and measuring for such a small pellet pose significant difficulties. A micro heat exchanger was designed and manufactured by us, with a diameter of 10 mm and 12 internal channels (Fig. 4. 9). However, the experimental analysis revealed that it demanded strict specifications for both flow rate and viscosity of the heat transfer fluid. Additionally, the measured fluid temperature at the inlet and outlet had a large error, making it unsuitable for the intended experiment. As a result, a complete heat balance equation for each tested sample can't be given here. It is imperative to conduct this work using larger-sized material and incorporate a surface-mounted heat exchanger to facilitate a more accurate calculation of the energy distribution. As a result, the scope of this work will be restricted to constructing a high-efficiency solar simulator, assessing the process's reliability and conducting a comparative analysis on the performance of different materials based on their chemical composition and structure.

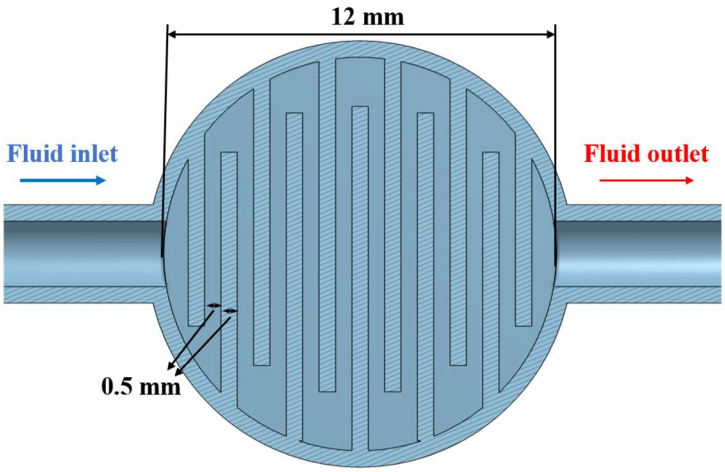

Fig. 4. 9 Schematic diagram of designed micro heat exchanger

4.4.2 Experimental set-up

The solar absorption and heat transfer experiments were conducted on the prepared composite pellets. The details were given in Section 2.4.2.3, Chapter 2. The temperature variations at different locations in the set-up were recorded over a specific period of time by the thermocouples (Fig. 4. 10). T1 to T4 measured the air temperature: T1 was inside the ellipsoidal reflector, close to the lamp; T2 was at the outer half height of the ellipsoidal reflector in the framework; T3 was inside the junction of the ellipsoidal reflector and the secondary reflector; T4 was next to the output aperture. T5 and T6 measured the temperature at the center of the pellet's top and bottom surface, respectively. A pyrometer (CTH-SF10, Micro-Epsilon, Germany) was also employed to detect the temperature of the top surface of the pellet, but the obtained results fluctuated greatly. This could be attributed to the small surface area of the target pellet, making precise measurement challenging.

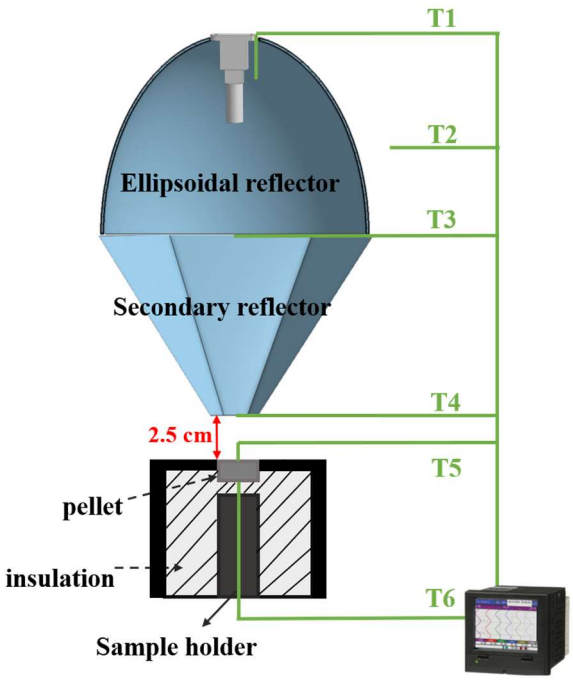

Fig. 4. 10 Sectional diagram of the reflector, pellet and temperature measurement positions

As mentioned above, the mirror-polished plate of the reflectors underwent an oxidation. Its specular reflectance was also affected and reduced. Fig. 4. 11 gives the temperature variation over time of α-SiC(pellet) during the thermal performance test before and after the mirror plate was oxidized, as well as the comparison of the plate surface. It's obvious that the temperature of the surrounding air near the lamp can reach approximately 780 °C during the initial experiment (Fig. 4. 11 (a-1)), providing a reasonable explanation for the transformation of the plate from mirror-surface to oxidized-surface under high temperature. After oxidation, the recorded decrease in T1, T3, T4 within the reflectors (for example, T1 decreases to 680 °C) proves the reduction in the reflectivity of the reflector surface and, consequently, the diminution of the radiative flux that the reflector could concentrate (Fig. 4. 11 (b-1)). This also provides the evidence for the temperature difference of the top surface of the pellet in the two experiments, which is, T5 at steady state decreases from 580 ℃ to 412 ℃ after the reflector surface's oxidation. Furthermore, T2 has been consistently maintained at a low

level without significant changes, which implies effective concentration of radiation within the reflector, minimizing any dissipation.

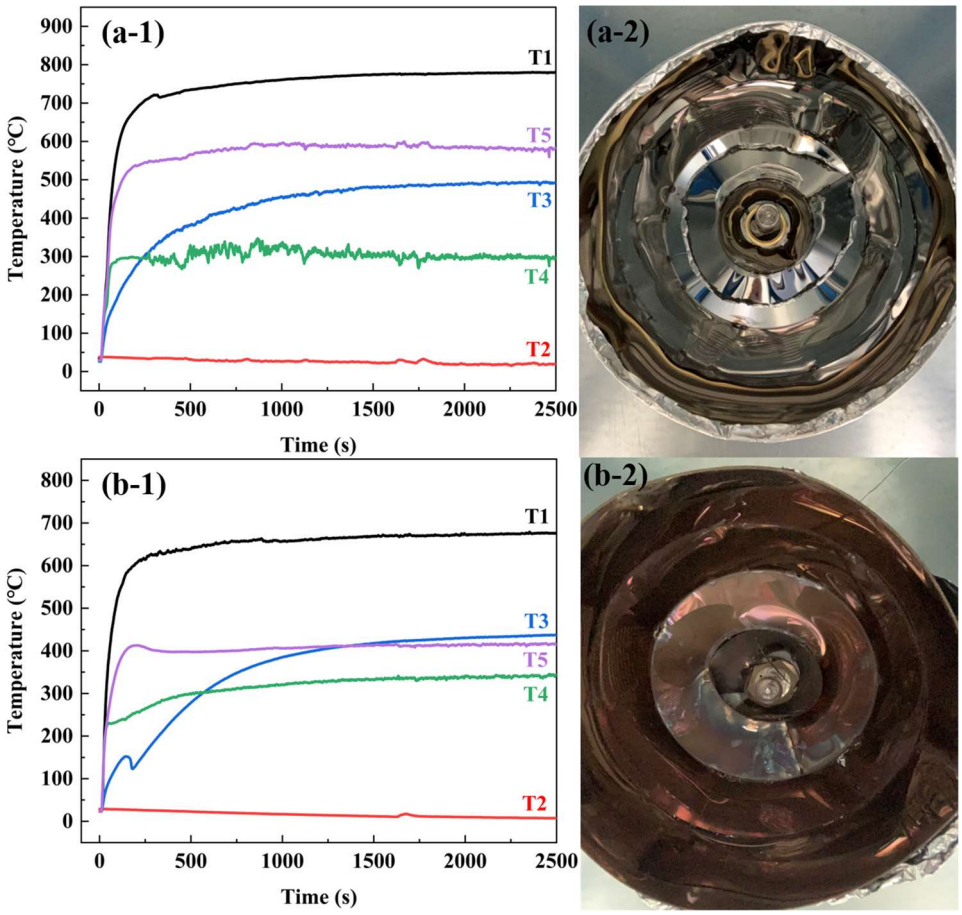

Fig. 4. 11 Temperature variation over time of α-SiC(pellet), (a-1) before the mirror plate was oxidized and (b-1) after the mirror plate was oxidized; Photo of the inner surface of the ellipsoidal reflector, (a-2) before the mirror plate was oxidized and (b-2) after the mirror plate was oxidized

4.4.3 Thermal performance of composite solar receiver material

Fig. 4. 12 shows the temperature variation over time for all the tested samples after the oxidation of the reflector surface. It's observed that the air temperature across various points within the set-up at steady state is stable in each experiment, suggesting that the irradiance (G) on the sample pellet remains relatively consistent. This forms a reliable foundation for comparing the surface temperatures between different samples directly.

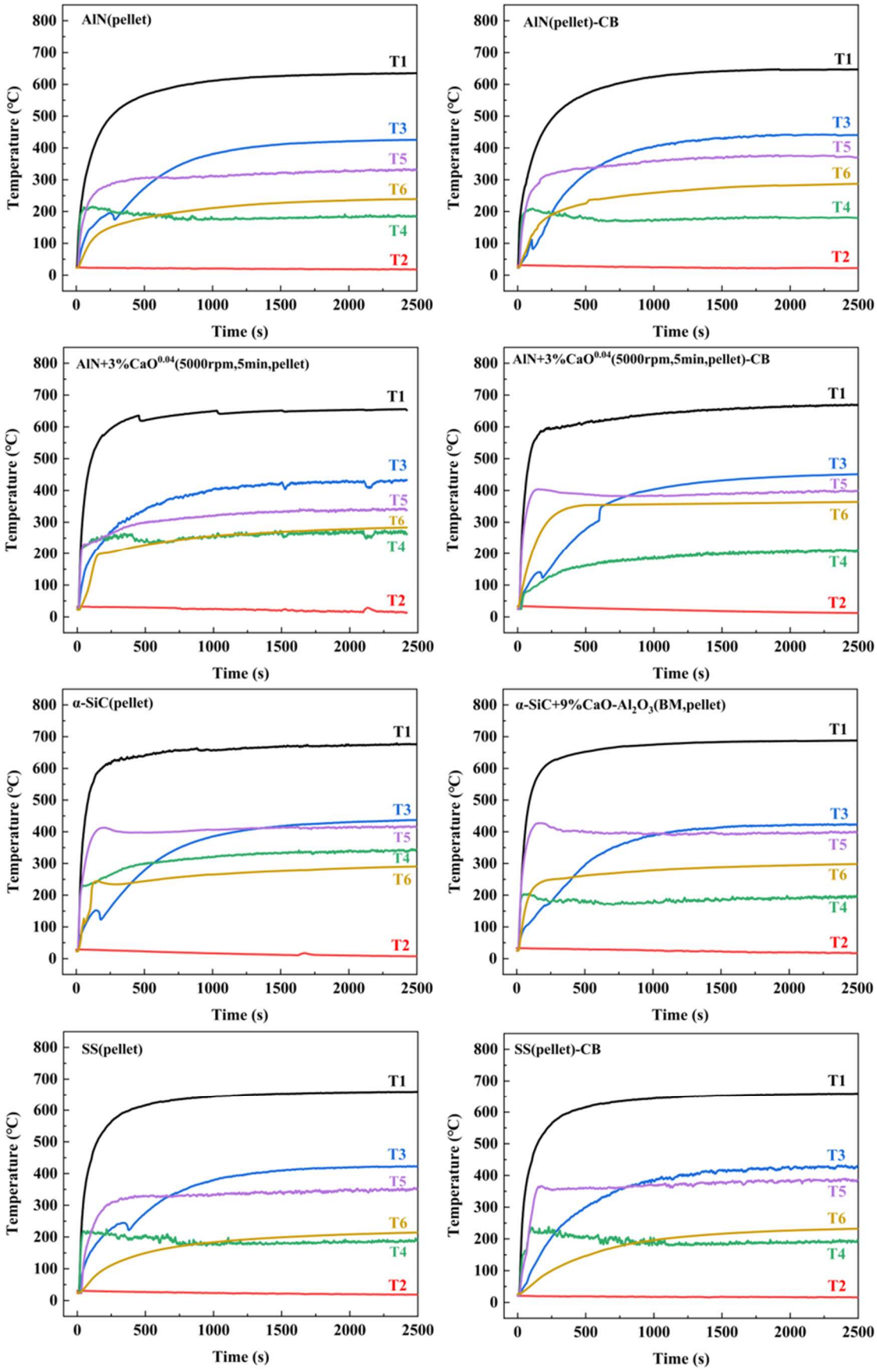

Fig. 4. 12 Temperature variation over time of the tested samples

Given the limitations in calculating thermal efficiency, the further analysis will primarily focus on comparing the temperature variations of the top and bottom surface (T5 and T6) of all samples with time (Fig. 4. 13). In the initial experiment, a substantial temperature differential between the top and bottom surface of the pellet (ΔT) at steady state was observed. This was most likely attributed to the inversion of the thermocouple leading to inadequate contact with the bottom surface, or even the potential measurement of the surrounding air temperature in close proximity to the bottom. To address this issue, a practical solution was implemented for every pellet to be tested. An indentation was carefully made at the center of the pellet's bottom surface using a sharp tool. This aimed to enhance the contact between the thermocouple and the sample surface, compensating for the limitations arising from the set-up design. As a result of implementing the aforementioned method, the temperature disparity at steady state between T5 and T6 was reduced.

As shown in Fig. 4. 13, T5 of all samples exhibits rapid ascent and typically stabilizes within approximately 250 s. There exist certain fluctuations in the T5 curve during the relatively constant plateau, which could be attributed to the impact of ventilation within the set-up. While the bottom surface shows a steady heating trend. It's obvious that the composite pellet with the carbon absorption layer (especially AlN+3%$CaO^{0.04}$(5000rpm,5min,pellet)-CB), as well as α-SiC-based pellet, exhibit notably higher steady-state temperatures than the pellet without the carbon layer. This can be attributed to the high α of carbon black and α-SiC. α-SiC(pellet) and α-SiC+9%CaO-Al_2O_3(BM,pellet) demonstrate similar temperature characteristics (Fig. 4. 13 (c)), yet ΔT is smaller for α-SiC+9%CaO-Al_2O_3(BM,pellet) as a result of its higher thermal conductivity (Tab. 4. 3).

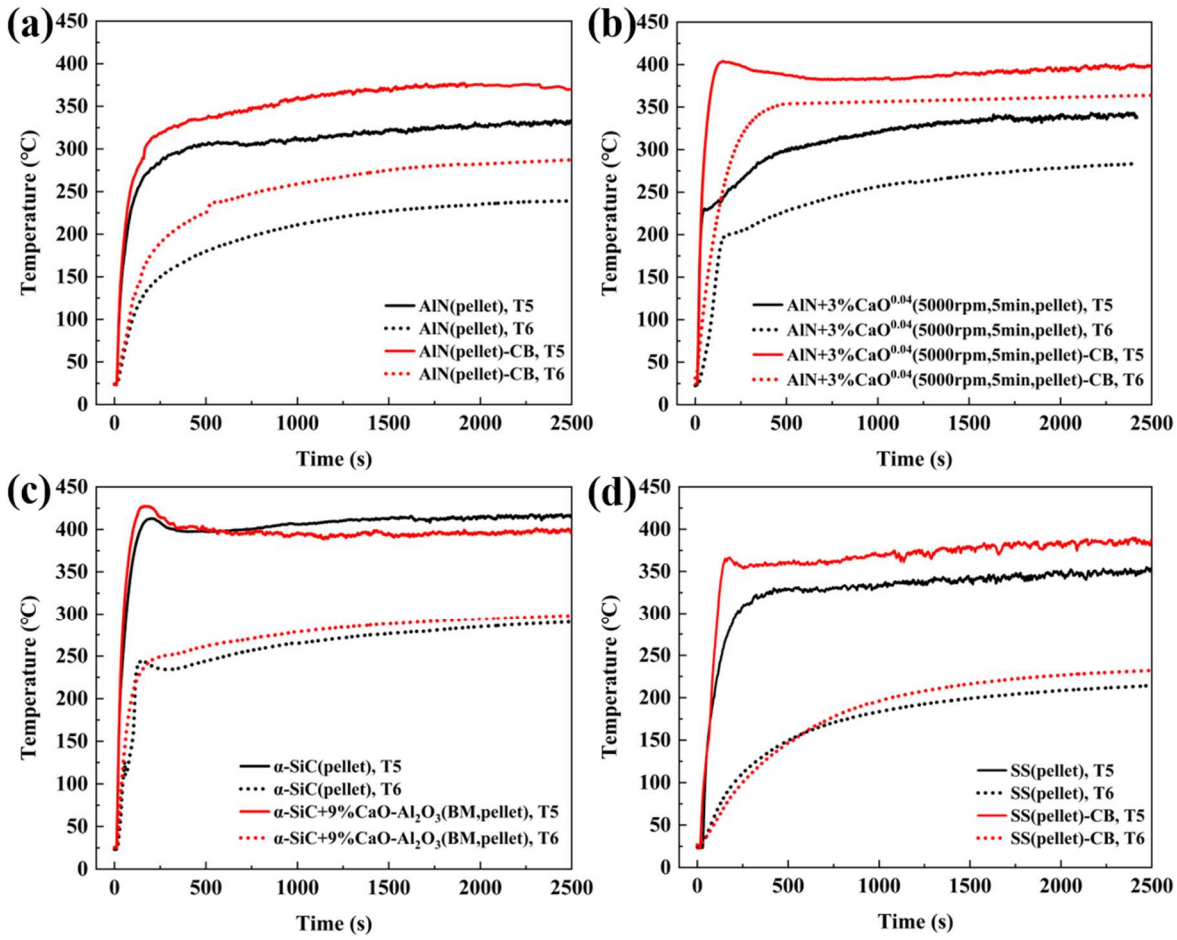

Fig. 4. 13 Temperature variation of top surface (T5) and bottom surface (T6) of pellets over time

Tab. 4. 3 lists the thermal conductivity (k), porosity (φ) and ΔT of tested samples. For composite materials, the influence of the carbon layer on the overall k and φ is not considered. Considering the extremely thin thickness, the ΔT of all pellets remains notably substantial, indicating a possible inaccuracy in the measurement by thermocouple. Given that all samples underwent testing under uniform conditions, meaningful comparisons among them were feasible. Since the thermal conductivity of AlN+3%$CaO^{0.04}$(5000rpm,5min,pellet) (135.3 W/m·K) is higher than that of AlN(pellet) (48.1 W/m·K), the steady-state ΔT associated with sample AlN+3%$CaO^{0.04}$(5-000rpm,5min,pellet) (52 ℃) is correspondingly smaller than that of AlN(pellet) (88 ℃). Similarly, the ΔT of AlN+3%$CaO^{0.04}$(5000rpm,5min,pellet)-CB (45 ℃) is also

comparatively smaller than that of AlN(pellet)-CB (86 ℃). Out of all the tested samples, SS(pellet) and SS(pellet)-CB display the largest ΔT values, measuring 126 ℃ and 147 ℃, respectively. This could be due to their lower thermal conductivity (14.4 W/m·K). Another possible reason is the weak adhesion and heat transmission between their relatively smoother surface and the carbon layer, which is further supported by the faster heating rate observed in sample SS(pellet) compared to SS(pellet)-CB. α-SiC-based pellets display unexpected ΔT values, which are inconsistent with their high thermal conductivity. This prompts consideration of the potential impact of high porosity on the pellet's thermal performance, which would be achieved through numerical modeling analysis.

Tab. 4. 3 Thermal conductivity, porosity and ΔT of tested samples

Sample	k (W/m·K)	φ	ΔT (℃)
AlN+3%$CaO^{0.04}$(5000rpm,5min,pellet)	135.3	15.8%	52
AlN+3%$CaO^{0.04}$(5000rpm,5min,pellet)-CB	135.3	15.8%	45
AlN(pellet)	48.1	20.9%	88
AlN(pellet)-CB	48.1	20.9%	92
α-SiC+9%CaO-Al_2O_3(BM,pellet)	114.4	22%	94
α-SiC(pellet)	57.1	30%	124
SS(pellet)	14.4	9.8%	126
SS(pellet)-CB	14.4	9.8%	147

In conclusion, while the exact thermal efficiency remains unquantified, the comparative analysis of temperatures highlights the potential of AlN+3%$CaO^{0.04}$(5000rpm,5min,pellet)-CB and α-SiC+9%CaO-Al_2O_3(BM,pellet) as promising solar receiver materials.

4.5 Conclusions

This chapter presents the characterization analyses, as well as the solar energy absorption and heat transfer experimental results of prepared composite solar receiver

materials. Firstly, carbon black with high solar absorptivity was successfully deposited as the absorption layer on the pellet. Secondly, despite mirror-polished plate oxidation issues, the designed solar simulator with the ellipsoidal and secondary reflector installed demonstrated effective radiation concentration. The irradiance on the sample was approximately 6753 W/m^2 when the lamp power was 1000 W. Lastly, through comparative analysis of temperature under identical experimental conditions, it was demonstrated that both AlN+3%$CaO^{0.04}$(5000rpm,5min,pellet)-CB and α-SiC+9%CaO-Al_2O_3(BM,pellet) exhibited notable solar energy absorption, as well as efficient heat transfer properties. This indicated their potential for utilization in solar thermal applications.

Chapter 5: Numerical modeling of thermal conduction in the porous material (pellet)

5.1 Introduction

The modelling work is divided into two parts. The study of thermal conduction through a porous medium is first presented in Chapter 5, then the coupling of radiative and conductive heat transfer is presented in Chapter 6. The geometry of a pellet with varying sizes and porosities was applied, which enabled the comparisons between the numerical calculations and experimental results using the pellet.

As discussed in Chapter 1, modeling of heat transfer in porous pellets has important implications for improving the fabrication and application of porous substrates in solar thermal applications. Finite element method (FEM) is ideally suited for heat transfer studies in porous bodies. To closely align the numerical model with the solid matrix structure employed in the experiment and facilitate a meaningful comparison, two models of conductive heat transfer in porous pellet are introduced and compared in this chapter. The first model (model I) assumes the geometry as a solid matrix with uniformly distributed average porosity. The second model (model II) considers the pellet as a composition of orderly stacked spherical particles with a consistent porosity. The effects of various factors are studied.

The COMSOL Multiphysics (provided by COMSOL Group, Sweden) was applied as the carrier of numerical modeling and calculation. It is a cross-platform commercial FEM program created for modeling and analysis to understand, predict and optimize equipment, processes and designs in engineering, industrial and scientific research fields. The models in the current study were conducted by the COMSOL Multiphysics version 5.4 (Academic license) using a laboratory computer (equipped with a processor of Intel(R) Core(TM) i5-10500 CPU@3.1 GHz, 3096 MHz, 6 cores and 12 logic processors).

5.2. Model I: thermal conduction in the continuous porous material (pellet)

In the thermal conduction experiments on the prepared pellets, the sample size was limited to a diameter of 10 mm and a thickness ranging from 1.5 mm to 2.5 mm. This was determined by the spark plasma sintering instrument used to fabricate the pellet. Therefore, the geometry of a pellet with varying sizes and porosities was applied in this model, and the effects of different geometric parameters, types of material and thermal conductivity on its thermal performance could be studied.

The component is a fundamental part of the model and contains a geometry with its associated physics interface, mesh, variables and other definitions that are local to that component. Following sections which contain the definitions and modifications in various aspects, were normally added under the component: definitions, geometry, materials, physics interface and meshes (Fig. 5. 1).

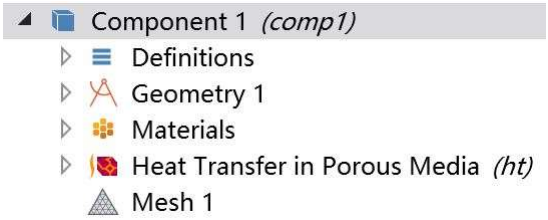

Fig. 5. 1 COMSOL window: different sections under the component

5.2.1 Model set-up

The three-dimensional (3D) space dimension was set for this model. The unit system was chosen as International System of Units (SI). In order to simulate the conductive heat transfer of porous pellet, a cylinder with a radius of 5 mm and a height of 10 mm was built as the geometry (Fig. 5. 2). In the follow-up study, the thickness (e) and radius (R) were varied to study their effects on pellet heat transfer efficiency.

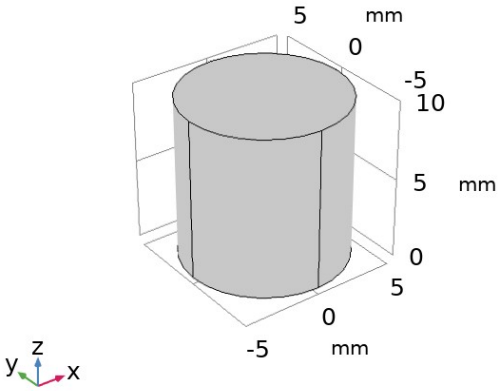

Fig. 5. 2 Geometry of model I (at e = 10 mm)

Under materials section, a blank material without defined properties was added and labeled as “Conductive Material”. A specific material was not selected here because the thermal conductivity (k) would be changed later to study its influence. The “air” from COMSOL materials database was added as well. Several properties were introduced for “Conductive Material” and air and the value ranges or equations are detailed in Tab. 5. 1, where T stands for existing absolute temperature (K) and p_A stands for atmospheric absolute pressure (Pa). Different values were assigned to thermal conductivity (isotropic), density, heat capacity at constant pressure of Conductive Material according to the actual value of AlN, to study their effects on porous pellet thermal conduction ability.

Tab. 5. 1 Conditions and parameters in model I set-up

Parameter	Specification
Thickness of geometry, e (mm)	1, 10, 50, 100, 500
Radius of geometry, R (mm)	5, 50, 100
Thermal conductivity of Conductive Material, $k_{Conductive}$ (W/m·K)	10, 50, 100, 200, 300
Density of Conductive Material, $\rho_{Conductive}$ (kg/m^3)	3000, 3200, 3500
Specific heat capacity of Conductive Material at constant pressure, $c_{p,Conductive}$ (J/(kg·K))	700, 1000, 1200
Thermal conductivity of air, k_{air} (W/m·K)	0.00227583562+1.15480022E-4*T-7.90252856E-8*T^2+4.11702505E-11*T^3-7.43864331E-15*T^4 (0.026 at 298.15 K)
Density of air, ρ_{air} (kg/m^3)	p_A*0.02897/8.314/T (1.18 at 298.15 K)
Specific heat capacity of air at constant pressure, $c_{p,air}$ (J/(kg·K))	1047.63657-0.372589265*T^1+9.45304214E-4*T^2-6.02409443E-7*T^3+1.2858961E-10*T^4 (1.01 at 298.15 K)
Porosity of porous pellet, φ_p	0.1, 0.3, 0.5, 0.7, 0.9
Effective thermal conductivity computing model, k_{eff} (W/m·K)	volume average, reciprocal average, power law
Heating temperature, T_h (K)	773.15
Refractive index of the medium material, n	2.05
Mesh element type	free tetrahedral, hexahedra, prism
Mesh element size	normal, finer, extremely fine

For the main modeling and simulation in this part, the "Heat transfer in porous media" and "Radiation in participating media" physics interfaces in heat transfer module were applied and coupled for the domain. In COMSOL, the "Heat transfer in porous media" physics studies the conduction of heat flow in a porous matrix. It could be used for a wide range of porous materials, such as porous structures in the pulp and paper industry and the simulation of heat transfer in soil and rocks. Under this interface, the domain was set as porous medium and all properties about the porous matrix were defined. Air that was added in materials was chosen as fluid. Its velocity was set as 0 m/s in the three directions of x, y, and z as the convection is negligible when the pore size is small. The immobile solid material was the Conductive Material. The volume fraction of solid material in porous matrix (θ_s) was set as 0.9, 0.7, 0.5, 0.3, 0.1 in turn, indicating the porosity of the porous matrix (φ_p) was 0.1, 0.3, 0.5, 0.7, 0.9 respectively according to Eq. 1. 16 (Chapter 1), which can study the effect of porosity (void fraction) on heat transfer. The model for computing of effective thermal conductivity (k_{eff}) was chosen as volume average model, reciprocal average model and power law model (see Section 1.5.2.2, Chapter 1) successively, and then validated by the relative experimental results. The initial value of temperature of the whole domain was set as 293.15 K. As shown in Fig. 5. 3, the peripheral boundary condition of the domain was set to thermal insulation meaning that there was no heat flux across the boundary. The remaining two boundaries parallel to the xy plane in the domain are named top boundary and bottom boundary, corresponding to the planes at z = 10 mm and z = 0 mm, respectively. For the bottom boundary, the condition was set to a fixed temperature at 773.15 K (500 °C) and is named as heating boundary. While for the top boundary, a convective heat flux was added and the type was set as external natural convection which means a fluid cools or heats the boundary surface by natural convection. The horizontal plate exposed to convection was chosen and the characteristic length was calculated and input according to the following equation[163]:

$$L = \frac{S_c}{P_c} \qquad \text{Eq. 5. 1}$$

where S_c is the surface area and P_c is the perimeter. The fluid was set as air and the absolute pressure (p_A) was 1 atm (101325 Pa) and external temperature (T_{ext}) was 293.15 K.

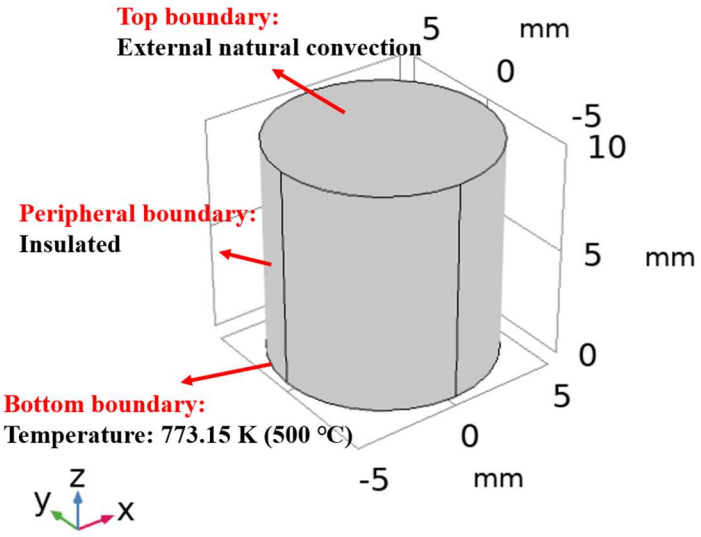

Fig. 5. 3 Boundary conditions in model I

The "Radiation in participating media" physics is used to model radiative heat transfer inside participating media. Under this interface, P1 approximation was chosen as the radiation discretization method. The absorption coefficient (κ) and the scattering coefficient (σ_s) were calculated according to Eq. 1. 27 and Eq. 1. 28 (Chapter 1), where d_{pore} of the porous matrix was set as 6.5 nm based on the data acquired from N_2 adsorption-desorption measurement of AlN(pellet) (Tab. 3. 3). And the refractive index of the medium material (n) was set as 2.05 according to the actual value of AlN.

All the relative parameters needed for heat conduction and thermodynamic calculation are listed in Tab. 5. 1.

Meshing process enables the discretization of the geometry into small units of simple shapes, referred to as mesh elements. Under mesh section, three different types of mesh element, free tetrahedral, hexahedra and prism were applied successively to verify the mesh effect (Fig. 5. 4). Different mesh sizes were set to limit the computation time and cost while achieving an acceptable discretization error at the same time because fine mesh would bring more accurate calculation results, but also greatly

increase the calculation time and computational resources (Fig. 5. 5). The specific mesh element sizes and their parameters are listed in Tab. 5. 2 as predefined in COMSOL Multiphysics.

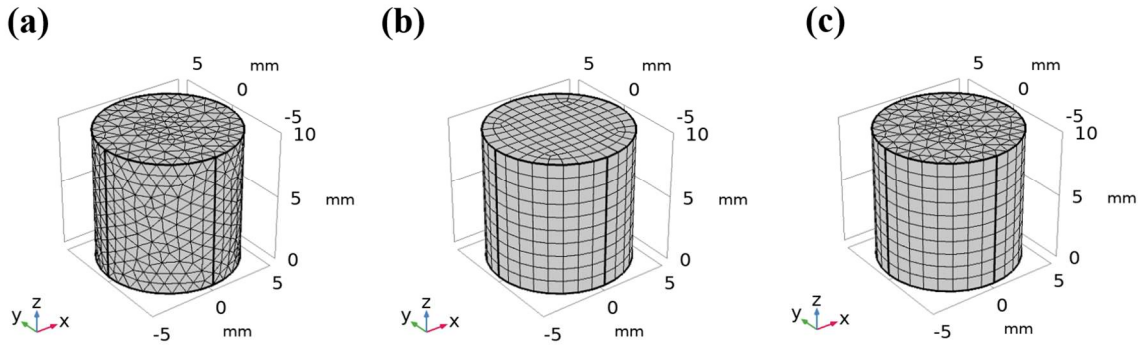

Fig. 5. 4 Three mesh types of the domain: (a) free tetrahedral, (b) hexahedra and (c) prism

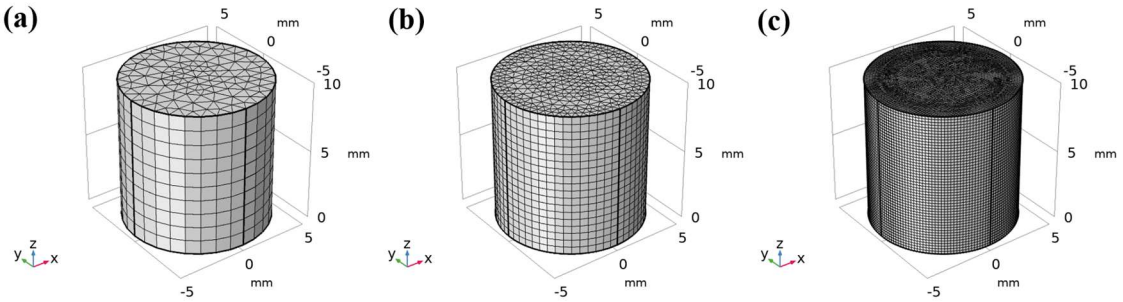

Fig. 5. 5 Mesh sizes of prism: (a) normal, (b) finer and (c) extremely fine

Tab. 5. 2 Mesh element size parameters in modeling

Element size	Maximum element size (mm)	Minimum element size (mm)	Maximum element growth	Curvature factor	Resolution for narrow regions
Normal	1	0.18	1.5	0.6	0.5
Finer	0.55	0.04	1.4	0.4	0.7
Extremely fine	0.2	0.002	1.3	0.2	1

5.2.2 Study and solver configuration

After all the settings about the model were completed, the solutions for the model were computed. Time dependent study step was added to compute the domain temperature changes over time. Except for deciding the study type, a solver configuration containing information about which physics interface and geometry to use, which variables to solve for, and which solvers to use for the type of study to perform was also indispensable. Here, a relative time-dependent solver was applied where temperature was the dependent variable. The time step was 0.001 s and the general time range was 250 s. For some specific cases, such as when the geometry thickness was 500 mm, the time range would be stretched. The relative tolerance was set as 10^{-6} and the factor of absolute tolerance was 0.1 (Fig. 5. 6 (a)). The maximum number of iterations was set to be 20 so that the results could converge fittingly during the computation. As a result, the temperature of the domain changes with time and finally stabilizes and the specific values can be computed through the study and solver. In results, the average temperature of top surface of the geometry was marked as T_{top}, and the average temperature of bottom surface of the geometry was marked as T_{bottom} (Fig. 5. 6 (b)). The temperature difference (ΔT) was also calculated according to Eq. 5. 2:

$$\Delta T = T_{bottom} - T_{top} \qquad \text{Eq. 5. 2}$$

Smaller ΔT denotes higher heat transfer efficiency in pellet and less heat loss.

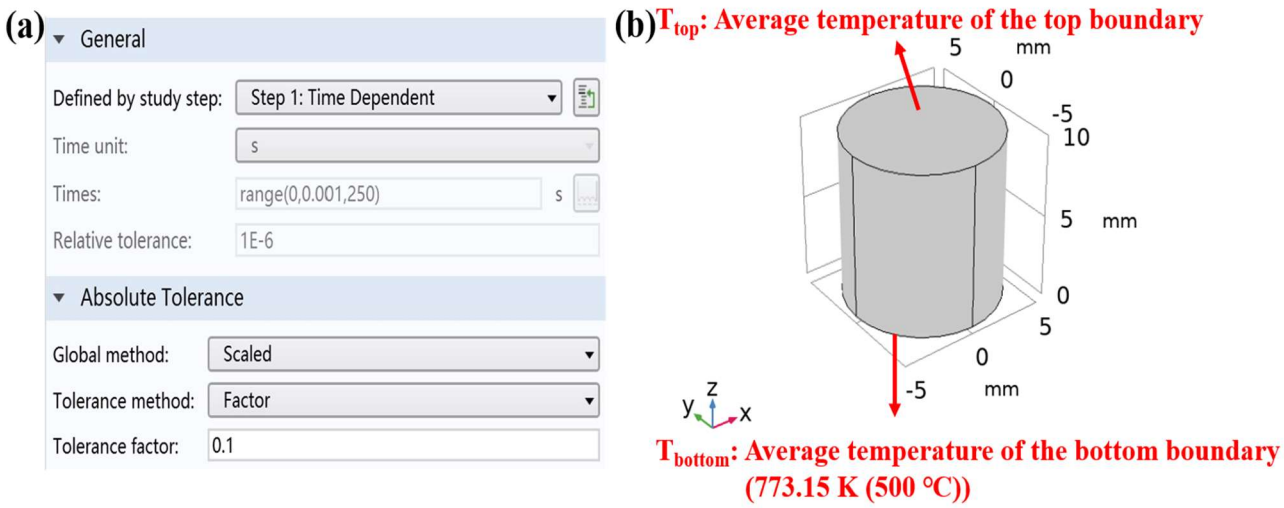

Fig. 5. 6 (a) COMSOL window: Time dependent solver setting; (b) Schematic diagram of T_{top} and T_{bottom}

5.2.3 Governing equations and boundary conditions

For the domain, the heat transfer equation for porous media is derived from the mixture rule on energies appearing in solid and fluid heat transfer equations. Here the Local Thermal Equilibrium hypothesis was taken into account that assumed equality of temperature in both fluid and solid phases as the flow was not considered. Q stands for the heat source. The introduction of relative equations has been displayed in Section 1.5.2, Chapter 1, which was summarized below in Tab. 5. 3.

Tab. 5. 3 Governing equations in model I

Physics	Governing equations
Heat transfer in porous media	$(\rho_m c_{p,m})_{eff}\frac{\partial T}{\partial t} + \rho_f c_{p,f}\boldsymbol{u}\cdot\nabla T + \nabla\cdot\boldsymbol{q} = Q + Q_r + Q_p$ $(\rho_m c_{p,m})_{eff} = \theta_s\rho_s c_{p,s} + \varphi_p\rho_f c_{p,f}$ $\boldsymbol{q} = -k_{eff}\nabla T$ $Q_p = \alpha_f T\left(\frac{\partial p_A}{\partial t} + u\cdot\nabla p_A\right)$ $\alpha_f = -\frac{1}{\rho_f}\frac{\partial \rho_f}{\partial T}$
Radiation in participating media	$Q_r = \kappa(G - 4\pi I_b(T))$ $\nabla\cdot(D_{p1}\nabla G) = Q_r$

$$D_{P1} = \frac{1}{3(\kappa + \sigma_s)}$$

$$I_b(T) = \frac{n^2 \sigma T^4}{\pi}$$

For the boundaries shown in Fig. 5. 7, first, the computation for the thermal insulation peripheral boundary can be explained by following equation:

$$-\boldsymbol{n} \cdot \boldsymbol{q} = 0 \qquad \text{Eq. 5. 3}$$

where **n** is the normal vector on the boundary toward exterior. Second, the prescribed temperature on the heating bottom boundary was set as T_0 and the following equation was applied:

$$T = T_0 \qquad \text{Eq. 5. 4}$$

Last, for the top boundary parallel to the xy plane in the domain with external convective heat flux, the mathematical equation is described as following:

$$-\boldsymbol{n} \cdot \boldsymbol{q} = q_0 \qquad \text{Eq. 5. 5}$$

where q_0 (W/m^2) is the inward heat flux on the external boundary which is a scalar quantity defined as a convective heat flux as follows:

$$q_0 = h(T_{ext} - T) \qquad \text{Eq. 5. 6}$$

where h (W/(m^2·K)) is the heat transfer coefficient, T_{ext} is the temperature of the external air far from the boundary. For the calculation of heat transfer coefficient, it depends on the fluid's material properties and the surface temperature. In addition, the geometrical configuration affects the coefficient. The functions for the calculation of h coefficient in external natural convection are as following[47]. When the top boundary was faced with external natural convection:

$$h = \begin{cases} \frac{k_{f,ext}}{L} 0.54 Ra_L^{\frac{1}{4}} & if\ T > T_{ext}\ and\ 10^4 \le Ra_L \le 10^7 \\ \frac{k_{f,ext}}{L} 0.15 Ra_L^{\frac{1}{3}} & if\ T > T_{ext}\ and\ 10^7 \le Ra_L \le 10^{11} \\ \frac{k_{f,ext}}{L} 0.27 Ra_L^{\frac{1}{4}} & if\ T \le T_{ext}\ and\ 10^5 \le Ra_L \le 10^{10} \end{cases} \qquad \text{Eq. 5. 7}$$

where $k_{f,ext}$ is the thermal conductivity of the external air flow applied in convection, Ra_L is the Rayleigh number defined by Eq. 5. 8:

$$Ra_L = \frac{g\alpha_{f,ext}\rho_{f,ext}^2 C_{p,ext}(T-T_{ext})L^3}{k_{f,ext}\mu} \quad \text{Eq. 5. 8}$$

where g (m/s^2) is the gravitational acceleration that equals to 9.81 m/s^2, $\alpha_{f,ext}$ is the thermal expansion coefficient of the external fluid, $\rho_{f,ext}$ is the density of the external fluid, $c_{p,ext}$ is the specific heat capacity of external fluid at constant pressure, L is the characteristic length defined by Eq. 5. 1, μ represents the external fluid's dynamic viscosity.

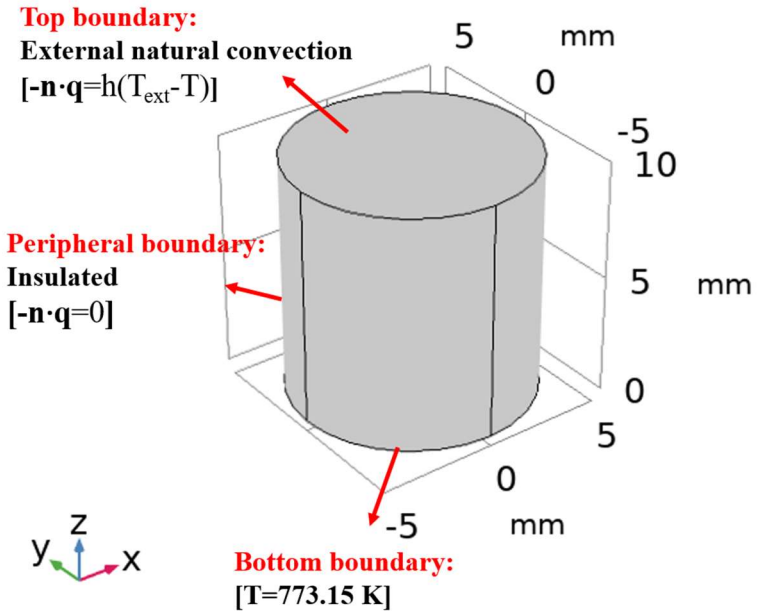

Fig. 5. 7 Boundary conditions and equations in model I

5.2.4 Results and discussion

5.2.4.1 Optimization of the model

In order to confirm the fit between the model and the experimental results and the accuracy of its calculation, it is necessary to optimize several parameters in the model to achieve relatively more accurate results while saving calculation time and computation power. In the experiment, the tested pellet was heated at 500 ℃ by a hot plate and the ΔT was calculated through measuring its surface temperature (displayed in Section 3.6, Chapter 3). The model was optimized by these heating experimental data, acquired from sample AlN(pellet) and AlN+3%CaO$^{0.04}$(5000rpm,5min,pellet). Relevant optimization parameters include the averaging model for the computation of

effective thermal conductivity, mesh type and mesh size. The remaining parameters of geometry and Conductive Material in the model were set to the same values as the two pellets in the experiment (Tab. 5. 4). The ΔT calculated from model and measured from experiments for these two pellets were compared.

Tab. 5. 4 Values of AlN-based pellets properties

Parameter	AlN(pellet)	AlN+3%$CaO^{0.04}$(5000rpm,5min,pellet)
Thickness (mm)	2.50	1.88
Radius (mm)	5	5
Thermal conductivity (W/m·K)	48.1	135.3
Density (kg/m^3)	3234.6	3384.8
Specific heat capacity at constant pressure (J/(kg·K))	497	996
Porosity	0.21	0.16

Firstly, the different k_{eff} calculating models were tested. The mesh type was fixed as free tetrahedral and the mesh element size was fixed as extremely fine to exclude the impacts of these two parameters. The ΔT results of three ways in modeling, volume average, reciprocal average and power law are shown in Fig. 5. 8, along with the ΔT from experiment. It can be seen that whether for sample AlN(pellet) or AlN+3%$CaO^{0.04}$(5000rpm, 5min, pellet), the ΔT calculated according to power law model is the closest to that from experiment. This is consistent with the research of Pichler that determined the power-law relationship between the effective thermal conductivity and the phase volume fraction of the solid material[241]. Moreover, according to the research from Bannach, when the internal structure of a porous matrix is a check pattern that is closer to the actual porous material structure, the approximation for its effective thermal conductivity is more accurate by the power law model[173]. As a result, the optimized effective thermal conductivity computation model was set as power law.

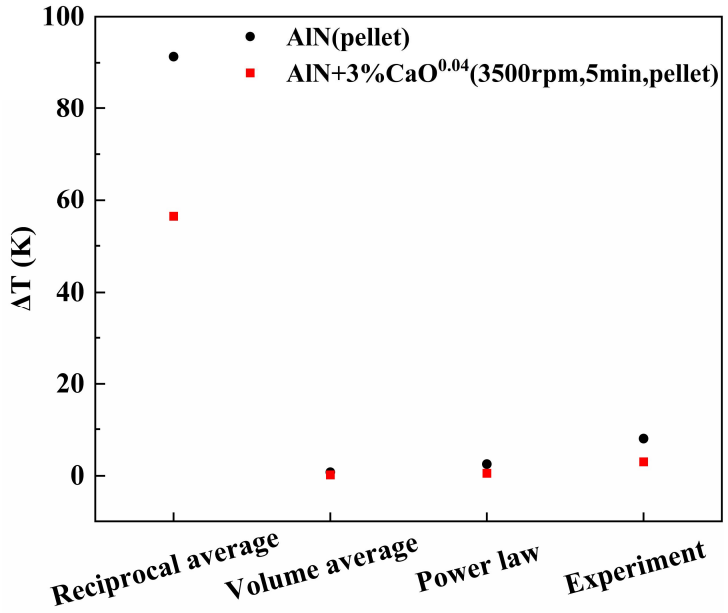

Fig. 5. 8 ΔT from modeling with different k_{eff} calculating models and experiment

Then the different mesh types, free tetrahedral, hexahedra and prism were applied and tested. The effective thermal conductivity computation model was set as power law and the mesh element size was chosen as extremely fine. The model results showed that when the mesh type was changed, there was no variation among ΔT of both AlN(pellet) and AlN+3%$CaO^{0.04}$(5000rpm, 5min, pellet) samples, which were 2.5 K and 0.56 K, respectively. This indicates that the final calculation results at steady state will not be affected by mesh type parameter. However, it will have an impact on the model degrees of freedom (DOF) (introduced in Section 1.5.3, Chapter 1) and the time required to solve the solution. For example, Tab. 5. 5 lists the DOF and solution time of the model of sample AlN(pellet) with different mesh types. The DOF of the model with free tetrahedral is nearly twice those of the other two mesh types, as is the solution time. While the values of hexahedra and prism are comparable. As a result, the mesh type was fixed as prism to reduce computing power.

Tab. 5. 5 DOF and solution time of the model of sample AlN(pellet) corresponding to different mesh types

Mesh type	DOF	Solution time (s)	ΔT (K)
Free tetrahedral	74112	13919	2.5
Hexahedra	39214	5385	2.5
Prism	39060	5136	2.5

At last, the different mesh element sizes, extremely fine, finer and normal were applied and tested. The effective thermal conductivity computation model was set as power law and the mesh type was prism. Like the mesh type, the variation of the mesh element size would not affect the final result of the steady state phase calculated by the model for two samples, but would result in different degree of freedom and solution time. Tab. 5. 6 shows DOF and solution time with different mesh element sizes and it can be seen that when the size increases to finer and normal scale, DOF of the model decreased and the solution time is shortened significantly. While the difference between finer and normal scale is small. Therefore, in the optimized model, a finer-scale mesh element size was chosen to reduce computing time and computing power while ensuring the refinement of the results of domain temperature changing over time.

Tab. 5. 6 DOF and solution time corresponding to different mesh element sizes

Mesh element size	DOF	Solution time (s)	ΔT (K)
Extremely fine	39060	5136	2.5
Finer	2076	462	2.5
Normal	484	232	2.5

After optimizing of the aforesaid parameters, model I was validated through all the samples (AlN(pellet), AlN+3%$CaO^{0.04}$(5000rpm,5min,pellet), α-SiC(pellet), α-SiC+9%CaO-Al_2O_3(BM,pellet), Cu(pellet), Cu+2%β-SiC(5000rpm,5min,pellet), SS(pellet)) from the heating experiment, which used the hot plate and is introduced in Section 3.6, Chapter 3. The model was parameterized with the actual measured values

of the samples, and then modeling results were computed. The average temperature of top surface (T_{top}, Fig. 5. 9) over time between experiment and model I results after optimizing were compared.

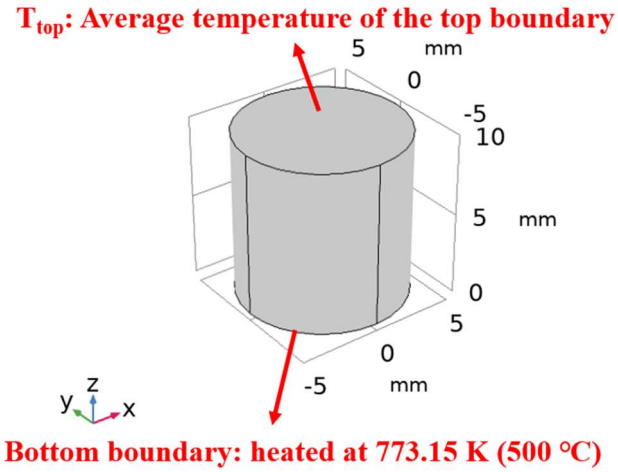

Fig. 5. 9 Schematic diagram of T_{top}

As shown in Fig. 5. 10, for all the porous pellet samples, their T_{top} closely match between the model results and experimental results when reaching a steady state. This indicates that the model effectively predicts the heating behavior of the pellets. The discrepancy in the time required to achieve the steady state between the experimental and simulated T_{top} is observed. This should be attributed to two reasons. The first is the hysteresis caused by the thermal contact between the pellet and hot plate in the experiment. Secondly, the model assumes that the solid matrix has homogeneous porosity distribution, which could result in faster heat propagation compared to the experimentally prepared pellet.

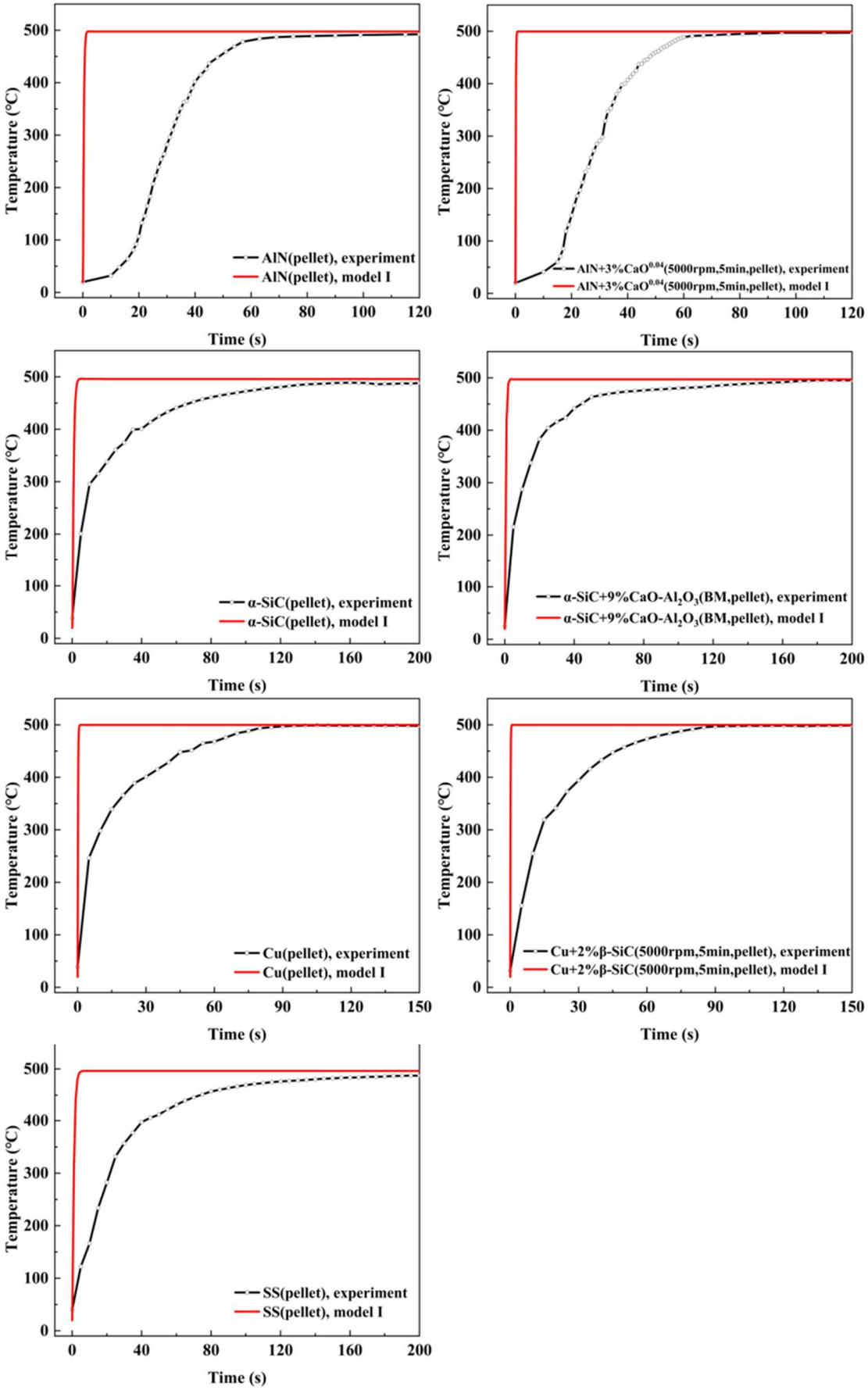

Fig. 5. 10 Comparison of T_{top} over time between experiment and model I results

In the following parts, the impact of geometric parameters, material's thermal conductivity and porosity of the pellet on the conductive heat transfer process will be analyzed.

5.2.4.2 Effect of thickness and radius of the porous pellet

As the model was optimized, the effects of different parameters on the model results were also investigated. The first part was the size parameter of the pellet. The effect of pellet thickness (e) was first studied. Here, e was set as 1, 10, 50, 100, 500 mm, respectively, while the rest of the parameters were fixed. The radius of the pellet was fixed at 5 mm, and the thermal conductivity was set as 100 W/m·K. The density of Conductive Material for the pellet was fixed at 3500 kg/m^3 and the specific heat capacity was 700 J/(kg·K). The porosity of the whole porous matrix was set as 0.1. ΔT and boundary convective heat flux ($q_{convection}$) of the top surface were calculated according to Eq. 5. 2 and Eq. 5. 6 (Chapter 5) after the computation of model. Fig. 5. 11 (a) shows the isothermal surfaces of geometry at heat transfer steady state (t = 50 s) when e is 10 mm. The isothermal surfaces are all on the xy plane and parallel to each other, indicating that the temperatures on this plane are equal. The curves of ΔT and $q_{convection}$ changing with thickness are shown in Fig. 5. 11 (b). It can be seen that there is an approximate proportional relationship between ΔT and thickness, and ΔT increases with the increase of thickness. While when the thickness increases to 500 mm, the slope of the curve decreases. $q_{convection}$ shows the opposite trend. As the thickness increases, the flux on the top surface gradually decreases, exhibiting an approximately proportional relationship with the thickness as well.

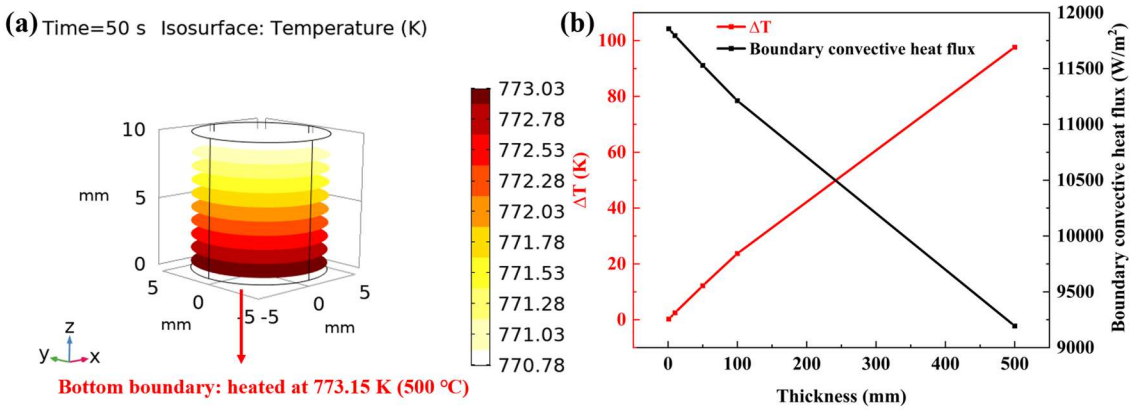

Fig. 5. 11 (a) Isothermal surfaces of geometry with e = 10 mm at steady state; (b) Effect of thickness of geometry on ΔT and $q_{convection}$ in model I

Fig. 5. 12 shows the temperature of the top boundary changing with time at different thicknesses. It's obvious that with the thickness increases, the rate at which the temperature rises is slower and the time it takes to reach a steady state is longer. Fig. 5. 13 (a) shows an example of the temperature distribution on the cut plane and, where the cut plane is the xz plane when the y coordinate is 0 mm. The temperature on the cut surface decreases evenly with the increase of the z coordinate at different e (Fig. 5. 13 (b)). These impacts of thickness are in consistent with those on ΔT and $q_{convection}$.

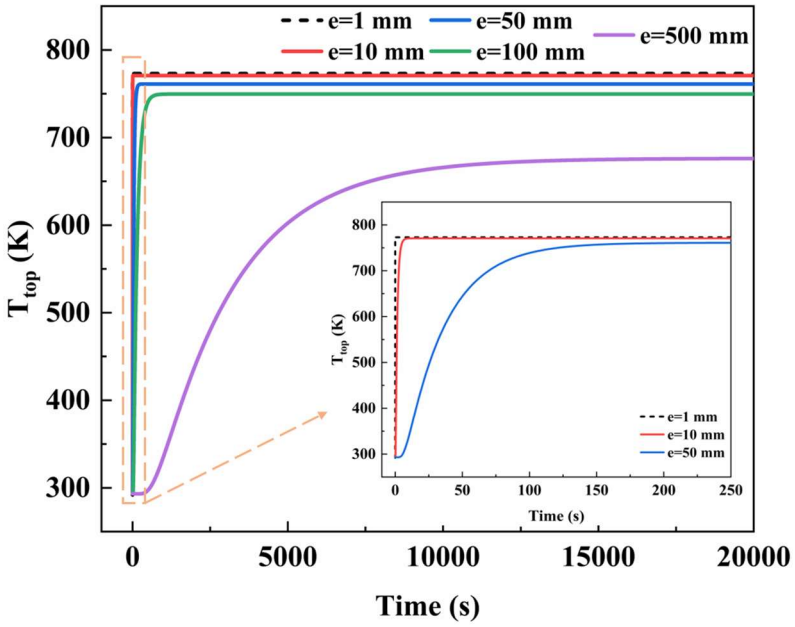

Fig. 5. 12 Effect of thickness of geometry on the variation of T_{top} with time in model I

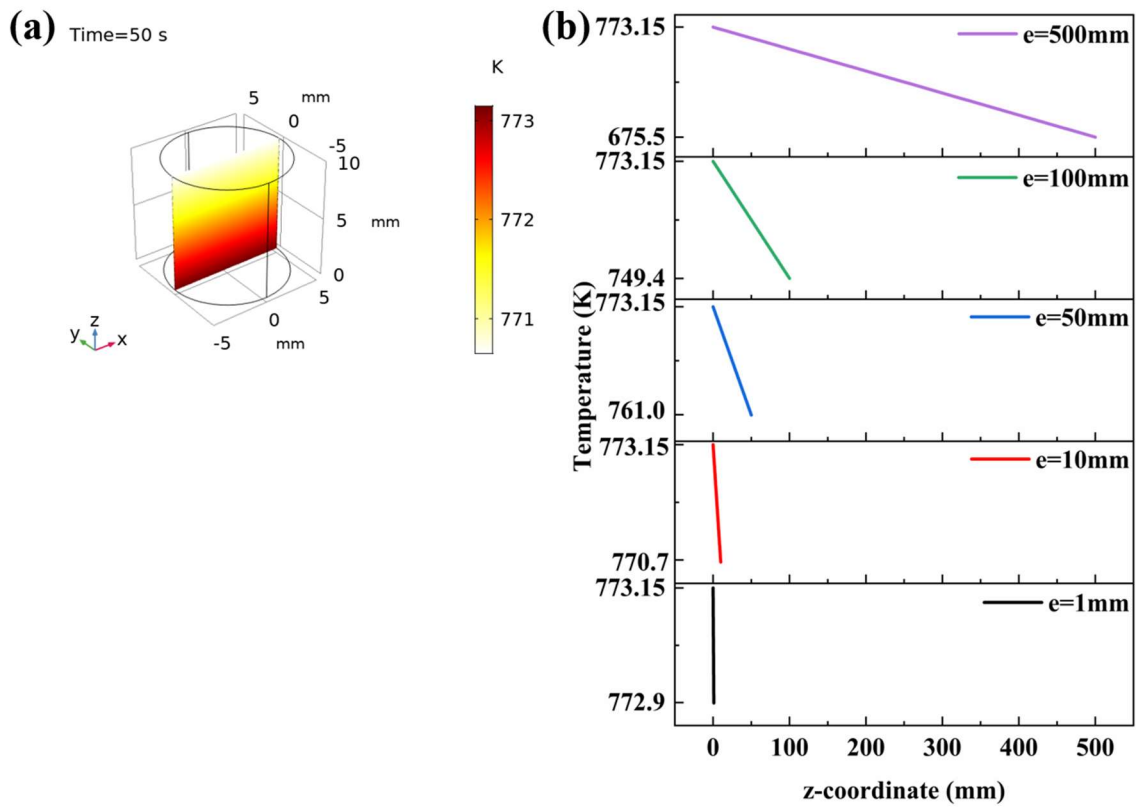

Fig. 5. 13 (a) Temperature distribution on the cut plane; (b) Effect of thickness of geometry on the variation of temperature on the cut plane with z coordinate at steady state in model I

Then the effect of radius of the pellet (R) was studied. The pellet thickness, e, was kept as 10 mm and other parameters remained unchanged. R set as 5, 50, 100 mm respectively. Correspondingly, the characteristic length also varied in the convective setting, which were 2.5, 25, 50 mm. It can be seen that after the geometric radius was changed, the heat transfer rate and efficiency of the model remained the same (Fig. 5. 14), which is consistent with the results of the isothermal surface. Therefore, R was fixed to 5 mm in the latter models.

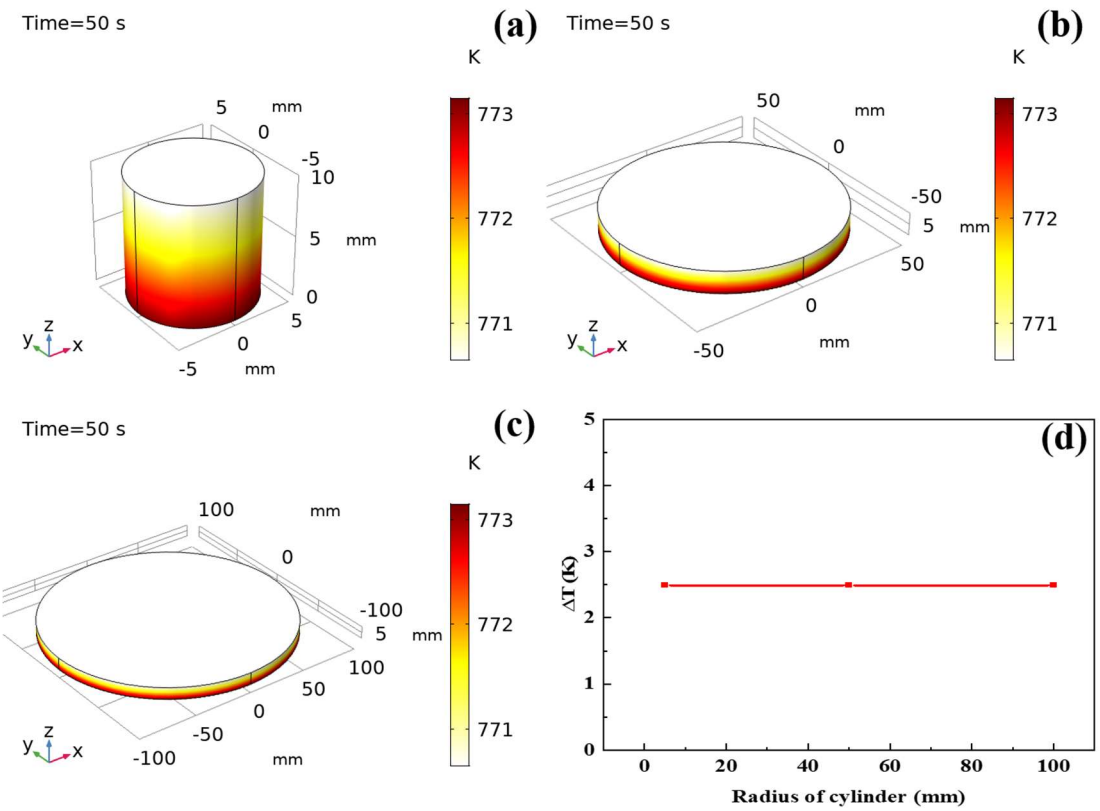

Fig. 5. 14 Steady-state temperature distribution of geometries with different radii: (a) 5 mm; (b) 50 mm; (c) 5 mm; (d) ΔT at steady state with different radii

5.2.4.3 Effect of material property

The effects of material property including thermal conductivity, specific heat capacity and density on pellet heat transfer were studied successively. Firstly, the $k_{Conductive}$ was set as 10, 50, 100, 200, 300 W/m·K, respectively, while the rest of the parameters were fixed. The radius of geometry was fixed at 5 mm and thickness was 10 mm. The density of Conductive Material was fixed at 3500 kg/m^3 and specific heat capacity was 700 J/(kg·K). The porosity of the whole porous matrix was set as 0.1. Fig. 5. 15 shows the variation of ΔT and boundary convective heat flux with $k_{Conductive}$. Compared to the other $k_{Conductive}$ values, there is a large decrease of 14.4 K in ΔT when $k_{Conductive}$ increases from 10 W/m·K to 50 W/m·K. While when $k_{Conductive}$ is greater than 100 W/m·K, the curve is almost flattened and the ΔT difference between each point is extremely small. $q_{convection}$ quickly increases by 396 W/m^2 when $k_{Conductive}$ is from

10 W/m·K to 50 W/m·K, and changes little when $k_{Conductive}$ is larger than 100 W/m·K. This indicates that under the current conditions, the heat transfer efficiency of the porous pellet would not be greatly increased when $k_{Conductive}$ is greater than 100 W/m·K.

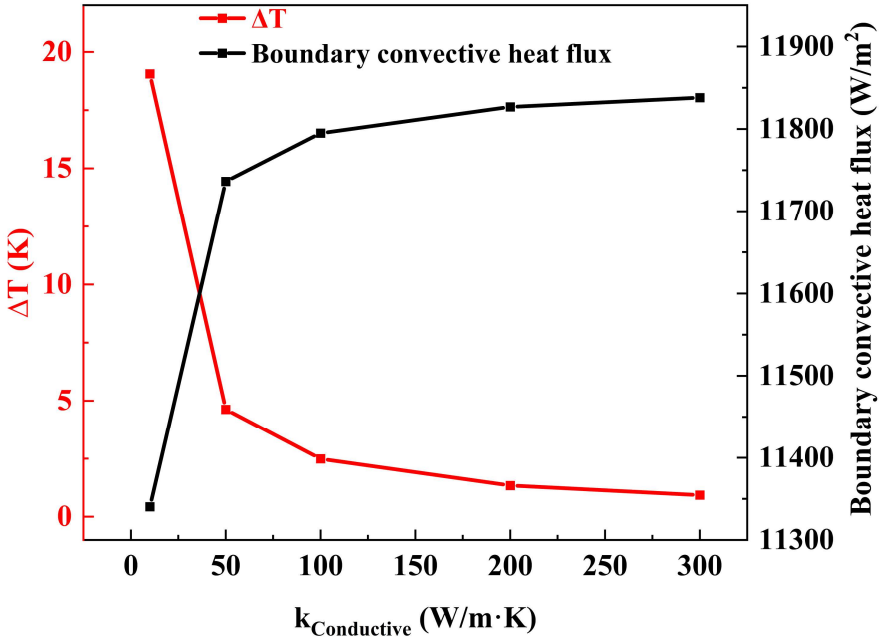

Fig. 5. 15 Effect of $k_{Conductive}$ on ΔT and $q_{convection}$ in model I

Fig. 5. 16 (a) shows the effects of $k_{Conductive}$ on the variation of T_{top} with time and temperature gradient distribution in z direction. The pattern of geometry heating is consistent. As $k_{Conductive}$ increases, the speed at which the pellets achieve thermal equilibrium increases. The difference of heating rate is extremely small when $k_{Conductive}$ is greater than 50 W/m·K, as well as the difference between their T_{top}. In addition, the temperature on the cut plane which is the xz plane when the y coordinate is 0 mm as shown in Fig. 5. 13 (a), decreases evenly with the increase of the z coordinate. The temperature gradient is approximate when $k_{Conductive}$ is larger than 50 W/m·K. These impacts of $k_{Conductive}$ are in consistent with those on ΔT and $q_{convection}$.

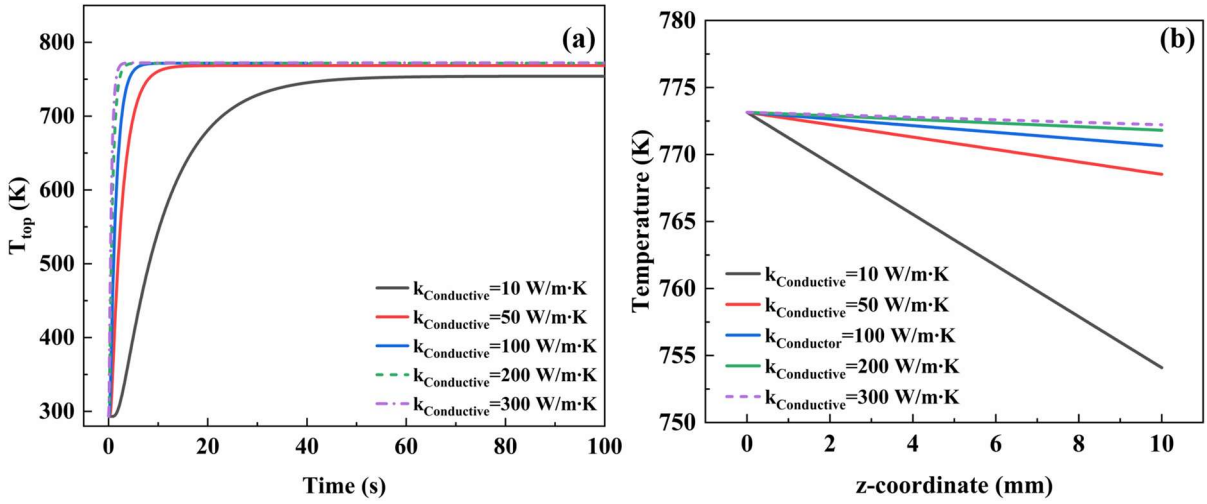

Fig. 5. 16 (a) Effect of $k_{Conductive}$ on the variation of T_{top} with time in model I; (b) Effect of $k_{Conductive}$ on the variation of temperature on the cut plane with z coordinate at steady state in model I

Then the effect of $c_{p,Conductive}$ was investigated. The $k_{Conductive}$ was kept as 100 W/m·K and other parameters remained unchanged. $c_{p,Conductive}$ was set as 700, 1000, 1200 J/(kg·K). On the other hand, the effect of $\rho_{Conductive}$ was investigated which was set as 3000, 3200, 3500 kg/m^3, respectively. The $k_{Conductive}$ and $c_{p,Conductive}$ were still kept as 100 W/m·K and 700 J/(kg·K), and other parameters remained unchanged. The results of T_{top} of geometry steady state are displayed in Fig. 5. 17. It is distinct that the stable top surface temperature does not change with the variation of either $c_{p,Conductive}$ or $\rho_{Conductive}$, which implies that the heat transfer efficiency of the geometry does not change under the current conditions. Therefore, the influence of these two parameters on the model could be excluded. And in the next parts, $c_{p,Conductive}$ would be fixed to 700 J/(kg·K) and $\rho_{Conductive}$ would be fixed to 3500 kg/m^3.

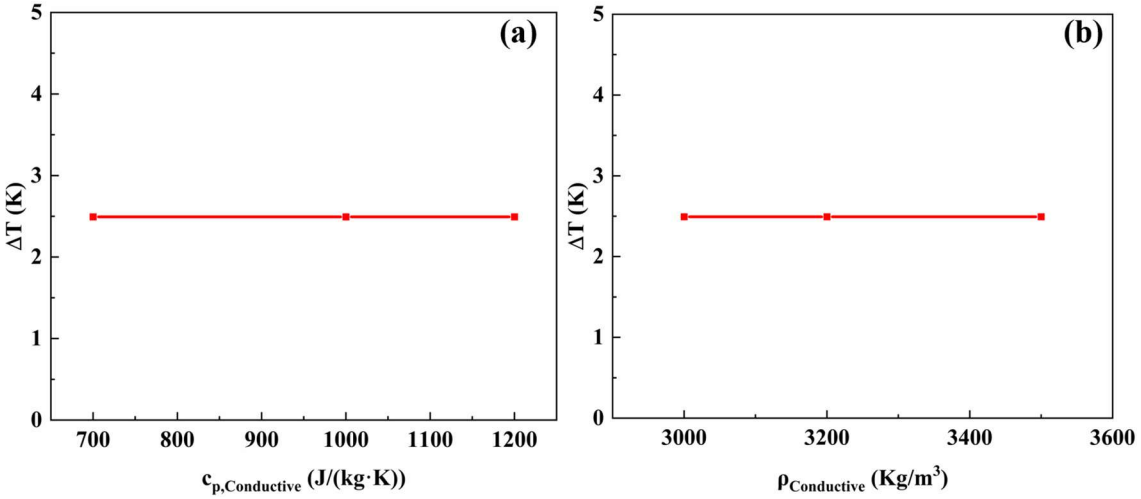

Fig. 5. 17 (a) ΔT at steady state with different specific heat capacity of Conductive Material; (b) ΔT at steady state with different density of Conductive Material

5.2.4.4 Effect of porosity of the pellet

Porosity is a critical parameter in porous pellet heat transfer because the presence of air with low thermal conductivity in the pores can considerably impede the effective transfer of heat flow. As a result, the effect of porosity of the pellet on heat transfer was analyzed in this section. Here, the volume fraction of solid material in porous matrix was set as 0.9, 0.7, 0.5, 0.3, 0.1 in sequence, representing the porosity of the porous matrix (φ_p) was 0.1, 0.3, 0.5, 0.7, 0.9, respectively. The thickness of geometry was fixed at 10 mm. The thermal conductivity of Conductive Material was set as 100 W/m·K. The variation of ΔT and boundary convective heat flux with φ_p are shown in Fig. 5. 18. When φ_p increases from 0.1 to 0.5, ΔT does not alter noticeably. In the interval from 0.5 to 0.7, ΔT progressively increases and the rate of growth accelerates (from 45.3 K to 153.2 K). When φ_p increases from 0.7 to 0.9, the slope of this line increases significantly, indicating that ΔT has grown significantly in comparison to other φ_p values (from 153.2 K to 323.2 K). As demonstrated above, $q_{convection}$ still shows the opposite trend, with a significant decrease after $\varphi_p > 0.5$. This shows that under the current conditions, when φ_p is greater than 0.5, it has a more significant impact on the heat transfer of the pellet, reducing the heat transfer efficiency.

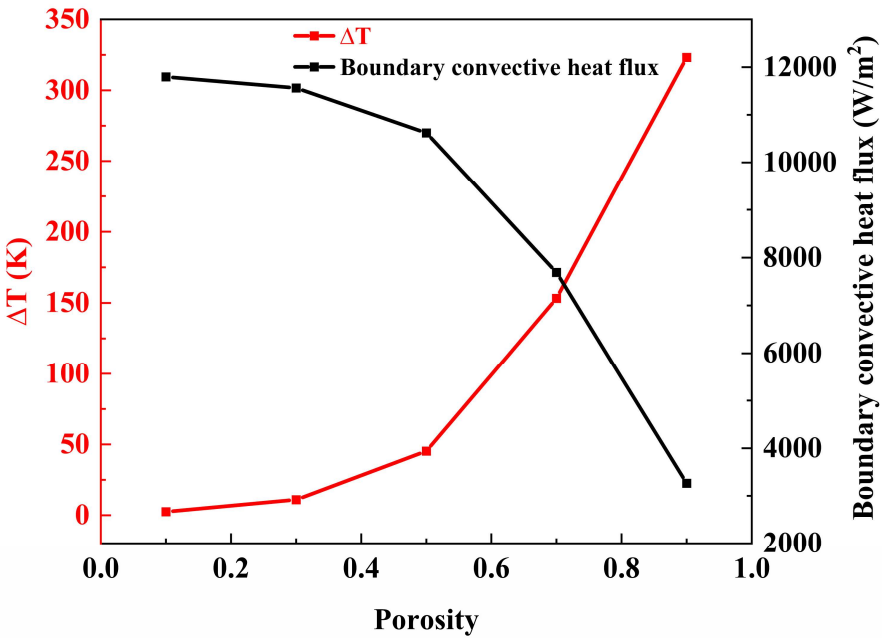

Fig. 5. 18 Effect of φ_p on ΔT and $q_{convection}$ in model I

The effect of φ_p on the variation of T_{top} with time, and temperature gradient distribution in z direction are shown in Fig. 5. 19. As φ_p increases, T_{top} at steady state gradually decreases, and the time for T_{top} or the entire pellet to reach the thermal steady state becomes longer. It is clear that when φ_p is greater than 0.5, the gap between the stable value of T_{top} and the heating time is obviously widened, which is consistent with the shift of ΔT. In Fig. 5. 19(b), the cut plane is the xz plane when the y coordinate is 0 mm. The temperature difference of the pellet in the z direction still exhibits a uniform distribution. As φ_p increases, especially when it is greater than 0.5, the vertical temperature gradient rises significantly. These impacts of φ_p are in consistent with those on ΔT and $q_{convection}$.

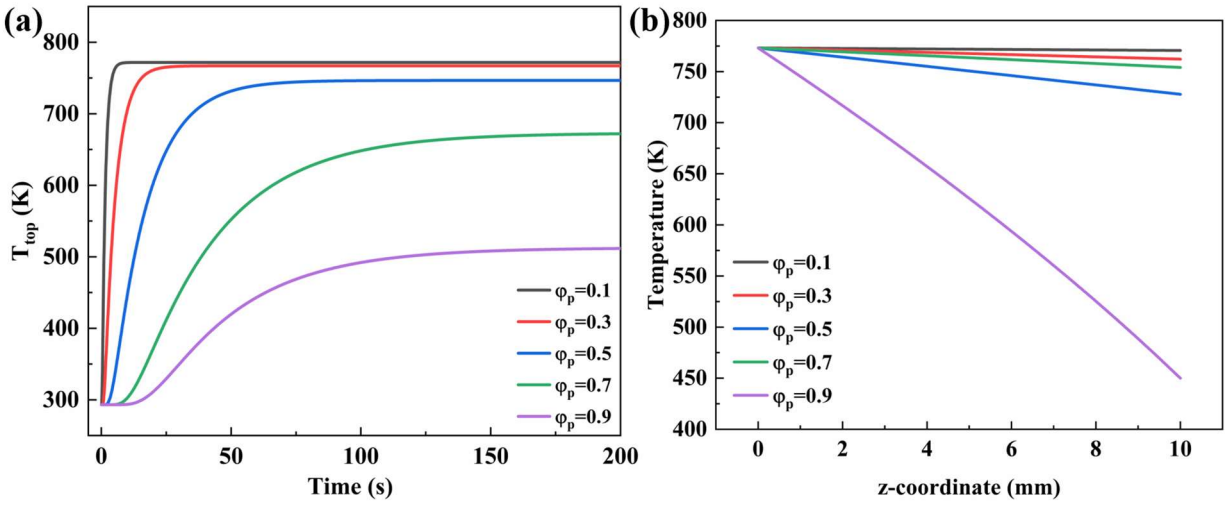

Fig. 5. 19 (a) Effect of φ_p on the variation of T_{top} with time in model I; (b) Effect of φ_p on the variation of temperature on the cut plane with z coordinate at steady state in model I

5.2.4.5 Combined effect of thickness, thermal conductivity of material and porosity of the porous pellet

Following model optimization, the individual effects of thickness and radius of pellet, material properties and porosity of the pellet in the model on pellet heat transfer were investigated in the preceding section. It is concluded that thickness, thermal conductivity of material and porosity of pellets have significant impacts on heat transfer. When ΔT is used as the evaluation standard, it grows in a roughly proportional relationship with the increase of thickness. ΔT decreases with $k_{Conductive}$ increases, however the decrease in ΔT is exceedingly minor when $k_{Conductive}$ is greater than 100 W/m·K. For φ_p, ΔT increases as it increases, and the rate of rise also accelerates especially when φ_p is greater than 0.7. In actual situations, these three parameters do not work independently. They have an effect on one another, which was considered as the combined effect and was studied.

First of all, the combined effects of thickness and $k_{Conductive}$ were considered. φ_p was set as 0.1. As shown in Fig. 5. 20, ΔT and boundary convective heat flux vary with different thickness and $k_{Conductive}$ of pellet. The general trend of the curves is similar to

that shown in Fig. 5. 15. When 10 W/m·K ≤ $k_{Conductive}$ ≤ 50 W/m·K, ΔT has a significant decline with the increase of $k_{Conductive}$ and the downward trend gradually slows down, except that when e = 1 mm, it changes little compared to other e values. When $k_{Conductive}$ ≥ 50 W/m·K, ΔT of the pellets corresponding to e = 1 mm and e = 10 mm rarely changes, while the ΔT of the pellets corresponding to e = 50 mm and e = 100 mm decreases slightly and hardly decreases until $k_{Conductive}$ is higher than 200 W/m·K. And when e = 500 mm, ΔT decreases with increasing $k_{Conductive}$ all the time, despite the slowing down of deceleration. Correspondingly, when e ≤ 10 mm, $q_{convection}$ barely rises after $k_{Conductive}$ ≥ 50 W/m·K; when 10 mm ≤ e ≤ 100 mm, $q_{convection}$ barely rises after $k_{Conductive}$ ≥ 200 W/m·K; and when e ≥ 100 mm, the increased $k_{Conductive}$ still leads to a relative larger growth in $q_{convection}$. This suggests that the increase of thickness of the pellet has a significant influence on the variation of ΔT and $q_{convection}$ with thermal conductivity of pellet material. As the thickness increases, the corresponding k value becomes larger when the curve starts to slow down. In other words, the larger the thickness, the higher the thermal conductivity of pellet material required to achieve higher heat transfer efficiency. In the current case of φ_p = 0.1, better heat transfer efficiency has been achieved with k less than 100 W/m·K and thickness less than 50 mm.

This conclusion may also be compared to the heat transfer experimental results of Cu and stainless steel cylinders of 3 thicknesses (1 mm, 10 mm, 50 mm) presented in Section 3.6, Chapter 3. For stainless steel samples with low thermal conductivity (13 W/m·K), the ΔT corresponding to the thickness of 50 mm (51 K) is significantly larger than that corresponding to the thickness of 1 mm (5 K) or 10 mm (19 K). For Cu sample with extremely high thermal conductivity (398 W/m·K), the ΔT among the three groups of varying thicknesses shows a relatively small difference. The difference in ΔT between Cu and stainless steel samples of the same thickness steadily grows as the thickness increases.

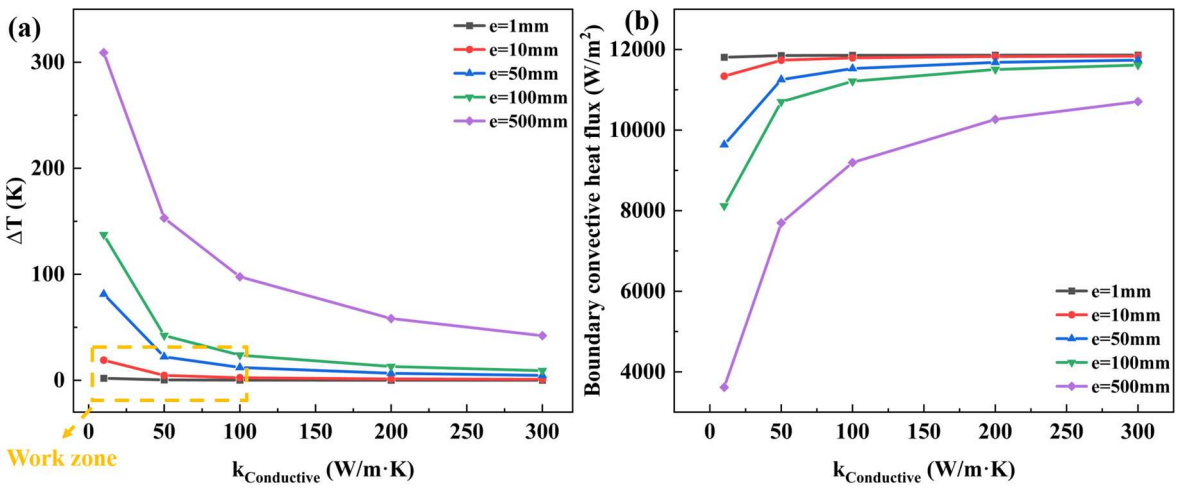

Fig. 5. 20 Combiend effect of thickness and $k_{Conductive}$ on (a) ΔT and (b) $q_{convection}$

Then the combined effects of φ_p and $k_{Conductive}$ in model I were studied. The pellet thickness, e, was set as 10 mm. ΔT and $q_{convection}$ results are shown in Fig. 5. 21. The general trend of the curves is similar to that seen in Fig. 5. 20. When $\varphi_p \leq 0.3$, the change of ΔT after $k_{Conductive}$ is greater than 50 W/m·K is almost negligible. And the ΔT values of the same $k_{Conductive}$ corresponding to $\varphi_p = 0.1$ and $\varphi_p = 0.3$ are very close. When $\varphi_p \geq 0.3$, ΔT still keeps decreasing with the increase of $k_{Conductive}$, although the speed of this decrease slows down. In addition, as φ_p increases, the disparity between the ΔT values corresponding to different φ_p at the same $k_{Conductive}$ also increases, which is extremely obvious when φ_p is 0.9. $q_{convection}$ also increases as $k_{Conductive}$ increases. When $\varphi_p \leq 0.3$, $q_{convection}$ hardly increases when $k_{Conductive}$ exceeds 50 W/m·K. And when $\varphi_p \geq 0.3$, $q_{convection}$ keeps increasing with the increase of $k_{Conductive}$. This implies that in the current case of e = 10 mm, when porosity of pellet is less than 0.3, a relatively small thermal conductivity of pellet material (around 50 W/m·K) might achieve high-efficiency of pellet heat transfer, and raising this conductivity cannot significantly enhance the heat transfer efficiency further. While when porosity is more than 0.3, the material thermal conductivity is generally required to be higher, for example, higher than 100 W/m·K. And the greater the porosity, the higher the thermal conductivity required for effective heat transfer.

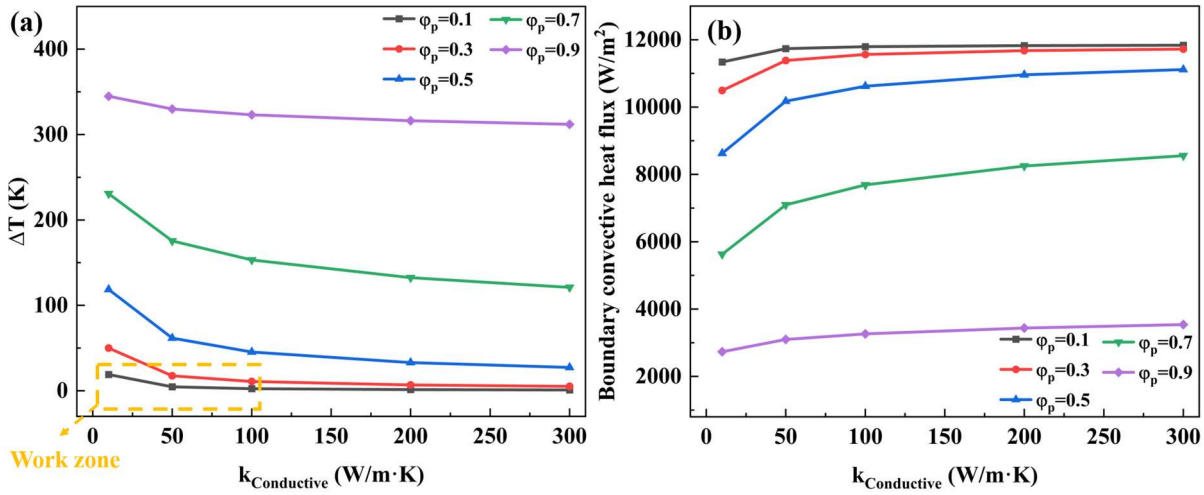

Fig. 5. 21 Combiend effect of φ_p and $k_{Conductive}$ on (a) ΔT and (b) $q_{convection}$

At last, the combined effects of thickness and φ_p were explored. $k_{Conductive}$ was set as 100 W/m·K. ΔT and $q_{convection}$ results are shown in Fig. 5. 22. When compared with Fig. 5. 11, it could be seen that except when $\varphi_p = 0.1$, the change of ΔT and $q_{convection}$ is approximately proportional to thickness, the growth rate of ΔT and the decreasing rate of $q_{convection}$ slows down with increasing thickness in other cases. It shows that as φ_p is greater than 0.1, the thickness becomes highly critical and smaller thickness has a greater impact on the heat transfer efficiency of the pellet. For example, when $\varphi_p = 0.9$, ΔT increases by 239.5 K as the thickness increases from 1 mm to 10 mm (only 9 mm of growth). This impact eventually diminishes as the thickness grows. For example, when $\varphi_p = 0.9$, ΔT only increases by 20.9 K as the thickness increases from 100 mm to 500 mm (400 mm of growth).

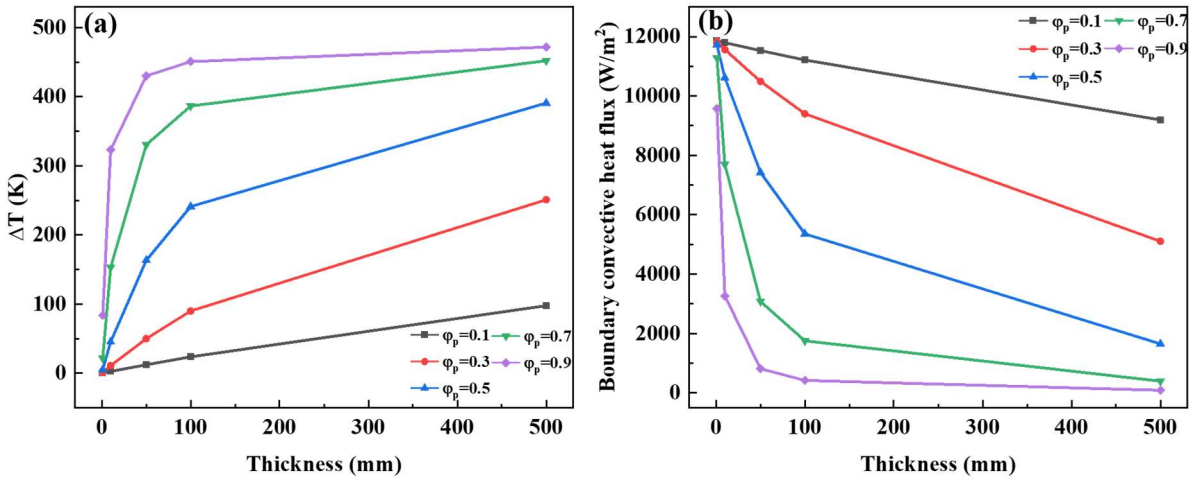

Fig. 5. 22 Combiend effect of thickness and φ_p on (a) ΔT and (b) $q_{convection}$

In summary, a work zone is defined in Fig. 5. 20 and Fig. 5. 21 where a high conductive heat transfer efficiency of the porous materials can be achieved, depending on its thickness, thermal conductivity and porosity. This may provide a reference for preparing efficient thermal conductive materials applied in solar thermal process.

5.3 Model II: thermal conduction in the porous material (pellet) composed of stacked spherical particles

5.3.1 Model set-up

Model I simulates a continuous medium, while in reality, the material is formed through the densification of individual particles. It would be interesting to examine the process of conductive heat transfer through a stack of particles (model II).

The coordinate system in this model was likewise configured to Cartesian coordinates, with the default spatial coordinate names for 3D space dimension being x, y, and z. The unit system was International System of Units (SI). Model I set up a continuous geometric body, which matches the physical interface of conductive heat transfer in porous continuum. While in model II, a geometry of stacked spheres was built to directly simulate the connection of microscopic particles in the pellet, as shown

in Fig. 5. 23. The non-porous spheres (particles) formed a continuous solid network, with direct heat transfer from one to another. Here, the radius of each sphere was 0.25 mm, and each layer was composed of 4 spheres arranged in a square. In total, 20 layers were built in the z-axis direction, resulting in a height of 10 mm. At the same time, the gas layer was represented by a cuboid with dimensions of 1 mm in length and breadth and 10 mm in height. The sphere radius was varied to investigate its effect on pellet heat transfer. Air and the blank material labeled as “Conductive Material” were chosen as the material for the gas layer and spheres, respectively. Different values were assigned to thermal conductivity (isotropic) of Conductive Material. Several properties were introduced for two materials and the value ranges or equations are detailed in Tab. 5. 7.

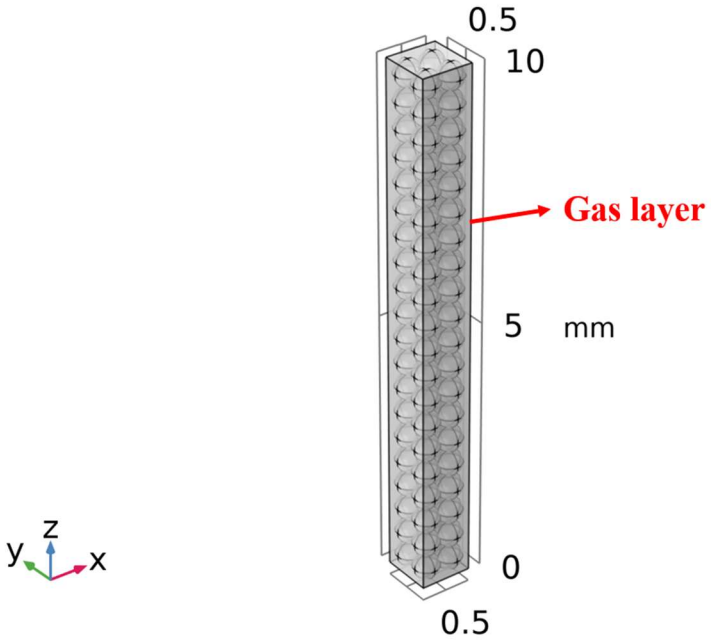

Fig. 5. 23 Geometry of model II

The “Heat transfer in solids and fluids” which is used to model heat transfer in solids and fluids by conduction and convection, and the “Radiation in participating media” physics interfaces in heat transfer module were applied for the domain. The bottom boundaries of the spheres in the bottom layer and the bottom gas boundary were given a temperature of 773.15 K (Fig. 5. 24). Other settings were the same as in model

I. Due to the geometric settings, the swept mesh was no longer applicable, thus the mesh type was selected as free tetrahedral, with an element size of "finer".

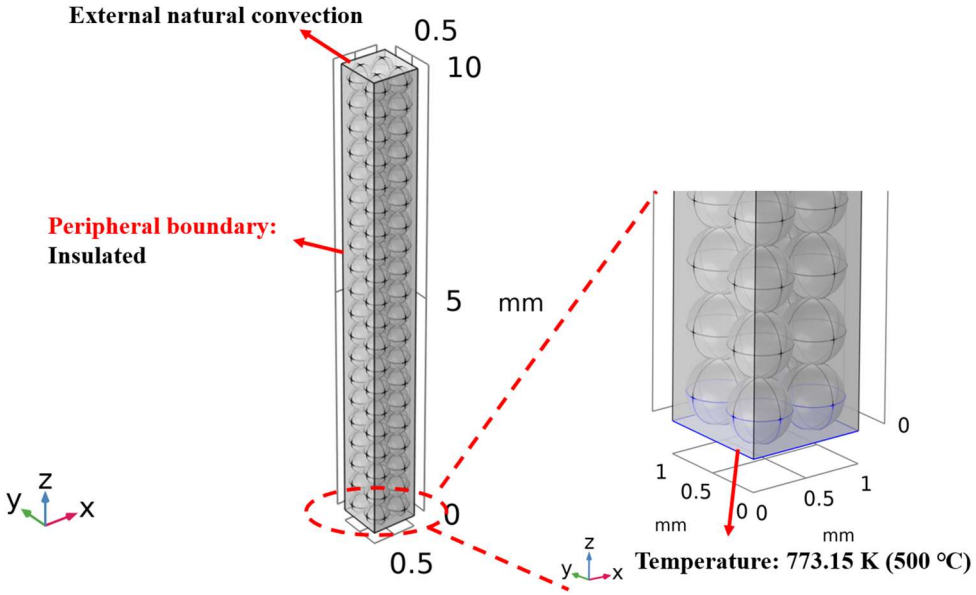

Fig. 5. 24 Boundary condition in model II

All the relative parameters that needed for heat conduction and thermodynamic calculation are listed in Tab. 5. 7.

Tab. 5. 7 Conditions and parameters in model II set-up

Parameter	Specification
Radius of sphere, r_s (mm)	0.1, 0.25, 0.5, 1
Thermal conductivity of Conductive Material, $k_{Conductive}$ (W/m·K)	10, 50, 100, 200, 300
Density of Conductive Material, $\rho_{Conductive}$ (kg/m^3)	3500
Specific heat capacity of Conductive Material at constant pressure, $c_{p,\ Conductive}$ (J/(kg·K))	700
Thermal conductivity of air, k_{air} (W/m·K)	0.00227583562+1.15480022E-4*T-7.90252856E-8*T^2+4.11702505E-11*T^3-7.43864331E-15*T^4 (0.026 at 298.15 K)
Density of air, ρ_{air} (kg/m^3)	p_A*0.02897/8.314/T (1.18 at 298.15 K)
Specific heat capacity of air at constant pressure, $c_{p,air}$ (J/(kg·K))	1047.63657-0.372589265*T^1+9.45304214E-4*T^2-6.02409443E-7*T^3+1.2858961E-10*T^4 (1.01 at 298.15 K)
Heating temperature, T_h (K)	773.15

Refractive index of the medium material, n	2.05
Mesh element type	free tetrahedral
Mesh element size	finer

5.3.2 Study and solver configuration

Here, the time dependent study step was added to compute domain temperature changes over time. The time-dependent solver was applied where temperature was the dependent variable. The time step was 0.001 s while the time range was 1000 s depending on different model parameters. The relative tolerance was set as 10^{-6} and the factor of absolute tolerance was 0.1. The maximum number of iterations was set to be 20. ΔT was calculated according to Eq. 5. 2 (Chapter 5). Here T_{top} and T_{bottom} were the average temperatures of the top boundaries of the top layer spheres and the bottom boundaries of the bottom layer spheres, respectively (Fig. 5. 25). The boundary convective heat flux ($q_{convection}$) of the top boundaries were calculated according to Eq. 5. 6 (Chapter 5).

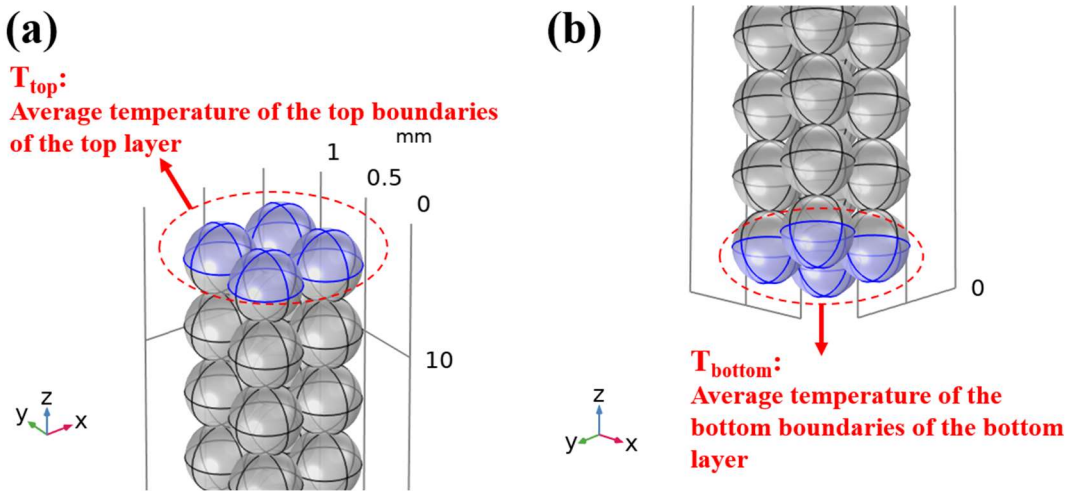

Fig. 5. 25 Schematic diagram of (a) T_{top} and (b) T_{bottom} in model II

5.3.3 Governing equations and boundary conditions

The temperature equations defined in both solid and fluid domains corresponded to the differential form of the Fourier's law and were derived from the heat balance

equation displayed in Section 1.5, Chapter 1. As summarized below in Tab. 5. 8, in the equations, Q stands for the heat source, Q_{ted} is the thermoelastic damping and accounts for thermoelastic effects in solids, α_s is the thermal expansion coefficient of solid phase, S is the second Piola-Kirchhoff stress tensor.

Tab. 5. 8 Governing equations in model II

Physics	Governing equations
Heat transfer in solids and fluids (solid domain)	$\rho_s C_{p,s}\frac{\partial T}{\partial t} + \nabla \cdot \boldsymbol{q} = \mathrm{Q} + Q_r + Q_{ted}$ $\boldsymbol{q} = -k_s \nabla T$ $Q_{ted} = -\alpha_s T : \frac{dS}{dt}$
Heat transfer in solids and fluids (fluid domain)	$\rho_f C_{p,f}(\frac{\partial T}{\partial t} + \boldsymbol{u} \cdot \nabla \mathrm{T}) + \nabla \cdot \boldsymbol{q} = \mathrm{Q} + Q_r + Q_p$ $\boldsymbol{q} = -k_f \nabla T$ $Q_p = \alpha_f T\left(\frac{\partial p_A}{\partial t} + u \cdot \nabla p_A\right)$ $\alpha_f = -\frac{1}{\rho_f}\frac{\partial \rho_f}{\partial T}$
Radiation in participating media	$Q_r = \kappa(G - 4\pi I_b(T))$ $\nabla \cdot (D_{p1} \nabla G) = Q_r$ $D_{P1} = \frac{1}{3(\kappa + \sigma_s)}$ $I_b(T) = \frac{n^2 \sigma T^4}{\pi}$

For the boundaries, the conditions and equations are the same with those in model I (Section 5.2.3, Chapter 5) and summarized in Tab. 5. 9.

Tab. 5. 9 Boundary conditions in model II

Boundary	Equations
Peripheral boundary	$-\boldsymbol{n} \cdot \boldsymbol{q} = 0$
Bottom boundary	$T = T_0$
Top boundary	$-\boldsymbol{n} \cdot \boldsymbol{q} = q_0$

$$q_0 = h(T_{ext} - T)$$

$$h = \begin{cases} \frac{k_{f,ext}}{L} 0.54 Ra_L^{\frac{1}{4}} & if\ T > T_{ext}\ and\ 10^4 \le Ra_L \le 10^7 \\ \frac{k_{f,ext}}{L} 0.15 Ra_L^{\frac{1}{3}} & if\ T > T_{ext}\ and\ 10^7 \le Ra_L \le 10^{11} \\ \frac{k_{f,ext}}{L} 0.27 Ra_L^{\frac{1}{4}} & if\ T \le T_{ext}\ and\ 10^5 \le Ra_L \le 10^{10} \end{cases}$$

$$Ra_L = \frac{g \alpha_{f,ext} \rho_{f,ext}^2 C_{p,ext} (T - T_{ext}) L^3}{k_{f,ext} \mu}$$

5.3.4 Results and discussion

For model II, the simulation results cannot be directly compared with experimental results as the porosity is fixed (detailed in Section 5.3.4.1, Chapter 5) and cannot be altered. Consequently, this section focuses on comparing the results of model II with those of model I.

5.3.4.1 Effect of sphere radius

In order to explore the effect of spheres (particles) size on porous pellet heat transfer efficiency in model II, varying radius values of 0.1, 0.25, 0.5, and 1 mm were applied. The thermal conductivity of Conductive Material was fixed at 100 W/m·K. Simultaneously, a comparison was made with the calculation results of model I. Here for model I with a cylinder geometry, the parameters were set according to those in model II, specifically:

-the thickness (e) was set as 10 mm and the radius (R) was 5 mm;

-the thermal conductivity of Conductive Material was 100 W/m·K, the density was 3500 kg/m^3, the specific heat capacity was 700 J/(kg·K);

-the porosity was 0.48.

This porosity input in model I was calculated based on the geometry of model II:

$$\varphi_p = \frac{V_g}{V_{total}} \qquad \text{Eq. 5. 9}$$

where V_g is the gas volume in the domain and V_{total} is the volume of both spheres and gas in model II. This porosity keeps constant as the sphere radius changes, owning to

that the spheres in the geometry are stacked orderly. ΔT for different sphere radii in model II, and in model I were computed (Fig. 5. 26). In model II, the overall trend of the ΔT value gradually decreases as the radius of sphere increases. When r_s is 0.1 mm, ΔT from model II is 35.8 K, which is the nearest with that from model I (38.6 K). This shows that the result of model II with a smaller sphere size is closer with model I dominated by continuum. The similar value might lead to the hypothesis that when employing stacked spheres to simulate the heat transfer of porous pellets, a smaller sphere radius might be more practical.

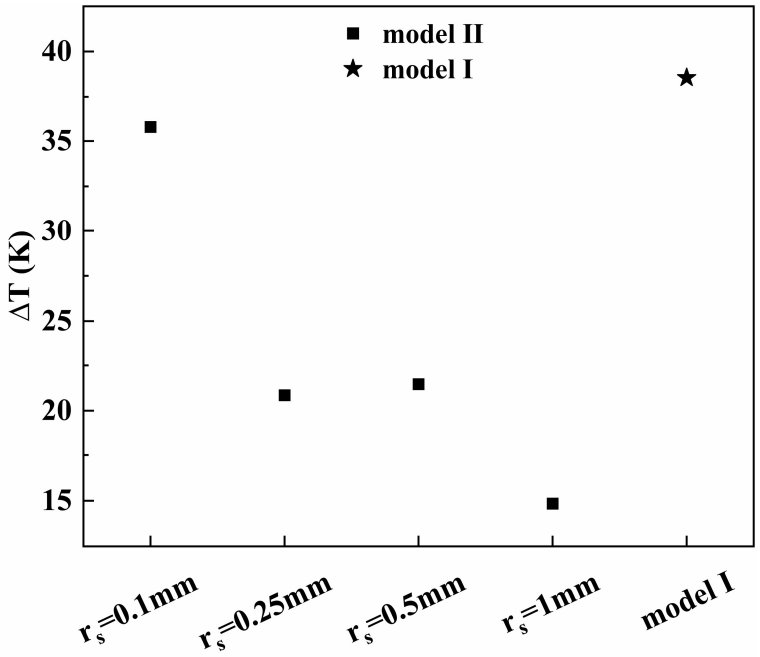

Fig. 5. 26 Comparison of ΔT from model II with different sphere radii and model I

5.3.4.2 Effect of thermal conductivity

The effect of material thermal conductivity on porous pellet heat transfer in model II was also studied. Here $k_{Conductive}$ was varied from 10 W/m·K to 300 W/m·K. The radius of the sphere was fixed at 0.25 mm. In addition, its results were compared with those of model I, where the $k_{Conductive}$ changed synchronously with model II. For model I, the parameters were set according to those in model II, specifically:

-the thickness was set as 10 mm and the radius was 5 mm;

-the thermal conductivity of Conductive Material was also varied from 10 W/m·K to 300 W/m·K which was in accordance with model II, the density was 3500 kg/m^3, the specific heat capacity was 700 J/(kg·K);

-the porosity was 0.48, which was calculated as introduced in Section 5.3.4.1, Chapter 5.

Fig. 5. 27 compares the results of ΔT and $q_{convection}$ in the two models. For model II, when $k_{Conductive}$ increases from 10 W/m·K to 100 W/m·K, ΔT shows a significant decline. When $k_{Conductive}$ is greater than 100 W/m·K, the downward trend of ΔT slows and the variances between the points are negligible. The $q_{convection}$ exhibits similar characteristics, gradually rising as $k_{Conductive}$ exceeds 100 W/m·K. Overall, the trends of ΔT and $q_{convection}$ changing with material thermal conductivity are comparable in these two models. When $k_{Conductive}$ is less than 50 W/m·K, model II's curve is steeper than that of model I. This might be due to the fact that, the principle of the thermal equation of solids and fluids in model II is similar to the theory of calculating the effective thermal conductivity of the matrix through volume average method (Eq. 1. 20, Chapter1) in porous media. When $k_{Conductive}$ increases from 10 W/m·K to 300 W/m·K, this method increases the k_{eff} substantially more than the power law method applied in model I. This leads to a larger gap of ΔT (or $q_{convection}$) between 10 W/m·K and 300 W/m·K in model II.

A work zone is also given in Fig. 5. 27 for model II for the reference.

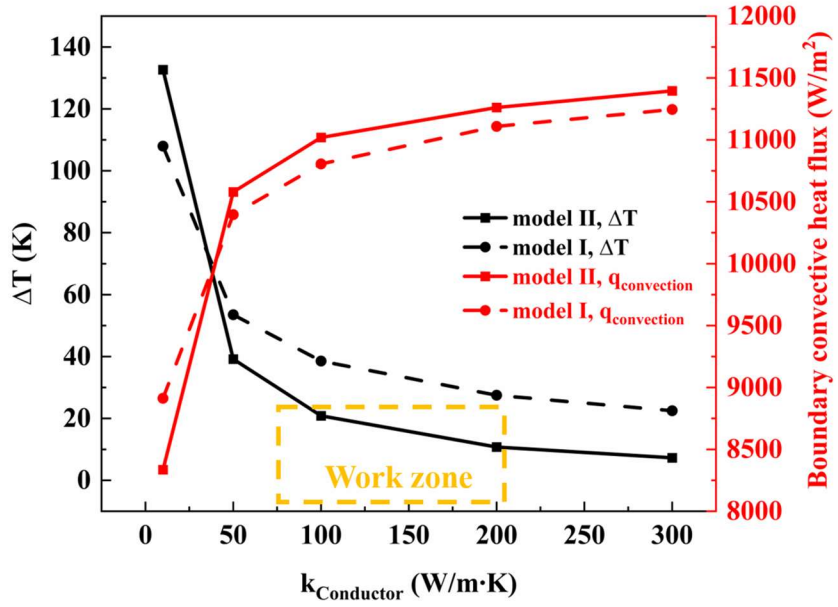

Fig. 5. 27 Comparison of effect of $k_{Conductive}$ on ΔT and $q_{convection}$ in model I and II

5.4 Conclusions

In this chapter, two numerical models of heat transfer in porous pellet based on continuum and stacked spheres respectively, were established and compared. The effects of pellet thickness, porosity and material thermal conductivity on the heat transfer efficiency were simulated. The conclusions can be summarized as follows:

(1) In the case of porosity = 0.1, when the pellet thickness was less than 100 mm, the heat transfer efficiency of the porous pellet could not be greatly improved even if the material thermal conductivity continued to rise beyond 100 W/m·K. When the pellet thickness was less than 50 mm, this value was around 50 W/m·K.

(2) In the case of thickness = 10 mm, when porosity of pellet was less than 0.3, a relatively low material thermal conductivity (around 50 W/m·K) might achieve high-efficiency of pellet heat transfer, and raising this conductivity would not significantly enhance the heat transfer efficiency.

(3) When the porosity exceeded 0.1, the thickness became highly critical and a smaller thickness had a greater impact on the heat transfer efficiency of the porous pellet.

(4) In terms of the effect of thermal conductivity on the heat transfer of porous pellet, the model based on stacked spheres acquired similar results to the continuum model. Using a smaller sphere radius (0.1 mm) was more feasible.

Chapter 6: Numerical modeling of solar absorption and thermal conduction in porous material (pellet)

6.1 Introduction

In Chapter 5, the numerical modeling of thermal conduction in the porous material and the effects of various factors were studied. Accordingly, the coupling of solar energy absorption (radiative) and thermal conduction process of the composite porous material was further simulated and presented in this chapter. The porous material was represented in the form of a pellet, allowing for a direct comparison with the experimental results obtained by the pellet. As in Chapter 5, two numerical models of solar absorption and thermal conduction in the composite porous material were investigated and compared. The first model (model III) assumes the geometry as a solid matrix with uniformly distributed average porosity. The second model (model IV) considers the pellet as a composition of orderly stacked spherical particles with a consistent porosity. Varying factors including the thickness, thermal conductivity and absorptivity of absorption layer of composite pellet on the solar absorption and thermal conduction efficiency were explored.

Finite element method was applied and COMSOL Multiphysics was used as the carrier for model set-up and calculation. The models in the current study were conducted by the COMSOL Multiphysics version 5.4 (Academic license) using a laboratory computer (equipped with a processor of Intel(R) Core(TM) i5-10500 CPU@3.1 GHz, 3096 MHz, 6 cores and 12 logic processors).

6.2 Model III: solar absorption and thermal conduction in the continuous porous material (pellet)

In this section, a model that assumes the geometry as a solid matrix with uniformly distributed average porosity and studies its thermal performance, is introduced. In the corresponding solar radiation absorption and thermal conduction experiments, the tested pellets were confined to a standardized dimension: 10 mm in diameter and 1.5 to 2 mm in thickness. The dimension was restricted by the spark plasma sintering device, and it was difficult to form pellets of varying sizes and study their heat transfer efficiency. Consequently, the model offers an alternative to explore the influence of diverse geometric parameters, distinct material compositions and thermal properties.

6.2.1 Model set-up

The coordinate system in this model was likewise configured to Cartesian coordinates, with the default spatial coordinate names for 3D space dimension being x, y, and z. And the unit system was International System of Units (SI). In order to simulate the solar energy absorption and thermal conduction of pellet, a cylinder with a radius of 5 mm and a height of 10.1 mm consisting of two layers was built in the geometry section (Fig. 6. 1). The top layer (absorption layer) with a thickness of 0.1 mm represents the solar absorber; the bottom layer (thermal conduction layer) with a thickness of 10 mm represents the thermal conductive substrate.

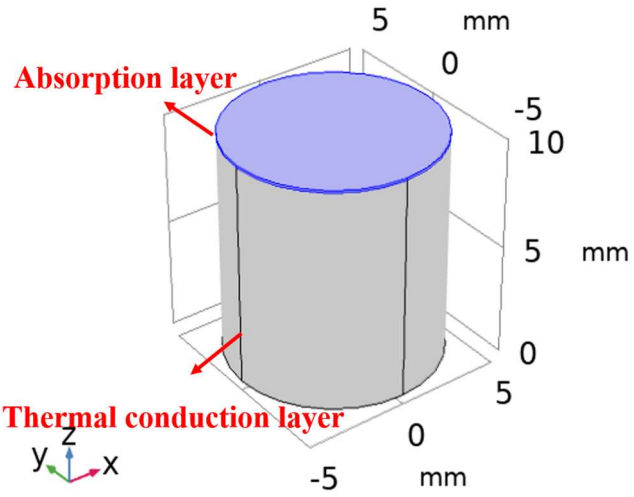

Fig. 6. 1 Geometry of model III

For the thermal conduction layer, the "Conductive Material" and "air" were added as in model I. Several properties were introduced for "Conductive Material" and "air" , and the value ranges or equations are detailed in Tab. 6. 1. The material of the absorption layer was chosen as "blank material", which means that the properties can be added according to the needs of model calculation. It was labeled as "Absorber". A specific material was not selected here because the absorptivity (α) would be changed later to study its influence. Three material properties, thermal conductivity, specific heat capacity at constant pressure and density were added for Absorber. The thermal conductivity was set to 1 W/m·K and changed subsequently to study its effect on thermal conduction of absorption layer. For the initial value of the remaining two properties, carbon was chosen as a reference because of its high solar absorption and photo-thermal conversion characteristic and its application in practice[242]. As a result, the density of Absorber ($\rho_{absorber}$) was set to 1900 kg/m^3 and the specific heat capacity ($c_{p,absorber}$) at constant pressure was set to 890 J/(kg·K)[243].

Tab. 6. 1 Conditions and parameters in model III set-up

Parameter	Specification
Thickness of absorption layer, $e_{absorption}$ (mm)	0.1, 1, 10
Thickness of thermal conduction layer, $e_{conduction}$ (mm)	10
Radius of geometry, R (mm)	5
Thermal conductivity of Absorber, $k_{Absorber}$ (W/m·K)	1, 50, 100, 200
Density of Absorber, $\rho_{Absorber}$ (kg/m^3)	1900
Specific heat capacity of Absorber at constant pressure, $c_{p,Absorber}$ (J/(kg·K))	680
Thermal conductivity of Conductive Material, $k_{Conductive}$ (W/m·K)	100
Density of Conductive Material, $\rho_{Conductive}$ (kg/m^3)	3500
Specific heat capacity of Conductive Material at constant pressure, $c_{p,Conductive}$ (J/(kg·K))	700
Thermal conductivity of air, k_{air} (W/m·K)	0.00227583562+1.15480022E-4*T-7.90252856E-8*T^2+4.11702505E-11*T^3-7.43864331E-15*T^4 (0.026 at 298.15 K)
Density of air, ρ_{air} (kg/m^3)	p_A*0.02897/8.314/T (1.18 at 298.15 K)
Specific heat capacity of air at constant pressure, $c_{p,air}$ (J/(kg·K))	1047.63657-0.372589265*T^1+9.45304214E-4*T^2-6.02409443E-7*T^3+1.2858961E-10*T^4 (1.01 at 298.15 K)
Porosity of thermal conduction layer (void fraction), φ_p	0.1
Effective thermal conductivity computing model, k_{eff} (W/m·K)	power law
Refractive index of the medium material, n	2.05
Absorber surface absorptivity at solar band, α_{sb}	0.1, 0.3, 0.5, 0.7, 0.9
Absorber surface absorptivity at ambient band, α_{ab}	0
Ambient emissivity	0
Source heat rate, P_s (W)	1000
Mesh element type	prism
Mesh element size	finer

For the main modeling in this part, the “Heat transfer in porous media”, “Radiation in participating media” and the “Surface-to-surface radiation” physics interface in heat transfer module were applied. The first two physics interfaces were applied across the whole domain, with the absorption layer set as solid and the thermal conduction layer set as porous medium (Fig. 6. 2). Air was selected as the fluid material in the porous medium. Its velocity was set as 0 m/s in the three directions of x, y, and z, since the convection in the porous matrix was not considered here. The porosity of the porous medium (φ_p) was set as 0.1. The averaging model for the computation of effective thermal conductivity (k_{eff}) was chosen as power law (Eq. 1. 22, Chapter 1) based on the optimization results from model I (Chapter 5). Under the “Radiation in participating media” physics interface, P1 approximation was chosen as the radiation discretization method (introduced in Section 1.5.2.3, Chapter 1). The settings of all parameters including the absorption coefficient (κ), the scattering coefficient (σ_s) and the refractive index (n) of the medium, were determined to the same values as in model I. These two physics for the domain were coupled then. The initial value of temperature of the whole domain was set as 293.15 K. The peripheral boundary condition of the domain was set to thermal insulation. The remaining two boundaries parallel to the xy plane in the domain are labeled as absorption boundary and bottom boundary as shown in Fig. 6. 2. For the bottom boundary, an external natural convective heat flux was added. The horizontal plate with downside exposed to convection was chosen and the characteristic length was calculated according to Eq. 5. 1 (Chapter 5). While for the absorption boundary, the surface-to-surface radiation physics interface was applied (Fig. 6. 2).

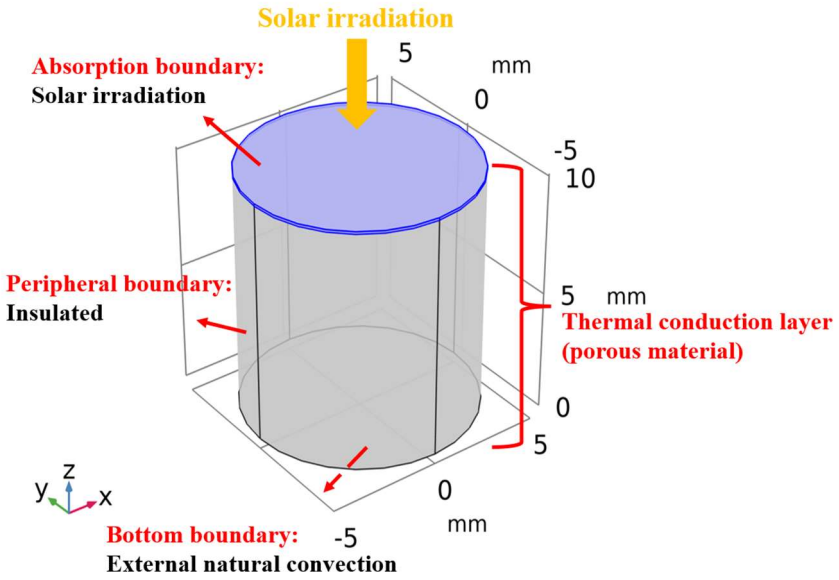

Fig. 6. 2 Boundary conditions of model III

The "Surface-to-surface radiation" physics interface in COMSOL Multiphysics treats thermal radiation as an energy transfer between boundaries and external heat sources where the medium does not participate in the radiation. The wavelength dependence of surface properties was defined as "solar and ambient", referring to two spectral bands of the diffuse spectral radiation model. And the separation point between the two spectral bands was 2.5 μm due to the reason that about 97% of the radiated power from a blackbody at 5780 K (the sun) is at wavelengths of 2.5 μm or shorter[47]. The band of [0, 2.5 μm] represented solar radiation, whereas the band of [2.5 μm, +∞] represented ambient radiation (Fig. 6. 3). Under this interface, the diffuse surface was added for the absorption boundary which reflected radiative intensity uniformly in all directions. The fractional emissive power was set as blackbody so that it was automatically calculated for each spectral band as a function of the band endpoints and surface temperature. Due to the division of the bands at 2.5 μm, the proportion of absorbed solar radiation on the surface is defined primarily by the solar absorptivity (α) and the emission at longer wavelengths (especially for objects with the temperature below 700 K) is defined primarily via the emissivity. The opaque surface was defined for the absorption boundary. Most opaque bodies also behave as ideal gray bodies,

indicating that the absorptivity and emissivity are equal[47]:

$$\alpha = \varepsilon \qquad \text{Eq. 6. 1}$$

As a result, the surface absorptivity was defined for each spectral band in this model. The one at solar radiation band ([0, 2.5 μm]) was denoted as α_{sb} with an initial value of 0.9. α_{sb} would be set to 0.1, 0.3, 0.5, 0.7 and 0.9 in order to explore the effect of absorptivity on heat transfer. While the one at ambient radiation band ([2.5 μm, +∞]) was denoted as α_{ab} with a value of 0 to exclude the loss of the absorption boundary's emission power to the environment at the long-wavelength band.

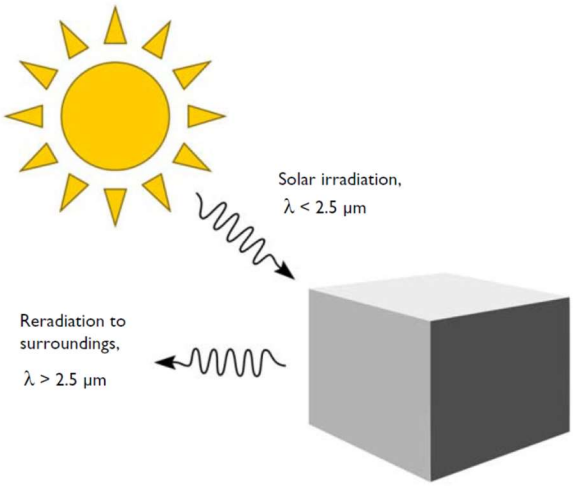

Fig. 6. 3 Absorption of solar radiation and emission to the ambient[244]

With the surface properties and the absorptivity of the absorption boundary defined, the external radiation source was added. A coherent modeling of the solar radiation over a fixed point would take into account the sun's position as a function of time. For this study, the source position was set to "point coordinate" where the source radiated uniformly in all directions, to exclude the influence of unstable solar power. The source location (x, y, z) was defined as (0 m, 0 m, 0.29 m) in the coordinate. The radiative source was chosen as blackbody, with a temperature of 5780 K and a heat rate of 1000 W to simulate solar radiation. The surface irradiation ($Q_{irradiation}$) on the absorption boundary was computed as 1015.5 W/m^2 as some of the irradiation was scattered into the environment. This value was approximate to real solar irradiance (1000 W/m^2)[245].

As the absorption layer thickness ($e_{absorption}$) changed, the corresponding source location was also modified to guarantee that the irradiation on the absorption boundary remained constant. The ambient temperature was set to 293.15 K, and the ambient emissivity was set to 0 to exclude the irradiation from the environment on the absorption boundary. The physics interfaces assigned to the absorption boundary were coupled as well under the Multiphysics section.

The mesh type was set as prism and the size was set as finer (Fig. 6. 4) according to the optimized results in model I. All the involved parameters and specification for model III are listed in Tab. 6. 1 as predefined in COMSOL Multiphysics.

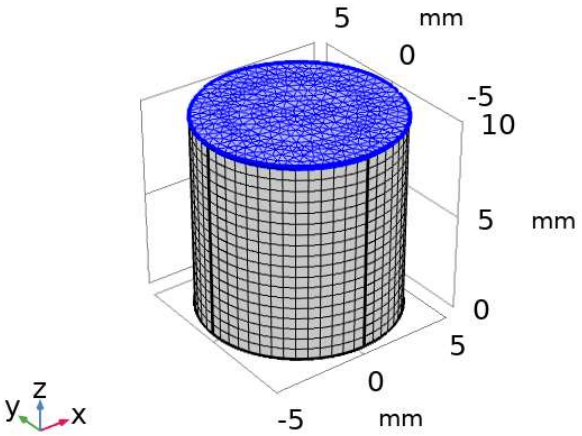

Fig. 6. 4 Mesh of geometry in model III (reference geometry with $e_{absorption}$ = 0.1 mm)

6.2.2 Study and solver configuration

Time dependent study step was added for model III to compute domain temperature changes over time. And a relative time-dependent solver was applied where temperature was the dependent variable. The time step was 0.001 min while the time range was 500 min. The relative tolerance was set as 10^{-6} and the factor of absolute tolerance was 0.1 (Fig. 6. 5 (a)). The maximum number of iterations was set to be 20 so that the results could converge fittingly during the computation. As a result, the temperature of the domain changes with time and finally stabilizes and the specific values can be computed through the study and solver. In results, the average temperature of the absorption boundary was marked as T_{top}, and the average temperature of bottom boundary was

marked as T_{bottom} (Fig. 6. 5 (b)). The temperature difference (ΔT) was calculated according to the following equation:

$$\Delta T = T_{top} - T_{bottom} \quad \text{Eq. 6. 2}$$

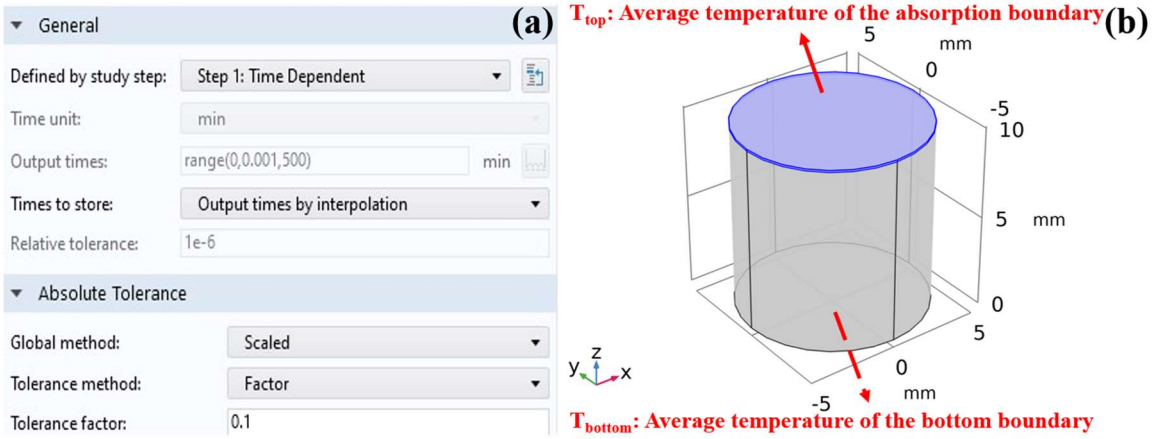

Fig. 6. 5 (a) COMSOL window: Time dependent solver setting; (b) Schematic diagram of T_{top} and T_{bottom}

6.2.3 Governing equations and boundary conditions

In model III, the equations involved in the "Heat transfer in porous media" and "Radiation in participating media" physics for the domain were the same as shown in model I (Section 5.2.3, Chapter 5), and also summarized in Tab. 6. 2. Q stands for the heat source, which is the inward radiative heat flux here.

Tab. 6. 2 Governing equations in model III

Physics	Governing equations
Heat transfer in porous media	$(\rho_m c_{p,m})_{eff}\frac{\partial T}{\partial t} + \rho_f c_{p,f}\boldsymbol{u}\cdot\nabla T + \nabla\cdot\boldsymbol{q} = Q + Q_r + Q_p$
	$(\rho_m c_{p,m})_{eff} = \theta_s\rho_s c_{p,s} + \varphi_p\rho_f c_{p,f}$
	$\boldsymbol{q} = -k_{eff}\nabla T$
	$Q_p = \alpha_f T\left(\frac{\partial p_A}{\partial t} + u\cdot\nabla p_A\right)$
	$\alpha_f = -\frac{1}{\rho_f}\frac{\partial \rho_f}{\partial T}$
Radiation in participating media	$Q_r = \kappa(G - 4\pi I_b(T))$
	$\nabla\cdot(D_{p1}\nabla G) = Q_r$

$$D_{P1} = \frac{1}{3(\kappa + \sigma_s)}$$

$$I_b(T) = \frac{n^2 \sigma T^4}{\pi}$$

For the peripheral and bottom boundaries, the conditions and equations are summarized in Tab. 6. 3. For the absorption boundary, the net radiative heat flux ($q_{r,net}$, W/m^2) was combined with conductive heat transfer through a source term added to the governing heat equation in "Heat transfer in porous media" physics. The conditions and equations of absorption boundary are listed in Tab. 6. 3, where N is the number of the spectral bands defined and for each band, $Band_i = [\lambda_{i-1}, \lambda_i]$. Here N equals 2 as the solar and ambient radiation model was applied and $1 \leq i \leq 2$, J_i is the radiosity in each interval. α_i is the surface absorptivity in each band. $e_b(T)$ (W/m^2) is the blackbody total emissive power defined by Eq. 1. 24 (Chapter 1), T (K) is the surface temperature, $FEP_i(T)$ is the fractional blackbody emissive power over $Band_i$ at T, $\rho_{d,i}$ is diffuse reflectivity in each band, G_i (W/m^2) is the irradiation power in each band, $G_{m,i}$ (W/m^2) is the mutual irradiation in each band coming from other boundaries in the model, $G_{amb,i}$ (W/m^2) is the ambient irradiation in each band, $G_{ext,i}$ (W/m^2) is the irradiation from external radiation sources in each band, $q_{r,net,i}$ (W/m^2) is the net inward radiative heat flux in each band on the surface and is the net inward radiative heat flux on the top surface.

Tab. 6. 3 Boundary conditions in model III

Boundary	Equations
Peripheral boundary	$-\boldsymbol{n} \cdot \boldsymbol{q} = 0$
Absorption boundary	$J = \sum_{i=1}^{N} J_i$
	$J_i = \varepsilon_i e_b(T) FEP_i(T) + \rho_{d,i} G_i$
	$\varepsilon_i = \alpha_i = 1 - \rho_{d,i}$
	$e_b(T) = n^2 \sigma T^4$
	$G_i = G_{m,i} + G_{amb,i} + G_{ext,i}$
	$q_{r,net,i} = G_i - J_i = \alpha_i (G_i - e_b(T))$

	$$q_{r,net} = \sum_{i}^{N} q_{r,net,i}$$
Bottom boundary	$$-\boldsymbol{n} \cdot \boldsymbol{q} = q_0$$ $$q_0 = h(T_{ext} - T)$$ $$h = \begin{cases} \frac{k_{f-ext}}{L} 0.54 Ra_L^{\frac{1}{4}} & if\ T \le T_{ext}\ and\ 10^4 \le Ra_L \le 10^7 \\ \frac{k_{f-e}}{L} 0.15 Ra_L^{\frac{1}{3}} & if\ T \le T_{ext}\ and\ 10^7 \le Ra_L \le 10^{11} \\ \frac{k_{f-ext}}{L} 0.27 Ra_L^{\frac{1}{4}} & if\ T > T_{ext}\ and\ 10^5 \le Ra_L \le 10^{10} \end{cases}$$ $$Ra_L = \frac{g \alpha_{f,ext} \rho_{f,ext}^2 C_{p,ext} (T - T_{ext}) L^3}{k_{f,ext} \mu}$$

6.2.4 Results and discussion

6.2.4.1 Comparison of modeling and experimental results

Before the studied parameters are varied, it is crucial to verify the model's validity. Here, all the samples which were tested in the solar energy absorption and thermal performance experiments (presented in Section 4.4.3, Chapter 4), were employed in model III for the comparative analysis. The different parameter values for each sample in the model were derived from experimental tests conducted on that respective sample. Given that the surface irradiance for the tested pellet in experiment was approximately 6753 W/m^2, the radiation source coordinate and rate were calibrated accordingly to fit this value in model III. Fig. 6. 6 depicts the variation of the pellet's T_{top} in both experiment and model III. It is observed that the simulated curve aligns with relative experimental data, supporting the viability of model III. For sample AlN+3%CaO$^{0.04}$(5000rpm,5min,pellet) and AlN(pellet), there exists a larger discrepancy in the steady-state T_{top} between the model and the experimental results (Fig. 6. 6 (a–b)). For all the samples, the relative error in the steady-state T_{top}, between model and experiment results ranges from 0.25% to 18%.

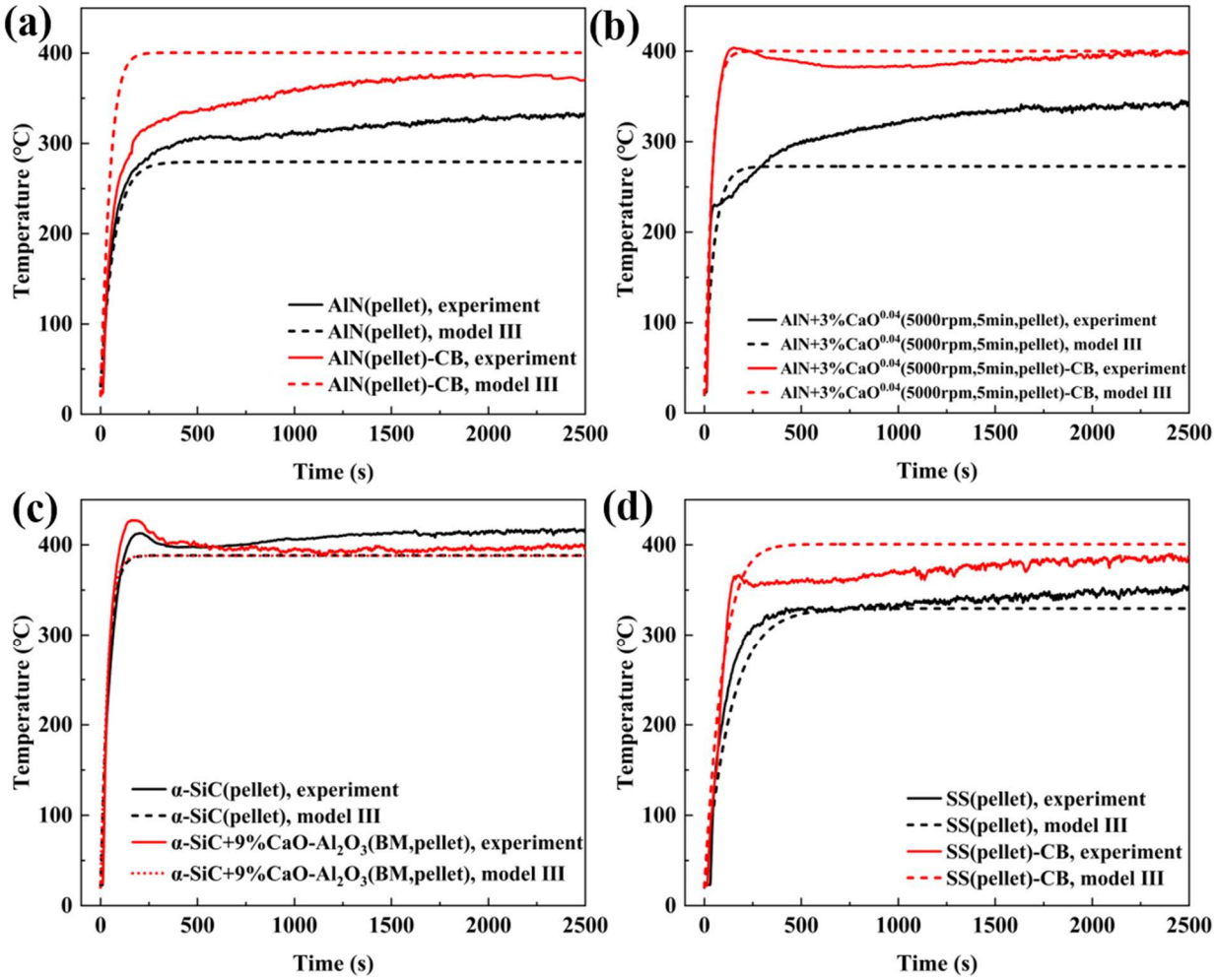

Fig. 6. 6 Comparison of T_{top} with time between experimental and model III results

A parametric analysis through numerical modeling to assess the impact of absorption layer's thickness, thermal conductivity and absorptivity, is presented in the following parts.

6.2.4.2 Effect of the thickness of the absorption layer

The effect of the absorption layer thickness was first studied. Here, $e_{absorption}$ was set as 0.1, 1, 10 mm, while the rest of the parameters were fixed. The thermal conductivity of Absorber was set as 1 W/m·K, and the Absorber surface absorptivity at solar band was fixed at 0.9. The conditions of the thermal conduction layer were listed in Tab. 6. 1. Fig. 6. 7 shows the isothermal surfaces of the geometry at heat transfer steady state when $e_{absorption}$ is 0.1 mm. The isothermal surfaces are all parallel to each

other and on the xy plane, indicating that the temperature of any point with the same z coordinate in geometry is the same. Therefore, it is reasonable to choose the surface average temperature to calculate T_{top} and T_{bottom}. The temperature of the isothermal surface of the whole geometry might be observed to be between 381.86 K and 382.1 K, with a very tiny difference.

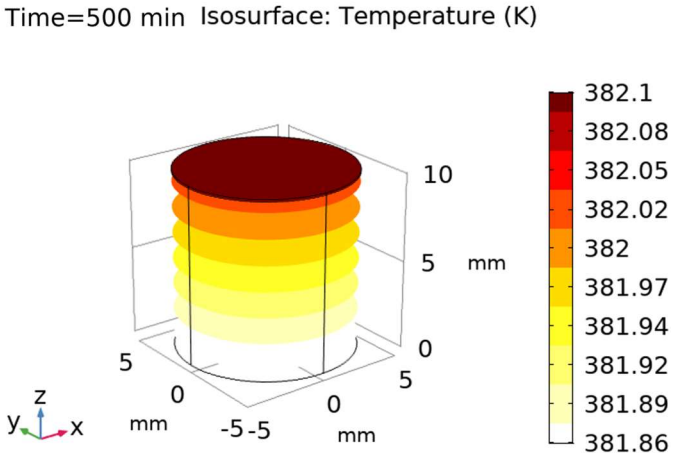

Fig. 6. 7 Isothermal surfaces of geometry with $e_{absorption}$ = 0.1 mm at steady state (The conditions of the thermal conduction layer were listed in Tab. 6. 1)

ΔT was calculated according to Eq. 5. 2 (Chapter 5) and the curve of ΔT changing with $e_{absorption}$ are shown in Fig. 6. 8 (a). It can be seen that there is an approximate proportional relationship between ΔT and $e_{absorption}$, with ΔT increasing as $e_{absorption}$ increases. Fig. 6. 8 (b) shows the temperature of the bottom boundary changing with time at different $e_{absorption}$. It's evident that as $e_{absorption}$ increases, the T_{bottom} rises more slowly and the time to attain the steady state increases. When it comes to the practical implementation of solar energy, time is particularly crucial. It is vital for the materials to maximize the absorption of solar energy and convert into heat within the shortest duration, which optimizes the benefits derived from solar thermal applications.

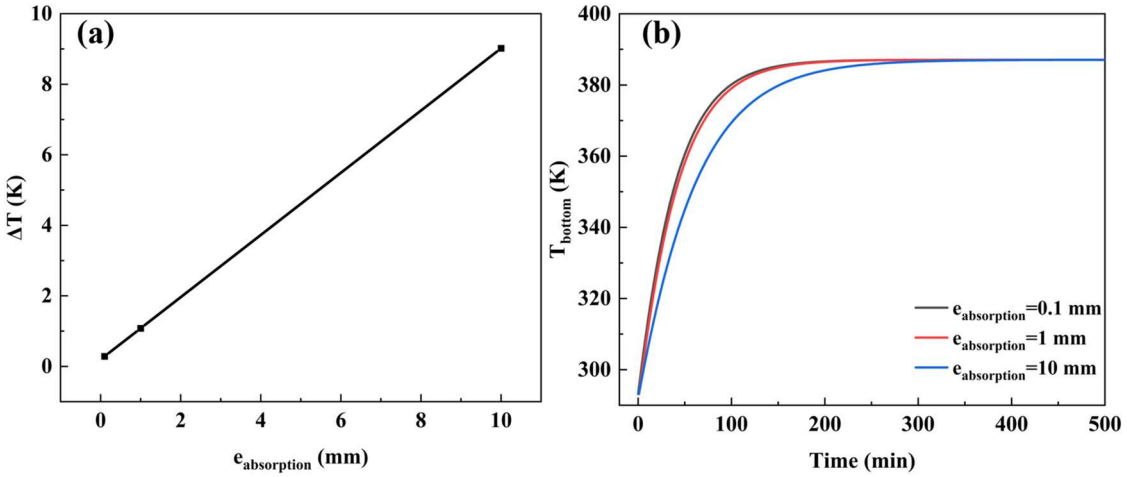

Fig. 6. 8 (a) Effect of thickness of absorption layer on ΔT in model III, (b) Effect of thickness of absorption layer on the variation of T_{bottom} with time in model III

6.2.4.3 Effect of the thermal conductivity of absorption layer material

The effect of thermal conductivity of Absorber at different absorption layer thickness was investigated. The $k_{Absorber}$ was set as 1, 50, 100, 200 W/m·K, and $e_{absorption}$ was set as 0.1, 1, 10 mm. The Absorber surface absorptivity at solar band was fixed at 0.9. The conditions of the thermal conduction layer were listed in Tab. 6. 1. Fig. 6. 9 (a) shows the variation of ΔT with different $k_{Absorber}$ at different $e_{absorption}$. When $e_{absorption}$ is 0.1 mm, the disparity in ΔT across different $k_{Absorber}$ variations is minimal. As $e_{absorption}$ progressively increases, within the range where $k_{Absorber}$ is less than 50 W/m·K, a notable disparity in ΔT emerges among different $k_{Absorber}$. Furthermore, this difference amplifies with the augmentation of $e_{absorption}$. The ΔT difference between $k_{Absorber}$ = 1 W/m·K and $k_{Absorber}$ = 50 W/m·K remains relatively small, with only a 9.1 K variation, when $e_{absorption}$ is up to 10 mm. Regardless of the value of $e_{absorption}$, it could be observed that when $k_{Absorber}$ exceeds 50 W/m·K, the temperature difference between the top and bottom surfaces of the geometry becomes exceedingly negligible. This reveals that, for the absorption layer, a smaller thickness necessitates a lower thermal conductivity requirement. In general, $k_{Absorber}$ values around 50 W/m·K are typically sufficient to fulfill the requirements for efficient solar absorption and heat

transfer. Fig. 6. 9 (b) depicts the variation of T_{bottom} with time at different $k_{Absorber}$ when $e_{absorption}$ is 0.1 mm. When the value of $k_{Absorber}$ changes, the rate at which T_{bottom} increases over time and the time required to reach a steady state remain constant. In other words, variations in $k_{Absorber}$ do not affect the rate at which the pellet absorbs solar energy and transfers heat.

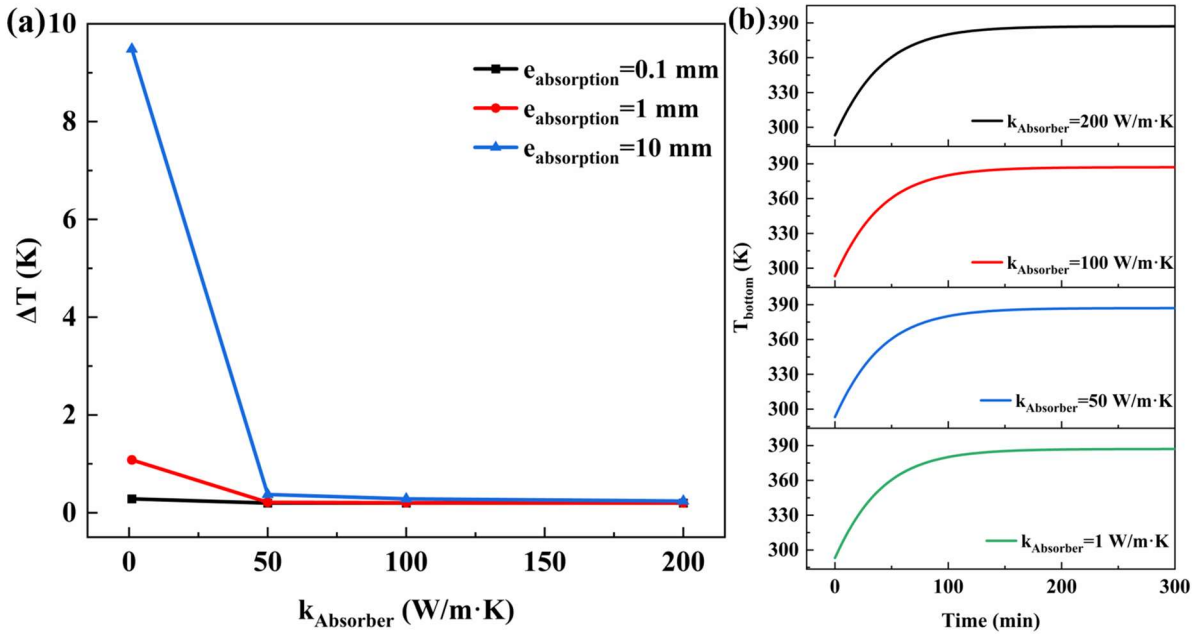

Fig. 6. 9 (a) Effect of $k_{Absorber}$ on ΔT in model III; (b) Variation of T_{bottom} with time at different $k_{Absorber}$ when $e_{absorption}$ = 0.1 mm in model III

6.2.4.4 Effect of the absorption layer surface absorptivity

The effect of Absorber surface absorptivity at solar band was investigated. The α_{sb} was set at 0.1, 0.3, 0.5, 0.7 and 0.9, while the rest of the parameters were fixed:

-the absorption layer thickness was set as 0.1 mm;

-the thermal conductivity of Absorber was set as 1 W/m·K;

- the thermal conduction layer thickness was 10 mm, and its thermal conductivity was 100 W/m·K, its porosity was 0.1.

Fig. 6. 10 (a) displays the variation of ΔT and T_{bottom} with different α_{sb}. Both ΔT and T_{bottom} increase proportionally with the increase of α_{sb}, since the absorptivity is defined as the fraction of the incident radiation intensity that is absorbed by the surface.

Indeed, the variation of ΔT in this case is quite small, ranging from 0.1 to 0.3 K. This minimal change might be considered negligible for practical purposes. The variation of T_{bottom} with time at different α_{sb} is shown in Fig. 6. 10 (b). The rate at which T_{bottom} changes with time is unaffected by variations in α_{sb}. Different α_{sb} values only impact the geometric temperature profile at the steady state, while the speed of temperature change with time remains constant.

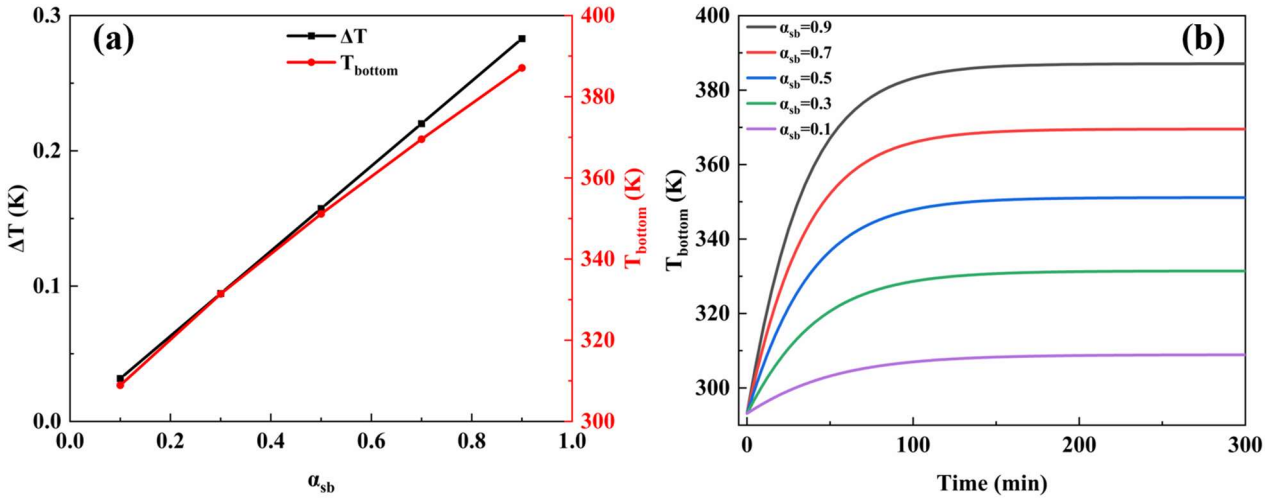

Fig. 6. 10 (a) Effect of α_{sb} on ΔT and T_{bottom} in model III; (b) Variation of T_{bottom} with time at different α_{sb} in model III

6.3 Model IV: solar absorption and thermal conduction in the composite porous material (pellet) composed of stacked spherical particles

In this section, a model that assumes the geometry (composite pellet) as a composition of orderly stacked spherical particles with a consistent porosity and studies its thermal performance, is introduced. Similar to the comparison made between model I and II in Chapter 5, this section compares model III and IV, with distinct geometric configurations. The effects of different sphere sizes, the thermal conductivity and absorptivity of the absorption material were explored.

6.3.1 Model set-up

The coordinate system in model IV was configured to Cartesian coordinates, with the default spatial coordinate names for 3D space dimension being x, y, and z. And the unit system was International System of Units (SI). Similar to the comparison between model I and model II regarding geometry and domain continuity, in order to conduct a similar comparison with model III, the geometry in model IV was also defined as stacked spheres which formed a continuous solid network, as shown in Fig. 6. 11. Here, the radius of each sphere was 0.25 mm, and 4 spheres formed one layer. 20 layers (thermal conduction layer) were built in the z-axis direction with a height of 10 mm, representing the thermal conductive substrate. Two more layers (absorption layer) were built on the thermal conduction layer with a height of 1 mm, representing the solar absorber. At the same time, the gas layer was represented by a cuboid with dimensions of 1 mm in length and breadth and 11 mm in height. Several sphere radii were implemented to investigate its effect on the solar absorption and thermal conduction of pellet (Tab. 6. 4).

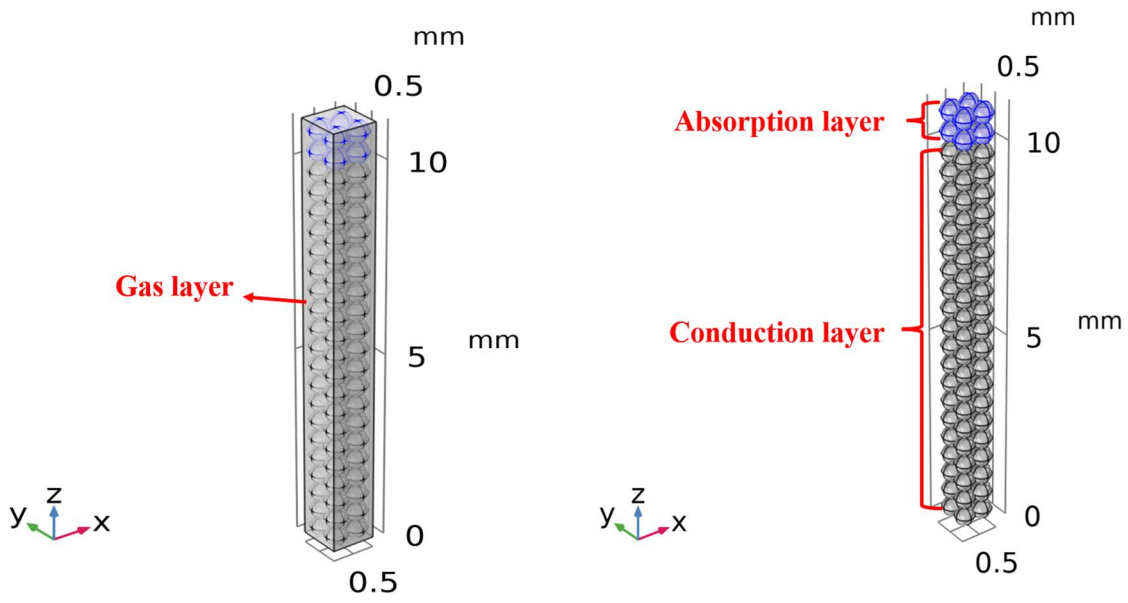

Fig. 6. 11 Geometry of model IV

Tab. 6. 4 Conditions and parameters in model IV set-up

Parameter	Specification
Radius of sphere, r_s (mm)	0.1, 0.25, 0.5
Thickness of absorption layer, $e_{absorption}$ (mm)	1
Thickness of thermal conduction layer, $e_{conduction}$ (mm)	10
Thermal conductivity of Absorber, $k_{Absorber}$ (W/m·K)	1, 50, 100, 200
Density of Absorber, $\rho_{Absorber}$ (kg/m^3)	1900
Specific heat capacity of Absorber at constant pressure, $c_{p,Absorber}$ (J/(kg·K))	680
Thermal conductivity of Conductive Material, $k_{Conductive}$ (W/m·K)	100
Density of Conductive Material, $\rho_{Conductive}$ (kg/m^3)	3500
Specific heat capacity of Conductive Material at constant pressure, $c_{p,Conductive}$ (J/(kg·K))	700
Thermal conductivity of air, k_{air} (W/m·K)	0.00227583562+1.15480022E-4*T-7.90252856E-8*T^2+4.11702505E-11*T^3-7.43864331E-15*T^4 (0.026 at 298.15 K)
Density of air, ρ_{air} (kg/m^3)	p_A*0.02897/8.314/T (1.18 at 298.15 K)
Specific heat capacity of air at constant pressure, $c_{p,air}$ (J/(kg·K))	1047.63657-0.372589265*T^1+9.45304214E-4*T^2-6.02409443E-7*T^3+1.2858961E-10*T^4 (1.01 at 298.15 K)
Porosity of porous matrix, φ_p	0.1
Effective thermal conductivity computing model, k_{eff} (W/m·K)	power law
Refractive index of the medium material, n	2.05
Absorber surface absorptivity at solar band, α_{sb}	0.1, 0.3, 0.5, 0.7, 0.9
Absorber surface absorptivity at ambient band, α_{ab}	0
Ambient emissivity	0
Source heat rate, P_s (W)	1000
Mesh element type	free tetrahedral
Mesh element size	finer

As in model III, air and two blank materials labeled as Conductive Material and Absorber were added. Conductive Material was selected as the material for Thermal conduction layer, Absorber was selected as the material for absorption layer and air was for the gas layer. Several properties were introduced for these three materials and the value ranges or equations are detailed in Tab. 6. 4. Different values were assigned to thermal conductivity (isotropic) of Absorber to explore their influences.

The "Heat transfer in solids and fluids" and the "Radiation in participating media" physics interfaces in heat transfer module were applied for the domains, with stacked spheres as solid part and gas layer as fluid part. For the top boundaries of the spheres in the top layer, labeled as absorption boundaries (Fig. 6. 12), the surface-to-surface radiation physics interface was applied. Furthermore, other settings under these two physics which were coupled in Multiphysics interface remained unchanged from model III.

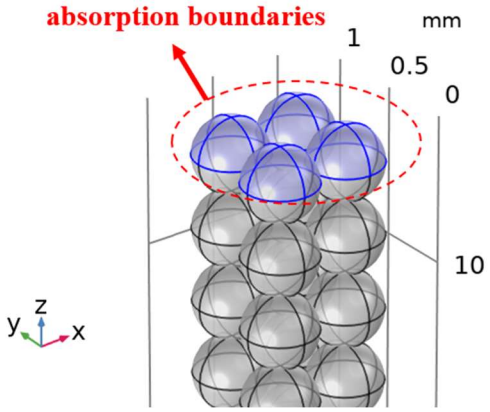

Fig. 6. 12 Absorption boundaries in model IV

In the "Surface-to-surface radiation" physics interface, the surface absorptivity was also defined for solar radiation band ([0, 2.5 μm]) (α_{sb}) and ambient band ([2.5 μm, +∞]) (α_{ab}) in this model. α_{sb} was set to 0.1, 0.3, 0.5, 0.7 and 0.9, in order to explore the emission effect on solar absorption and heat transfer of the composite material. α_{ab} was fixed at 0 as in model III. The external radiation source type was set as "point coordinate", and the source location (x, y, z) was fixed at (0 m, 0 m, 0.2909 m) in the

coordinate considering the total thickness of the geometry to be 11 mm. The source was assigned a blackbody temperature of 5780 K and a heat rate of 1000 W. The physics interfaces assigned to the absorption boundaries were coupled as well under the Multiphysics section.

Due to the geometric settings, the mesh type was selected as free tetrahedral, with an element size chosen as “finer” (Fig. 6. 13). All the relative parameters that needed for solar absorption, heat conduction and thermodynamic calculation are listed in Tab. 6. 4.

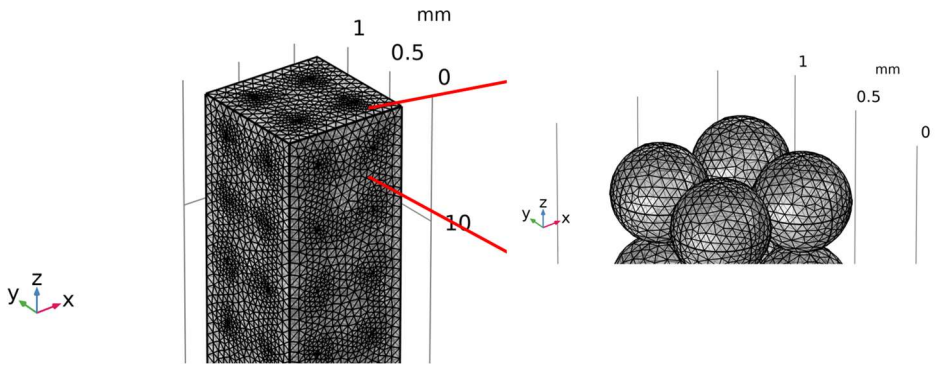

Fig. 6. 13 Mesh of geometry in model IV

6.3.2 Study and solver configuration

The time dependent study step was added to compute domain temperature changes over time. The time-dependent solver was applied where temperature was the dependent variable. The time step was 0.001 min while the time range was 500 min. The relative tolerance was set as 10^{-6} and the factor of absolute tolerance was 0.1 (see Fig. 6. 5). The maximum number of iterations was set to be 20. ΔT was calculated according to Eq. 6. 2 (Chapter 6). Here T_{top} and T_{bottom} were the average temperatures of the absorption boundaries and the bottom boundaries of the bottom layer spheres, respectively (Fig. 6. 14).

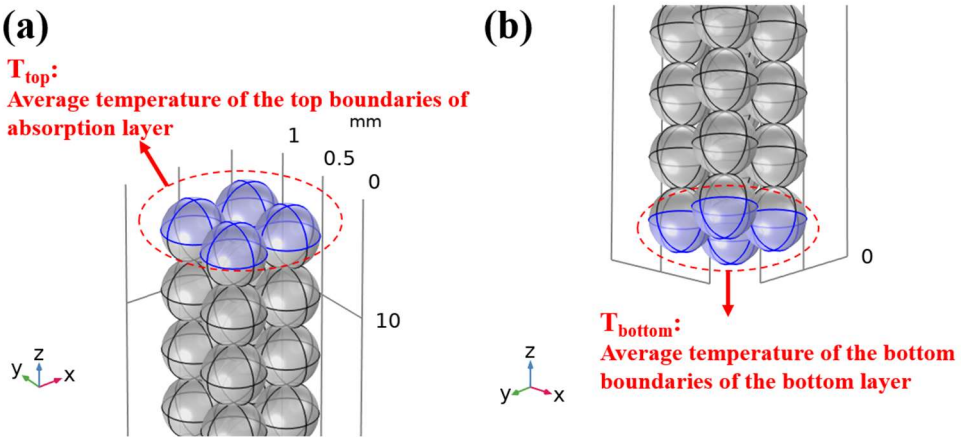

Fig. 6. 14 Schematic diagram of (a) T_{top} and (b) T_{bottom} in model IV

6.3.3 Governing equations and boundary conditions

In model IV, the equations involved in the "Heat transfer in solids and fluids" and "Radiation in participating media" physics for the domains were the same as shown in model III (Section 6.2.3, Chapter 6), and also summarized in Tab. 6. 5. Q stands for the heat source, which is the inward radiative heat flux here.

Tab. 6. 5 Governing equations in model IV

Physics	Governing equations
Heat transfer in solids and fluids (solid domain)	$\rho_s C_{p,s}\frac{\partial T}{\partial t} + \nabla \cdot \boldsymbol{q} = \mathrm{Q} + Q_r + Q_{ted}$ $\boldsymbol{q} = -k_s \nabla T$ $Q_{ted} = -\alpha_s T : \frac{dS}{dt}$
Heat transfer in solids and fluids (fluid domain)	$\rho_f C_{p,f}(\frac{\partial T}{\partial t} + \boldsymbol{u} \cdot \nabla \mathrm{T}) + \nabla \cdot \boldsymbol{q} = \mathrm{Q} + Q_r + Q_p$ $\boldsymbol{q} = -k_f \nabla T$ $Q_p = \alpha_f T\left(\frac{\partial p_A}{\partial t} + u \cdot \nabla p_A\right)$ $\alpha_f = -\frac{1}{\rho_f}\frac{\partial \rho_f}{\partial T}$
Radiation in participating media	$Q_r = \kappa(G - 4\pi I_b(T))$ $\nabla \cdot (D_{p1} \nabla G) = Q_r$

	$D_{P1} = \frac{1}{3(\kappa + \sigma_s)}$
	$I_b(T) = \frac{n^2 \sigma T^4}{\pi}$

For the peripheral, absorption and bottom boundaries, the conditions and equations are summarized in Tab. 6. 6.

Tab. 6. 6 Boundary conditions in model IV

Boundary	Equations
Peripheral boundary	$-\boldsymbol{n} \cdot \boldsymbol{q} = 0$
Absorption boundaries	$J = \sum_{i=1}^{N} J_i$ $J_i = \varepsilon_i e_b(T) FEP_i(T) + \rho_{d,i} G_i$ $\varepsilon_i = \alpha_i = 1 - \rho_{d,i}$ $e_b(T) = n^2 \sigma T^4$ $G_i = G_{m,i} + G_{amb,i} + G_{ext,i}$ $q_{r,net,i} = G_i - J_i = \alpha_i (G_i - e_b(T))$ $q_{r,net} = \sum_{i}^{N} q_{r,net,i}$
Bottom boundaries	$-\boldsymbol{n} \cdot \boldsymbol{q} = q_0$ $q_0 = h(T_{ext} - T)$ $h = \begin{cases} \frac{k_{f-ext}}{L} 0.54 Ra_L^{\frac{1}{4}} & if\ T \le T_{ext}\ and\ 10^4 \le Ra_L \le 10^7 \\ \frac{k_{f-ext}}{L} 0.15 Ra_L^{\frac{1}{3}} & if\ T \le T_{ext}\ and\ 10^7 \le Ra_L \le 10^{11} \\ \frac{k_{f-ext}}{L} 0.27 Ra_L^{\frac{1}{4}} & if\ T > T_{ext}\ and\ 10^5 \le Ra_L \le 10^{10} \end{cases}$ $Ra_L = \frac{g \alpha_{f,ext} \rho_{f,ext}^2 C_{p,ext} (T - T_{ext}) L^3}{k_{f,ext} \mu}$

6.3.4 Results and discussion

For model IV, the simulation results cannot be directly compared with experimental results as the porosity is fixed (detailed in Section 5.3.4.1, Chapter 5) and

cannot be altered. Consequently, this section focuses on comparing the results of model IV with those of model III.

6.3.4.1 Effect of the sphere radius

To investigate the impact of spheres (particles) size on the composite porous pellet solar absorption and heat transfer efficiency, different radius (r_s) values of 0.1, 0.25, 0.5 mm were employed. The steady-state ΔT results corresponding to different radii were utilized as the basis for the research analysis. Fig. 6. 15 shows the isothermal surfaces of geometry at heat transfer steady state when $r_s = 0.25$ mm, $k_{Absorber} = 1$ W/m·K and $\alpha_{sb} = 0.9$. The isothermal surfaces are prominently distributed along the spherical surface within each layer on the xy plane. This indicates that the temperature of the absorption boundaries is all the same, as well as bottom boundaries, enabling the calculation of average temperatures as T_{top} and T_{bottom}.

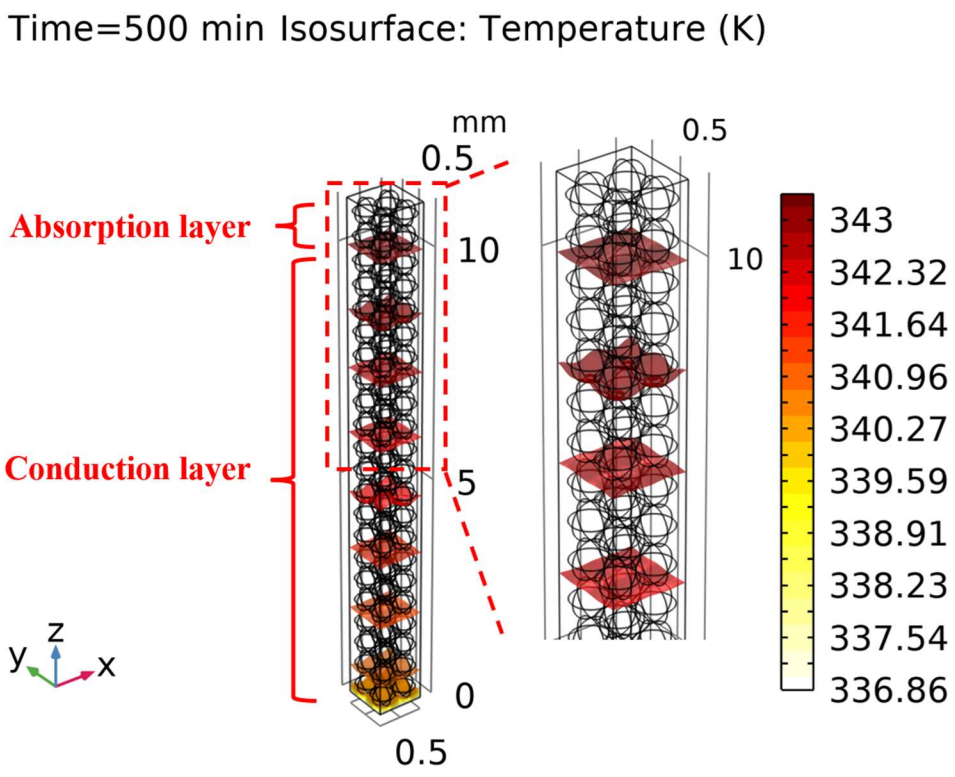

Fig. 6. 15 Isothermal surfaces at steady state

A comparison was conducted with the ΔT value of model III as well. Here, the r_s in model IV was altered across three values: 0.1, 0.25, 0.5 mm. The $k_{Absorber}$ and α_{sb} was constant at 1 W/m·K and 0.9, respectively. The conditions of the thermal conduction layer were listed in Tab. 6. 4. For model III used for comparison, the relevant parameters were set as follows:

-the porosity of porous medium (thermal conduction layer) was changed to 0.48 (same calculation described in Section 5.3.4.1, Chapter 5); its thickness was 10 mm and its thermal conductivity was 100 W/m·K;

-the thickness of absorption layer was 1 mm;

-the $k_{Absorber}$ was 1 W/m·K and the α_{sb} was 0.9.

ΔT for different sphere radii in model IV, as well as ΔT in model III are presented in Fig. 6. 16. In model IV, the overall trend of the ΔT value shows a gradual decrease as the sphere radius increases. When r_s is 0.1 mm, ΔT from model IV is 9.6 K, while that from model III is 7.3 K. In fact, as mentioned in Section 6.2.1 (Chapter 6), model III defined the absorption layer as a solid rather than a porous medium. Therefore, the porosity of the entire geometry in model III here is smaller than that in model IV. Taking into account the difference in porosity, the ΔT value in model III should be higher than 7.3 K and closer to the ΔT value corresponding to a r_s of 0.1 mm in model IV. This comparison aligns well with the analysis of sphere radius effect in the two heat transfer models presented in Section 5.3.4.1 (Chapter 5), where employing a smaller sphere radius might be more practical.

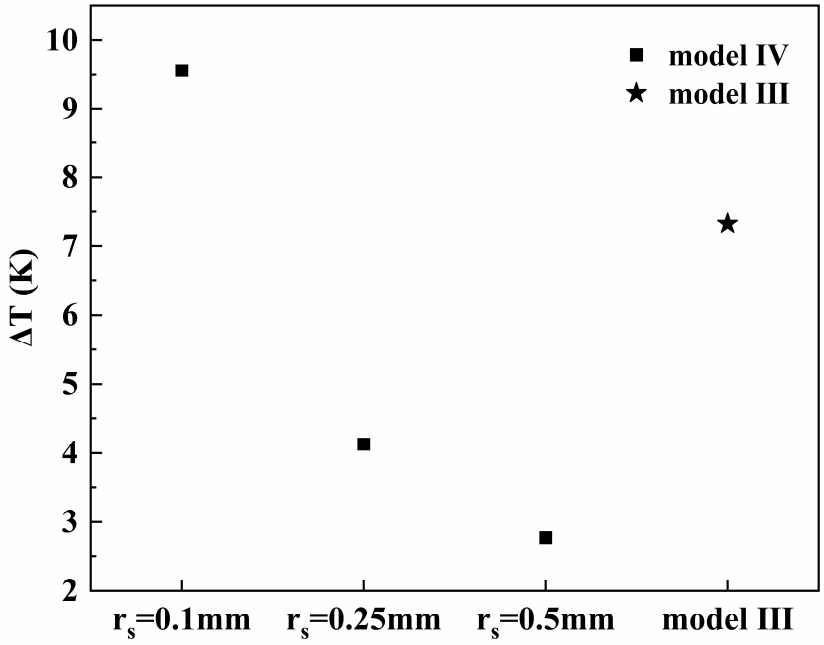

Fig. 6. 16 Comparison of ΔT from model IV with different sphere radii and model III

6.3.4.2 Effect of the thermal conductivity of absorption layer material

The effect of the thermal conductivity of Absorber was also investigated here, with $k_{Absorber}$ set as 1, 50, 100, 200 W/m·K. The sphere radius was 0.25 mm and the Absorber surface absorptivity at solar band was fixed at 0.9. The conditions of the thermal conduction layer were listed in Tab. 6. 4. Due to the unequal overall porosity in model IV and III, a direct comparison between their results under the same remaining parameters was not feasible. Fig. 6. 17 shows the variation of ΔT with different $k_{Absorber}$ values at steady state. When $k_{Absorber}$ is less than 50 W/m·K, there is a noticeable difference in ΔT between 1 W/m·K and 50 W/m·K compared to other $k_{Absorber}$ values. When $k_{Absorber}$ exceeds 50 W/m·K, the ΔT difference according to various $k_{Absorber}$ is extremely small. This trend aligns closely with the findings from the research on the influence of the Absorber thermal conductivity on the solar energy absorption and heat transfer of composite porous pellet in model III. When the value of $k_{Absorber}$ is less than 50 W/m·K, it exerts a significant effect on the heat transfer of pellet; when $k_{Absorber}$ exceeds 50 W/m·K, its impact becomes relatively negligible.

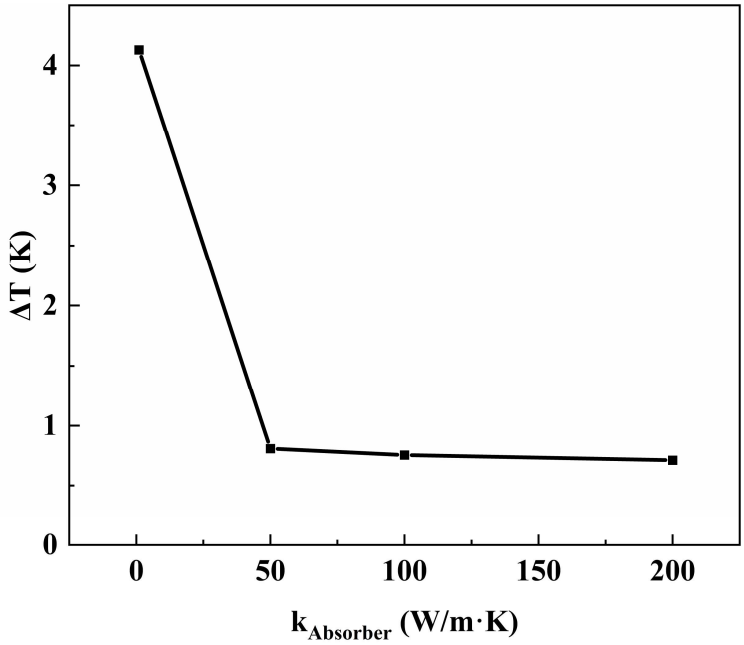

Fig. 6. 17 Effect of $k_{Absorber}$ on ΔT in model IV

6.3.4.3 Effect of the absorption layer surface absorptivity

The effect of the Absorber surface absorptivity at solar band was investigated, with α_{sb} set at 0.1, 0.3, 0.5, 0.7 and 0.9, while the rest of the parameters were fixed. The sphere radius was set as 0.25 mm and the thermal conductivity of Absorber was set as 1 W/m·K. The conditions of the thermal conduction layer were listed in Tab. 6. 4. Fig. 6. 18 presents the variation of ΔT and T_{bottom} with different α_{sb}. A similar trend is observed as in model III (Fig. 6. 10), where both ΔT and T_{bottom} exhibit a proportional increase with the rise in α_{sb}. This could be attributed to the fact that α, which is equivalent to α_{sb}, represents the absorptivity of the irradiated surface, determining the amount of incident radiation absorbed and subsequently affecting the temperature of the pellet. Moreover, in this case where the thickness of absorption layer is 1 mm, the variation of ΔT ranges from 0.6 to 4.1 K.

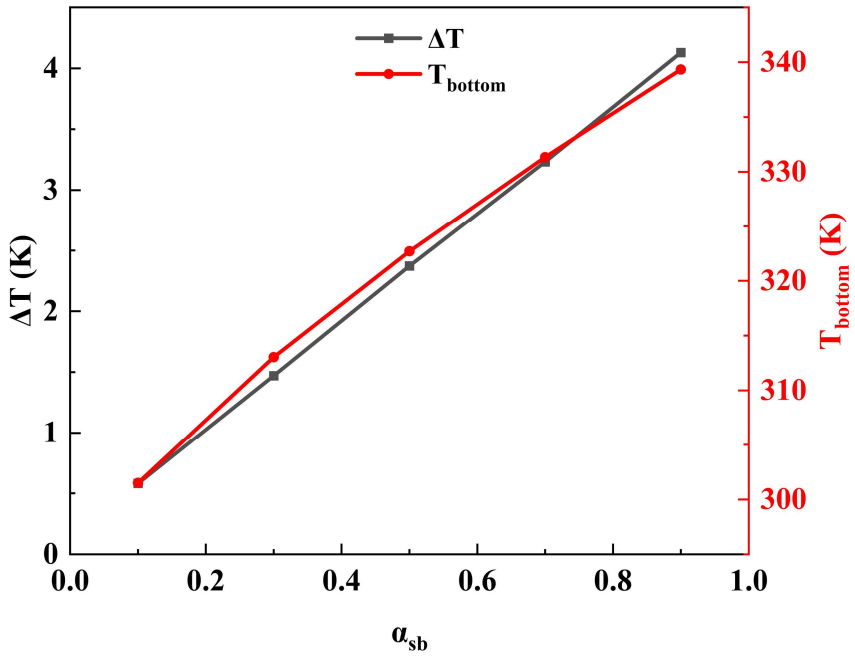

Fig. 6. 18 Effect of α_{sb} on ΔT and T_{bottom} in model IV

6.4 Conclusions

In this chapter, two numerical models of solar absorption and heat transfer in composite porous pellets were established and compared. The model III utilized a continuum approach, while the model IV employed a stacked spheres approach. The simulations focused on investigating the effects of the thickness, thermal conductivity and absorptivity of absorption layer of composite pellet on the solar absorption and heat transfer efficiency. The conclusions can be summarized as follows:

(1) As the thickness of the absorption layer increases, the ΔT of the pellet increases proportionally. A slower rise in the temperature of the composite porous pellet and an extended time required to reach a steady state are also observed.

(2) When the Absorber thermal conductivity is less than 50 W/m·K, the difference in ΔT between different $k_{Absorber}$ increases as $e_{absorption}$ increases. However, when $k_{Absorber}$ exceeds 50 W/m·K, it has minimal effect on the heat transfer efficiency of pellet. Furthermore, the $k_{Absorber}$ does not affect the heating rate of the composite porous pellet.

(3) Both ΔT and T_{bottom} increase proportionally with the increase of absorption layer surface absorptivity, and the temperature rising rate is unaffected as well.

(4) The model IV which is based on stacked spheres acquires similar results to the continuum model (model III). Moreover, utilizing a smaller sphere radius (0.1 mm) proves to be more coherent with the continuum model.

General conclusions

In the present study, new processes and methodologies were proposed to prepare novel composite solar receiver materials applied in solar thermal systems, which consist of the solar absorber layer and thermal conductive substrate. The numerical modeling was also implemented using Finite Element Method to investigate the impact of various factors on the heat transfer process (radiative and conductive) of the porous composite material.

In the experimental section, several ceramic thermal conductive substrates with high thermal conductivity were fabricated by spark plasma sintering. AlN ceramic was prepared by sintering with CaO as the additive. AlN and CaO powders were dry-mixed through a novel high-shear dry-mixer (Picomix) before sintering. The influence of CaO powder properties such as particle size, size distribution, flowability on the mixed powders, and on the porosity and thermal conductivity of AlN pellets, were investigated. The influence of mixing conditions, including additive content and rotational speed of Picomix, were studied. Additionally, different mixing techniques including high-shear mixing, ball milling and manual mixing were compared. Another ceramic, α-SiC, was mixed with CaO and Al_2O_3 additives in the ball mill and then sintered into pellet. Aside from ceramics, Cu pellet was sintered and applied due to its high thermal conductivity. In order to provide anti-oxidation protection and enhance its stability, Cu particles were dry-coated with β-SiC which has high intrinsic thermal conductivity in the Picomix. Stainless steel pellet was also sintered for comparison. Various properties of the prepared powders and pellets, including physical properties, morphology, chemical composition, and thermal properties were characterized. The composite solar receiver materials were prepared based on the above pellets with carbon black as the solar absorption layer due to its high absorptivity. α-SiC-based pellet was directly used without absorbing layer, as SiC exhibited a relative high absorptivity. The performance of the prepared substrate was tested through the conductive heat transfer experiments

using the hot plate. In order to test the solar energy absorption and heat transfer ability of the composite solar receiver materials, a significant effort has been made to design and assemble the solar simulator. This solar simulator was adaptable and applicable for a single lamp up to multiple lamps, thereby adjusting the radiative flux. It can be used for both small and large-sized materials. A high level of security was maintained through the surveillance camera and real-time temperature monitoring throughout the installation. Several experiments were carried out within the solar simulator, with the temperature variation of the samples measured and compared. The conclusions can be summarized as follows:

(1) AlN powders were dry-mixed with CaO sintering additive by a high-shear mixer (Picomix) and then spark plasma sintered. The optimal CaO content was found to be 3 wt% and the optimal rotational speed of the Picomix was 5000 rpm. Under these conditions, the CaO additive could be distributed throughout the AlN powder matrix, forming a homogenous liquid phase and improving the pellet's thermal conductivity. Reduced dimensions of the CaO (especially in the case of submicron- and nano-scale particles) led to coating of the AlN after mixing in the Picomix, which improved the flowability of the mixed powder. This in turn promoted the formation of a continuous liquid phase which encapsulated the AlN particles during sintering, leading to a higher thermal conductivity of the resultant AlN pellets (135.3 W/m·K). Additionally, it confirmed the feasibility of applying nano-scale additives to AlN. When compared with traditional ball milling and manual mixing, the high-shear mixer (Picomix) was found to be substantially superior, as it is a solvent-free process, requires a considerably shorter mixing time, consumes less energy, generates less powder-oxidation. This process is ideally suited for the environmental protection strategies and the application of clean energy.

(2) The α-SiC powder and 9 wt% CaO-Al_2O_3 additive powder were dry-mixed by ball milling and then sintered. The fine CaO particle (submicron-scale) adhered onto the surface of larger α-SiC particles after dry-mixing process, forming a discontinuous

coating. While Al_2O_3 particles were relatively evenly distributed with the mixed powder. When compared with pure α-SiC pellet, the porosity of the pellet with additives decreased from 30% to 22% and the thermal conductivity increased from 57 W/m·K to 114 W/m·K. The reduced number of pores in pellet was also observed, indicating that the additives may facilitate better particle packing and result in a denser microstructure during sintering.

(3) The Cu particles were dry-coated with 2 wt% β-SiC in the Picomix and sintered. The fine β-SiC particles predominantly adhered to the surface of the spherical Cu particle, creating a discontinuous coating. After sintering, the β-SiC phase exhibited a uniform distribution and a good bonding with Cu matrix, resulting in a dense structure and decreased porosity of the pellet. Although the thermal conductivity of the β-SiC coated Cu pellet has decreased, its degree of oxidation has also been relatively reduced. The dry coating process using Picomix may also be an effective method for treating particle surfaces to impart antioxidant properties.

(4) Heat transfer experiments showed that when the thickness of the thermal conductive substrate was small, the thermal conductivity might have little effect on its heat transfer efficiency.

(5) The self-constructed solar simulator installation ran well and showed a high irradiance with approximately 6753 W/m^2 when the lamp power was 1000 W. Through comparative analysis of temperature under identical experimental conditions, it was demonstrated that both AlN+3%$CaO^{0.04}$(5000rpm,5min,pellet) with carbon black layer and α-SiC+9%CaO-Al_2O_3(BM,pellet) exhibited notable solar energy absorption, as well as efficient heat transfer properties. This indicated their utilization potential in solar thermal applications.

In the numerical modeling section, two types of models were set up to study the heat transfer process (conductive, coupling of radiative and conductive) of the porous material due to the size limitation of the pellet. For each type of model, two geometric shapes were set for simulating the pellet. One assumed the geometry as a solid matrix

with uniformly distributed average porosity, while the other considered the pellet as a composition of orderly stacked spherical particles with a consistent porosity. The effects of various parameters, including porosity, thermal conductivity, thickness, and absorptivity were analyzed. The conclusions can be summarized as follows:

(1) When the pellet's porosity was 0.1, and thickness was less than 100 mm, the heat transfer efficiency of the porous pellet could not be greatly improved even if the material thermal conductivity continued to rise beyond 100 W/m·K. When the pellet thickness was less than 50 mm, this value was around 50 W/m·K.

(2) In the situation where the pellet's thickness was 10 mm, and porosity was less than 0.3, a relatively low material thermal conductivity (around 50 W/m·K) might achieve high-efficiency of pellet heat transfer, and raising this conductivity would not significantly enhance the heat transfer efficiency.

(3) When the pellet's porosity exceeded 0.1, the thickness became highly critical and a smaller thickness had a greater impact on the heat transfer efficiency of the porous pellet.

(4) As the thickness of the absorption layer increased, the ΔT of the pellet increased proportionally. A slower rise in the temperature of the composite porous pellet and an extended time required to reach a steady state were also observed.

(5) The difference in ΔT between different $k_{Absorber}$ increased as $e_{absorption}$ increased when the Absorber thermal conductivity was less than 50 W/m·K. However, when $k_{Absorber}$ exceeded 50 W/m·K, it had minimal effect on the heat transfer efficiency of pellet. Furthermore, the $k_{Absorber}$ did not affect the heating rate of the composite porous pellet.

(6) Both ΔT and T_{bottom} increased proportionally with the increase of absorption layer surface absorptivity, and the temperature rising rate was unaffected as well.

(7) The model based on stacked spheres acquired similar results to the continuum model. Moreover, utilizing a smaller sphere radius (0.1 mm) proved to be more feasible.

Researches in the field of solar thermal applications is continuously evolving and progressing. For example, in France, the PROMES (Procédés Matériaux et Energie Solaire) laboratory has been developing fluidized bed solar receivers since 2010 (G. Flamant and his team), using a suspension of solid particles as the heat transfer fluid and reaching temperatures of 700 °C at the outlet. The results of this work will enable the advancement and development of strategies for solar thermal applications such as house heating, industrial production and electricity generation, providing sustainable solutions for energy utilization. These advances are crucial for harnessing solar energy more efficiently and facilitating the transition to clean, renewable energies.

Perspectives

This study presented a novel methodology, for preparing several thermal conductive substrates with enhanced thermal conductivity and applicability utilized in the solar thermal system. The thermal performance of the composite solar receiver materials with carbon black as absorption layer was tested through a self-constructed solar simulator. The finite element method was employed to simulate the solar energy absorption and heat transfer of the porous solar receiver materials. However, the research still presents the following issues that need further exploration and improvement:

(1) In the process of utilizing Picomix for dry mixing/coating, there are also some factors worth studying. For instance, investigating the impact of air resistance on particle behavior during shearing would be valuable.

(2) It is essential to explore alternative techniques for the preparation of materials with larger sizes. Previous attempts to utilize 3D printing (Admaflex 130, Admatec, the Netherlands) in Centrale Lille for material manufacturing have been unsuccessful, due to its specific requirements for raw powders and time constraints. Hence, exploring the application of this technique to achieve a broader range of material sizes is a promising area for further research.

(3) The viability of incorporating graphite into ceramics to prepare thermal conductive substrates for solar thermal application is a potential avenue for further investigation.

(4) When testing the heat transfer capabilities of materials, a well-designed heat exchanger should be incorporated to obtain precise and reliable data.

(5) The current solar simulator needs to be enhanced in various ways:

-Addition of a water-cooled sensor that measures high-level radiative and convective heat fluxes (HFS01, Hukseflux);

-Integrating an infrared camera to detect and visualize temperature variation inside and around the solar simulator;

-Reconstructing the ellipsoidal and secondary truncated hexagonal pyramid reflectors using oxidation-resistant materials;

-Employing more QTH lamps to achieve higher radiative heat flux.

(6) The efforts should be made to improve the durability, efficiency and stability of these coatings in order to optimize the conversion of solar energy into heat.

(7) The numerical modelling needs to take account of all the parameters that affect radiative heat transfer:

-Applying a model that takes into account the real distribution of pores within the material;

-Integrating the convection resulting from the radiant heating of the air surrounding the material;

-Estimating the heat loss and optimizing the heat exchange considering the material type.

References

1. Climate Change 2014: Mitigation of Climate Change; Intergovernmental Panel on Climate Change, Geneva, Switzerland, **2015**.
2. K. Qin, B. Dong, S. Wang. Improving the stability of metal halide perovskite solar cells from material to structure. *Journal of energy chemistry* **2019**, 33, 90–99.
3. G.O.G. Löf, J.A. Duffie, C.O. Smith. World distribution of solar radiation. *Solar Energy* **1966**, 10 (1), 27–37.
4. N. Kannan, D. Vakeesan. Solar energy for future world: - A review. *Renewable and Sustainable Energy Reviews* **2016**, 62, 1092–1105.
5. E. Kabir, P. Kumar, S. Kumar, A.A. Adelodun, K.-H. Kim. Solar energy: Potential and future prospects. *Renewable and Sustainable Energy Reviews* **2018**, 82, 894–900.
6. S. Mekhilef, R. Saidur, A. Safari. A review on solar energy use in industries. *Renewable and Sustainable Energy Reviews* **2011**, 15 (4), 1777–1790.
7. L. Zhu, M. Gao, C.K.N. Peh, G.W. Ho. Solar-driven photothermal nanostructured materials designs and prerequisites for evaporation and catalysis applications. *Materials Horizons* **2018**, 5 (3), 323–343.
8. K. Ravi Kumar, N.V.V. Krishna Chaitanya, N. Sendhil Kumar. Solar thermal energy technologies and its applications for process heating and power generation – A review. *Journal of Cleaner Production* **2021**, 282, 125296.
9. Y. Tian, C.Y. Zhao. A review of solar collectors and thermal energy storage in solar thermal applications. *Applied Energy* **2013**, 104, 538–553.
10. H. Tanaka. Solar thermal collector augmented by flat plate booster reflector: Optimum inclination of collector and reflector. *Applied Energy* **2011**, 88 (4), 1395–1404.
11. L. Kumar, M. Hasanuzzaman, N.A. Rahim. Global advancement of solar thermal energy technologies for industrial process heat and its future prospects: A review. *Energy Conversion and Management* **2019**, 195, 885–908.
12. D.Y. Goswami. Principles of Solar Engineering, 4th ed.; CRC Press, Boca Raton, **2022**.
13. R. Dobriyal, P. Negi, N. Sengar, D.B. Singh. A brief review on solar flat plate collector by incorporating the effect of nanofluid. *Materials Today: Proceedings* **2020**, 21, 1653–1658.
14. R. Foster, M. Ghassemi, A. Cota. Solar Energy: Renewable Energy and the Environment; CRC Press, Boca Raton, **2009**.

15. S. Suman, Mohd.K. Khan, M. Pathak. Performance enhancement of solar collectors—A review. *Renewable and Sustainable Energy Reviews* **2015**, 49, 192–210.

16. Evacuated Tube Collector for Solar Hot Water System https://www.alternative-energy-tutorials.com/solar-hot-water/evacuated-tube-collector.html (accessed Apr 2, 2023).

17. H.L. Zhang, J. Baeyens, J. Degrève, G. Cacères. Concentrated solar power plants: Review and design methodology. *Renewable and Sustainable Energy Reviews* **2013**, 22, 466–481.

18. A.C. Plaza. Accelerated aging and durability of selective materials for concentrating solar power plant receivers. phdthesis, Université de Perpignan, **2021**.

19. M.J. Blanco, S. Miller. Introduction to concentrating solar thermal (CST) technologies. In *Advances in Concentrating Solar Thermal Research and Technology*; Blanco, M. J., Santigosa, L. R., Eds.; Woodhead Publishing Series in Energy; Woodhead Publishing, **2017**; pp 3–25.

20. N.E. Gharbi, H. Derbal, S. Bouaichaoui, N. Said. A comparative study between parabolic trough collector and linear Fresnel reflector technologies. *Energy Procedia* **2011**, 6, 565–572.

21. G. Flamant. Solar Power Plants: State of the Art. In *Concentrating Solar Thermal Energy*; John Wiley & Sons, Ltd, **2022**; pp 1–43.

22. F. Gomez-Garcia, D. Gauthier, G. Flamant. Design and performance of a multistage fluidised bed heat exchanger for particle-receiver solar power plants with storage. *Applied Energy* **2017**, 190, 510–523.

23. G. Flamant, D. Gauthier, H. Benoit, et al. Dense suspension of solid particles as a new heat transfer fluid for concentrated solar thermal plants: On-sun proof of concept. *Chemical Engineering Science* **2013**, 102, 567–576.

24. O. Behar, B. Grange, G. Flamant. Design and performance of a modular combined cycle solar power plant using the fluidized particle solar receiver technology. *Energy Conversion and Management* **2020**, 220, 113108.

25. G. Colomer, J. Chiva, O. Lehmkuhl, A. Oliva. Advanced CFD&HT Numerical Modeling of Solar Tower Receivers. *Energy Procedia* **2014**, 49, 50–59.

26. L.M. Ayompe, A. Duffy, M. Mc Keever, M. Conlon, S.J. McCormack. Comparative field performance study of flat plate and heat pipe evacuated tube collectors (ETCs) for domestic water heating systems in a temperate climate. *Energy* **2011**, 36 (5), 3370–3378.

27. S. Faisal Ahmed, M. Khalid, M. Vaka, et al. Recent progress in solar water heaters and solar collectors: A comprehensive review. *Thermal Science and Engineering Progress* **2021**, 25, 100981.

28. A.M. El-Sawi, A.S. Wifi, M.Y. Younan, E.A. Elsayed, B.B. Basily. Application of folded sheet metal in flat bed solar air collectors. *Applied Thermal Engineering* **2010**, 30 (8), 864–871.

29. A. Abdelhamid. Solar Heating and Cooling Your Home & Business https://cleantechnica.com/2015/05/04/solar-thermal-panels-heating-cooling/ (accessed Apr 3, 2023).

30. A. Bhagwati, M. Shah, M. Prajapati. Emerging technologies to sustainability: A comprehensive study on solar desalination for sustainable development. *Sustainable Manufacturing and Service Economics* **2023**, 100007.

31. F. Selimefendigil, C. Şirin, H.F. Öztop. Experimental analysis of combined utilization of CuO nanoparticles in latent heat storage unit and absorber coating in a single-slope solar desalination system. *Solar Energy* **2022**, 233, 278–286.

32. T. Arunkumar, A.E. Kabeel, K. Raj, et al. Productivity enhancement of solar still by using porous absorber with bubble-wrap insulation. *Journal of Cleaner Production* **2018**, 195, 1149–1161.

33. Y. Zheng, R.A. Caceres Gonzalez, K.B. Hatzell, M.C. Hatzell. Large-scale solar-thermal desalination. *Joule* **2021**, 5 (8), 1971–1986.

34. W. Fuqiang, M. Lanxin, C. Ziming, et al. Radiative heat transfer in solar thermochemical particle reactor: A comprehensive review. *Renewable and Sustainable Energy Reviews* **2017**, 73, 935–949.

35. M. Alvarez Rivero, D. Rodrigues, C.I.C. Pinheiro, J.P. Cardoso, L.F. Mendes. Solid–gas reactors driven by concentrated solar energy with potential application to calcium looping: A comparative review. *Renewable and Sustainable Energy Reviews* **2022**, 158, 112048.

36. M. Shahabuddin, M.A. Alim, T. Alam, et al. A critical review on the development and challenges of concentrated solar power technologies. *Sustainable Energy Technologies and Assessments* **2021**, 47, 101434.

37. J. Costandy, N. El Ghazal, M.T. Mohamed, et al. Effect of reactor geometry on the temperature distribution of hydrogen producing solar reactors. *International Journal of Hydrogen Energy* **2012**, 37 (21), 16581–16590.

38. T. Melchior, C. Perkins, P. Lichty, A.W. Weimer, A. Steinfeld. Solar-driven biochar gasification in a particle-flow reactor. *Chemical Engineering and Processing: Process Intensification* **2009**, 48 (8), 1279–1287.

39. X. Li, L. Wei, C.W. Lim, et al. Experimental and numerical study on thermal performance of an indirectly irradiated solar reactor with a clapboard-type internally circulating fluidized bed. *Applied Energy* **2022**, 305, 117976.

40. S. Sobek, S. Werle. Solar pyrolysis of waste biomass: Part 1 reactor design. *Renewable Energy* **2019**, 143, 1939–1948.

41. Q. Bellouard, S. Abanades, S. Rodat, N. Dupassieux. Solar thermochemical gasification of wood biomass for syngas production in a high-temperature continuously-fed tubular reactor. *International Journal of Hydrogen Energy* **2017**, 42 (19), 13486–13497.

42. M. Shahabuddin, M.A. Alim, T. Alam, et al. A critical review on the development and challenges of concentrated solar power technologies. *Sustainable Energy Technologies and Assessments* **2021**, 47, 101434.

43. N.S. Fuzil, N.H. Othman, N.H. Alias, et al. A review on photothermal material and its usage in the development of photothermal membrane for sustainable clean water production. *Desalination* **2021**, 517, 115259.

44. M. Gao, L. Zhu, C.K. Peh, G.W. Ho. Solar absorber material and system designs for photothermal water vaporization towards clean water and energy production. *Energy & Environmental Science* **2019**, 12 (3), 841–864.

45. Y. Zhang, Y.-J. Heo, Y.-R. Son, et al. Recent advanced thermal interfacial materials: A review of conducting mechanisms and parameters of carbon materials. *Carbon* **2019**, 142, 445–460.

46. Z. Xie, Y. Duo, Z. Lin, et al. The Rise of 2D Photothermal Materials beyond Graphene for Clean Water Production. *Advanced Science* **2020**, 7 (5), 1902236.

47. F.P. Incropera, D.P. DeWitt, T.L. Bergman, A.S. Lavine. Fundamentals of heat and mass transfer, 6th ed.; John Wiley&Sons, the United States of America, **1996**.

48. P. Satvasheel. Characterizing Performance of Dye Sensitized Solar Cells, Dalarna University, **2005**.

49. Standard Tables for Reference Solar Spectral Irradiances: Direct Normal and Hemispherical on 37° Tilted Surface.

50. Nitride solar cell achieves peak EQE of 72% https://www.semiconductor-today.com/news_items/2011/JAN/UCSB_200111.htm (accessed Apr 8, 2023).

51. Solar energy — Reference solar spectral irradiance at the ground at different receiving conditions — Part 1: Direct normal and hemispherical solar irradiance for air mass 1.5 https://www.iso.org/obp/ui/#iso:std:iso:9845:-1:ed-2:v1:en (accessed Apr 9, 2023).

52. X. Wu, G.Y. Chen, G. Owens, D. Chu, H. Xu. Photothermal materials: A key platform enabling highly efficient water evaporation driven by solar energy. *Materials Today Energy* **2019**, 12, 277–296.

53. A. Guo, Y. Fu, G. Wang, X. Wang. Diameter effect of gold nanoparticles on photothermal conversion for solar steam generation. *RSC Adv.* **2017**, 7 (8), 4815–4824.

54. P. Fan, H. Wu, M. Zhong, et al. Large-scale cauliflower-shaped hierarchical copper nanostructures for efficient photothermal conversion. *Nanoscale* **2016**, 8 (30), 14617–14624.

55. V. Amendola, R. Saija, O.M. Maragò, M.A. Iatì. Superior plasmon absorption in iron-doped gold nanoparticles. *Nanoscale* **2015**, 7 (19), 8782–8792.

56. W.F. Bogaerts, C.M. Lampert. Materials for photothermal solar energy conversion. *J Mater Sci* **1983**, 18 (10), 2847–2875.

57. B.P. Kafle, B. Basnet, B. Timalsina, et al. Optical, structural and thermal performances of black nickel selective coatings for solar thermal collectors. *Solar Energy* **2022**, 234, 262–274.

58. M. Ye, J. Jia, Z. Wu, et al. Synthesis of Black TiO_x Nanoparticles by Mg Reduction of TiO_2 Nanocrystals and their Application for Solar Water Evaporation. *Advanced Energy Materials* **2017**, 7 (4), 1601811.

59. J. Moon, T.K. Kim, B. VanSaders, et al. Black oxide nanoparticles as durable solar absorbing material for high-temperature concentrating solar power system. *Solar Energy Materials and Solar Cells* **2015**, 134, 417–424.

60. S. Ge-Zhang, H. Yang, H. Mu. Interfacial solar steam generator by MWCNTs/carbon black nanoparticles coated wood. *Alexandria Engineering Journal* **2023**, 63, 1–10.

61. K.-T. Lin, H. Lin, T. Yang, B. Jia. Structured graphene metamaterial selective absorbers for high efficiency and omnidirectional solar thermal energy conversion. *Nat Commun* **2020**, 11 (1), 1389.

62. X. Li, W. Xu, M. Tang, et al. Graphene oxide-based efficient and scalable solar desalination under one sun with a confined 2D water path. *Proceedings of the National Academy of Sciences* **2016**, 113 (49), 13953–13958.

63. J. Yang, J. Choi, D. Bang, et al. Convertible Organic Nanoparticles for Near-Infrared Photothermal Ablation of Cancer Cells. *Angewandte Chemie International Edition* **2011**, 50 (2), 441–444.

64. K. Wang, Z. Cheng, P. Li, et al. Three-dimensional self-floating foam composite impregnated with porous carbon and polyaniline for solar steam generation. *Journal of Colloid and Interface Science* **2021**, 581, 504–513.

65. L. Zhang, B. Tang, J. Wu, R. Li, P. Wang. Hydrophobic Light-to-Heat Conversion Membranes with Self-Healing Ability for Interfacial Solar Heating. *Advanced Materials* **2015**, 27 (33), 4889–4894.

66. X. Wu, G.Y. Chen, W. Zhang, X. Liu, H. Xu. A Plant-Transpiration-Process-Inspired Strategy for Highly Efficient Solar Evaporation. *Advanced Sustainable Systems* **2017**, 1 (6), 1700046.

67. J. Wang, Y. Li, L. Deng, et al. High-performance photothermal conversion of narrow-bandgap Ti_2O_3 nanoparticles. *Advanced Materials* **2017**, 29 (3), 1–6.

68. Q. Liao, P. Zhang, H. Yao, et al. Reduced Graphene Oxide–Based Spectrally Selective Absorber with an Extremely Low Thermal Emittance and High Solar Absorptance. *Advanced Science* **2020**, 7 (8), 1903125.

69. R.N. Abed, N.K. Al-Sahib, A.J. N.Khalifa. Utilizing nano-material in selective surfaces to scalable up the absorptivity. *IJREI* **2017**, 1 (3), 142–149.

70. L. Noč, I. Jerman. Review of the spectrally selective (CSP) absorber coatings, suitable for use in SHIP. *Solar Energy Materials and Solar Cells* **2022**, 238, 111625.

71. C. Atkinson, C.L. Sansom, H.J. Almond, C.P. Shaw. Coatings for concentrating solar systems–A review. *Renewable and Sustainable Energy Reviews* **2015**, 45, 113–122.

72. N. Selvakumar, H.C. Barshilia. Review of physical vapor deposited (PVD) spectrally selective coatings for mid- and high-temperature solar thermal applications. *Solar Energy Materials and Solar Cells* **2012**, 98, 1–23.

73. F. Cao, K. McEnaney, G. Chen, Z. Ren. A review of cermet-based spectrally selective solar absorbers. *Energy Environ. Sci.* **2014**, 7 (5), 1615–1627.

74. C. Uher. Thermal Conductivity of Metals. In *Thermal Conductivity: Theory, Properties, and Applications*; Tritt, T. M., Ed.; Physics of Solids and Liquids; Springer US, Boston, MA, **2004**; pp 21–91.

75. What is thermal conduction? https://techtimes.dexerials.jp/en/electronics/heat-conduction/ (accessed Apr 17, 2023).

76. K. Xu, M. Du, L. Hao, et al. A review of high-temperature selective absorbing coatings for solar thermal applications. *Journal of Materiomics* **2020**, 6 (1), 167–182.

77. T. Arunkumar, D. Murugesan, K. Raj, et al. Effect of nano-coated CuO absorbers with PVA sponges in solar water desalting system. *Applied Thermal Engineering* **2019**, 148, 1416–1424.

78. H. El Aakib, N. Rochdi, J.F. Pierson, A. Outzourhit. Reactively sputtered cobalt oxide coatings for solar selective absorber applications. *Materials Today: Proceedings* **2021**, 39, 1157–1162.

79. Y. Deng, J. Li, T. Qian, et al. Thermal conductivity enhancement of polyethylene glycol/expanded vermiculite shape-stabilized composite phase change materials with silver nanowire for thermal energy storage. *Chemical Engineering Journal* **2016**, 295, 427–435.

80. A. Sommers, Q. Wang, X. Han, et al. Ceramics and ceramic matrix composites for heat exchangers in advanced thermal systems—A review. *Applied Thermal Engineering* **2010**, 30 (11), 1277–1291.

81. Z. Li, L. Wang, Y. Li, Y. Feng, W. Feng. Carbon-based functional nanomaterials: Preparation, properties and applications. *Composites Science and Technology* **2019**, 179, 10–40.

82. S.A. Memon, H. Cui, T.Y. Lo, Q. Li. Development of structural–functional integrated concrete with macro-encapsulated PCM for thermal energy storage. *Applied Energy* **2015**, 150, 245–257.

83. Z. Said, R. Saidur, M.A. Sabiha, N.A. Rahim, M.R. Anisur. Thermophysical properties of Single Wall Carbon Nanotubes and its effect on exergy efficiency of a flat plate solar collector. *Solar Energy* **2015**, 115, 757–769.

84. H. Yoon, P. Matteini, B. Hwang. Review on three-dimensional ceramic filler networking composites for thermal conductive applications. *Journal of Non-Crystalline Solids* **2022**, 576, 121272.

85. S. Chen, Y. Chen, Y. Zhao, et al. Status and strategies for fabricating flexible oxide ceramic micro-nanofiber materials. *Materials Today* **2022**, 61, 139–168.

86. R. Ma, D. Ma, E. Long. Experimental study on the dynamic thermal performance of V-Ti black ceramic solar collector under multiple factors. *Solar Energy* **2020**, 201, 615–620.

87. M. Zukowski, G. Woroniak. Experimental testing of ceramic solar collectors. *Solar Energy* **2017**, 146, 532–542.

88. Y. Yang, S. Cao, J. Xu, B. Cai. All-ceramic solar collectors. *Ceramics International* **2013**, 39 (5), 6009–6012.

89. X. Liu, H. Wang, Q. Xu, et al. High thermal conductivity and high energy density compatible latent heat thermal energy storage enabled by porous AlN ceramics composites. *International Journal of Heat and Mass Transfer* **2021**, 175, 121405.

90. W. Chen, C. Zou, X. Li, L. Li. Experimental investigation of SiC nanofluids for solar distillation system: Stability, optical properties and thermal conductivity with saline water-based fluid. *International Journal of Heat and Mass Transfer* **2017**, 107, 264–270.

91. L. Fan, J.M. Khodadadi. Thermal conductivity enhancement of phase change materials for thermal energy storage: a review. *Renewable and Sustainable Energy Reviews* **2011**, 15 (1), 24–46.

92. I.-L. Ngo, S. Jeon, C. Byon. Thermal conductivity of transparent and flexible polymers containing fillers: a literature review. *International journal of heat and mass transfer* **2016**, 98, 219–226.

93. Y. Lin, Y. Jia, G. Alva, G. Fang. Review on thermal conductivity enhancement, thermal properties and applications of phase change materials in thermal energy storage. *Renewable and Sustainable Energy Reviews* **2018**, 82, 2730–2742.

94. Y. Chang, X. Yao, Y. Chen, L. huang, D. Zou. Review on ceramic-based composite phase change materials: Preparation, characterization and application. *Composites Part B: Engineering* **2023**, 254, 110584.

95. D.H.A. Besisa, E.M.M. Ewais, Y.M.Z. Ahmed, et al. Densification and characterization of SiC-AlN composites for solar energy applications. *Renewable Energy* **2018**, 129, 201–213.

96. R. Yu, G. Liu, G. Wang, et al. Ultrawide-bandgap semiconductor AlN crystals: growth and applications. *J. Mater. Chem. C* **2021**, 9 (6), 1852–1873.

97. P.O. Jarvinen. Solar-heated-air receivers. *Solar Energy* **1977**, 19 (2), 139–147.

98. Y.-L. He, S. Du, S. Shen. Advances in porous volumetric solar receivers and enhancement of volumetric absorption. *Energy Reviews* **2023**, 2 (3), 100035.

99. S. Chen, L. Brown, M. Levendorf, et al. Oxidation Resistance of Graphene-Coated Cu and Cu/Ni Alloy. *ACS Nano* **2011**, 5 (2), 1321–1327.

100. M.N. Rahaman. Sintering of Ceramics; CRC Press, Boca Raton, **2013**.

101. A.I. Kadim. Electrical Properties & Microstructure Of ZnO-Based Varistor Ceramics Doped With Rare Earth, University of Baghdad, **2015**.

102. T. Molla. Modeling Macroscopic Shape Distortions during Sintering of Multi-layers. PhD thesis, University of Melbourne, **2014**.

103. C.V. Nguyen, S.K. Sistla, S.V. Kempen, et al. A comparative study of different sintering models for Al_2O_3. *Journal of the Ceramic Society of Japan* **2016**, 124 (4), 301–312.

104. A. Lakshmanan. Sintering of Ceramics - New Emerging Techniques; IntechOpen, **2012**.

105. Z.A. Munir, U. Anselmi-Tamburini, M. Ohyanagi. The effect of electric field and pressure on the synthesis and consolidation of materials: A review of the spark plasma sintering method. *J Mater Sci* **2006**, 41 (3), 763–777.

106. G.A. Slack. Nonmetallic crystals with high thermal conductivity. *Journal of Physics and Chemistry of Solids* **1973**, 34 (2), 321–335.

107. D. Huang, Z. Tian, W. Cui, et al. Effects of Y_2O_3 and yttrium aluminates as sintering additives on the thermal conductivity of AlN ceramic substrates. *Ceramics International* **2018**, 44 (16), 20556–20559.

108. Z. Cheng, Y.R. Koh, A. Mamun, et al. Experimental observation of high intrinsic thermal conductivity of AlN. *Physical Review Materials* **2020**, 4 (4), 1–7.

109. R.M. German, P. Suri, S.J. Park. Review: liquid phase sintering. *J Mater Sci* **2009**, 44 (1), 1–39.

110. A.L. Molisani, H. Goldenstein, H.N. Yoshimura. The role of CaO additive on sintering of aluminum nitride ceramics. *Ceramics International* **2017**, 43 (18), 16972–16979.

111. A. Chen, M. Li, J. Wu, et al. Enhancement mechanism of mechanical performance of highly porous mullite ceramics with bimodal pore structures prepared by selective laser sintering. *Journal of Alloys and Compounds* **2019**, 776, 486–494.

112. A.S. Ganie, S. Bano, N. Bashar, et al. Chapter 8 - Piezoelectric ceramics: Advanced applications in electrochemical and electronic fields. In *Advanced Ceramics for Versatile Interdisciplinary Applications*; Singh, S., Kumar, P., Mondal, D. P., Eds.; Elsevier Series on Advanced Ceramic Materials; Elsevier, **2022**; pp 167–179.

113. K. Watari, M.C. Valecillos, M.E. Brito, M. Toriyama, S. Kanzaki. Densification and Thermal Conductivity of AIN Doped with Y_2O_3, CaO, and Li_2O. *Journal of the American Ceramic Society* **1996**, 79 (12), 3103–3108.

114. A.L. Molisani, H.N. Yoshimura, H. Goldenstein, K. Watari. Effects of $CaCO_3$ content on the densification of aluminum nitride. *Journal of the European Ceramic Society* **2006**, 26 (15), 3431–3440.

115. A.L. Molisani, H.N. Yoshimura, H. Goldenstein. Sintering mechanisms in aluminum nitride with Y or Ca-containing additive. *Journal of Materials Science: Materials in Electronics* **2009**, 20 (1), 1–8.

116. H.-S. Kim, Y.-W. Kim. Thermal conductivity of liquid-phase sintered silicon carbide ceramics: A review. *Journal of the European Ceramic Society* **2023**, 43 (9), 3855–3874.

117. J. Qiu, Y. Hotta, K. Watari, K. Mitsuishi. Enhancement of Densification and Thermal Conductivity in AlN Ceramics by Addition of Nano-Sized Particles. *Journal of the American Ceramic Society* **2006**, 89 (1), 377–380.

118. H.-J. Lee, W.-S. Cho, H.J. Kim, et al. Effect of Additive Size on the Densification and Thermal Conductivity of AlN Ceramics with $MgO–CaO–Al_2O_3–SiO_2$ Additives. *J. Korean Ceram. Soc* **2017**, 54 (1), 43–48.

119. Y.-K. Seo, Y.-W. Kim, T. Nishimura, W.-S. Seo. High thermal conductivity of spark plasma sintered silicon carbide ceramics with yttria and scandia. *Journal of the American Ceramic Society* **2017**, 100 (4), 1290–1294.

120. M. Alonso, F.J. Alguacil. Dry mixing and coating of powders. *Revista de Metalurgia* **1999**, 35 (5), 315–328.

121. J.A. Hersey. Ordered mixing: A new concept in powder mixing practice. *Powder Technology* **1975**, 11 (1), 41–44.

122. X. Liu. Conception en voie sèche de catalyseurs propres Co/Al_2O_3 pour la synthèse Fischer-Tropsch et modélisation numérique DEM. These de doctorat, Ecole centrale de Lille, **2018**.

123. M.U. Ghori, B. Conway. Triboelectrification of Pharmaceutical powders: A critical review. *British Journal of Pharmacy* **2018**, 3 (1).

124. J. Fitz-Gerald, R.K. Singh, H. Gao, S.J. Pennycook. Nanometric Dry Powder Coatings Using a Novel Process. *KONA Powder and Particle Journal* **1999**, 17, 173–182.

125. V.A. Saharan, K. V, M. Kataria, V. Kharb, P. Choudhury. Ordered Mixing: Mechanism, Process and Applications in Pharmaceutical Formulations. *Asian J. Pharm. Sci.* **2008**, 3, 240–259.

126. M. Kumar, X. Xiong, Z. Wan, et al. Ball milling as a mechanochemical technology for fabrication of novel biochar nanomaterials. *Bioresource Technology* **2020**, 312, 123613.

127. M. Lu. New technology development for advanced “Clean” solid catalysts for Fischer-Tropsch synthesis. These de doctorat, Université Lille 1, **2015**.

128. C. C. Piras, S. Fernández-Prieto, W.M.D. Borggraeve. Ball milling: a green technology for the preparation and functionalisation of nanocellulose derivatives. *Nanoscale Advances* **2019**, 1 (3), 937–947.

129. R.S. Fediuk, R.A. Ibragimov, V.S. Lesovik, et al. Processing equipment for grinding of building powders. *IOP Conf. Ser.: Mater. Sci. Eng.* **2018**, 327 (4), 042029.

130. S. Xi, P. Zhang, Y. Huang, et al. Laser sintering of cryogenically ground polymer powders into high-performance parts: The role of dry particle coating with a conductive flow agent. *Polymer* **2020**, 186, 1–10.

131. S. AKPINAR. Characterization of surface properties of dry-coated anhydrous borax powders. *Journal of Boron* **2020**, 5 (3), 131–143.

132. R. Kobayashi, Y. Nakajima, K. Mochizuki, et al. Densification of AlN ceramics by spark plasma sintering under 1550 °C. *Advanced Powder Technology* **2016**, 27 (3), 860–863.

133. R. Kobayashi, K. Oh-ishi, R. Tu, T. Goto. Sintering behavior, microstructure, and thermal conductivity of dense AlN ceramics processed by spark plasma sintering with Y_2O_3–CaO–B additives. *Ceramics International* **2015**, 41 (1, Part B), 1897–1901.

134. J. Zhan, Y. Wu, H. Zhang, et al. Secondary phases, microstructures and properties of AlN ceramics sintered by adding nitrate sintering additives. *Advances in Applied Ceramics* **2015**, 114 (2), 77–81.

135. J. Zhan, Y. Cao, H. Zhang, et al. Low-Temperature Sintering of AlN Ceramics by Sm_2O_3-Y_2O_3-CaO Sintering Additives Formed via Decomposition of Nitrate Solutions. *Journal of Materials Engineering and Performance* **2017**, 26 (1), 453–459.

136. P. Yang, L. Wang, W. Zhao, L. Cai, Y. Feng. Hot-pressing sintered AlN-BN ceramics with high thermal conductivity and low dielectric loss. *Ceramics International* **2020**, 46 (6), 8431–8437.

137. Q. Li, Y. Zhang, H. Gong, et al. Effects of graphene on the thermal conductivity of pressureless-sintered SiC ceramics. *Ceramics International* **2015**, 41 (10, Part A), 13547–13552.

138. K.J. Kim, K.-Y. Lim, Y.-W. Kim. Electrical and Thermal Properties of SiC Ceramics Sintered with Yttria and Nitrides. *Journal of the American Ceramic Society* **2014**, 97 (9), 2943–2949.

139. J.-H. Eom, Y.-K. Seo, Y.-W. Kim. Mechanical and Thermal Properties of Pressureless Sintered Silicon Carbide Ceramics with Alumina–Yttria–Calcia. *Journal of the American Ceramic Society* **2016**, 99 (5), 1735–1741.

140. W. Wang, D. Yao, H. Liang, et al. Effect of in-situ formed Y_2O_3 by metal hydride reduction reaction on thermal conductivity of β-Si_3N_4 ceramics. *Journal of the European Ceramic Society* **2020**, 40 (15), 5316–5323.

141. W. Wang, D. Yao, H. Liang, et al. Improved thermal conductivity of β-Si_3N_4 ceramics through the modification of the liquid phase by using GdH_2 as a sintering additive. *Ceramics International* **2021**, 47 (4), 5631–5638.

142. C. Yang, F. Ye, J. Ma, et al. Comparative study of fluoride and non-fluoride additives in high thermal conductive silicon nitride ceramics fabricated by spark plasma sintering and post-sintering heat treatment. *Ceramics International* **2018**, 44 (18), 23202–23207.

143. M. Darabi, M. Rajabi, N. Nasiri. Microstructural, mechanical and thermal properties of microwave sintered Cu-MWCNT nanocomposites. *Journal of Alloys and Compounds* **2020**, 822, 153675.

144. M.S. Abd-Elwahed, A.F. Meselhy. Experimental investigation on the mechanical, structural and thermal properties of Cu–ZrO_2 nanocomposites hybridized by graphene nanoplatelets. *Ceramics International* **2020**, 46 (7), 9198–9206.

145. F. Ogawa, S. Yamamoto, C. Masuda. Thermal Conductivity and Tensile Properties of Carbon Nanofiber-Reinforced Aluminum-Matrix Composites Fabricated via Powder Metallurgy: Effects of Ball Milling and Extrusion Conditions on Microstructures and Resultant Composite Properties. *Acta Metall. Sin. (Engl. Lett.)* **2019**, 32 (5), 573–584.

146. Y.D. Kim, N.L. Oh, S.-T. Oh, I.-H. Moon. Thermal conductivity of W–Cu composites at various temperatures. *Materials Letters* **2001**, 51 (5), 420–424.

147. X. He, F. Ye, H. Zhang, Z. Zhou. Study on microstructure and thermal conductivity of Spark Plasma Sintering AlN ceramics. *Materials & Design* **2010**, 31 (9), 4110–4115.

148. A.L. Molisani, H. Goldenstein, H.N. Yoshimura. Second-phase evolution and densification behavior of AlN with $CaO–Y_2O_3–C$ multicomponent additive system. *Ceramics International* **2022**, 48 (5), 6615–6626.

149. C. Liu, W. Guo, S. Sun, et al. Texture, microstructures, and mechanical properties of AlN-based ceramics with $Si_3N_4–Y_2O_3$ additives. *Journal of the American Ceramic Society* **2017**, 100 (8), 3380–3384.

150. L. Qiao, S. Chen, L. Jiang, K. Shinozaki, S. Che. Sintering behavior of aluminum nitride powder prepared by self-propagating high-temperature synthesis method. *Rare Metals* **2018**, 37 (12), 1091–1095.

151. H. Zhou, Y. Liu, W. Miao, Y. Wu. Effects of binary additives $B_2O_3–Y_2O_3$ on the microstructure and thermal conductivity of aluminum nitride ceramics. *Journal of Materials Science* **1999**, 34 (24), 6165–6168.

152. H.M. Lee, K. Bharathi, D.K. Kim. Processing and Characterization of Aluminum Nitride Ceramics for High Thermal Conductivity. *Advanced Engineering Materials* **2014**, 16 (6), 655–669.

153. J. Lv, Z. Wang, S. Ma. Calculation method and its application for energy consumption of ball mills in ceramic industry based on power feature deployment. *Advances in Applied Ceramics* **2020**, 119 (4), 183–194.

154. M. Lu, N. Fatah, A.Y. Khodakov. New shearing mechanical coating technology for synthesis of alumina-supported cobalt Fischer–Tropsch solid catalysts. *Journal of Materials Chemistry A* **2017**, 5 (19), 9148–9155.

155. Cyclomix | high shear impact mixer | Hosokawa Micron https://www.hosokawa-micron-bv.com/process-technologies/powder-mixers/cyclomix-high-shear-impact-mixer.html (accessed Apr 26, 2023).

156. M. Hertel, E. Schwarz, M. Kobler, et al. The influence of high shear mixing on ternary dry powder inhaler formulations. *International Journal of Pharmaceutics* **2017**, 534 (1), 242–250.

157. C.M. Lampert. Coatings for enhanced photothermal energy collection I. Selective absorbers. *Solar Energy Materials* **1979**, 1 (5), 319–341.

158. H.O. Pierson. Handbook of Chemical Vapor Deposition: Principles, Technology and Applications; William Andrew, **1999**.

159. D.M. Mattox. Handbook of Physical Vapor Deposition (PVD) Processing; William Andrew, **2010**.

160. Chemical Solution Deposition of Functional Oxide Thin Films, 1st ed.; Schneller, T., Waser, R., Kosec, M., Payne, D., Eds.; Springer, Vienna, **2013**.

161. Sol-Gel Technologies for Glass Producers and Users; Aegerter, M. A., Mennig, M., Eds.; Springer US, Boston, MA, **2004**.

162. H.-J. Streitberger, A. Goldschmidt. BASF Handbook Basics of Coating Technology, 3rd Edition.; European Coatings, **2018**.

163. A. Bejan. Heat Transfer; John Wiley & Sons, Newyork, **1993**.

164. D. Baillis, M. Raynaud, J.F. Sacadura. Determination of Spectral Radiative Properties of Open Cell Foam: Model Validation. *Journal of Thermophysics and Heat Transfer* **2000**, 14 (2), 137–143.

165. P.J. Burns, C.L. Tien. Natural convection in porous media bounded by concentric spheres and horizontal cylinders. *International Journal of Heat and Mass Transfer* **1979**, 22 (6), 929–939.

166. L.W. Hrubesh, R.W. Pekala. Thermal properties of organic and inorganic aerogels. *Journal of Materials Research* **1994**, 9 (3), 731–738.

167. S. Du, M.-J. Li, Q. Ren, Q. Liang, Y.-L. He. Pore-scale numerical simulation of fully coupled heat transfer process in porous volumetric solar receiver. *Energy* **2017**, 140, 1267–1275.

168. Handbook of Porous Media, 3rd ed.; Vafai, K., Ed.; CRC Press, Boca Raton, **2015**.

169. G.A. Maugin. The Thermomechanics of Nonlinear Irreversible Behaviors: An Introduction; World Scientific Series on Nonlinear Science Series A; WORLD SCIENTIFIC, **1999**; Vol. 27.

170. D. Nield. Effects of local thermal nonequilibrium in steady convective processes in a saturated porous medium: Forced convection in a channel. *Journal of Porous Media* **1998**, 1.

171. J. Bear, Y. Bachmat. Introduction to Modeling of Transport Phenomena in Porous Media; Springer Science & Business Media, **2012**.

172. D.A. Nield, A. Bejan. Convection in Porous Media; Springer, New York, NY, **2013**.

173. N. Bannach. Thermal Equilibrium and Nonequilibrium Heat Transfer in Porous Media. *COMSOL Blog*.

174. J. Wang, Z. Xu, H. Wang, et al. Structural Design and Thermal Performance Analysis of Heat Source Used in Radioisotope Thermophotovoltaic. Rochester, NY June 24, 2022.

175. Solomenko. Heat Transfer with Radiation in Participating Media and the Discrete Ordinates Method. *COMSOL*.

176. A.L. Avila-Marin, J. Fernandez-Reche, A. Martinez-Tarifa. Modelling strategies for porous structures as solar receivers in central receiver systems: A review. *Renewable and Sustainable Energy Reviews* **2019**, 111, 15–33.

177. M.F. Modest. Radiative Heat Transfer, 2nd edition.; Academic Press, San Diego, **2013**.

178. N. Bannach. 4 Methods to Account for Radiation in Participating Media.

179. P. Crnjac, L. Škerget, J. Ravnik, M. Hriberšek. Implementation of the Rosseland and the P1 Radiation Models in the System of Navier-Stokes Equations with the Boundary Element Method. *Int. J. CMEM* **2017**, 5 (3), 348–358.

180. Y. Sun, S. Zheng, B. Jiang, J. Tang, F. Liu. One-dimensional P1 method for gas radiation heat transfer in spherical geometry. *International Journal of Heat and Mass Transfer* **2019**, 145, 118777.

181. N. Reddy. Introduction to the Finite Element Method, 4th Edition.; McGraw-Hill Education, **2019**.

182. G. Dhatt, G. Touzot, E. Lefrancois. Introduction. In *Finite Element Method*; John Wiley & Sons, Ltd, **2012**; pp 1–19.

183. Y. Jusheng, Y. Nan. A brief review of FEM software technique. *Advances in Engineering Software* **1993**, 17 (3), 195–200.

184. S.E. Benzley, K. Merkley, T.D. Blacker, L. Schoof. Pre- and post-processing for the finite element method. *Finite Elements in Analysis and Design* **1995**, 19 (4), 243–260.

185. Ch. Reichl, K. Kramer, Ch. Thoma, P. Benovsky, T. Lemée. Comparison of modelled heat transfer and fluid dynamics of a flat plate solar air heating collector towards experimental data. *Solar Energy* **2015**, 120, 450–463.

186. P. Wang, J.B. Li, F.W. Bai, et al. Experimental and theoretical evaluation on the thermal performance of a windowed volumetric solar receiver. *Energy* **2017**, 119, 652–661.

187. D.A. Jerebtsov, G.G. Mikhailov. Phase diagram of $CaO–Al_2O_3$ system. *Ceramics International* **2001**, 27 (1), 25–28.

188. M. Khodaei, O. Yaghobizadeh, A.A. Shahraki, S. Esmaeeli. Investigation of the effect of $Al_2O_3–Y_2O_3–CaO$ (AYC) additives on sinterability, microstructure and mechanical properties of SiC matrix composites: A review. *International Journal of Refractory Metals and Hard Materials* **2019**, 78, 9–26.

189. W. Wang, B. Zhang, Y. Shi, et al. Improved chemical mechanical polishing performance in 4H-SiC substrate by combining novel mixed abrasive slurry and photocatalytic effect. *Applied Surface Science* **2022**, 575, 151676.

190. Y.-W. Kim, S. Kultayeva, J. Sedláček, et al. Thermal and electrical properties of additive-free rapidly hot-pressed SiC ceramics. *Journal of the European Ceramic Society* **2020**, 40 (2), 234–240.

191. P. Nguyen, D. Edouard, J.-M. Nhut, et al. High thermal conductive β-SiC for selective oxidation of H2S: A new support for exothermal reactions. *Applied Catalysis B: Environmental* **2007**, 76 (3), 300–310.

192. Y. Ouabbas, J. Dodds, L. Galet, A. Chamayou, M. Baron. Particle–particle coating in a cyclomix impact mixer. *Powder Technology* **2009**, 189 (2), 245–252.

193. A. Sato, E. Serris, P. Grosseau, et al. Experiment and simulation of dry particle coating. *Chemical Engineering Science* **2013**, 86, 164–172.

194. G. Thomas, Y. Ouabbas, P. Grosseau, et al. Modeling the mean interaction forces between powder particles. Application to silica gel–magnesium stearate mixtures. *Applied Surface Science* **2009**, 255 (17), 7500–7507.

195. S. Islak, D. Kır, S. Buytoz. Effect of sintering temperature on electrical and microstructure properties of hot pressed Cu-TiC composites. *Science of Sintering* **2014**, 46 (1), 15–21.

196. R. Shrinivas Mahale, V. Shamanth, P.C. Sharath, R. Shashanka, K. Hemanth. A review on spark plasma sintering of duplex stainless steels. *Materials Today: Proceedings* **2021**, 45, 138–144.

197. B.B. Bokhonov, D.V. Dudina, A.V. Ukhina, et al. Formation of self-supporting porous graphite structures by Spark Plasma Sintering of nickel–amorphous carbon mixtures. *Journal of Physics and Chemistry of Solids* **2015**, 76, 192–202.

198. AccuPyc II: Gas Displacement Pycnometry System https://www.micromeritics.com/accupyc-ii/.

199. S.J. Blott, D.J. Croft, K. Pye, S.E. Saye, H.E. Wilson. Particle size analysis by laser diffraction. *Geological Society, London, Special Publications* **2004**, 232 (1), 63–73.

200. C. Tang, B. Auguié, E.C. Le Ru. Thin-shell approximation of Mie theory for a thin anisotropic layer spaced away from a spherical core: Application to dye-coated nanostructures. *Phys. Rev. A* **2021**, 104 (3), 033502.

201. N. Fatah. Study and comparison of micronic and nanometric powders: Analysis of physical, flow and interparticle properties of powders. *Powder Technology* **2009**, 190 (1), 41–47.

202. Overview of Important Particle Characterization Techniques https://www.azom.com/article.aspx?ArticleID=9937.

203. S. Brunauer, P.H. Emmett, E. Teller. Adsorption of Gases in Multimolecular Layers. *J. Am. Chem. Soc.* **1938**, 60 (2), 309–319.

204. Determination of specific surface by the BET method | SpringerLink https://link.springer.com/article/10.1007/BF02479039.

205. T. Horikawa, D.D. Do, D. Nicholson. Capillary condensation of adsorbates in porous materials. *Advances in Colloid and Interface Science* **2011**, 169 (1), 40–58.

206. H.Y. Saw, C.E. Davies, A.H.J. Paterson, J.R. Jones. Correlation between Powder Flow Properties Measured by Shear Testing and Hausner Ratio. *Procedia Engineering* **2015**, 102, 218–225.

207. S. Santhalakshmy, S.J. Don Bosco, S. Francis, M. Sabeena. Effect of inlet temperature on physicochemical properties of spray-dried jamun fruit juice powder. *Powder Technology* **2015**, 274, 37–43.

208. Theoretical analysis of SE and BSE signals applied to SEM multiple detector systems https://9lib.org/document/nq76d4dy-theoretical-analysis-bse-signals-applied-multiple-detector-systems.html (accessed Oct 5, 2022).

209. A.S. Ali. Application of Nanomaterials in Environmental Improvement; IntechOpen, **2020**.

210. C.Y. Tang, Z. Yang. Chapter 8 - Transmission Electron Microscopy (TEM). In *Membrane Characterization*; Hilal, N., Ismail, A. F., Matsuura, T., Oatley-Radcliffe, D., Eds.; Elsevier, **2017**; pp 145–159.

211. L.R.B. Elton, D.F. Jackson. X-Ray Diffraction and the Bragg Law. *American Journal of Physics* **1966**, 34 (11), 1036–1038.

212. S. Baskaran. Structure and regulation of yeast glycogen synthase. Thesis, **2010**.

213. X-Ray Fluorescence Spectroscopy (XRF) – Basics https://xrf-spectroscopy.com/ (accessed May 28, 2023).

214. R.C. Kerschbaumer, S. Stieger, M. Gschwandl, et al. Comparison of steady-state and transient thermal conductivity testing methods using different industrial rubber compounds. *Polymer Testing* **2019**, 80, 106121.

215. S. Min, J. Blumm, A. Lindemann. A new laser flash system for measurement of the thermophysical properties. *Thermochimica Acta* **2007**, 455 (1), 46–49.

216. H. Wang, W.D. Porter, R.B. Dinwiddie. Laser-induced pressure-wave and barocaloric effect during flash diffusivity measurements. *Appl. Phys. Lett.* **2017**, 111 (5), 051901.

217. S. Breuer, F.R. Schilling. Improving Thermal Diffusivity Measurements by Including Detector Inherent Delayed Response in Laser Flash Method. *Int J Thermophys* **2019**, 40 (10), 95.

218. R.L. Danley. New heat flux DSC measurement technique. *Thermochimica Acta* **2002**, 395 (1), 201–208.

219. E. Morîntale, A. Harabor, C. Constantinescu, P. Rotaru. Use of heat flows from DSC curve for calculation of specific heat of the solid materials. *Physics AUC* **2013**, 23, 89–94.

220. J.A. Jacquez, H.F. Kuppenheim. Theory of the Integrating Sphere. *J. Opt. Soc. Am., JOSA* **1955**, 45 (6), 460–470.

221. 63362 Quartz Tungsten Halogen Lamp https://www.newport.com/p/63362 (accessed Jul 23, 2023).

222. Solar Power Plants: Fundamentals, Technology, Systems, Economics; Winter, C.-J., Sizmann, R. L., Vant-Hull, L. L., Eds.; Springer, Berlin, Heidelberg, **1991**.

223. D.S. Codd, A. Carlson, J. Rees, A.H. Slocum. A low cost high flux solar simulator. *Solar Energy* **2010**, 84 (12), 2202–2212.

224. Y. Kang, N. Li, C. Weng, C. Wang. Acoustic characteristics of pulse detonation engine with ellipsoidal reflector*. *Chinese Phys. B* **2018**, 27 (10), 104703.

225. M.A. Kant, P. Rudolf von Rohr. Determination of surface heat flux distributions by using surface temperature measurements and applying inverse techniques. *International Journal of Heat and Mass Transfer* **2016**, 99, 1–9.

226. A.S. Nouman, A. Chokhachian, D. Santucci, T. Auer. Prototyping of Environmental Kit for Georeferenced Transient Outdoor Comfort Assessment. *ISPRS International Journal of Geo-Information* **2019**, 8 (2), 76.

227. M. Saifullah, Y.A. Yusof, N.L. Chin, M.G. Aziz. Physicochemical and flow properties of fruit powder and their effect on the dissolution of fast dissolving fruit powder tablets. *Powder Technology* **2016**, 301, 396–404.

228. J. Kang, G.X. Dong, Q.X. Liu. Research on Properties of AlN-Mo Composite Ceramic. *Advanced Materials Research* **2012**, 482–484, 1695–1698.

229. M. Qin, H. Lu, H. Wu, et al. Powder injection molding of complex-shaped aluminium nitride ceramic with high thermal conductivity. *Journal of the European Ceramic Society* **2019**, 39 (4), 952–956.

230. R.-X. Luo, M. Kermani, Z.-L. Guo, et al. Ultrafast high-temperature sintering of silicon nitride: A comparison with the state-of-the-art techniques. *Journal of the European Ceramic Society* **2021**, 41 (13), 6338–6345.

231. G. Nie, P. Sheng, Y. Li, et al. Enhanced mechanical and thermal properties of AlN ceramics via a chemical precipitation process. *International Journal of Applied Ceramic Technology* **2021**, 18 (4), 1255–1268.

232. M. Thommes, K. Kaneko, A.V. Neimark, et al. Physisorption of gases, with special reference to the evaluation of surface area and pore size distribution (IUPAC Technical Report). *Pure and Applied Chemistry* **2015**, 87 (9–10), 1051–1069.

233. R. Malik, Y.-H. Kim, Y.-W. Kim. Effect of additive content on the mechanical and thermal properties of pressureless liquid-phase sintered SiC. *Journal of Asian Ceramic Societies* **2020**, 8 (2), 448–459.

234. Q. Li, V. Rudolph, W. Peukert. London-van der Waals adhesiveness of rough particles. *Powder Technology* **2006**, 161 (3), 248–255.

235. M. Shabani, M.H. Paydar, R. Zamiri, M. Goodarzi, M.M. Moshksar. Microstructural and sliding wear behavior of SiC-particle reinforced copper matrix composites fabricated by sintering and sinter-forging processes. *Journal of Materials Research and Technology* **2016**, 5 (1), 5–12.

236. P. Bazarnik, S. Nosewicz, B. Romelczyk-Baishya, et al. Effect of spark plasma sintering and high-pressure torsion on the microstructural and mechanical properties of a Cu–SiC composite. *Materials Science and Engineering: A* **2019**, 766, 138350.

237. C. Heisel, C. Caliot, T. Chartier, et al. Digital design and 3D printing of innovative SiC architectures for high temperature volumetric solar receivers. *Solar Energy Materials and Solar Cells* **2021**, 232, 111336.

238. B. Rousseau, S. Guevelou, J. Vicente, C. Caliot, G. Flamant. Tuning the Spectral Selectivity of Sic-Based Volumetric Solar Receivers With Ultra-High Temperature Ceramic Coatings. In *Ceramics for Energy Conversion, Storage, and Distribution Systems*; John Wiley & Sons, Ltd, **2016**; pp 227–238.

239. J. Sarasook, C. Thongchaisuratkrul. An Implementation of Illuminance Meter Using Light Dependent Resistor Integrated with Labview Program. *Industry Technology Lampang Rajabhat University* **2018**, 11 (1), 1–11.

240. E. Marín. Linear relationships in heat transfer. *Latin-American Journal of Physics Education* **2009**, 3 (2), 9.

241. Ch. Pichler, R. Traxl, R. Lackner. Power-law scaling of thermal conductivity of highly porous ceramics. *Journal of the European Ceramic Society* **2015**, 35 (6), 1933–1941.

242. V. Dao, H. Choi. Carbon-Based Sunlight Absorbers in Solar-Driven Steam Generation Devices. *Global Challenges* **2018**, 2 (2), 1700094.

243. A. Dobrosavljevic, N. Perovic, K. Maglic. Thermophysical properties of POCO AXM-5Q1 graphite in the 300 to 1800 K range. *High Temperatures-High Pressures* **1987**, 19, 303–310.

244. COMSOL Multiphysics. Wavelength Dependence of Surface Emissivity and Absorptivity https://doc.comsol.com/5.5/doc/com.comsol.help.heat/heat_ug_theory.07.38.html (accessed Mar 25, 2023).

245. P.R. Michael, D.E. Johnston, W. Moreno. A conversion guide: solar irradiance and lux illuminance. *Journal of Measurements in Engineering* **2020**, 8 (4), 153–166.

Nouveau procédé de mise en forme de matériaux composites et modélisation numérique pour les applications par voie solaire thermique

L'énergie solaire, une alternative durable et non polluante aux combustibles fossiles, gagne en importance grâce aux propriétés améliorées des matériaux. Cette étude propose une approche novatrice pour les matériaux composites de récepteur solaire, intégrant une couche d'absorption et un substrat conducteur thermique. Diverses poudres, dont l'AlN, l'α-SiC, le Cu, l'acier inoxydable, le CaO (à l'échelle micronique, submicronique et nanométrique), le β-SiC, le γ-Al_2O_3 et le noir de carbone, ont été explorées. Des procédés innovants sans solvants et sans traitement thermique ont été introduits pour le mélange et le revêtement des poudres. Les pastilles, produites par frittage à plasma, comprennent de l'AlN avec des additifs CaO, de l'α-SiC avec des additifs CaO et Al_2O_3, du Cu avec du β-SiC, et de l'acier inoxydable. Le dépôt du matériau absorbeur solaire a utilisé du noir de carbone. Le simulateur solaire auto-construit a évalué l'absorption d'énergie et l'efficacité de transfert de chaleur. La méthode des éléments finis a simulé le transfert de chaleur radiatif et conducteur dans les pastilles poreuses composites. Les formes géométriques alignées avec les structures des pastilles pour des comparaisons précises. Le Picomix s'est avéré supérieur au broyage à billes traditionnel pour préparer des poudres mélangées, offrant une approche sans solvant et respectueuse de l'environnement. Atteignant une conductivité thermique de 135,3 W/m·K, la pastille d'AlN avec 3 % en poids de nano CaO à une vitesse de rotation de 5000 tr/min a excellé. Le revêtement à sec de β-SiC par Picomix a efficacement réduit l'oxydation du Cu tout en maintenant une conductivité thermique élevée, présentant une méthode prometteuse de traitement anti-oxydation. L'ajout de 9 % en poids d'Al_2O_3 et de CaO à l'α-SiC a élevé la conductivité thermique de sa pastille à 114 W/m·K. Sous le flux thermique radiatif élevé du simulateur solaire, les composites AlN-additif avec couche de carbone et les pastilles α-SiC-additif ont présenté une amélioration de l'absorption d'énergie solaire et du transfert de chaleur. Les résultats de la modélisation ont souligné l'influence combinée de l'épaisseur, de la porosité et de la conductivité thermique sur le transfert de chaleur des pastilles poreuses. Pour des pastilles d'épaisseur inférieure à 50 mm, une porosité inférieure à 0,3 et une conductivité thermique dépassant 100 W/m·K, l'efficacité de transfert de chaleur est restée comparable. L'épaisseur de la couche d'absorption solaire a eu un impact significatif sur le taux de transfert de chaleur des pastilles poreuses/composites. La conductivité thermique du matériau absorbeur solaire a eu peu d'impact sur l'absorption d'énergie solaire et l'efficacité de transfert de chaleur au-delà de 50 W/m·K. Diverses configurations géométriques ont produit des résultats de simulation comparables.

Mots-clefs : Solaire thermique, transfert thermique, procédé de mélange sans solvant, élaboration des matériaux, simulateur solaire, modélisation FEM

New fabrication process for composite materials and numerical modelling for solar thermal applications

Solar energy, a sustainable and non-polluting alternative to fossil fuels, gains momentum with enhanced material properties. This study proposes a novel approach for composite solar receiver materials, integrating an absorption layer and a thermal conductive substrate. Various powders, including AlN, α-SiC, Cu, stainless steel, CaO (micron, submicron, and nano-scale), β-SiC, γ-Al_2O_3, and carbon black, were explored. Innovative solvent-free processes and heat-treatment-free techniques were introduced for powder mixing and coating. Pellets, produced by spark plasma sintering, include AlN with CaO additives, α-SiC with CaO and Al_2O_3 additives, Cu with β-SiC, and stainless steel. Solar absorber material deposition utilized carbon black. The self-constructed solar simulator assessed energy absorption and heat transfer efficiency. Finite element method simulated radiative and conductive heat transfer in composite porous pellets. Geometric shapes aligned with pellet structures for accurate comparisons. The Picomix proved superior to traditional ball milling for preparing mixed powders, offering a solvent-free and eco-friendly approach. Achieving a thermal conductivity of 135.3 W/m·K, the AlN pellet with 3 wt% nano CaO at 5000 rpm rotational speed exceled. Dry-coating β-SiC by Picomix effectively reduced Cu oxidation while maintaining high thermal conductivity, presenting a promising anti-oxidation treatment. Adding 9 wt% Al_2O_3 and CaO to α-SiC elevated its pellet thermal conductivity to 114 W/m·K. Under the solar simulator's high radiative heat flux, AlN-additive with carbon layer composites and α-SiC-additive pellets exhibited enhanced solar energy absorption and heat transfer. Modeling results underscored the combined influence of thickness, porosity, and thermal conductivity on porous pellet heat transfer. For pellets with thickness below 50 mm, porosity less than 0.3, and thermal conductivity surpassing 100 W/m·K, heat transfer efficiency remained comparable. The solar absorption layer's thickness significantly impacted composite porous pellet heat transfer rate. Solar absorber material's thermal conductivity minimally affected solar energy absorption and heat transfer efficiency beyond 50 W/m·K. Diverse geometric model configurations yielded comparable simulation outcomes.

Keywords: Solar thermal, heat transfer, dry mixing, material manufacturing, solar simulator, FEM modeling

Centrale Lille
Cité Scientifique – CS20048 – 59651 Villeneuve d'Ascq Cedex – France
Tél. + 33 (0)3 20 33 53 53 – https://centralelille.fr